SHANGHAI JIAO TONG UNIVERSITY

# Structure-preserving Parametric Finite Element Methods for Extrinsic Anisotropic Geometric Flows

Yulin Zhang

Doctoral Dissertation

School of Mathematical Sciences
Mathematics

Supervisor: Prof. Wenjun Ying

Shanghai, 2026

# Preface

This English edition follows the organization and mathematical scope of the Chinese doctoral dissertation. The chapters draw on the author's published and unpublished work on anisotropic geometric flows. Their terminology and exposition have been harmonized for a single thesis, while the equation labels, proofs, and numerical examples are retained wherever possible.

Chapters 2 and 3 are based on the stabilized surface-diffusion method and the method with an optimal energy stability condition, respectively. Chapter 5 develops the unified $\alpha$-surface energy matrix framework. Chapters 6 and 7 treat surfaces and moving contact lines. Chapter 8 includes the numerical results from the author's manuscript on coupled orientation and curvature dependence, arXiv:2609.36419v1. The experimental data and figures in that chapter are reproduced from this source; they are not newly computed for this edition.

The English edition uses a customized `amsbook` layout. All figures and tables are placed within the main text.

# Abstract

Anisotropic geometric flows arise in crystal growth, thin-film evolution, solid-state dewetting, and other models of interfacial motion. Their driving energy depends on the interface orientation, and their evolution is governed by geometric constraints and physical laws such as energy dissipation, conservation of enclosed area or volume, and contact-line dynamics. Strong nonlinearity and anisotropy can produce corners, necking, and topological changes. A numerical method must therefore resolve the evolving geometry while retaining the relevant structural laws and an adequate mesh.

This thesis develops structure-preserving parametric finite element methods for anisotropic geometric flows on planar curves and surfaces in three dimensions. The analysis proceeds from a surface energy matrix to a conservative weak formulation, a local energy estimate, and a fully discrete energy inequality. This approach treats anisotropic surface diffusion and curvature flow, and extends to crystalline thin films and solid-state dewetting with moving contact lines.

The main contributions are as follows.

- We characterize optimal energy stability conditions within the local energy estimate framework. In two dimensions, a symmetric surface energy matrix attains the condition $3\hat{\gamma}(\theta) - \hat{\gamma}(\theta - \pi) \geq 0$, without an additional restriction at equality. The resulting surface-diffusion scheme preserves enclosed area and dissipates energy without a time-step restriction. A preceding stabilized formulation also accommodates globally $C^1$, piecewise $C^2$ densities under its stated critical-case assumptions.
- We introduce an $\alpha$-surface energy matrix that unifies a family of conservative formulations and parametric discretizations. The framework gives a common energy stability analysis and identifies the symmetric choice $\alpha = -1$ as the unique parameter attaining the non-strict optimal directional condition within the analyzed family. The corresponding three-dimensional condition is $2\gamma(\boldsymbol{n}) - \gamma(-\boldsymbol{n}) \geq 0$. A formulation of the normal velocity as a map depending on both geometric quantities and the background manifold provides a consistent extension to other anisotropic flows.
- We extend the methods to crystalline-film evolution and solid-state dewetting. A relaxed contact-angle condition couples the interface to the moving contact line within the weak formulation. The resulting schemes preserve enclosed area or volume and dissipate the discrete energy. Numerical examples investigate anisotropy-induced necking, multiple equilibria, and the effects of initial geometry and contact-line dynamics.

The thesis also treats energies $W(\Gamma) = \int_\Gamma f(\boldsymbol{n}, H)\,\mathrm{d}A$ coupling orientation and mean curvature. A mass-lumped projection of the curvature derivative pairs the symmetric surface energy matrix with a discrete curvature evolution equation. Under convexity in curvature and the local directional energy estimate, the fully discrete scheme dissipates energy. Its conservative variants preserve discrete volume. Numerical results taken from the author's manuscript on coupled orientation and curvature dependence exhibit approximately second-order convergence in the manifold distance, confirm the structural properties to nonlinear-solver accuracy, and illustrate anisotropic bending and Helfrich-type shape relaxation. Solvability, rigorous error analysis, and the consistency of evolved and geometric curvature remain subjects for further study.

**Keywords:** geometric flows; parametric finite element method; anisotropic surface energy; structure preservation; area and volume conservation; energy stability; curvature-dependent energy.

# Contents


Preface i

Abstract iii

List of Figures vii

List of Tables xiii

Notation xv

Chapter 1. Introduction 1
1.1. Physical background 1
1.2. Surface energy and anisotropy 2
1.3. Typical anisotropic geometric flows 5
1.4. Equilibria of conservative geometric flows 7
1.5. Literature review 7
1.6. Contributions of this thesis 11

Chapter 2. A stabilized parametric finite element method for curve evolution 15
2.1. Common anisotropic surface energies 16
2.2. A conservative form for two-dimensional surface diffusion 16
2.3. A stabilized parametric finite element method for surface diffusion 18
2.4. Proof of unconditional energy stability 24
2.5. Numerical experiments 29
2.6. Chapter summary 32

Chapter 3. A structure-preserving parametric finite element method with an optimal energy stability condition 35
3.1. A symmetric surface energy matrix and a symmetrized conservative form 35
3.2. A symmetrized structure-preserving parametric finite element scheme 36
3.3. Proof of unconditional energy stability 38
3.4. Numerical experiments 41
3.5. Chapter summary 44

Chapter 4. Applications: two-dimensional crystalline film evolution and solid-state dewetting 47
4.1. Two-dimensional crystalline film evolution 47
4.2. Two-dimensional solid-state dewetting 49

Chapter 5. Structure-preserving parametric approximation via an $\alpha$-surface energy matrix: anisotropic curve evolution 61
5.1. A unified $\alpha$-surface energy matrix 62
5.2. Structure-preserving parametric finite element discretization via the $\alpha$-surface energy matrix 63
5.3. Proof of unconditional energy stability 66
5.4. Existence of the minimal stabilizing function 68
5.5. Extensions to other geometric flows 71
5.6. Numerical experiments 74
5.7. Chapter summary 85

Chapter 6. Structure-preserving parametric approximation based on the $\alpha$-surface energy matrix: anisotropic surface evolution 87
6.1. Geometric evolution equations 87
6.2. The $\alpha$-surface energy matrix and a conservative formulation 89
6.3. Structure-preserving parametric finite element discretization 90
6.4. Proof of unconditional energy stability 93
6.5. Existence of the minimal stabilizing function 96
6.6. Numerical experiments 104
6.7. Summary 110

Chapter 7. Application: solid-state dewetting in three dimensions 113
7.1. The sharp interface model 113
7.2. Structure-preserving parametric finite element discretization 114
7.3. Morphological evolution of open surfaces in solid-state dewetting 117

Chapter 8. Geometric gradient flows with curvature-dependent surface energy 123
8.1. Surface energy and geometric identities 123
8.2. First variation and conservative weak formulations 124
8.3. A symmetric surface energy matrix at fixed curvature 126
8.4. A fully discrete scheme with an auxiliary projection 126
8.5. Fully discrete energy dissipation 128
8.6. Volume-preserving gradient flows 128
8.7. Numerical results 129
8.8. Concluding remarks 136

Chapter 9. Conclusions and future work 139
9.1. Main results 139
9.2. Directions for further study 140

Appendix A. Solvers for the nonlinear schemes 141
A.1. Iterative solvers for curve evolution 141
A.2. Iterative solvers for surface evolution 142

Appendix B. Three-dimensional anisotropic surface energies 143

Bibliography 145

Notation Index 153

Subject Index 155

# List of Figures


1.1 Under surface-diffusion-driven dewetting, a solid thin film breaks up into multiple isolated hemispherical islands; the image is adapted from [136]. 1

1.2 Instabilities induced by anisotropy: pinch-off (top), fingering instability (bottom left), and faceting instability (bottom right). The figure is adapted from [100, 152, 146]. 2

1.3 Several Frank diagrams of two-dimensional anisotropies. From left to right, top to bottom: three-fold symmetric anisotropy with $\beta = \frac{1}{9}$; three-fold symmetric anisotropy with $\beta = \frac{1}{3}$; piecewise anisotropy; piecewise BGN anisotropy; $l^1$-norm anisotropy; $\gamma(\boldsymbol{n}) = 1 + \frac{1}{4}(n_1^4 + n_2^4)$; $\gamma(\boldsymbol{n}) = 1 + \frac{1}{2}(n_1^6 + n_2^6)$. 3

1.4 Several Frank diagrams of three-dimensional anisotropies. From left to right, top to bottom: three-fold symmetric anisotropy with $\beta = \frac{1}{4}$; cubic anisotropy with $\beta = \frac{1}{3}$; [001]-oriented anisotropy with $\beta = \frac{1}{2}$; piecewise BGN anisotropy; $l^4$-norm anisotropy; [111]-oriented anisotropy with $\beta = \frac{1}{2}$. 4

1.5 Several $\xi$-plots of three-dimensional anisotropies. From left to right, top to bottom: isotropic; ellipsoidal anisotropy; piecewise BGN anisotropy; three-fold symmetric anisotropy with $\beta = \frac{1}{4}$; cubic anisotropy with $\beta = \frac{1}{4}$; cubic anisotropy with $\beta = 1$. 5

1.6 Wulff shapes of several anisotropies corresponding to the Frank diagrams in Figure 1.4. 7

1.7 The $\gamma$-plots, Frank diagrams, $\xi$-plots, and Wulff shapes for several three-dimensional anisotropies. From top to bottom: $l^1$-norm anisotropy; piecewise BGN anisotropy; cubic anisotropy with $\beta = \frac{1}{4}$; cubic anisotropy with $\beta = 1$. 8

1.8 Evolution of a spindle-shaped surface under mean curvature flow simulated by Dziuk's method; the figure is adapted from [102]. 9

1.9 Evolution of a spindle-shaped surface under mean curvature flow simulated by the BGN method; the figure is adapted from [102]. 10

1.10 Dissertation structure overview. 12

2.1 Convergence rates of the SPFEM (2.52) with $k(\theta) = k_0(\theta)$ for (a) anisotropy in Case I at $t = 0.5$ with different $\beta$; (b) anisotropy in Case II with $b = -0.8$ at different times $t = 0.125, 0.25, 0.5$. 30

2.2 Convergence rates of the SPFEM (2.52) for Case I at $t = 0.5$ with different $k(\theta)$: (a) $\beta = 0$; (b) $\beta = 1/9$. 31

2.3 Weighted mesh ratio of the SPFEM (2.52) with $k(\theta) = k_0(\theta)$ for (a) anisotropy in Case I with $\beta = \frac{1}{9}$; (b) anisotropy in Case II with $b = -0.8$. 31

2.4 Normalized area loss (blue dashed line) and number of Newton iterations (red line) of the SPFEM (2.52) with $k(\theta) = k_0(\theta)$ and $h = 2^{-7}, \tau = 2^{-10}$ for (a) anisotropy in Case I with $\beta = \frac{1}{2}$; (b) anisotropy in Case II with $b = -0.8$. 31

2.5 Normalized energy for (a) anisotropy in Case I with $\beta = \frac{1}{2}$; (b) anisotropy in Case II with $b = -0.8$. 32

2.6 Morphological evolution of an ellipse with major axis 4 and minor axis 1 under anisotropic surface diffusion with different surface energies: (a) anisotropy in Case I with $\beta = \frac{1}{2}$; (b) anisotropy in Case II with $b = -0.8$; (c) $\hat{\gamma}(\theta) = 1 + \frac{1}{16}\cos 4\theta$; (d)

$\hat{\gamma}(\theta) = \sqrt{\left(\frac{5}{2} + \frac{3}{2}\mathrm{sgn}(n_1)\right) n_1^2 + n_2^2}$ with $\boldsymbol{n} = (n_1, n_2)^T = (-\sin\theta, \cos\theta)^T$. The red and blue lines represent the initial shape and the numerical equilibrium, respectively. The black dashed lines represent the intermediate curves. The mesh size and the time step are taken as $h = 2^{-7}, \tau = 2^{-10}$. 33

2.7 Morphological evolution of a four-fold star-shaped curve and a rotated ellipse under anisotropic surface diffusion with different surface energies: (a) anisotropy in Case I with $\beta = \frac{1}{2}$; (b) anisotropy in Case II with $b = -0.8$; (c) $\hat{\gamma}(\theta) = 1 + \frac{1}{16}\cos 4\theta$; (d) $\hat{\gamma}(\theta) = \sqrt{\left(\frac{5}{2} + \frac{3}{2}\mathrm{sgn}(n_1)\right) n_1^2 + n_2^2}$ with $\boldsymbol{n} = (n_1, n_2)^T = (-\sin\theta, \cos\theta)^T$. The red and blue lines represent the initial shape and the numerical equilibrium, respectively. The black dashed lines represent the intermediate curves. The mesh size and the time step are taken as $h = 2^{-7}, \tau = 2^{-10}$. 34

3.1 Minimal stabilizing function $k_0(\theta)$ and upper bound $K(\theta)$ in (3.17) for Case I with $\beta = \frac{1}{2}$. 42

3.2 Convergence rates of the SP-PFEM (3.12) for Case I with $\beta = 1/9$ (a) at different times with $k(\theta) = k_0(\theta)$, and (b) at $t = 0.5$ with different $k(\theta)$; and for Case II (c) at different times with $k(\theta) = k_0(\theta)$, and (d) at $t = 0.5$ with different $k(\theta)$. 42

3.3 Normalized area loss (blue dashed line) and number of Newton iterations (red line) of the SP-PFEM (3.12) with $k(\theta) = k_0(\theta)$ and $h = 2^{-6}, \tau = 2^{-12}$ for (a) Case I with $\beta = 1/2$; (b) Case II. 43

3.4 Normalized energy of the SP-PFEM (3.12) with $k(\theta) = k_0(\theta)$ for (a) Case I with $\beta = 1/2$; (b) Case II. 43

3.5 Weighted mesh ratio of the SP-PFEM (3.12) for Case I with $\beta = 1/9$ is illustrated in (a) for $k(\theta) = k_0(\theta)$ with different $h$, and in (b) for different $k(\theta)$ with $h = 2^{-6}$; and for Case II is presented in (c) for $k(\theta) = k_0(\theta)$ with different $h$, and in (d) for different $k(\theta)$ with $h = 2^{-6}$. 44

3.6 Morphological evolution of an ellipse with major axis 4 and minor axis 1 under anisotropic surface diffusion with different surface energies: (a) Case I with $\beta = 1/2$; (b) Case II; (c) the 4-fold anisotropy $\hat{\gamma}(\theta) = 1 + \frac{1}{10}\cos 4\theta$; (d) the regularized crystalline anisotropy $\hat{\gamma}(\theta) = 1 + \sqrt{\varepsilon^2 + (1-\varepsilon^2)\sin^2\frac{m}{2}\theta}$, with $\varepsilon = 0.1, m = 7$. The red and blue lines represent the initial shape and the numerical equilibrium, respectively. The black dashed lines represent the intermediate curves. 45

4.1 Normalized area and energy of a long thin film (aspect ratio of 50) governed by anisotropic surface diffusion with the 4-fold anisotropy $\hat{\gamma}(\theta) = 1 + \frac{1}{16}\cos 4\theta$. 47

4.2 The number of islands formed from the pinch-off of a $2L \times 1$ long thin film as a function of $L$ and anisotropy strength $\beta$ for: (left) the 2-fold anisotropy $\hat{\gamma}(\theta) = 1 + \beta\cos 2\theta$; (right) the 3-fold anisotropy $\hat{\gamma}(\theta) = 1 + \beta\cos 3\theta$. The solid curves separate regions producing one and two islands, and regions producing two and three islands. 48

4.3 The number of islands formed from the pinch-off of a $2L \times 1$ long thin film as a function of $L$ and anisotropy strength $\beta$ for: (left) the 4-fold anisotropy $\hat{\gamma}(\theta) = 1 + \beta\cos 4\theta$; (right) the 6-fold anisotropy $\hat{\gamma}(\theta) = 1 + \beta\cos 6\theta$. The solid curves separate regions producing one and two islands, and regions producing two and three islands. 48

4.4 Snapshots of the evolution of a $140 \times 1$ thin film under anisotropic surface diffusion with 3-fold anisotropy $\hat{\gamma}(\theta) = 1 + \frac{1}{9}\cos 3\theta$. 49

4.5 Morphological evolution of a thin film with aspect ratio 80 under surface diffusion: (left) isotropic; (right) 6-fold anisotropy $\hat{\gamma}(\theta) = 1 + \frac{1}{35.1}\cos 6\theta$. 50

4.6 An illustration of solid-state dewetting of a thin film on a flat rigid substrate in 2D, where $\gamma_{FV} = \hat{\gamma}(\theta), \gamma_{VS}, \gamma_{FS}$ denote the surface energy densities of the film/vapor, vapor/substrate, and film/substrate interfaces, respectively, and $x_c^l, x_c^r$ are the left and right contact points. 51

4.7 Convergence rates of the SPFEM (4.14) with $k(\theta) = k_0(\theta)$ and $\sigma = -\frac{\sqrt{2}}{2}$ for (a) anisotropy in Case I at $t = 0.5$ with different $\beta$; (b) anisotropy in Case II with $b = 2$ at different times $t = 0.125, 0.25, 0.5$. 54

4.8 Weighted mesh ratio of the SPFEM (4.14) with $k(\theta) = k_0(\theta)$ and $\sigma = -\frac{\sqrt{2}}{2}$ for (a) anisotropy in Case I with $\beta = \frac{1}{9}$; (b) anisotropy in Case II with $b = 2$. 54

4.9 Normalized area loss (blue dashed line) and number of Newton iterations (red line) of the SPFEM (4.14) with $k(\theta) = k_0(\theta)$, $\sigma = -\frac{\sqrt{2}}{2}$ and $h = 2^{-7}, \tau = 2^{-10}$ for (a) anisotropy in Case I with $\beta = \frac{1}{9}$; (b) anisotropy in Case II with $b = 2$. 55

4.10 Normalized energy of the SPFEM (4.14) with $k(\theta) = k_0(\theta)$ and $\sigma = -\frac{\sqrt{2}}{2}$ for (a) anisotropy in Case I with $\beta = \frac{1}{9}$; (b) anisotropy in Case II with $b = 2$. 55

4.11 Morphological evolution of an open $4 \times 1$ rectangle under anisotropic surface diffusion with different surface energies: (a) anisotropy in Case I with $\beta = \frac{1}{9}$; (b) anisotropy in Case II with $b = 2$; (c) $\hat{\gamma}(\theta) = 1 + \frac{1}{16}\cos 4\theta$; (d) $\hat{\gamma}(\theta) = \sqrt{\left(\frac{5}{2} + \frac{3}{2}\mathrm{sgn}(n_1)\right) n_1^2 + n_2^2}$ with $\boldsymbol{n} = (n_1, n_2)^T = (-\sin\theta, \cos\theta)^T$. The red and blue lines represent the initial shape and the numerical equilibrium, respectively. The black dashed lines represent the intermediate curves. The parameters are $\sigma = -\frac{\sqrt{2}}{2}, h = 2^{-7}, \tau = 2^{-10}$. 56

4.12 Generalized Winterbottom construction for surface energy $\hat{\gamma}(\theta) = 1 + 0.4\cos 4\theta$ and $\sigma = \cos\frac{5\pi}{6}$. The green and blue shaded regions are stable equilibrium shapes. 57

4.13 Multiple equilibrium shapes for the 4-fold surface energy $\hat{\gamma}(\theta) = 1 + \beta\cos 4\theta$ starting with different initial curves (shown in red dash-dotted line). The corresponding Wulff envelope is shown as a black dashed curve. The parameters are $\beta = 0.4$, $\sigma = \cos\frac{5\pi}{6}$ and $\eta = 100$. 58

4.14 Illustration of the generalized Winterbottom construction (a) and numerical equilibrium shapes (b)–(c) starting with different initial curves for the 4-fold surface energy $\hat{\gamma}(\theta) = 1 + 0.3\cos 4(\theta + \frac{\pi}{6})$ and $\sigma = 0.2$. 58

4.15 Morphological evolution of different initial shapes with the 4-fold anisotropy $\hat{\gamma}(\theta) = 1 + 0.3\cos 4\left(\theta + \frac{\pi}{6}\right)$, $\sigma = 0.2$: (a) a unit square; (b) a right trapezoid. The red and blue lines represent the initial shape and the numerical equilibrium, respectively. The black dashed lines represent the intermediate curves. 59

4.16 Illustration of the generalized Winterbottom construction (a) and numerical equilibrium shapes (b)–(c) starting with different initial curves for the 3-fold surface energy $\hat{\gamma}(\theta) = 1 + 0.3\cos 3(\theta + \frac{\pi}{6})$ and $\sigma = -0.2$. 59

4.17 Morphological evolution of different initial shapes with the 3-fold anisotropy $\hat{\gamma}(\theta) = 1 + 0.3\cos 3\left(\theta + \frac{\pi}{6}\right)$, $\sigma = -0.2$: (a) a unit square; (b) a right trapezoid. The red and blue lines represent the initial shape and the numerical equilibrium, respectively. The black dashed lines represent the intermediate curves. 59

5.1 Convergence rates for (5.30) at $t = 0.25$ for different values of $\alpha$: (A)–(B) Case I with $\beta = 1/9$; (C) Case II. 75

5.2 Error comparison for (5.30) at $t = 0.25$: (A) Case I with $\beta = 1/7$ and $\alpha = 0, \pm 0.5, \pm 0.9, \pm 1, \pm 1.1$; (B) Case II with $\alpha = 0, \pm 1, \pm 3, \pm 6, \pm 10$. 75

5.3 Minimal stabilizing functions in Case I and the ratios of their $L^\infty$ norms to the $L^\infty$ norm of the anisotropy. 76

5.4 Minimal stabilizing functions for different values of $\alpha$ in Case I with $\beta = 1/9$. 77

5.5 Weighted mesh ratios for (5.78) with different values of $\alpha$. The initial curve is an ellipse with major axis 4 and minor axis 1, evolving by anisotropic surface diffusion with $\hat{\gamma}(\theta) = 1 + \frac{1}{16}\cos 4\theta$. The mesh sizes are $(h, \tau) = (2^{-6}, 4^{-6})$. 77

5.6 Area and area decay rate of an ellipse with major axis 4 and minor axis 1 evolving by anisotropic curvature flow under (5.30), with $\alpha = 0$. 77

5.7 Morphological evolution of an ellipse with major axis 4 and minor axis 1 under anisotropic curvature flow computed with (5.30): (A) Case I with $\beta = 1/7$; (B) Case II. Red curves show the initial shapes, blue curves show the numerical solutions at (A) $t = 0.45$ and (B) $t = 0.35$, and black dashed curves show intermediate stages. The parameters are $\alpha = 0, (h, \tau) = (2^{-7}, 4^{-7})$. 78

5.8 Normalized energy for (5.30): (A) Case I with $\beta = 1/7, \alpha = 0$; (B) Case II with different values of $\alpha$. The mesh sizes in panel (B) are $(h, \tau) = (2^{-7}, 4^{-7})$. 78

5.9 Morphological evolution of a nonconvex initial curve with large curvature variations under anisotropic curvature flow computed with (5.30), with $\alpha = 2$. Red curves show the initial shapes, blue curves show the numerical solutions at $t = 0.32$, and black dashed curves show intermediate stages. 79

5.10 Morphological evolution of an initial curve with $C^0$ regularity under anisotropic curvature flow computed with (5.30), with $\alpha = -2$. Red curves show the initial shapes, blue curves show the numerical solutions at $t = 0.24$, and black dashed curves show intermediate stages. 79

5.11 Anisotropic evolution of a self-intersecting initial curve 80

5.12 Morphological evolution of an ellipse with major axis 8 and minor axis 1 under area-preserving anisotropic curvature flow computed with (5.74). The surface energy density is the $l^4$-norm metric anisotropy $\hat{\gamma}(\theta) = \sqrt[4]{n_1^4 + n_2^4}$, where $\boldsymbol{n} = (n_1, n_2)^T = (-\sin\theta, \cos\theta)^T$. Red and blue curves show the initial shape and numerical equilibrium, respectively, and black dashed curves show intermediate stages. The parameters are $\alpha = 2.5, (h, \tau) = (2^{-6}, 4^{-6})$. 81

5.13 Time evolution for the simulation in Figure 5.12: (A) normalized area loss (blue dashed curve) and iteration count (red curve); (B) normalized energy. The scheme is (5.74). 81

5.14 Morphological evolution of a bowtie-shaped initial curve under area-preserving anisotropic curvature flow with (A) $\hat{\gamma}(\theta) = 1 + \frac{1}{28}\cos 2\theta$ and (B) $\hat{\gamma}(\theta) = 1 + \frac{1}{30}\cos 6\theta$. Red and blue curves show the initial shapes and numerical equilibria, respectively, and black dashed curves show intermediate stages. The remaining parameters are $\alpha = 0.5, (h, \tau) = (2^{-6}, 4^{-6})$. 82

5.15 Snapshots of a flower-shaped initial curve evolving by area-preserving anisotropic curvature flow with the anisotropy in Case II, at $t = 0, 0.05, 0.15, 0.25, 0.4, 2.5$. The remaining parameters are $\alpha = -0.5, h = 2^{-7}, \tau = 0.005$. 82

5.16 Morphological evolution of an ellipse with major axis 8 and minor axis 1 under anisotropic surface diffusion with Case I and $\beta = 1/9$. Red and blue curves show the initial shape and numerical equilibrium, respectively, and black dashed curves show intermediate stages. The mesh sizes are $(h, \tau) = (2^{-6}, 4^{-6})$. 83

5.17 Time evolution for the anisotropic surface diffusion simulation in Figure 5.16: (A) normalized area loss (blue dashed curve) and iteration count (red curve); (B) normalized energy. The scheme is (5.78). 83

5.18 Anisotropic surface diffusion of a quadrifolium with Case I at $t = 0, 0.15, 0.5, 0.9$. The parameters are $\alpha = 0.5, \beta = 1/5, h = 2^{-7}, \tau = 0.001$. 83

5.19 Anisotropic surface diffusion of an almost slit domain with the fourfold anisotropy $\hat{\gamma}(\theta) = 1 + \frac{1}{16}\cos 4\theta$, at $t = 0, 5\times10^{-6}, 7\times10^{-5}, 2.5\times10^{-4}, 5\times10^{-4}, 7.5\times10^{-4}, 0.002, 0.02, 0.1$. The parameters are $\alpha = 1, h = 1/288, \tau = 1\times10^{-6}$. 84

5.20 Evolution of Bernoulli's lemniscate under anisotropic surface diffusion with Case I, at $t = 0$, 0.008, 0.015, 0.025, 0.035, 0.04, 0.0425. The parameters are $\beta = 1/9, (h, \tau) = (2^{-7}, 4^{-7})$. 85

6.1 Anisotropic surface diffusion of a closed, orientable surface $\Gamma(t)$ in $\mathbb{R}^3$ with anisotropic surface energy $\hat{\gamma}(\theta, \phi)$ (left), and the spherical-coordinate representation of the local orthonormal frame $\{\boldsymbol{n}, \boldsymbol{\tau}_1, \boldsymbol{\tau}_2\}$ (right). Here $\boldsymbol{\xi}(\theta, \phi)$ denotes the Cahn–Hoffman $\boldsymbol{\xi}$-vector. 88

6.2 Schematic illustration of the local energy estimate in Lemma 6.4. 94

6.3 Normalized volume loss for (a) Case I, (b) Case II with $\beta = \frac{1}{8}$, and (c) Case II with $\beta = \frac{1}{4}$. The parameter values are $\alpha = 0, 1, -1$, respectively. 106

6.4 Newton iteration counts for (a) Case I, (b) Case II with $\beta = \frac{1}{8}$, and (c) Case II with $\beta = \frac{1}{4}$. The parameter values are $\alpha = 0, 1, -1$, respectively. 106

6.5 Normalized energy for (a) Case I with $\alpha = 0$, (b) Case II with $\beta = \frac{1}{8}$, (c) Case II with $\beta = \frac{1}{4}$ and $\alpha = -1$, and (d) Case I. 107

6.6 Evolution of a $3 \times 3 \times 2$ cuboid under anisotropic surface diffusion for Case I with $\alpha = 0$, at different times. 107

6.7 Evolution of a $3 \times 3 \times 2$ cuboid under anisotropic surface diffusion for Case II with $\beta = \frac{1}{4}$ and $\alpha = -1$, at different times. 108

6.8 Snapshots of an $8 \times 1 \times 1$ cuboid evolving under anisotropic surface diffusion up to pinch-off, for fourfold anisotropy $\hat{\gamma}(\theta, \phi) = 1 + \frac{1}{4}\left(\cos^4\theta + \sin^4\theta\cos^4\phi + \sin^4\theta\sin^4\phi\right)$ with $\alpha = -0.5$. 109

6.9 Snapshots of a $16 \times 1 \times 1$ cuboid evolving under anisotropic surface diffusion up to pinch-off, for Case II with $\beta = \frac{1}{8}$ and $\alpha = -0.5$. 110

6.10 Snapshots of a $(1, 0.25)$-torus evolving under anisotropic surface diffusion for Case II with $\beta = 1/4$ and $\alpha = 0.5$. 110

6.11 Snapshots of a $(1, 0.2)$-torus evolving under anisotropic surface diffusion up to pinch-off, for Case II with $\beta = 1/4$ and $\alpha = 0.5$. 110

6.12 Evolution of an orthogonal cross-beam under anisotropic surface diffusion up to pinch-off, for fourfold anisotropy $\hat{\gamma}(\theta, \phi) = 1 + \frac{1}{4}\left(\cos^4\theta + \sin^4\theta\cos^4\phi + \sin^4\theta\sin^4\phi\right)$. 111

6.13 Evolution of an orthogonal cross-beam under anisotropic surface diffusion: (a) iteration count, (b) normalized volume loss, and (c) normalized energy. 111

6.14 Evolution of a spherical lattice under anisotropic surface diffusion for Case II with $\beta = \frac{1}{4}$. 111

7.1 Solid-state dewetting of a solid thin film on a rigid flat substrate. Left: $\Gamma$ is the film/vapor interface, $S$ is the film/substrate interface, and $C$ is the contact line; $\boldsymbol{n}_C$ is the outward unit normal to $C$ in $S$. Right: geometry of the contact angle $\theta_C = \arccos(\boldsymbol{n}_C \cdot \boldsymbol{\nu}_C)$, where $\boldsymbol{\nu}_C$ is the conormal to $C$. 113

7.2 Evolution of a $3 \times 3 \times 2$ cuboid in solid-state dewetting for Case II with $\beta = 1/4$, $\alpha = 0$ and $\theta_Y = 2\pi/3$. 117

7.3 Evolution of a $3.2 \times 3.2 \times 0.2$ cuboid in solid-state dewetting for Case I with $\alpha = -1$ and $\theta_Y = 3\pi/4$. 118

7.4 Evolution of a $16 \times 1 \times 1$ cuboid in solid-state dewetting up to pinch-off, for fourfold anisotropy $\hat{\gamma}(\theta, \phi) = 1 + \frac{1}{4}\left(\cos^4\theta + \sin^4\theta\cos^4\phi + \sin^4\theta\sin^4\phi\right)$ with $\theta_Y = 5\pi/6$. 119

7.5 Evolution in solid-state dewetting of an initially wide square ring obtained by removing a $2 \times 2 \times 1$ cuboid from the center of a $7 \times 7 \times 1$ cuboid, together with its cross-sections in the plane $x = y$, for fourfold anisotropy $\hat{\gamma}(\theta, \phi) = 1 + \frac{1}{4}\left(\cos^4\theta + \sin^4\theta\cos^4\phi + \sin^4\theta\sin^4\phi\right)$ with $\theta_Y = 3\pi/4$. 119

7.6 Snapshots of an initially narrow square ring evolving in solid-state dewetting up to pinch-off, for Case II with $\beta = \frac{1}{4}$ and $\theta_Y = 3\pi/4$. 120

7.7 Snapshots of an initially narrow square ring evolving in solid-state dewetting up to pinch-off, for fourfold anisotropy $\hat{\gamma}(\theta, \phi) = 1 + \frac{1}{4}\left(\cos^4\theta + \sin^4\theta\cos^4\phi + \sin^4\theta\sin^4\phi\right)$ with $\theta_Y = 3\pi/4$. 120

7.8 Evolution in solid-state dewetting of an initially very narrow square ring obtained by removing a $6 \times 6 \times 1$ cuboid from the center of a $7 \times 7 \times 1$ cuboid, for fourfold anisotropy $\hat{\gamma}(\theta, \phi) = 1 + \frac{1}{4}\left(\cos^4\theta + \sin^4\theta\cos^4\phi + \sin^4\theta\sin^4\phi\right)$ with $\theta_Y = 3\pi/4$. 121

7.9 Equilibrium island shapes and their cross-sections in the plane $x = y$ for Case II with $\beta = \frac{1}{4}$, at different values of $\theta_Y$. 121

7.10 Equilibrium island shapes and their cross-sections in the plane $x = y$ for Case II with $\theta_Y = 7\pi/12$, at different anisotropy strengths $\beta$. 122

8.1 Volume histories and Newton iteration counts with $h = 2^{-3}$: (left) $V^h(t)/V^h(0)$ for the $L^2$ flow; (right) $\Delta V^h(t)/V^h(0)$ for surface diffusion. 131
8.2 Normalized energy for: (a) $L^2$ flow; (b) surface diffusion. 132
8.3 Evolution of the ellipsoid under the $L^2$ flow. 133
8.4 Evolution of the ellipsoid under surface diffusion. 133
8.5 Evolution of the six-lobed surface under the $L^2$ flow. 134
8.6 Evolution of the six-lobed surface under surface diffusion. 134
8.7 Evolution of the torus under the $L^2$ flow with 896 vertices and $\tau = 0.005$. 135
8.8 Evolution of the biconcave disk under surface diffusion with energy (8.63). 136

# List of Tables


5.1 Numerical errors $e^h(t)$ and convergence rates for the fully discrete scheme (5.30) with $\alpha = 0, \pm 1$. The anisotropy is Case I with $\beta = 1/9$. The remaining parameters are $h_0 = 2^{-4}, \tau_0 = h_0^2$. 74

5.2 Total iteration counts and average CPU times for (5.30) at $t = 0.1$ for Case I with $\beta = 1/7$. 76

6.1 Numerical errors and convergence rates for Case I. 105

6.2 Numerical errors and convergence rates for Case II with $\beta = \frac{1}{8}$. 105

8.1 Error and convergence rates for the $L^2$ flow of surfaces. 131

8.2 Error and convergence rates for surface diffusion. 131

8.3 Wall-clock time per step and Newton iterations. 132

# Notation

| Symbol | Meaning |
|---|---|
| $d \in \{2, 3\}$ | Ambient dimension |
| $\mathbb{R}^d$ | $d$-dimensional Euclidean space |
| $\mathbb{R}_{\geq 0}$ | Nonnegative real numbers |
| $t$ | Time |
| $\Gamma, \Gamma(t)$ | A planar curve or a surface in three dimensions |
| $\boldsymbol{X}$ | Position vector |
| $\boldsymbol{n}$ | Outward unit normal |
| $\boldsymbol{\tau}$ | Unit tangent to a curve |
| $\boldsymbol{\tau}_1, \boldsymbol{\tau}_2$ | Orthonormal basis of the surface tangent plane |
| $\boldsymbol{\nu}$ | Conormal |
| $V_n$ | Normal velocity |
| $\gamma(\boldsymbol{n})$ | Orientation-dependent surface energy density |
| $\gamma(\boldsymbol{p})$ | Positively one-homogeneous extension of $\gamma(\boldsymbol{n})$ |
| $\boldsymbol{I}_d$ | $d$-dimensional identity matrix |
| $\boldsymbol{v}^\perp$ | Clockwise rotation $\boldsymbol{v}^\perp = (v_2, -v_1)^T$ through $\pi/2$ |
| $\boldsymbol{v}^T, \boldsymbol{V}^T$ | Transpose of a vector or matrix |
| $\theta$ | Normal angle in the planar convention $\boldsymbol{n} = (-\sin\theta, \cos\theta)^T$ |
| $\hat{\gamma}(\theta)$ | Planar angular representation of the energy density |
| $\hat{\gamma}(\theta, \phi)$ | Spherical-coordinate representation of the density |
| $\tilde{\gamma} = \hat{\gamma} + \hat{\gamma}''$ | Surface stiffness in two dimensions |
| $W(\Gamma)$ | Total surface energy |
| $\mu$ | Chemical potential; weighted curvature for orientation-only energies |
| $\kappa$ | Signed curvature of a planar curve |
| $H$ | Mean curvature, defined as the sum of principal curvatures |
| $\boldsymbol{\xi}$ | Cahn–Hoffman vector |
| $s, \partial_s$ | Arclength and differentiation with respect to arclength |
| $\nabla_\Gamma$ | Surface gradient |
| $\nabla_\Gamma \cdot$ | Surface divergence |
| $\underline{D}_i$ | $i$th component of the surface gradient |
| $\Delta_\Gamma$ | Laplace–Beltrami operator $\nabla_\Gamma \cdot \nabla_\Gamma$ |
| $\mathcal{F}, \mathcal{W}$ | Frank diagram and Wulff shape |
| $\hat{\boldsymbol{G}}_k(\theta)$ | Stabilized surface energy matrix |
| $\hat{\boldsymbol{Z}}_k(\theta)$ | Symmetric surface energy matrix |
| $\hat{\boldsymbol{G}}_k^\alpha$ | $\alpha$-surface energy matrix |
| $k$ | Stabilizing function |
| $k_0, k_{\min}$ | Minimal stabilizing functions in the relevant construction |
| $M(\Gamma_1, \Gamma_2)$ | Manifold distance between two curves or surfaces |
| $f(\boldsymbol{n}, H), f_H$ | Coupled energy density and its curvature derivative |
| $r$ | Auxiliary scalar representing or projecting $f_H$ |
| $\boldsymbol{A}$ | Weingarten matrix |

CHAPTER 1

# Introduction

This chapter first explains the motivation for studying extrinsic anisotropic geometric flows. We introduce surface energies to describe anisotropy, derive the basic form of extrinsic anisotropic geometric flows from the first variation of the surface energy functional, and discuss two particular flows with gradient flow structures. We then briefly review the relevant theory and numerical methods before outlining the contributions of this thesis.

## 1.1. Physical background

Curvature-driven interface evolution arises in many scientific fields, particularly materials science and solid-state physics. The study of curvature-driven problems is central to understanding and simulating interfaces in solid materials. In his 1956 and 1957 works, Mullins introduced mean curvature flow and surface diffusion as mathematical models for grain boundary evolution and capillarity-driven migration of atoms or molecules along interfaces [113, 114]. Curvature-driven geometric partial differential equations have since become a principal framework for interface dynamics. Subsequent studies have examined their physical basis, variational structures, and well-posedness. In geometric analysis and partial differential equations, research on curvature flows has addressed existence and uniqueness [110, 75, 66], regularity [86, 75], singularity formation [87, 140, 43], and long-time behavior [88, 89]. In materials science and solid-state physics, these models describe epitaxial growth [64, 79], surface phase formation [74, 40, 30], heterogeneous catalysis [122, 128], multiphase fluid dynamics [32, 5], and solid-state dewetting [132, 136, 139, 90]. As illustrated in Figure 1.1, surface diffusion coupled with moving contact lines describes the dewetting of solid films on rigid substrates [136, 94, 93, 145].

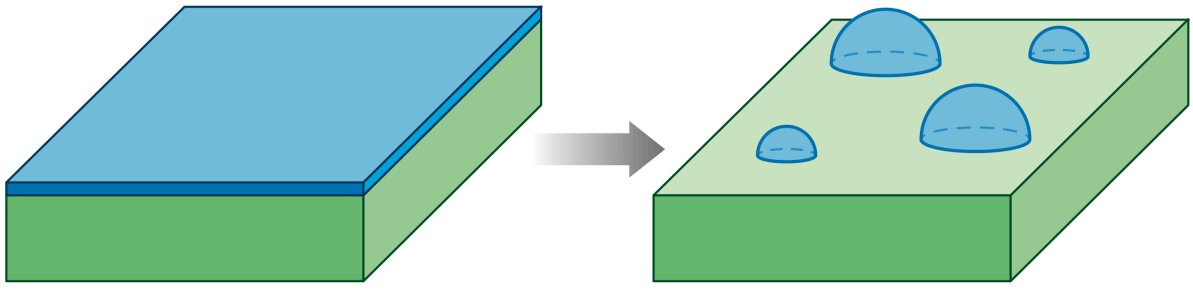


**Figure 1.1.** Under surface-diffusion-driven dewetting, a solid thin film breaks up into multiple isolated hemispherical islands; the image is adapted from [136].

The intrinsic lattice structure of a crystalline material naturally gives rise to a direction-dependent surface energy. Such anisotropy is essential in the study of crystal shapes and film evolution, whose interface dynamics depend strongly on the material symmetry. When the surface energy density depends on the interface normal, different orientations have different energy costs and driving forces, leading to preferred and competing orientations. This selection mechanism, governed by crystal

symmetry, can produce complex dynamics and induce instabilities and morphological transitions under suitable geometric and boundary conditions.

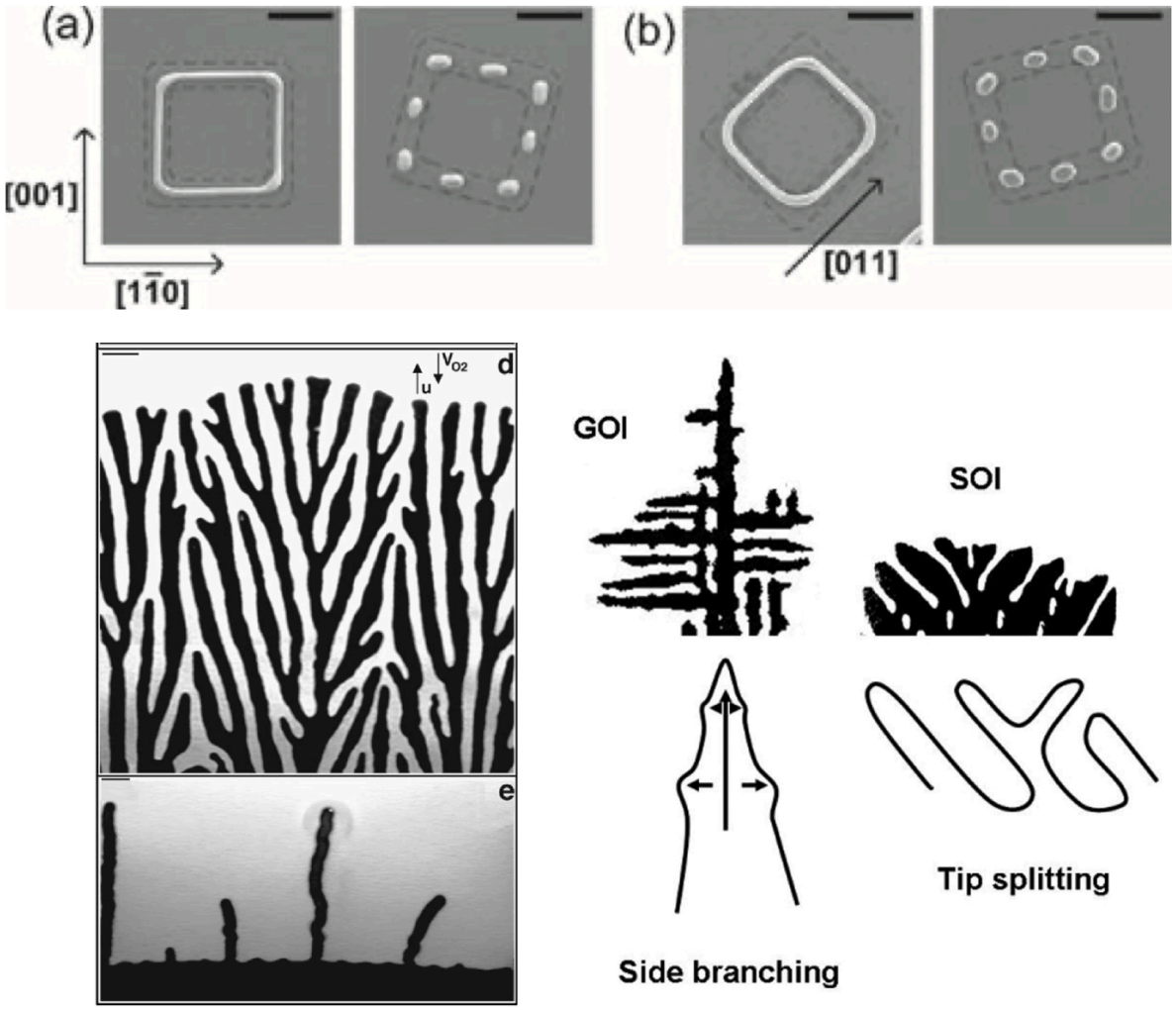



**Figure 1.2.** Instabilities induced by anisotropy: pinch-off (top), fingering instability (bottom left), and faceting instability (bottom right). The figure is adapted from [100, 152, 146].

Film retraction, the evolution of slender structures, and strong orientation preferences can give rise to several interface instabilities; see Figure 1.2. Examples include Rayleigh–Plateau instability [120, 77], faceting instability [100, 80, 34, 73], fingering instability [95, 96, 116], corner instability [145], and pinch-off [146, 131]. These processes can interact and occur in succession. For example, growing edge perturbations may first produce fingers; the slender fingers may then undergo pinch-off, separating into isolated islands. Such behavior involves evolution across multiple scales and changes in topology. These frequently observed experimental features directly reflect the dynamical effects of anisotropy.

These complexities make accurate simulation of anisotropic curvature flows challenging: numerical schemes must reliably capture the underlying physical mechanisms. The broad applications of anisotropic geometric flows motivate a systematic framework for designing structure-preserving numerical methods.

## 1.2. Surface energy and anisotropy

Anisotropic interface dynamics are often governed by the anisotropic surface energy, conventionally denoted by $\gamma$. In applications, $\gamma$ may depend on temperature, position, electromagnetic fields,

curvature, and other factors [82, 124, 129]. We first consider the simplified case $\gamma = \gamma(\boldsymbol{n}) > 0$, where $\boldsymbol{n} \in \mathbb{S}^{d-1}$ is the outward unit normal to the surface.

If $\gamma(\boldsymbol{n})$ is independent of direction, namely $\gamma(\boldsymbol{n}) \equiv$ constant, the anisotropy disappears and the surface energy is isotropic. A nonconstant surface energy is classified as either weakly anisotropic or strongly anisotropic. This distinction affects the well-posedness of geometric flows [3, 42, 130], the stability of equilibria [92, 37, 77], and the analysis of numerical methods [102, 57, 139, 11, 46].

**1.2.1. Frank diagrams.** We begin with the simpler two-dimensional setting. For the normal $\boldsymbol{n} = (-\sin\theta, \cos\theta)^T$, the surface energy $\gamma(\boldsymbol{n})$ has an equivalent $\hat{\gamma}(\theta)$ representation, namely $\hat{\gamma}(\theta) := \gamma(\boldsymbol{n}(\theta))$. The anisotropy can be classified using the *surface stiffness* $\tilde{\gamma}(\theta) := \hat{\gamma}(\theta) + \hat{\gamma}''(\theta)$ [115, 78]. If $\tilde{\gamma}(\theta)$ is strictly positive everywhere, the energy is *weakly anisotropic*; otherwise it is *strongly anisotropic*. For a general anisotropic surface energy $\gamma(\boldsymbol{n})$, this classification can be made using the *Frank diagram* [65]. Here $\gamma(\boldsymbol{p})$ denotes the degree-one homogeneous extension defined below:

$$\mathcal{F} := \left\{ \boldsymbol{p} \in \mathbb{R}^d \mid \gamma(\boldsymbol{p}) \le 1 \right\}, \tag{1.1}$$

In the direction $\boldsymbol{n}$, the radius of the Frank diagram is $\frac{1}{\gamma(\boldsymbol{n})}$; hence it is also called the $\frac{1}{\gamma}$-plot. Figures 1.3 and 1.4 show Frank diagrams for several anisotropies, whose formulas are given in Section 2.1 and Appendix B.

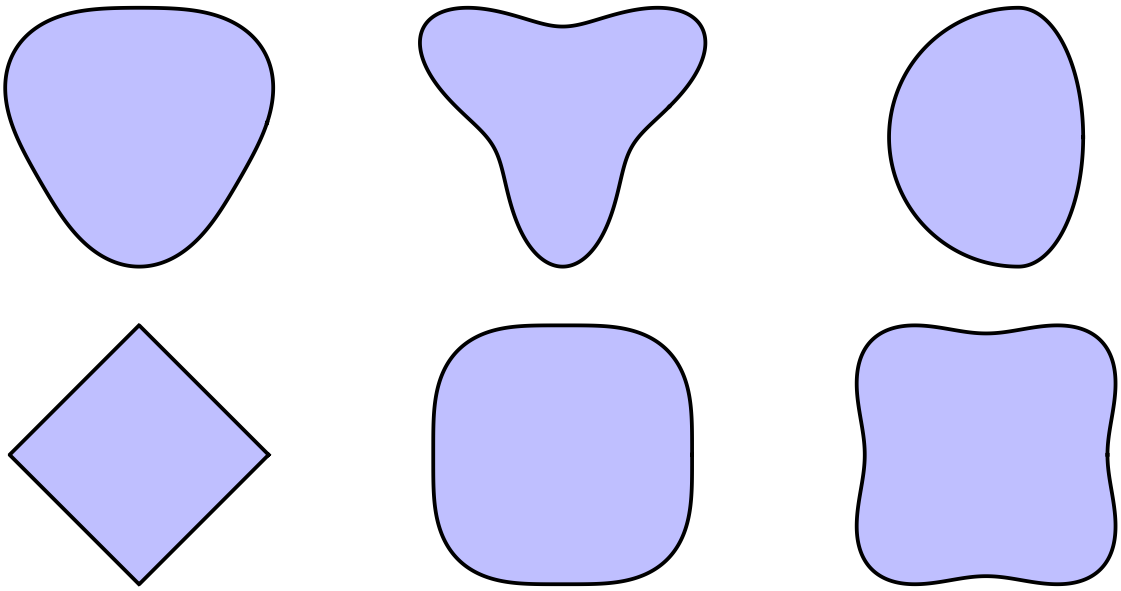


**Figure 1.3.** Several Frank diagrams of two-dimensional anisotropies. From left to right, top to bottom: three-fold symmetric anisotropy with $\beta = \frac{1}{9}$; three-fold symmetric anisotropy with $\beta = \frac{1}{3}$; piecewise anisotropy; piecewise BGN anisotropy; $l^1$-norm anisotropy; $\gamma(\boldsymbol{n}) = 1 + \frac{1}{4}(n_1^4 + n_2^4)$; $\gamma(\boldsymbol{n}) = 1 + \frac{1}{2}(n_1^6 + n_2^6)$.

The convexity of the Frank diagram determines the strength of the anisotropy $\gamma(\boldsymbol{n})$. If the diagram is convex, the anisotropy is weak; if it is nonconvex, the anisotropy is strong [137].

**1.2.2. Weighted curvature and the Cahn–Hoffman vector.** From the perspective of the second law of thermodynamics, decreasing total energy drives the evolution. For a surface $\Gamma$ in $\mathbb{R}^d$ with prescribed anisotropy $\gamma(\boldsymbol{n})$, we define the total surface energy by

$$W(\Gamma) := \int_\Gamma \gamma(\boldsymbol{n}) \, \mathrm{d}A, \tag{1.2}$$

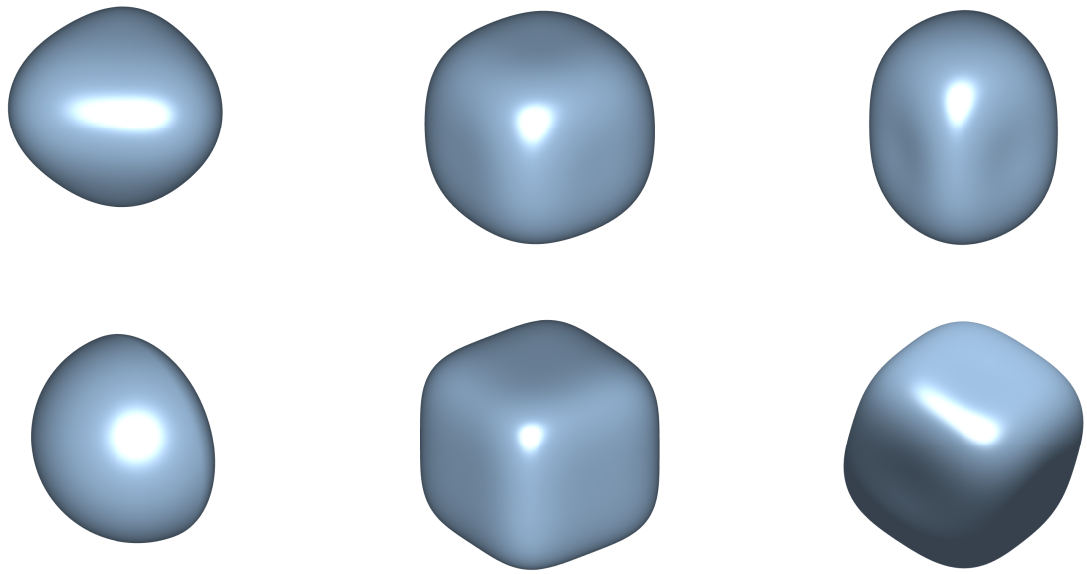


**Figure 1.4.** Several Frank diagrams of three-dimensional anisotropies. From left to right, top to bottom: three-fold symmetric anisotropy with $\beta = \frac{1}{4}$; cubic anisotropy with $\beta = \frac{1}{3}$; [001]-oriented anisotropy with $\beta = \frac{1}{2}$; piecewise BGN anisotropy; $l^4$-norm anisotropy; [111]-oriented anisotropy with $\beta = \frac{1}{2}$.

where $\mathrm{d}A$ is the area element on $\Gamma$. Let $\Gamma^\varepsilon$ be generated by a smooth normal variation $\eta \boldsymbol{n}$ of $\Gamma$. The *chemical potential* is defined as the *first variation* of the energy functional $W(\Gamma)$:

$$\mu := \frac{\delta W(\Gamma)}{\delta \Gamma}, \qquad \delta W(\Gamma)[\eta \boldsymbol{n}] = \int_\Gamma \mu \eta \, \mathrm{d}A. \tag{1.3}$$

In two dimensions, the $\hat{\gamma}(\theta)$ formulation gives the explicit expression for the chemical potential

$$\mu = \tilde{\gamma}(\theta)\kappa = [\hat{\gamma}(\theta) + \hat{\gamma}''(\theta)]\kappa, \tag{1.4}$$

where $\tilde{\gamma}(\theta)$ is the surface stiffness and $\kappa = -(\partial_{ss}\boldsymbol{X}) \cdot \boldsymbol{n}$ is the curvature. Thus $\mu$ is also called the weighted curvature. For the normalized isotropic density $\hat{\gamma} \equiv 1$, $\mu$ reduces to the usual curvature $\kappa$. Once the driving force $\mu$ is known, the physical mechanism determines how $\mu$ produces a normal velocity. Nonconservative evolution typically gives curvature motion, whereas transport dominated by diffusion along the surface gives surface diffusion. This leads to different geometric flow models.

In 1972, Cahn and Hoffman introduced what is now called the Cahn-Hoffman $\boldsymbol{\xi}$-vector to study anisotropy in crystalline materials [84, 37]. To define it mathematically, we first extend the anisotropy $\gamma(\boldsymbol{n})$, defined on $\mathbb{S}^{d-1}$, by degree-one homogeneity:

$$\gamma(\boldsymbol{p}) := \begin{cases} |\boldsymbol{p}| \, \gamma(\frac{\boldsymbol{p}}{|\boldsymbol{p}|}), & \forall \boldsymbol{p} \in \mathbb{R}^d \backslash \{\boldsymbol{0}\} \\ 0, & \boldsymbol{p} = \boldsymbol{0}. \end{cases} \tag{1.5}$$

The Cahn–Hoffman $\boldsymbol{\xi}$-vector is then defined by

$$\boldsymbol{\xi}(\boldsymbol{n}) = (\xi_1, \xi_2, \cdots, \xi_d)^T := \nabla \gamma(\boldsymbol{p})\Big|_{\boldsymbol{p}=\boldsymbol{n}}, \qquad \forall \boldsymbol{n} \in \mathbb{S}^{d-1}, \tag{1.6}$$

where $\nabla$ is the gradient in $\mathbb{R}^d$. Homogeneity implies that $\boldsymbol{\xi}$ satisfies

$$\boldsymbol{\xi} \cdot \boldsymbol{n} = \gamma(\boldsymbol{n}). \tag{1.7}$$

Figure 1.5 shows $\boldsymbol{\xi}$-plots for several anisotropies. For a weak anisotropy, the $\boldsymbol{\xi}$-plot is a simple closed surface; a strong anisotropy produces "ears", as shown in the last example of Figure 1.5.

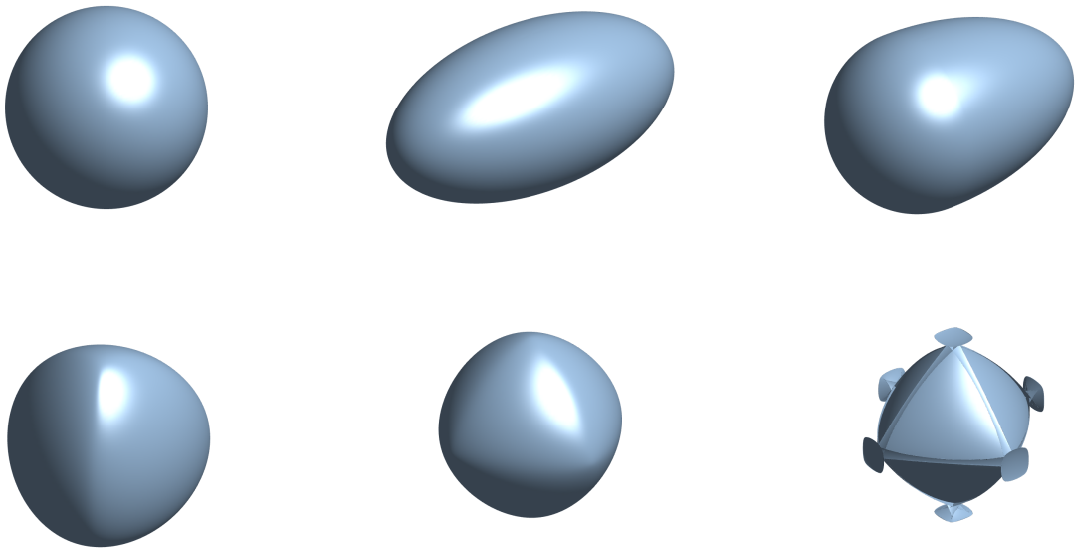


**Figure 1.5.** Several $\xi$-plots of three-dimensional anisotropies. From left to right, top to bottom: isotropic; ellipsoidal anisotropy; piecewise BGN anisotropy; three-fold symmetric anisotropy with $\beta = \frac{1}{4}$; cubic anisotropy with $\beta = \frac{1}{4}$; cubic anisotropy with $\beta = 1$.

In polar coordinates, the Cahn–Hoffman vector has an explicit expression. In the two-dimensional $\hat{\gamma}(\theta)$ formulation,

$$\boldsymbol{\xi}(\theta) = \hat{\gamma}(\theta)\boldsymbol{n} - \hat{\gamma}'(\theta)\boldsymbol{\tau}, \qquad \forall \theta \in 2\pi\mathbb{T}, \tag{1.8}$$

where $\boldsymbol{n} = (-\sin\theta, \cos\theta)^T$, $\boldsymbol{\tau} = (\cos\theta, \sin\theta)^T$ are the curve normal and tangent, respectively. In the three-dimensional $\hat{\gamma}(\theta, \phi)$ formulation, the vector decomposes as

$$\boldsymbol{\xi}(\theta, \phi) = \hat{\gamma}(\theta, \phi)\boldsymbol{n} + \frac{\partial \hat{\gamma}(\theta, \phi)}{\partial \theta}\boldsymbol{\tau}_1 + \frac{1}{\sin\theta}\frac{\partial \hat{\gamma}(\theta, \phi)}{\partial \phi}\boldsymbol{\tau}_2, \tag{1.9}$$

where $\{\boldsymbol{n}, \boldsymbol{\tau}_1, \boldsymbol{\tau}_2\}$ form the orthonormal frame

$$\boldsymbol{n}(\theta, \phi) = (\sin\theta\cos\phi, \sin\theta\sin\phi, \cos\theta)^T, \tag{1.10a}$$

$$\boldsymbol{\tau}_1(\theta, \phi) = (\cos\theta\cos\phi, \cos\theta\sin\phi, -\sin\theta)^T, \tag{1.10b}$$

$$\boldsymbol{\tau}_2(\theta, \phi) = (-\sin\phi, \cos\phi, 0)^T. \tag{1.10c}$$

For a hypersurface $\Gamma$ in $\mathbb{R}^d$, the weighted curvature $\mu$ and the Cahn–Hoffman vector satisfy [37]

$$\mu \coloneqq \nabla_\Gamma \cdot \boldsymbol{\xi}, \tag{1.11}$$

where $\nabla_\Gamma \cdot$ is the surface divergence on $\Gamma$. In two dimensions, when the curve is parameterized by arc length $s$, $\mu$ takes the form

$$\mu = -\partial_s\left(\boldsymbol{\xi}^\perp\right) \cdot \boldsymbol{n}, \tag{1.12}$$

Here $\perp$ denotes a clockwise rotation by $\frac{\pi}{2}$.

For the normalized isotropic density $\gamma \equiv 1$, $\boldsymbol{\xi}$ reduces to the normal $\boldsymbol{n}$. Since $H = \nabla_\Gamma \cdot \boldsymbol{n}$, the weighted curvature $\mu$ then equals the mean curvature $H$ of the surface.

## 1.3. Typical anisotropic geometric flows

Geometric flows are partial differential equations describing curve or surface evolution driven by geometric quantities such as curvature. A flow associated with the anisotropic surface energy

$\gamma(\boldsymbol{n})$ is specified by its normal velocity $V_n$. Widely used examples include *anisotropic curvature flow*, *area-preserving anisotropic curvature flow*, and *anisotropic surface diffusion*, with normal velocities

$$V_n = \begin{cases} -\mu, & \text{anisotropic curvature flow,} \\ -\mu + \lambda, & \text{volume-preserving anisotropic curvature flow,} \\ \Delta_\Gamma \mu, & \text{anisotropic surface diffusion,} \end{cases} \tag{1.13}$$

where $\lambda := \int_\Gamma \mu \, \mathrm{d}s / |\Gamma|$ is a Lagrange multiplier enforcing conservation of the enclosed volume, and $\Delta_\Gamma$ is the Laplace–Beltrami operator. Power geometric flows $V_n = \mu^k$ $(k \geq 2)$ and more general nonlinear geometric flows $V_n = f(\mu)$ also arise frequently [29, 2]. We briefly discuss anisotropic curvature flow and anisotropic surface diffusion below.

**1.3.1. Anisotropic curvature flow.** *Anisotropic curvature flow* is characterized by the normal velocity $V_n = -\mu$. It arises in crystal growth, film evolution, and grain boundary migration, and provides a basic geometric model for interface evolution in multiphase systems.

From a variational perspective, anisotropic curvature flow is the $L^2$ *gradient flow* of the surface energy functional $W(\Gamma)$: the interface evolves in the direction of the negative chemical potential, ensuring energy dissipation. More precisely, a closed surface $\Gamma$ satisfies the dissipation law

$$\frac{\mathrm{d}}{\mathrm{d}t} W(\Gamma) = \int_\Gamma V_n \mu \, \mathrm{d}A = -\int_\Gamma \mu^2 \, \mathrm{d}A \leq 0. \tag{1.14}$$

while its enclosed volume $\Omega$ satisfies

$$\frac{\mathrm{d}}{\mathrm{d}t} |\Omega| = \int_\Gamma V_n \, \mathrm{d}A = -\int_\Gamma \mu \, \mathrm{d}A. \tag{1.15}$$

Thus this flow generally does not conserve volume. Adding a Lagrange multiplier to the velocity to cancel the net volume flux gives volume-preserving anisotropic curvature flow, or area conservation in two dimensions.

**1.3.2. Anisotropic surface diffusion.** *Anisotropic surface diffusion* is another important geometric flow, in which mass transport along the surface drives interface evolution. Spatial variations of the chemical potential $\mu$ induce a tangential flux

$$\boldsymbol{J} = -\nabla_\Gamma \mu, \tag{1.16}$$

and mass conservation gives the normal velocity

$$V_n = -\nabla_\Gamma \cdot \boldsymbol{J} = \Delta_\Gamma \mu. \tag{1.17}$$

This model is the $H^{-1}$ *gradient flow* of the surface energy functional $W(\Gamma)$ under a conservation constraint. Since $\mu$ already contains curvature, anisotropic surface diffusion is a fourth-order geometric evolution equation. It has an energy dissipation structure analogous to that of curvature flow. For a closed surface, we formally obtain

$$\frac{\mathrm{d}}{\mathrm{d}t} W(\Gamma) = \int_\Gamma \mu \Delta_\Gamma \mu \, \mathrm{d}A = -\int_\Gamma (\nabla_\Gamma \mu)^2 \, \mathrm{d}A \leq 0. \tag{1.18}$$

and the enclosed volume satisfies

$$\frac{\mathrm{d}}{\mathrm{d}t} |\Omega| = \int_\Gamma \Delta_\Gamma \mu \, \mathrm{d}A = 0. \tag{1.19}$$

Thus surface diffusion preserves volume conservation under natural conditions. For two-dimensional curves parameterized by arc length, the surface differential operators are replaced by arc length derivatives, namely $V_n = \partial_{ss} \mu$. Its higher order makes surface diffusion more challenging to analyze and compute than anisotropic curvature flow.

### 1.4. Equilibria of conservative geometric flows

An *equilibrium* of a conservative geometric flow minimizes the total surface energy while preserving the enclosed volume. This is the following optimization problem with a fixed volume constraint:

$$\min_{\Omega} \left( \int_{\Gamma} \gamma(\boldsymbol{n}) \, \mathrm{d}A \right), \qquad |\Omega| = \text{constant}. \tag{1.20}$$

Gibbs first formulated this problem, and Wulff subsequently provided the construction now known as the Gibbs–Wulff theorem [141]. Wulff proposed that the distance from the crystal center to a facet should be proportional to its surface energy density. Accordingly, the minimizer of (1.20) is determined by

$$\mathcal{W} := \left\{ \boldsymbol{p} \in \mathbb{R}^d \mid \boldsymbol{p} \cdot \boldsymbol{n} \leq \gamma(\boldsymbol{n}) \right\}. \tag{1.21}$$

This geometric object is called the *Wulff shape* [134, 71, 33]. Although Wulff did not prove his assertion, subsequent work established rigorous mathematical proofs, providing the foundation of the theory of crystal equilibrium shapes [47, 36, 82, 99, 109, 83]. Figure 1.6 shows Wulff shapes for several commonly used anisotropic surface energies.

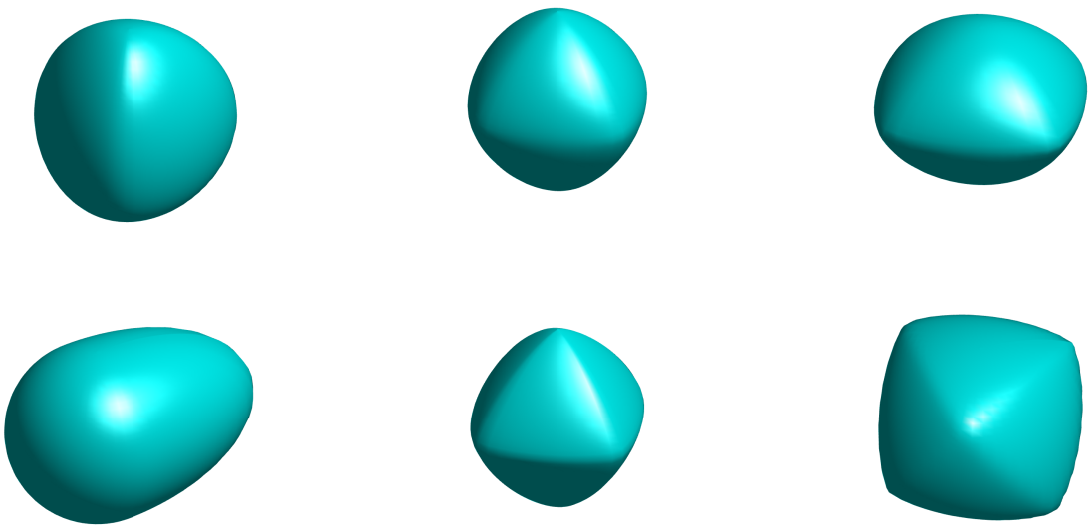


**Figure 1.6.** Wulff shapes of several anisotropies corresponding to the Frank diagrams in Figure 1.4.

By (1.7), the magnitude of the normal component of the Cahn–Hoffman $\xi$-vector is $\gamma(\boldsymbol{n})$. Together with (1.21), this suggests a close relation between the $\xi$-plot and the Wulff shape. For weak anisotropy, the $\xi$-plot has no "ears" and coincides with the Wulff shape boundary. For strong anisotropy, the "ears" of the $\xi$-plot must be removed to obtain that boundary. Figure 1.7 compares the $\gamma$-plots, Frank diagrams, $\xi$-plots, and Wulff shapes for several anisotropies.

### 1.5. Literature review

The mathematical theory of geometric flows is extensive. Elliott and Garcke established local existence and regularity for $C^4$ initial curves [58]. Escher, Mayer, and Simonett proved local well-posedness of surface diffusion in higher dimensions, together with global existence and exponential convergence for initial surfaces sufficiently close to spheres [61]. Their results provide a basis for the long-time theory of fourth-order flows; Escher and coauthors also discussed singular behavior such as pinch-off [62]. Chambolle and coauthors first proved existence and uniqueness for anisotropic mean curvature flow [39]. For volume-conserving anisotropic mean curvature flow with convex

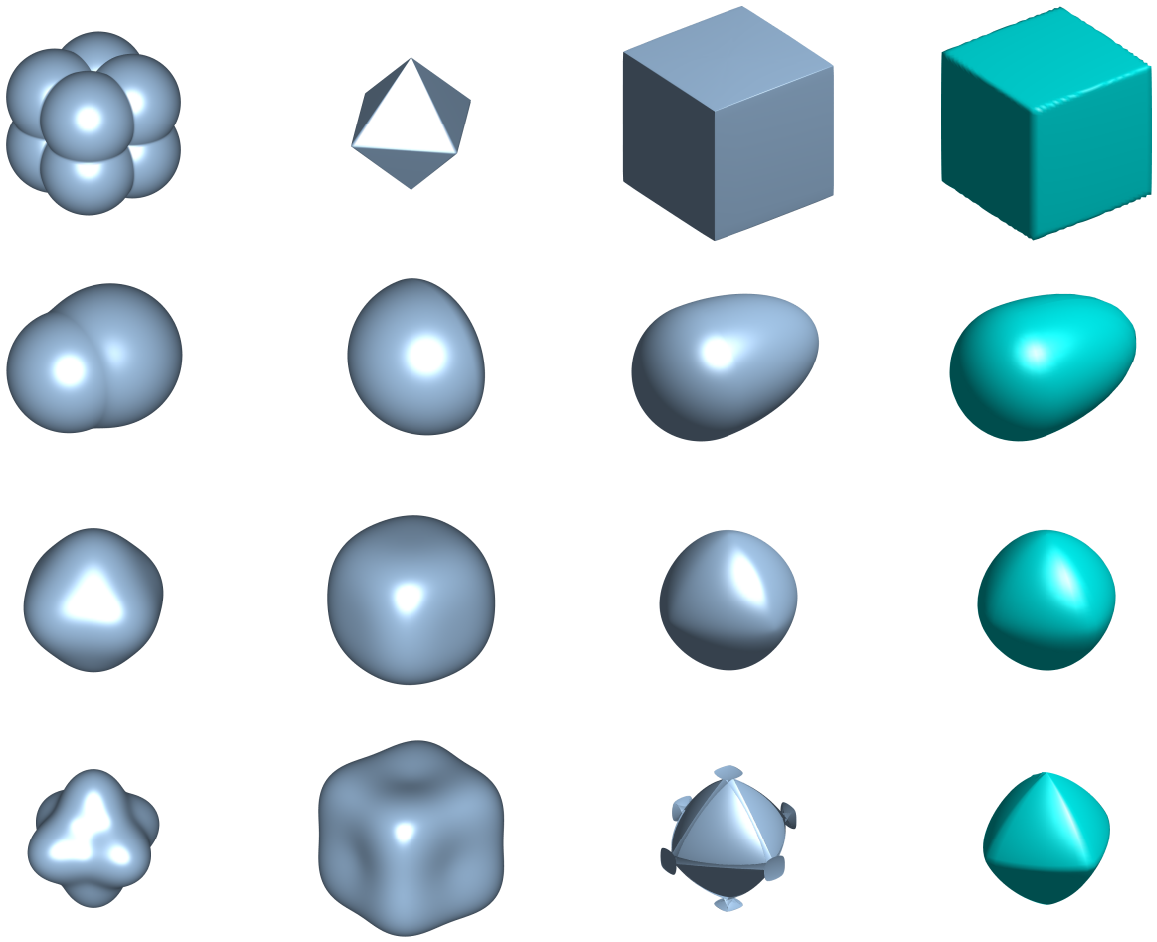


**Figure 1.7.** The $\gamma$-plots, Frank diagrams, $\xi$-plots, and Wulff shapes for several three-dimensional anisotropies. From top to bottom: $l^1$-norm anisotropy; piecewise BGN anisotropy; cubic anisotropy with $\beta = \frac{1}{4}$; cubic anisotropy with $\beta = 1$.

initial data, Andrews proved long-time existence and exponential convergence to the corresponding Wulff shape [1]. Further discussion can be found in the monograph by Giga and Požár [72].

Numerical methods for curvature-driven problems have been studied extensively over recent decades. These include level set methods [35, 117, 111], phase-field methods [51, 31, 121], marker-particle methods [50, 138], $\theta-L$ methods, finite element methods [44, 45], discontinuous Galerkin methods [142], evolving surface finite element methods [97, 98, 85], and parametric finite element methods [53, 22, 108, 11, 54]. A *level set method* represents the surface implicitly as the zero level set of a function in one higher dimension, allowing complex geometric and topological changes. A *marker-particle method* represents the surface by discrete particles and tracks their motion; it typically requires restrictive stability conditions and frequent particle redistribution. The *evolving surface finite element method* parameterizes the position vector $X$ on a fixed space and other variables, including the normal $\boldsymbol{n}$ and curvature $H$, on evolving spaces. Convergence can be proved for higher-order finite elements with polynomial degree $\geq 2$; see [85, 56, 97, 98]. However, the strong nonlinearity and evolving anisotropy often require artificial tangential velocities or mesh regularization to prevent distortion and vertex collisions. Moreover, most of these methods do not preserve structure at the fully discrete level and cannot simultaneously preserve energy dissipation and mass conservation or the mass decay rate.

The *parametric finite element method* has attracted increasing attention because of its mesh quality, accuracy, efficiency, and structure-preserving properties. It originated in Dziuk's work, which first takes a variation on the manifold, then discretizes, and finally introduces local parameterizations. The method approximates the surface $\Gamma(t_{m+1})$ by a parameterization over the surface $\Gamma(t_m)$ at the

preceding time level. Using the geometric identity $H\boldsymbol{n} = -\Delta_\Gamma \boldsymbol{X}$, Dziuk rewrote mean curvature flow $\partial_t \boldsymbol{X} = -H\boldsymbol{n}$ in the heat-equation form

$$\partial_t \boldsymbol{X} = \Delta_\Gamma \boldsymbol{X}. \tag{1.22}$$

and discretized the weak formulation

$$\int_{\Gamma(t)} \partial_t \boldsymbol{X} \cdot \boldsymbol{\omega} \,\mathrm{d}A + \int_{\Gamma(t)} \nabla_\Gamma \boldsymbol{X} : \nabla_\Gamma \boldsymbol{\omega} \,\mathrm{d}A = 0, \qquad \forall \boldsymbol{\omega} \in [H^1(\Gamma(t))]^d. \tag{1.23}$$

Unlike the evolving surface finite element method, the parametric finite element method parameterizes all variables, including the position vector $\boldsymbol{X}$, on evolving spaces. Dziuk's method is unconditionally energy stable: the area of the discrete surface decreases during evolution,

$$|\Gamma^{m+1}| \le |\Gamma^m|, \qquad \forall m \ge 0. \tag{1.24}$$

However, the absence of tangential vertex motion can cause mesh concentration and vertex collisions, degrading the numerical solution; see Figure 1.8. Long-time simulations therefore often require mesh redistribution. Since its introduction in 1991, the parametric finite element method has been extended to surface diffusion, Willmore flow, Gauss curvature flow, and other curvature-driven problems. Convergence studies have also advanced the numerical analysis of geometric flows. Detailed accounts are given in [44, 29, 102].

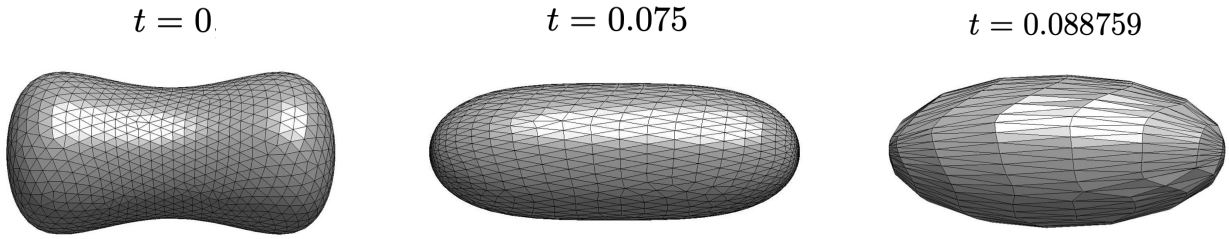



**Figure 1.8.** Evolution of a spindle-shaped surface under mean curvature flow simulated by Dziuk's method; the figure is adapted from [102].

Among parametric finite element methods, the *energy-stable method* of Barrett, Garcke, and Nürnberg [22, 25], commonly called the BGN method, is known for unconditional energy stability and good mesh quality. To improve mesh behavior, the method allows tangential vertex motion and imposes the mean curvature law only on the normal velocity $V_n = \boldsymbol{n} \cdot \partial_t \boldsymbol{X}$. It is based on the weak formulation

$$\int_{\Gamma(t)} \boldsymbol{n} \cdot \partial_t \boldsymbol{X} \,\varphi \,\mathrm{d}A + \int_{\Gamma(t)} H\varphi \,\mathrm{d}A = 0, \qquad \forall \varphi \in H^1((\Gamma(t))), \tag{1.25a}$$

$$\int_{\Gamma(t)} H\boldsymbol{n} \cdot \boldsymbol{\omega} \,\mathrm{d}A - \int_{\Gamma(t)} \nabla_\Gamma \boldsymbol{X} : \nabla_\Gamma \boldsymbol{\omega} \,\mathrm{d}A = 0, \qquad \forall \boldsymbol{\omega} \in [H^1(\Gamma(t))]^d. \tag{1.25b}$$

The resulting parametric finite element scheme retains the unconditional energy stability of Dziuk's method and improves mesh quality; see Figure 1.9. By designing a suitable discrete normal $\boldsymbol{n}$, Bao and Zhao subsequently developed a *structure-preserving parametric finite element method* that also preserves volume conservation or the volume decay rate [19, 7, 8].

The BGN method has been applied to many isotropic curvature-driven problems, including surface diffusion [21], Willmore and Gauss curvature flows [15, 16, 68], multiphase flow [67, 69], biomembranes [26], Stefan problems [63], Mullins–Sekerka problems [27], and open curve or surface evolution in solid-state dewetting [151, 20]. Numerical experiments indicate robust performance, particularly in long-time simulations. A central feature of BGN methods is the discretization of curvature in addition to the position vector $\boldsymbol{X}$ through the geometric identity

$$H\boldsymbol{n} = -\Delta_\Gamma \boldsymbol{X} = -\nabla_\Gamma \cdot (\boldsymbol{I}_d \nabla_\Gamma \boldsymbol{X}), \tag{1.26}$$

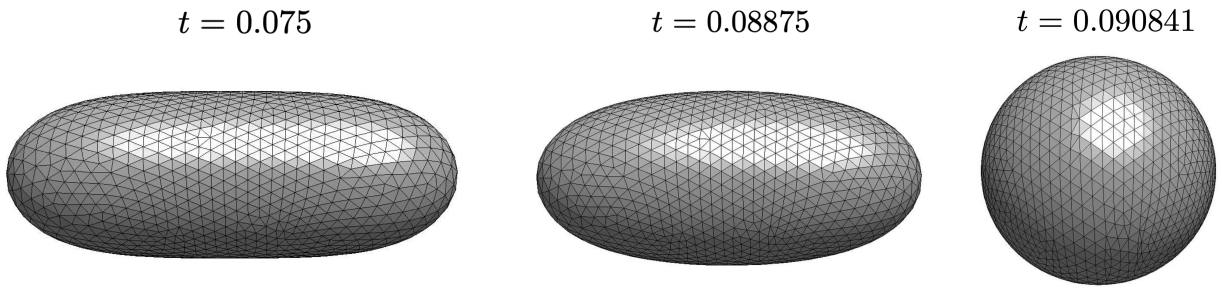



**Figure 1.9.** Evolution of a spindle-shaped surface under mean curvature flow simulated by the BGN method; the figure is adapted from [102].

This identity expresses the curvature vector and provides a natural framework for energy-stable discretization of $H$, where $\boldsymbol{I}_d$ is the $d$-dimensional identity matrix. Further discussion and applications are reviewed in [29].

Several attempts have extended the *BGN energy-stable parametric finite element method* to anisotropic flows. In two dimensions, Bao and coauthors used the explicit weighted curvature $\mu = [\hat{\gamma}(\theta)+\hat{\gamma}''(\theta)]\kappa$ to derive a parametric finite element method for anisotropic surface diffusion [11], where $\mu$ denotes weighted curvature. Zhao, Jiang, and coauthors introduced the Cahn–Hoffman $\boldsymbol{\xi}$-vector and the weak formulation

$$\int_{\Gamma(t)} \mu \boldsymbol{n} \cdot \boldsymbol{\omega} \,\mathrm{d}s - \int_{\Gamma(t)} \boldsymbol{\xi}^{\perp} \cdot \partial_s \boldsymbol{\omega} \,\mathrm{d}s = 0, \qquad \forall \boldsymbol{\omega} \in [H^1(\Gamma(t))]^2, \tag{1.27}$$

to construct a parametric finite element method for arbitrary anisotropies $\hat{\gamma}(\theta)$ [93]. It was applied successfully to open curves in two-dimensional solid-state dewetting. They subsequently used

$$\int_{\Gamma(t)} \mu \boldsymbol{n} \cdot \boldsymbol{\omega} \,\mathrm{d}A = \int_{\Gamma(t)} \gamma(\boldsymbol{n}) \nabla_\Gamma \boldsymbol{X} : \nabla_\Gamma \boldsymbol{\omega} \,\mathrm{d}A + \sum_{1\le i,j\le 3} \int_{\Gamma(t)} \xi_i n_j \nabla_\Gamma x_i \cdot \nabla_\Gamma \omega_j \,\mathrm{d}A, \tag{1.28}$$

to extend the method to open surfaces in three dimensions [150], observing energy decay numerically. Despite these numerical results, rigorous energy stability proofs remained difficult.

In 2008, Barrett and coauthors introduced the surface energy matrix $\frac{1}{\gamma(\boldsymbol{n})}\det(G)G^{-1}$ and derived an unconditionally energy-stable parametric finite element method for the special Riemannian metric anisotropy $\gamma(\boldsymbol{n}) = \sqrt{\boldsymbol{n}\cdot G\boldsymbol{n}}$. Subsequent studies applied this construction to various anisotropic curvature-driven problems. Li and Bao later introduced a new two-dimensional surface energy matrix [108]

$$\hat{\boldsymbol{G}}(\theta) = \begin{pmatrix} \hat{\gamma}(\theta) & -\hat{\gamma}'(\theta) \\ \hat{\gamma}'(\theta) & \hat{\gamma}(\theta) \end{pmatrix}, \qquad \hat{\gamma}(\theta) \in C^2(2\pi\mathbb{T}), \tag{1.29}$$

and proved that the weighted curvature $\mu$ satisfies the identity

$$\mu \boldsymbol{n} = -\partial_s \left( \hat{\boldsymbol{G}}(\theta) \partial_s \boldsymbol{X} \right). \tag{1.30}$$

Their work extended BGN energy-stable methods to general anisotropic surface energies, although energy stability still required restrictive conditions on $\hat{\gamma}(\theta)$. In 2023, Bao, Jiang, and Li introduced a stabilizing function and the symmetric surface energy matrix [9, 12]:

$$\boldsymbol{Z}_k(\boldsymbol{n}) = \gamma(\boldsymbol{n})\boldsymbol{I}_d - \boldsymbol{n}\boldsymbol{\xi}(\boldsymbol{n})^T - \boldsymbol{\xi}(\boldsymbol{n})\boldsymbol{n}^T + k(\boldsymbol{n})\boldsymbol{n}\boldsymbol{n}^T, \tag{1.31}$$

where $k(\boldsymbol{n})\colon \mathbb{S}^{d-1} \to \mathbb{R}_{\ge 0}$ is a prescribed stabilizing function and $\boldsymbol{\xi}(\boldsymbol{n})$ is the Cahn–Hoffman $\boldsymbol{\xi}$-vector. Based on this symmetric matrix, they proposed a *symmetrized structure-preserving parametric finite element method* for surface or curve evolution with symmetric anisotropy

$$\gamma(\boldsymbol{n}) = \gamma(-\boldsymbol{n}), \qquad \forall \boldsymbol{n} \in \mathbb{S}^{d-1}, \tag{1.32}$$

This enabled efficient structure-preserving computations for many anisotropic problems in materials science [103, 18, 52, 104, 105, 106]. However, some surface energies $\gamma(\boldsymbol{n})$ are asymmetric or fail to

satisfy these conditions, including three-fold symmetric anisotropies [136, 11]. More recently, Bao and Li introduced the nonsymmetric surface energy matrix

$$\boldsymbol{G}_k(\boldsymbol{n}) = \gamma(\boldsymbol{n})\boldsymbol{I}_d - \boldsymbol{n}\boldsymbol{\xi}(\boldsymbol{n})^T + \boldsymbol{\xi}(\boldsymbol{n})\boldsymbol{n}^T + k(\boldsymbol{n})\boldsymbol{n}\boldsymbol{n}^T. \tag{1.33}$$

Based on this construction, Bao and Li developed an analytical framework for proving the energy stability of parametric finite element methods [13, 14]. Energy stability follows from a local energy estimate when the stabilizing function $k(\boldsymbol{n})$ is at least a bounded minimal stabilizing function $k_0(\boldsymbol{n})$. This framework relaxes the condition on the anisotropy to

$$(5-d)\gamma(\boldsymbol{n}) > \gamma(-\boldsymbol{n}), \qquad \forall \boldsymbol{n} \in \mathbb{S}^{d-1},\ d = 2, 3. \tag{1.34}$$

The energy stability analyses of existing structure-preserving and energy-stable parametric finite element methods can be recast and improved within this framework. For example, [18] used a local energy estimate to relax the stability condition for the symmetrized method with matrix $\boldsymbol{Z}_k(\boldsymbol{n})$ from (1.32) to $3\gamma(\boldsymbol{n}) > \gamma(-\boldsymbol{n})$.

Although local energy estimates substantially improve the energy stability conditions for anisotropic parametric finite element methods, several questions remain. As shown in [14], a necessary condition for the local energy estimate associated with $\boldsymbol{G}_k(\boldsymbol{n})$ is

$$(5-d)\gamma(\boldsymbol{n}) \geq \gamma(-\boldsymbol{n}), \qquad d = 2, 3. \tag{1.35}$$

Thus condition (1.34) is almost optimal for their method. However, the critical case $(5-d)\gamma(\boldsymbol{n}^*) = \gamma(-\boldsymbol{n}^*)$ has not been analyzed in detail in the preceding work. Inspired by their analysis, we obtain the same necessary condition (1.35) for the surface energy matrix family analyzed here; see Remarks 3.5 and 6.6. This raises the question of whether the condition is also sufficient and, if so, which matrix achieves this optimal condition. Different surface energy matrices produce different numerical schemes and typically require different analytical approaches. A unified analysis would allow us to derive optimal stability conditions for these constructions and compare their computational performance systematically.

Different curvature-driven problems often require specially designed discretizations. The discrete variables must be chosen carefully to preserve the essential structures while maintaining computational efficiency. As models are extended and coupled, designing each scheme separately becomes cumbersome. The wide applications of anisotropic curvature-driven problems therefore motivate a systematic framework for structure-preserving discretization.

## 1.6. Contributions of this thesis

This thesis develops *structure-preserving parametric finite element methods* for *anisotropic geometric flows* of two-dimensional curves and three-dimensional surfaces. We first propose a stabilized method for planar anisotropic curve evolution and analyze the critical case in detail, proving unconditional energy stability under an additional mild constraint. We then construct a structure-preserving method with an optimal energy stability condition and prove that (1.35) is sufficient, achieving optimality within the local energy estimate framework. We apply both methods to crystalline film evolution and solid-state dewetting in two dimensions and identify new numerical phenomena. For two-dimensional anisotropic curvature flow, we introduce a parameter to construct a unified surface energy matrix including the existing formulations within the analyzed family and establish an energy stability framework for the associated fully discrete schemes. We also formulate a new perspective that provides a systematic approach to structure-preserving discretization of anisotropic curvature-driven problems. We extend this work to anisotropic evolution of surfaces in three dimensions and apply it to three-dimensional solid-state dewetting.

Chapter 2 studies closed planar curves under anisotropic surface diffusion. Using the $\hat{\gamma}(\theta)$ representation of the anisotropy, we introduce a stabilized conservative weak formulation and its stabilized parametric finite element discretization. A systematic analytical framework proves unconditional energy stability under mild conditions on $\hat{\gamma}(\theta)$, including the critical case $3\hat{\gamma}(\theta^*) = \hat{\gamma}(\theta^* - \pi)$. Numerical experiments with several surface energies $\hat{\gamma}(\theta)$ examine efficiency, accuracy, and structure preservation.

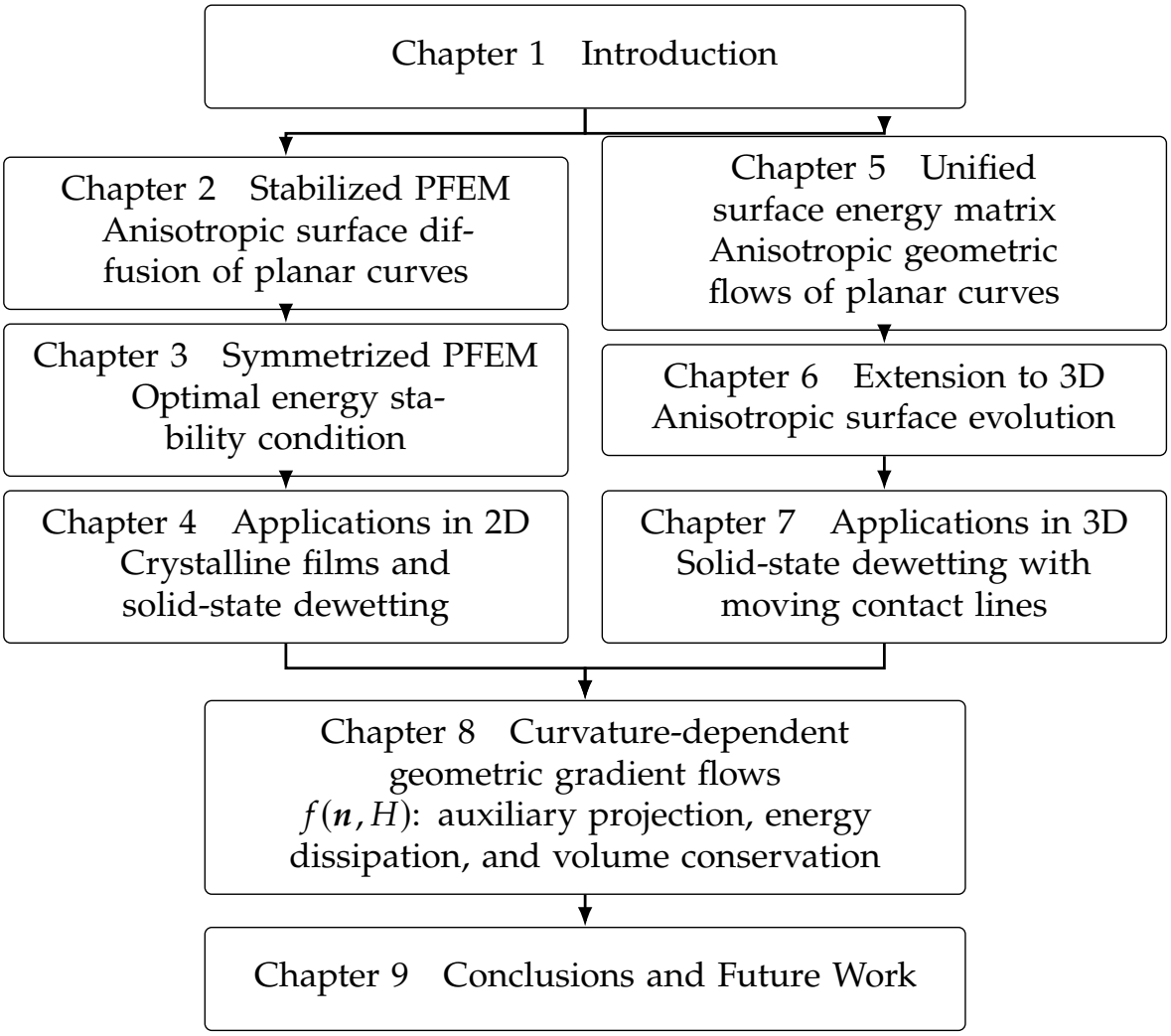



**Figure 1.10.** Dissertation structure overview.

Chapter 3 proposes and analyzes a structure-preserving parametric finite element method with an optimal energy stability condition for closed curves under anisotropic surface diffusion with energy density $\hat{\gamma}(\theta)$. Within the local energy estimate framework, we prove that $3\hat{\gamma}(\theta) - \hat{\gamma}(\theta - \pi) \geq 0$ is both necessary and sufficient for the local energy estimate underlying unconditional energy stability of the analyzed symmetric scheme. We introduce the symmetric surface energy matrix $\hat{\boldsymbol{Z}}_k(\theta)$ with stabilizing function $k(\theta)$, yielding a symmetrized conservative weak formulation. Under the stated condition, its fully discrete parametric finite element scheme rigorously preserves the enclosed area and dissipates energy unconditionally. Numerical experiments verify efficiency, accuracy, area conservation, and energy dissipation.

Chapter 4 applies these methods to two-dimensional crystalline film evolution under surface diffusion and to solid-state dewetting. We examine how the initial aspect ratio affects film pinch-off. For open curves in solid-state dewetting, we derive an accurate structure-preserving parametric finite element method and simulate evolution from different initial curves toward multiple equilibria under strong anisotropy.

Chapter 5 develops a structure-preserving parametric approximation for curvature flows with general anisotropy. Introducing the parameter $\alpha$ gives the surface energy matrix $\hat{\boldsymbol{G}}_k^{\alpha}(\theta)$, which unifies existing and admissible alternative formulations. We derive a fully discrete parametric scheme that exactly preserves the area decay rate. A unified analysis based on local energy estimates proves that $\alpha = -1$ is the unique value achieving the optimal energy stability condition $3\hat{\gamma}(\theta) \geq \hat{\gamma}(\theta - \pi)$. We also interpret the normal velocity as a mapping depending on both geometric quantities and the

background curve. This perspective leads naturally to a unified discretization framework with a consistent energy stability analysis.

Chapter 6 extends the structure-preserving parametric finite element method based on the $\alpha$-surface energy matrix to three dimensions. The three-dimensional $\alpha$-surface energy matrix yields a general conservative weak formulation for anisotropic surface diffusion. We discretize it using the semi-implicit Euler method in time and the parametric finite element method in space. We prove unconditional energy stability under a mild condition and show, as in two dimensions, that $\alpha = -1$ is the unique construction achieving the optimal energy stability condition. Numerical experiments examine the efficiency, accuracy, and structure-preserving properties of the scheme for anisotropic surface evolution.

Chapter 7 develops a structure-preserving parametric finite element method for three-dimensional anisotropic solid-state dewetting. We introduce a relaxed contact angle into the weak formulation to ensure energy stability, then discretize using the semi-implicit Euler and parametric finite element methods. The scheme evolves the interface and contact line together while preserving volume, or mass, and unconditional energy stability. Numerical experiments explore evolution from complex initial surfaces, the effects of anisotropy on moving contact lines, and pinch-off of solid films.

Chapter 8 extends the surface energy density to $f(\boldsymbol{n}, H)$, which depends on both the normal and mean curvature, and studies geometric gradient flows of closed surfaces in three dimensions. We combine a symmetric surface energy matrix at fixed curvature with the curvature evolution equation and introduce a mass-lumped projection of the curvature derivative of the energy to construct a parametric finite element scheme for generally coupled energies. Under convexity in curvature and the corresponding local energy estimate, we prove discrete energy dissipation. A time-averaged area normal additionally gives a volume-preserving gradient flow scheme. Three-dimensional numerical experiments examine convergence, energy dissipation, volume conservation, and computational cost, and illustrate evolution from ellipsoidal, six-lobed, toroidal, and biconcave initial surfaces.

Finally, Chapter 9 summarizes the main results and discusses directions for future research and improvement.

CHAPTER 2

# A stabilized parametric finite element method for curve evolution

In this chapter, we introduce a stabilized parametric finite element method (SPFEM) for two-dimensional anisotropic surface diffusion. The introduction of surface energy matrices marked an important advance in structure-preserving numerical methods for anisotropic geometric flows. The earliest work was the extension by Barrett and coauthors to surface energies of a special Riemannian metric form. Subsequently, using the $\hat{\gamma}(\theta)$ formulation, Li and Bao introduced the surface energy matrix $\hat{\boldsymbol{G}}(\theta)$ and extended the *BGN energy-stable parametric finite element method* from isotropic to general anisotropic surface diffusion [108]. Without a stabilizing term, their method requires relatively restrictive conditions to ensure energy stability. Bao, Jiang, and Li then used the $\gamma(\boldsymbol{n})$ formulation and a stabilizing function to construct the symmetric surface energy matrix $\boldsymbol{Z}_k(\boldsymbol{n})$. They proposed a *symmetrized structure-preserving parametric finite element method* in [9, 12] for anisotropic surface diffusion with symmetric anisotropies satisfying $\gamma(\boldsymbol{n}) = \gamma(-\boldsymbol{n})$. However, some surface energies arising in applications are asymmetric or fail to satisfy the earlier conditions, including the 3-fold anisotropy (2.1); see [11, 139]. More recently, using the $\gamma(\boldsymbol{n})$ formulation, Bao and Li introduced a new nonsymmetric surface energy matrix $\boldsymbol{G}_k(\boldsymbol{n})$ and developed a systematic analytical framework for proving unconditional energy stability [13, 14]. This framework allowed them to relax the condition on the anisotropy to $3\gamma(\boldsymbol{n}) > \gamma(-\boldsymbol{n}),\ \forall \boldsymbol{n} \in \mathbb{S}^1$.

However, their analytical framework did not address the critical case $3\gamma(\boldsymbol{n}^*) = \gamma(-\boldsymbol{n}^*),\ \boldsymbol{n}^* \in \mathbb{S}^1$. The framework relies on a gradient estimate for $\gamma(\boldsymbol{n})$, whose analysis is complicated because $\gamma(\boldsymbol{n})$ is defined on the unit circle $\mathbb{S}^1$. In contrast, the $\hat{\gamma}(\theta)$ formulation, defined on $2\pi\mathbb{T}$, has a simpler derivative structure and is therefore better suited to analyzing the critical case $3\hat{\gamma}(\theta^*) = \hat{\gamma}(\theta^* - \pi),\ \theta^* \in 2\pi\mathbb{T}$. Inspired by their analytical framework, we adopt the $\hat{\gamma}(\theta)$ formulation to investigate this critical case.

The main objective of this chapter is to propose a structure-preserving stabilized parametric finite element method for anisotropic surface diffusion under the following mild conditions:

(i) $3\hat{\gamma}(\theta) \geq \hat{\gamma}(\theta - \pi), \qquad \forall \theta \in 2\pi\mathbb{T}$,
(ii) whenever $3\hat{\gamma}(\theta^*) = \hat{\gamma}(\theta^* - \pi),\ \theta^* \in 2\pi\mathbb{T}$, we have $\hat{\gamma}'(\theta^*) = 0$,

Here the governing surface diffusion equation is (2.6) with surface energy $\hat{\gamma}(\theta)$.

Compared with the $\gamma(\boldsymbol{n})$ formulation, the $\hat{\gamma}(\theta)$ formulation has the following advantages:

(i) it is more intuitive and concise in applications;
(ii) it reduces the regularity requirement on the anisotropy from $C^2$ to globally $C^1$ and piecewise $C^2$;
(iii) it facilitates the analysis of the critical case in two dimensions, where $3\hat{\gamma}(\theta^*) = \hat{\gamma}(\theta^* - \pi)$ for some $\theta^* \in 2\pi\mathbb{T}$.

The remainder of this chapter is organized as follows. Section 2.1 lists anisotropic surface energies commonly used in materials science. In Section 2.2, we introduce the stabilized surface energy matrix $\hat{\boldsymbol{G}}_k(\theta)$ and derive a new conservative strong formulation for anisotropic surface diffusion. Section 2.3 presents a weak formulation based on this conservative form, its spatial semidiscretization, and a fully discrete stabilized parametric finite element scheme. In Section 2.4, we analyze area conservation and unconditional energy stability and develop a systematic framework for the energy stability analysis. We first define a minimal stabilizing function $k_0(\theta)$ and, assuming that $k_0(\theta)$ is well-defined, establish the main result through a local energy estimate. The existence of $k_0(\theta)$ is proved in Section 2.4.4. Finally, Section 2.5 presents numerical experiments demonstrating the efficiency, accuracy, and structure-preserving properties of the method.

### 2.1. Common anisotropic surface energies

We list several anisotropic surface energies widely used in materials science:

(1) *m-fold symmetric* anisotropy [11]

$$\hat{\gamma}(\theta) = 1 + \beta \cos m(\theta - \theta_0), \qquad \theta \in 2\pi\mathbb{T}, \tag{2.1}$$

where $m = 2, 3, 4, 6, |\beta| < 1$, with $\beta$ the dimensionless anisotropy strength and $\theta_0 \in 2\pi\mathbb{T}$ is a constant. The surface energy $\hat{\gamma}(\theta)$ is weakly anisotropic when $|\beta| < \frac{1}{m^2-1}$ and strongly anisotropic otherwise.

(2) *Ellipsoidal* anisotropy [135]

$$\hat{\gamma}(\theta) = \sqrt{a + b\cos^2\theta}, \qquad \theta \in 2\pi\mathbb{T}, \tag{2.2}$$

where $a, b$ are dimensionless constants satisfying $a > 0$ and $a + b > 0$.

(3) *Riemannian metric* anisotropy, also called *Barrett–Garcke–Nürnberg* or *BGN* anisotropy [24, 23]

$$\hat{\gamma}(\theta) = \sum_{l=1}^{L} \sqrt{\boldsymbol{n}(\theta)^T G_l \boldsymbol{n}(\theta)}, \qquad \boldsymbol{n} = (-\sin\theta, \cos\theta)^T, \qquad \theta \in 2\pi\mathbb{T}, \tag{2.3}$$

where $L \geq 1$ and the matrix $G_l \in \mathbb{R}^{2\times 2}$ is positive definite for every $1 \leq l \leq L$. When $L = 1, G_1 = \mathrm{diag}(a, a + b)$, (2.3) reduces to the ellipsoidal anisotropy (2.2).

(4) *Piecewise BGN* anisotropy [44]

$$\hat{\gamma}(\theta) = \sqrt{\left(\frac{5}{2} + \frac{3}{2}\mathrm{sgn}(n_1)\right) n_1^2 + n_2^2}, \tag{2.4}$$

where $\boldsymbol{n} = (n_1, n_2)^T := (-\sin\theta, \cos\theta)^T$, $\theta \in 2\pi\mathbb{T}$.

(5) *$l^r$-norm* anisotropy

$$\hat{\gamma}(\theta) = (|n_1|^r + |n_2|^r)^{\frac{1}{r}}, \qquad r \geq 2, \tag{2.5}$$

where $\boldsymbol{n} = (n_1, n_2)^T := (-\sin\theta, \cos\theta)^T$, $\theta \in 2\pi\mathbb{T}$.

### 2.2. A conservative form for two-dimensional surface diffusion

We first recall the evolution equation for two-dimensional *anisotropic surface diffusion*:

$$V_n = \partial_{ss}\mu, \tag{2.6}$$

where

$$\mu := [\hat{\gamma}(\theta) + \hat{\gamma}''(\theta)]\,\kappa, \tag{2.7}$$

and $\kappa := -(\partial_{ss}\boldsymbol{X}) \cdot \boldsymbol{n}$ denotes the curvature. In this section, we reformulate (2.6) by introducing a stabilized surface energy matrix and obtain a conservative form.

Using the geometric identity $\kappa\boldsymbol{n} = -\partial_{ss}\boldsymbol{X}$ [110], we rewrite the anisotropic surface diffusion equations (2.6)–(2.7) as

$$\boldsymbol{n} \cdot \partial_t \boldsymbol{X} - \partial_{ss}\mu = 0, \qquad 0 < s < L(t), \qquad t > 0, \tag{2.8a}$$

$$\mu\boldsymbol{n} + [\hat{\gamma}(\theta) + \hat{\gamma}''(\theta)]\,\partial_{ss}\boldsymbol{X} = \boldsymbol{0}, \tag{2.8b}$$

where $L(t) := \int_{\Gamma(t)} \mathrm{d}s$ is the length of $\Gamma(t)$.

Theorem 2.1. *The weighted curvature $\mu$ defined in* (2.7) *satisfies the identity*

$$\mu\boldsymbol{n} = -\partial_s\left(\hat{\boldsymbol{G}}_k(\theta)\partial_s\boldsymbol{X}\right), \tag{2.9}$$

*where*

$$\hat{\boldsymbol{G}}_k(\theta) := \begin{pmatrix} \hat{\gamma}(\theta) & -\hat{\gamma}'(\theta) \\ \hat{\gamma}'(\theta) & \hat{\gamma}(\theta) \end{pmatrix} + k(\theta)\begin{pmatrix} \sin^2\theta & -\cos\theta\sin\theta \\ -\cos\theta\sin\theta & \cos^2\theta \end{pmatrix}, \qquad \forall\theta \in 2\pi\mathbb{T}, \tag{2.10}$$

*and $k(\theta) : 2\pi\mathbb{T} \to \mathbb{R}_{\geq 0}$ is a nonnegative stabilizing function.*

Proof. We note that

$$\boldsymbol{n} = -\partial_s \boldsymbol{X}^\perp = (-\partial_s y, \partial_s x)^T, \qquad \partial_s x = \cos\theta, \qquad \partial_s y = \sin\theta, \tag{2.11}$$

and hence

$$\partial_{ss} x = -\sin\theta \partial_s \theta, \qquad \partial_{ss} y = \cos\theta \partial_s \theta, \tag{2.12}$$

which gives

$$\kappa = -(\partial_{ss}\boldsymbol{X}) \cdot \boldsymbol{n} = \partial_{ss} x \partial_s y - \partial_{ss} y \partial_s x = -(\sin^2\theta + \cos^2\theta)\partial_s\theta = -\partial_s\theta. \tag{2.13}$$

The geometric identity $\kappa \boldsymbol{n} = -\partial_{ss}\boldsymbol{X}$ and the relation $\partial_s \boldsymbol{X} = \tau = \boldsymbol{n}^\perp$ yield

$$\kappa \partial_s \boldsymbol{X} = \kappa \boldsymbol{n}^\perp = -\partial_{ss}\boldsymbol{X}^\perp, \qquad \kappa \partial_s \boldsymbol{X}^\perp = -\kappa \boldsymbol{n} = \partial_{ss}\boldsymbol{X}. \tag{2.14}$$

It follows from (2.13) and (2.14) that

$$\begin{aligned} \partial_s\Big(\hat{\gamma}(\theta)\partial_s \boldsymbol{X}\Big) &= \hat{\gamma}'(\theta)\partial_s\theta\partial_s\boldsymbol{X} + \hat{\gamma}(\theta)\partial_{ss}\boldsymbol{X} \\ &= -\kappa\hat{\gamma}'(\theta)\partial_s\boldsymbol{X} + \hat{\gamma}(\theta)\partial_{ss}\boldsymbol{X} \\ &= \hat{\gamma}'(\theta)\partial_{ss}\boldsymbol{X}^\perp + \hat{\gamma}(\theta)\partial_{ss}\boldsymbol{X}, \end{aligned} \tag{2.15}$$

and

$$\begin{aligned} \partial_s\Big(\hat{\gamma}'(\theta)\partial_s \boldsymbol{X}^\perp\Big) &= \hat{\gamma}''(\theta)\partial_s\theta\partial_s\boldsymbol{X}^\perp + \hat{\gamma}'(\theta)\partial_{ss}\boldsymbol{X}^\perp \\ &= -\kappa\hat{\gamma}''(\theta)\partial_s\boldsymbol{X}^\perp + \hat{\gamma}'(\theta)\partial_{ss}\boldsymbol{X}^\perp \\ &= -\hat{\gamma}''(\theta)\partial_{ss}\boldsymbol{X} + \hat{\gamma}'(\theta)\partial_{ss}\boldsymbol{X}^\perp. \end{aligned} \tag{2.16}$$

Since $\boldsymbol{n}^T\partial_s\boldsymbol{X} = \boldsymbol{n}\cdot\boldsymbol{\tau} \equiv 0$, the term $\partial_s\left(k(\theta)\boldsymbol{n}\boldsymbol{n}^T\partial_s\boldsymbol{X}\right)$ vanishes identically. Combining (2.8b), (2.15), and (2.16), we obtain

$$\begin{aligned} \mu\boldsymbol{n} &= -[\hat{\gamma}(\theta) + \hat{\gamma}''(\theta)]\partial_{ss}\boldsymbol{X} - \partial_s\left(k(\theta)\boldsymbol{n}\boldsymbol{n}^T\partial_s\boldsymbol{X}\right) \\ &= -\partial_s\Big(\hat{\gamma}(\theta)\partial_s\boldsymbol{X}\Big) + \partial_s\Big(\hat{\gamma}'(\theta)\partial_s\boldsymbol{X}^\perp\Big) - \partial_s\left(k(\theta)\boldsymbol{n}\boldsymbol{n}^T\partial_s\boldsymbol{X}\right) \\ &= -\partial_s\Big(\hat{\gamma}(\theta)\partial_s\boldsymbol{X} - \hat{\gamma}'(\theta)\partial_s\boldsymbol{X}^\perp + k(\theta)\boldsymbol{n}\boldsymbol{n}^T\partial_s\boldsymbol{X}\Big). \end{aligned} \tag{2.17}$$

Moreover, (2.11) gives

$$\begin{pmatrix} \sin^2\theta & -\sin\theta\cos\theta \\ -\sin\theta\cos\theta & \cos^2\theta \end{pmatrix} = \begin{pmatrix} -\sin\theta \\ \cos\theta \end{pmatrix}(-\sin\theta, \cos\theta) = \boldsymbol{n}\boldsymbol{n}^T, \tag{2.18}$$

and therefore

$$\begin{aligned} \hat{\boldsymbol{G}}_k(\theta)\partial_s\boldsymbol{X} &= \left[\begin{pmatrix} \hat{\gamma}(\theta) & -\hat{\gamma}'(\theta) \\ \hat{\gamma}'(\theta) & \hat{\gamma}(\theta) \end{pmatrix} + k(\theta)\begin{pmatrix} \sin^2\theta & -\sin\theta\cos\theta \\ -\sin\theta\cos\theta & \cos^2\theta \end{pmatrix}\right]\partial_s\boldsymbol{X} \\ &= \left[\hat{\gamma}(\theta)I_2 + \hat{\gamma}'(\theta)J + k(\theta)\boldsymbol{n}\boldsymbol{n}^T\right]\partial_s\boldsymbol{X} \\ &= \hat{\gamma}(\theta)\partial_s\boldsymbol{X} - \hat{\gamma}'(\theta)\partial_s\boldsymbol{X}^\perp + k(\theta)\boldsymbol{n}\boldsymbol{n}^T\partial_s\boldsymbol{X}, \end{aligned} \tag{2.19}$$

where $I_2$ is the $2\times 2$ identity matrix. Substituting (2.19) into (2.17) proves the desired identity (2.9). □

Using the identity (2.9), we rewrite the geometric partial differential equations (2.8) governing anisotropic surface diffusion in the following conservative form:

$$\boldsymbol{n}\cdot\partial_t\boldsymbol{X} - \partial_{ss}\mu = 0, \qquad 0 < s < L(t), \qquad t > 0, \tag{2.20a}$$

$$\mu\boldsymbol{n} + \partial_s\left(\hat{\boldsymbol{G}}_k(\theta)\partial_s\boldsymbol{X}\right) = \boldsymbol{0}. \tag{2.20b}$$

Remark 2.1. In the isotropic case, the curvature vector satisfies $\kappa\boldsymbol{n} = -\partial_{ss}\boldsymbol{X} = -\partial_s\Big(\boldsymbol{I}_2\partial_s\boldsymbol{X}\Big)$. This motivates the stabilized conservative form $\mu\boldsymbol{n} = -\partial_s\Big(\hat{\boldsymbol{G}}_k(\theta)\partial_s\boldsymbol{X}\Big)$ for anisotropic surface diffusion. The stabilizing term is designed according to two principles: (i) it should make no contribution at the continuous level, so the tangent vector $\partial_s\boldsymbol{X}$ lies in its kernel; and (ii) it should be positive

semidefinite to provide favorable numerical properties. We therefore choose the stabilizing term as $k(\theta)\boldsymbol{n}\boldsymbol{n}^T = k(\theta)\begin{pmatrix} \sin^2\theta & -\cos\theta\sin\theta \\ -\cos\theta\sin\theta & \cos^2\theta \end{pmatrix}$.

Remark 2.2. Taking (2.10) with the stabilizing function $k(\theta) \equiv 0$, we obtain $\hat{\boldsymbol{G}}_k(\theta) = \begin{pmatrix} \hat{\gamma}(\theta) & -\hat{\gamma}'(\theta) \\ \hat{\gamma}'(\theta) & \hat{\gamma}(\theta) \end{pmatrix}$ which reduces to the surface energy matrix in [108] denoted by $G(\theta)$. Moreover, in the $\gamma(\boldsymbol{n})$ formulation, the one-to-one correspondence $\boldsymbol{n} = \boldsymbol{n}(\theta) = (-\sin\theta, \cos\theta)^T$ allows us to define the stabilizing function by $k(\boldsymbol{n}) := k(\boldsymbol{n}(\theta)) = k(\theta)$, so the stabilizing term becomes $k(\boldsymbol{n})\boldsymbol{n}\boldsymbol{n}^T$. Thus $\hat{\boldsymbol{G}}_k(\theta)$ becomes the surface energy matrix in [13], denoted by $\boldsymbol{G}_k(\boldsymbol{n})$.

Remark 2.3. At the continuous level, the stabilizing function $k(\theta)$ makes no contribution because $\boldsymbol{n}^T\partial_s\boldsymbol{X} = 0$. Thus the conservative form (2.20) is equivalent to the original form (2.8). At the discrete level, however, $k(\theta)$ provides stabilization and relaxes the energy stability requirement on the anisotropy $\hat{\gamma}(\theta)$. For example, the surface energy matrix $G(\theta)$ in [108], which has no stabilizing term, ensures energy stability only for certain weak anisotropies. Adding the stabilizing term extends the formulation to more general anisotropies; see condition (2.56).

### 2.3. A stabilized parametric finite element method for surface diffusion

In this section, we derive a new weak formulation from the conservative form (2.20) and introduce its spatial semidiscretization. Applying the semi-implicit Euler method in time then gives a structure-preserving *stabilized parametric finite element method* that preserves area conservation and energy dissipation at the discrete level.

**2.3.1. Weak formulation.** To derive a weak formulation of (2.20), we introduce a time-independent parameter $\rho$ on the fixed interval $\mathbb{I} := [0, 1]$ and parameterize the curve $\Gamma(t)$ by

$$\Gamma(t) := \boldsymbol{X}(\rho, t) = (x(\rho, t), y(\rho, t))^T : \mathbb{I}\times\mathbb{R}^+ \to \mathbb{R}^2. \tag{2.21}$$

The arc length parameter $s$ is given by $s = \int_0^\rho |\partial_\rho \boldsymbol{X}(q, t)|\,\mathrm{d}q$. When no confusion arises, we use $\boldsymbol{X}(\rho, t)$ and $\boldsymbol{X}(s, t)$ interchangeably.

We introduce the following function space on the evolving curve $\Gamma(t)$:

$$L^2(\mathbb{I}) := \left\{ u : \mathbb{I} \to \mathbb{R} \mid \int_{\Gamma(t)} |u(s)|^2\,\mathrm{d}s = \int_{\mathbb{I}} |u(s(\rho, t))|^2 \partial_\rho s\,\mathrm{d}\rho < +\infty \right\}, \tag{2.22}$$

equipped with the $L^2$ inner product

$$\Big(u, v\Big)_{\Gamma(t)} := \int_{\Gamma(t)} u(s)v(s)\,\mathrm{d}s = \int_{\mathbb{I}} u(s(\rho, t))v(s(\rho, t))\partial_\rho s\,\mathrm{d}\rho, \tag{2.23}$$

where $u, v$ are arbitrary scalar- or vector-valued functions. The associated Sobolev spaces are defined by

$$H^1(\mathbb{I}) := \left\{ u : \mathbb{I} \to \mathbb{R} \mid u \in L^2(\mathbb{I}),\ \text{and } \partial_\rho u \in L^2(\mathbb{I}) \right\}, \tag{2.24a}$$

$$H^1_p(\mathbb{I}) := \left\{ u \in H^1(\mathbb{I}) \mid u(0) = u(1) \right\}. \tag{2.24b}$$

These definitions extend directly to the vector-valued spaces $[L^2(\mathbb{I})]^2$, $[H^1(\mathbb{I})]^2$ and $[H^1_p(\mathbb{I})]^2$.

Multiplying (2.20a) by a test function $\varphi \in H^1_p(\mathbb{I})$, integrating along $\Gamma(t)$, and applying integration by parts, we obtain

$$\Big(\boldsymbol{n}\cdot\partial_t\boldsymbol{X}, \varphi\Big)_{\Gamma(t)} + \Big(\partial_s\mu, \partial_s\varphi\Big)_{\Gamma(t)} = 0. \tag{2.25}$$

Similarly, taking the dot product of (2.20b) with the test function $\boldsymbol{\omega} = (\omega_1, \omega_2)^T \in [H_p^1(\mathbb{I})]^2$ and integrating by parts gives

$$\begin{aligned} 0 &= \left(\mu \boldsymbol{n} + \partial_s \left(\hat{\boldsymbol{G}}_k(\theta)\partial_s \boldsymbol{X}\right), \boldsymbol{\omega}\right)_{\Gamma(t)} \\ &= \left(\mu \boldsymbol{n}, \boldsymbol{\omega}\right)_{\Gamma(t)} + \left(\partial_s(\hat{\boldsymbol{G}}_k(\theta)\partial_s \boldsymbol{X}), \boldsymbol{\omega}\right)_{\Gamma(t)} \\ &= \left(\mu \boldsymbol{n}, \boldsymbol{\omega}\right)_{\Gamma(t)} - \left(\hat{\boldsymbol{G}}_k(\theta)\partial_s \boldsymbol{X}, \partial_s \boldsymbol{\omega}\right)_{\Gamma(t)} \end{aligned} \tag{2.26}$$

Combining (2.25) and (2.26), we obtain the following weak formulation of (2.20): given an initial closed curve $\Gamma(0) := \boldsymbol{X}(\cdot, 0) = \boldsymbol{X}_0 \in [H_p^1(\mathbb{I})]^2$, find $(\boldsymbol{X}(\cdot, t) = (x(\cdot, t), y(\cdot, t))^T, \mu(\cdot, t)) \in [H_p^1(\mathbb{I})]^2 \times H_p^1(\mathbb{I})$ such that

$$\left(\boldsymbol{n} \cdot \partial_t \boldsymbol{X}, \varphi\right)_{\Gamma(t)} + \left(\partial_s \mu, \partial_s \varphi\right)_{\Gamma(t)} = 0, \qquad \forall \varphi \in H_p^1(\mathbb{I}), \tag{2.27a}$$

$$\left(\mu \boldsymbol{n}, \boldsymbol{\omega}\right)_{\Gamma(t)} - \left(\hat{\boldsymbol{G}}_k(\theta)\partial_s \boldsymbol{X}, \partial_s \boldsymbol{\omega}\right)_{\Gamma(t)} = 0, \qquad \forall \boldsymbol{\omega} \in [H_p^1(\mathbb{I})]^2. \tag{2.27b}$$

The weak formulation (2.27) preserves two geometric properties: area conservation and energy dissipation.

Proposition 2.1 (Area conservation and energy dissipation). *Let $\Gamma(t)$ be determined by a solution $(\boldsymbol{X}(\cdot, t), \mu(\cdot, t))$ of the weak formulation* (2.27)*. Define its enclosed area and total free energy by*

$$A(t) := \int_{\Gamma(t)} y(s, t)\partial_s x(s, t)\, \mathrm{d}s, \qquad W(t) := \int_{\Gamma(t)} \hat{\gamma}(\theta)\, \mathrm{d}s. \tag{2.28}$$

*Then*

$$A(t) \equiv A(0), \qquad W(t) \le W(t_1) \le W(0), \qquad \forall t \ge t_1 \ge 0. \tag{2.29}$$

*More precisely,*

$$\frac{\mathrm{d}}{\mathrm{d}t} A(t) = 0, \qquad \frac{\mathrm{d}}{\mathrm{d}t} W(t) = -\int_{\Gamma(t)} |\partial_s \mu|^2\, \mathrm{d}s \le 0, \qquad t \ge 0. \tag{2.30}$$

To prove this proposition, we introduce the following transport lemma:

Lemma 2.1 (Transport lemma). *Let $\Gamma(t)$ be a two-dimensional piecewise $C^1$ curve parameterized by $\boldsymbol{X}(\rho, t)$, and let $f : \Gamma(t) \times \mathbb{R}^+ \to \mathbb{R}$ be differentiable. Then*

$$\frac{\mathrm{d}}{\mathrm{d}t} \int_{\Gamma(t)} f\, \mathrm{d}s = \int_{\Gamma(t)} \partial_t f + f\partial_s(\partial_t \boldsymbol{X}) \cdot \partial_s \boldsymbol{X}\, \mathrm{d}s. \tag{2.31}$$

Proof. Since $|\partial_\rho \boldsymbol{X}| = \sqrt{(\partial_\rho x)^2 + (\partial_\rho y)^2}$, we have

$$\begin{aligned} \partial_t |\partial_\rho \boldsymbol{X}| &= \frac{\partial_\rho x \partial_t(\partial_\rho x) + \partial_\rho y \partial_t(\partial_\rho y)}{\sqrt{(\partial_\rho x)^2 + (\partial_\rho y)^2}} \\ &= \frac{\partial_\rho \boldsymbol{X}}{|\partial_\rho \boldsymbol{X}|} \cdot \frac{\partial_\rho(\partial_t \boldsymbol{X})}{|\partial_\rho \boldsymbol{X}|} |\partial_\rho \boldsymbol{X}| \\ &= \partial_s \boldsymbol{X} \cdot \partial_s(\partial_t \boldsymbol{X}) |\partial_\rho \boldsymbol{X}|, \end{aligned} \tag{2.32}$$

and hence

$$\begin{aligned}\frac{\mathrm{d}}{\mathrm{d}t}\int_{\Gamma(t)} f\,\mathrm{d}s &= \frac{\mathrm{d}}{\mathrm{d}t}\int_0^1 f|\partial_\rho \boldsymbol{X}|\,\mathrm{d}\rho\\ &= \int_0^1 \partial_t f\,|\partial_\rho \boldsymbol{X}| + f\partial_t|\partial_\rho \boldsymbol{X}|\,\mathrm{d}\rho\\ &= \int_0^1 \partial_t f\,|\partial_\rho \boldsymbol{X}| + f\partial_s(\partial_t \boldsymbol{X})\cdot\partial_s \boldsymbol{X}|\partial_\rho \boldsymbol{X}|\,\mathrm{d}\rho\\ &= \int_{\Gamma(t)} \partial_t f + f\partial_s(\partial_t \boldsymbol{X})\cdot\partial_s \boldsymbol{X}\,\mathrm{d}s.\end{aligned} \tag{2.33}$$

□

We now prove Proposition 2.1:

Proof. Let $\Omega(t)$ be the region enclosed by $\Gamma(t)$. For area conservation, the Reynolds transport theorem [123] and the choice $\varphi \equiv 1$ in (2.27a) give

$$\begin{aligned}\frac{\mathrm{d}}{\mathrm{d}t}A(t) &= \frac{\mathrm{d}}{\mathrm{d}t}\int_{\Omega(t)} 1\,\mathrm{d}x\mathrm{d}y = \int_{\Gamma(t)} \boldsymbol{n}\cdot\partial_t \boldsymbol{X}\,\mathrm{d}s\\ &= \Big(\boldsymbol{n}\cdot\partial_t \boldsymbol{X}, 1\Big)_{\Gamma(t)} = -\Big(\partial_s\mu, \partial_s 1\Big)_{\Gamma(t)} = 0.\end{aligned} \tag{2.34}$$

For energy dissipation, Lemma 2.1 gives

$$\begin{aligned}\frac{\mathrm{d}}{\mathrm{d}t}W(t) &= \int_{\Gamma(t)} \partial_t\hat{\gamma}(\theta) + \hat{\gamma}(\theta)\partial_s(\partial_t \boldsymbol{X})\cdot\partial_s \boldsymbol{X}\,\mathrm{d}s\\ &= \int_{\Gamma(t)} \hat{\gamma}'(\theta)\partial_t\theta + \hat{\gamma}(\theta)\partial_s(\partial_t \boldsymbol{X})\cdot\partial_s \boldsymbol{X}\,\mathrm{d}s.\end{aligned} \tag{2.35}$$

On the other hand, using (2.32), we rewrite $\partial_s(\partial_t \boldsymbol{X})$ as

$$\begin{aligned}\partial_s(\partial_t \boldsymbol{X}) &= \frac{1}{|\partial_\rho \boldsymbol{X}|}\partial_\rho(\partial_t \boldsymbol{X})\\ &= \frac{1}{|\partial_\rho \boldsymbol{X}|}\partial_t\left(|\partial_\rho \boldsymbol{X}|(\cos\theta, \sin\theta)^T\right)\\ &= \frac{1}{|\partial_\rho \boldsymbol{X}|}\left(\partial_s \boldsymbol{X}\cdot\partial_s(\partial_t \boldsymbol{X})|\partial_\rho \boldsymbol{X}|(\cos\theta, \sin\theta)^T + |\partial_\rho \boldsymbol{X}|(-\sin\theta, \cos\theta)^T\partial_t\theta\right)\end{aligned} \tag{2.36}$$

Together with $\partial_s \boldsymbol{X}^\perp = (\sin\theta, -\cos\theta)^T$, this yields

$$\partial_t\theta = -\partial_s(\partial_t \boldsymbol{X})\cdot\partial_s \boldsymbol{X}^\perp. \tag{2.37}$$

Therefore,

$$\frac{\mathrm{d}}{\mathrm{d}t}W(t) = \int_{\Gamma(t)} \left[\hat{\gamma}(\theta)\partial_s \boldsymbol{X} - \hat{\gamma}'(\theta)\partial_s \boldsymbol{X}^\perp\right]\cdot\partial_s(\partial_t \boldsymbol{X})\,\mathrm{d}s. \tag{2.38}$$

Since $\boldsymbol{n}^T\partial_s \boldsymbol{X} \equiv 0$, we have

$$\begin{aligned}\hat{\gamma}(\theta)\partial_s \boldsymbol{X} - \hat{\gamma}'(\theta)\partial_s \boldsymbol{X}^\perp &= \hat{\gamma}(\theta)\partial_s \boldsymbol{X} - \hat{\gamma}'(\theta)\partial_s \boldsymbol{X}^\perp + k(\theta)\boldsymbol{n}\boldsymbol{n}^T\partial_s \boldsymbol{X}\\ &= \hat{\boldsymbol{G}}_k(\theta)\partial_s \boldsymbol{X},\end{aligned} \tag{2.39}$$

and consequently

$$\frac{\mathrm{d}}{\mathrm{d}t}W(t) = \int_{\Gamma(t)} \hat{\boldsymbol{G}}_k(\theta)\partial_s \boldsymbol{X}\cdot\partial_s(\partial_t \boldsymbol{X})\,\mathrm{d}s. \tag{2.40}$$

Taking $\varphi = \mu$ and $\boldsymbol{\omega} = \partial_t \boldsymbol{X}$ in (2.27a) and (2.27b), respectively, we obtain

$$\begin{aligned} \frac{\mathrm{d}}{\mathrm{d}t} W(t) &= \Big(\hat{\boldsymbol{G}}_k(\theta)\partial_s \boldsymbol{X}, \partial_s(\partial_t \boldsymbol{X})\Big)_{\Gamma(t)} \\ &= \Big(\mu \boldsymbol{n}, \partial_t \boldsymbol{X}\Big)_{\Gamma(t)} = -\Big(\partial_s \mu, \partial_s \mu\Big)_{\Gamma(t)} \leq 0. \end{aligned} \tag{2.41}$$

□

**2.3.2. Spatial semidiscretization.** For the spatial discretization, let $N > 2$ be an integer, set the mesh size $h = 1/N$ and the nodes $\rho_j = jh$, and define $I_j = [\rho_{j-1}, \rho_j]$ for $j = 1, 2, \cdots, N$. This gives a uniform partition $\mathbb{I} = \cup_{j=1}^{N} I_j$ of $\mathbb{I} = [0, 1]$. We approximate the closed curve $\Gamma(t) = \boldsymbol{X}(\cdot, t)$ by a polygonal curve $\Gamma^h(t) = \boldsymbol{X}^h(\cdot, t) = \big(x^h(\cdot, t), y^h(\cdot, t)\big)^T$ with initial condition $\boldsymbol{X}^h(\rho_j, 0) = \boldsymbol{X}(\rho_j, 0)$.

The polygonal curve $\Gamma^h(t)$ consists of the ordered edges $\{\boldsymbol{h}_j(t)\}_{j=1}^{N}$, namely

$$\Gamma^h(t) = \bigcup_{j=1}^{N} \boldsymbol{h}_j(t) \qquad \text{where} \quad \boldsymbol{h}_j(t) = (h_{j,x}, h_{j,y})^T := \boldsymbol{X}^h(\rho_j, t) - \boldsymbol{X}^h(\rho_{j-1}, t). \tag{2.42}$$

We assume that $h_{\min}(t) = \min\limits_{1 \leq j \leq N} |\boldsymbol{h}_j(t)| > 0$ for all $t > 0$.

The edge $\boldsymbol{h}_j$ determines the discrete geometric quantities on each interval: the unit tangent $\boldsymbol{\tau}^h$, the outward unit normal $\boldsymbol{n}^h$, and the inclination angle $\theta^h$. Specifically,

$$\boldsymbol{\tau}^h|_{I_j} = \frac{\boldsymbol{h}_j}{|\boldsymbol{h}_j|} := \boldsymbol{\tau}_j^h, \qquad \boldsymbol{n}^h|_{I_j} = -(\boldsymbol{\tau}_j^h)^{\perp} = -\frac{(\boldsymbol{h}_j)^{\perp}}{|\boldsymbol{h}_j|} := \boldsymbol{n}_j^h; \tag{2.43}$$

and

$$\theta^h|_{I_j} := \theta_j^h, \qquad \text{satisfying} \quad \cos\theta_j^h = \frac{h_{j,x}}{|\boldsymbol{h}_j|}, \quad \sin\theta_j^h = \frac{h_{j,y}}{|\boldsymbol{h}_j|}. \tag{2.44}$$

We introduce the finite element spaces

$$\mathbb{K}^h := \Big\{u^h \in C(\mathbb{I}) \mid u^h|_{I_j} \in \mathcal{P}^1(I_j),\ \forall j = 1, 2, \cdots, N\Big\} \subseteq H^1(\mathbb{I}), \tag{2.45a}$$

$$\mathbb{K}_p^h := \{u^h \in \mathbb{K}^h \mid u^h(0) = u^h(1)\}, \tag{2.45b}$$

where $\mathcal{P}^1(I_j)$ is the set of polynomials on $I_j$ of degree $\leq 1$.

For $u, v \in \mathbb{K}^h$, the mass-lumped inner product $\Big(\cdot, \cdot\Big)_{\Gamma^h(t)}^h$ on $\Gamma^h(t)$ is defined by

$$\Big(u, v\Big)_{\Gamma^h(t)}^h := \frac{1}{2} \sum_{j=1}^{N} |\boldsymbol{h}_j(t)| \ \Big((u \cdot v)(\rho_{j-1}^+) + (u \cdot v)(\rho_j^-)\Big), \tag{2.46}$$

where $u(\rho_j^{\pm}) = \lim\limits_{\rho \to \rho_j^{\pm}} u(\rho)$. For $f \in \mathbb{K}^h$, the discrete differential operator $\partial_s$ is defined by

$$\partial_s f|_{I_j} := \frac{f(\rho_j) - f(\rho_{j-1})}{|\boldsymbol{h}_j|}. \tag{2.47}$$

These definitions also apply to vector-valued functions.

The spatial semidiscretization of the weak formulation (2.27) reads as follows. Let $\Gamma_0^h := \boldsymbol{X}^h(\cdot, 0) \in [\mathbb{K}_p^h]^2$, $\mu(\cdot) \in \mathbb{K}_p^h$ approximate $\Gamma_0 := \boldsymbol{X}_0(\cdot), \mu_0(\cdot)$, respectively. For $t > 0$, find $\big(\boldsymbol{X}^h(\cdot, t), \mu^h(\cdot)\big) \in [\mathbb{K}_p^h]^2 \times \mathbb{K}_p^h$ such that

$$\Big(\boldsymbol{n}^h \cdot \partial_t \boldsymbol{X}^h, \varphi^h\Big)_{\Gamma^h(t)}^h + \Big(\partial_s \mu^h, \partial_s \varphi^h\Big)_{\Gamma^h(t)}^h = 0, \qquad \forall \varphi^h \in \mathbb{K}_p^h, \tag{2.48a}$$

$$\Big(\mu^h \boldsymbol{n}^h, \boldsymbol{\omega}^h\Big)_{\Gamma^h(t)}^h - \Big(\hat{\boldsymbol{G}}_k(\theta^h)\partial_s \boldsymbol{X}^h, \partial_s \boldsymbol{\omega}^h\Big)_{\Gamma^h(t)}^h = 0, \qquad \forall \boldsymbol{\omega}^h \in [\mathbb{K}_p^h]^2, \tag{2.48b}$$

where

$$\hat{\boldsymbol{G}}_k(\theta^h) = \begin{pmatrix} \hat{\gamma}(\theta^h) & -\hat{\gamma}'(\theta^h) \\ \hat{\gamma}'(\theta^h) & \hat{\gamma}(\theta^h) \end{pmatrix} + k(\theta^h) \begin{pmatrix} \sin^2\theta^h & -\cos\theta^h \sin\theta^h \\ -\cos\theta^h \sin\theta^h & \cos^2\theta^h \end{pmatrix}. \tag{2.49}$$

Let $A^h(t), W^h(t)$ denote the enclosed area and total free energy of the polygonal curve $\Gamma^h(t)$, respectively, defined by

$$A^h(t) = \frac{1}{2}\sum_{j=1}^{N}(x_j^h(t) - x_{j-1}^h(t))(y_j^h(t) + y_{j-1}^h(t)), \tag{2.50a}$$

$$W^h(t) = \sum_{j=1}^{N} |\boldsymbol{h}_j(t)|\hat{\gamma}(\theta_j^h), \tag{2.50b}$$

where $x_j^h(t) := x^h(\rho_j, t), y_j^h(t) := y^h(\rho_j, t),\ \forall 0 \le j \le N$.

An argument similar to the proof of Proposition 2.1 shows that the semidiscretization (2.48) preserves both geometric properties:

Proposition 2.2 (Area conservation and energy dissipation). *Let $\Gamma^h(t)$ be determined by a solution $(\boldsymbol{X}^h(\cdot,t), \mu^h(\cdot,t))$ of (2.48). Then*

$$A^h(t) \equiv A^h(0), \qquad W^h(t) \le W^h(t_1) \le W^h(0), \qquad \forall t \ge t_1 \ge 0. \tag{2.51}$$

**2.3.3. A structure-preserving stabilized parametric finite element scheme.** Let $\tau$ be a uniform time step. We approximate $\Gamma(t) = \boldsymbol{X}(\cdot,t)$ at $t_m = m\tau$ $(m = 0, 1, \cdots)$ by $\Gamma^m = \boldsymbol{X}^m(\cdot) = \cup_{j=1}^N \boldsymbol{h}_j^m$, where $\boldsymbol{h}_j^m := \boldsymbol{X}^m(\rho_j) - \boldsymbol{X}^m(\rho_{j-1})$. The mass-lumped inner product $(\cdot,\cdot)_{\Gamma^m}^h$, unit tangent $\boldsymbol{\tau}^m$, outward unit normal $\boldsymbol{n}^m$, and inclination angle $\theta^m$ on $\Gamma^m$ are defined analogously.

Inspired by the techniques used in [19, 91, 9, 8] to construct structure-preserving schemes for isotropic surface diffusion, we apply the semi-implicit Euler method in time. This yields the following *semi-implicit structure-preserving scheme* for anisotropic surface diffusion (2.8):

Let the initial approximation $\Gamma^0(\cdot) \in [\mathbb{K}_p^h]^2$ be given by $\boldsymbol{X}^0(\rho_j) = \boldsymbol{X}_0(\rho_j), \forall 0 \le j \le N$. For $m = 0, 1, 2, \ldots$, find $(\boldsymbol{X}^{m+1}(\cdot) = (x^{m+1}(\cdot), y^{m+1}(\cdot))^T, \mu^{m+1}(\cdot)) \in [\mathbb{K}_p^h]^2 \times \mathbb{K}_p^h$ such that

$$\left(\boldsymbol{n}^{m+\frac{1}{2}} \cdot \frac{\boldsymbol{X}^{m+1} - \boldsymbol{X}^m}{\tau}, \varphi^h\right)_{\Gamma^m}^h + \left(\partial_s \mu^{m+1}, \partial_s \varphi^h\right)_{\Gamma^m}^h = 0, \qquad \forall \varphi^h \in \mathbb{K}_p^h, \tag{2.52a}$$

$$\left(\mu^{m+1}\boldsymbol{n}^{m+\frac{1}{2}}, \boldsymbol{\omega}^h\right)_{\Gamma^m}^h - \left(\hat{\boldsymbol{G}}_k(\theta^m)\partial_s \boldsymbol{X}^{m+1}, \partial_s \boldsymbol{\omega}^h\right)_{\Gamma^m}^h = 0, \qquad \forall \boldsymbol{\omega}^h \in [\mathbb{K}_p^h]^2, \tag{2.52b}$$

where

$$\hat{\boldsymbol{G}}_k(\theta^m) = \begin{pmatrix} \hat{\gamma}(\theta^m) & -\hat{\gamma}'(\theta^m) \\ \hat{\gamma}'(\theta^m) & \hat{\gamma}(\theta^m) \end{pmatrix} + k(\theta^m) \begin{pmatrix} \sin^2\theta^m & -\cos\theta^m \sin\theta^m \\ -\cos\theta^m \sin\theta^m & \cos^2\theta^m \end{pmatrix}, \tag{2.53}$$

and

$$\boldsymbol{n}^{m+\frac{1}{2}} := -\frac{1}{2}\frac{1}{|\partial_\rho \boldsymbol{X}^m|}(\partial_\rho \boldsymbol{X}^m + \partial_\rho \boldsymbol{X}^{m+1})^\perp. \tag{2.54}$$

Remark 2.4. The scheme is weakly implicit: the integration domain is given explicitly, and each equation contains only one nonlinear term. This term is at most quadratic in the components of $\boldsymbol{X}^{m+1}$ and $\mu^{m+1}$, so the scheme can be solved efficiently and accurately by Newton iteration; see Appendix A.1.2 or [19].

Remark 2.5. The choice of $\boldsymbol{n}^{m+\frac{1}{2}}$ is essential for area conservation. Replacing it by $\boldsymbol{n}^m$ gives a semi-implicit scheme that preserves only energy dissipation.

**2.3.4. Structure preservation.** The enclosed area $A^m$ and total energy $W^m$ of the polygonal curve $\Gamma^m$ are given by

$$A^m = \frac{1}{2}\sum_{j=1}^{N}\left(x^m(\rho_j) - x^m(\rho_{j-1})\right)\left(y^m(\rho_j) + y^m(\rho_{j-1})\right), \tag{2.55a}$$

$$W^m = \sum_{j=1}^{N} |\boldsymbol{h}_j^m|\hat{\gamma}(\theta_j^m). \tag{2.55b}$$

In applications, $\hat{\gamma}(\theta)$ often has limited regularity. Throughout the following analysis, we assume that $\hat{\gamma}(\theta)$ is globally $C^1$ and piecewise $C^2$ on $2\pi\mathbb{T}$.

For convenience, we introduce the following energy stability condition:

Definition 2.1 (Energy stability condition). Suppose that $\hat{\gamma}(\theta)$ is globally $C^1$ and piecewise $C^2$. Its energy stability condition is defined by

$$3\hat{\gamma}(\theta) \geq \hat{\gamma}(\theta - \pi), \qquad \forall \theta \in 2\pi\mathbb{T}, \tag{2.56a}$$

$$\hat{\gamma}'(\theta^*) = 0, \qquad \text{whenever } 3\hat{\gamma}(\theta^*) = \hat{\gamma}(\theta^* - \pi), \qquad \theta^* \in 2\pi\mathbb{T}. \tag{2.56b}$$

The main theorem of this chapter establishes the structure-preserving properties of (2.52):

Theorem 2.2 (Structure preservation). *For any surface energy $\hat{\gamma}(\theta)$ satisfying* (2.56)*, the scheme* (2.52) *preserves area conservation and, for sufficiently large $k(\theta)$, unconditional energy dissipation, namely*

$$A^{m+1} = A^m = \cdots = A^0, \qquad W^{m+1} \leq W^m \leq \cdots \leq W^0, \qquad \forall m \geq 0. \tag{2.57}$$

We first prove area conservation. Energy dissipation is discussed in detail in the next section.

Proof. Let $\Gamma^h(\alpha) = \boldsymbol{X}^h(\rho, \alpha)$ be the linear interpolation between $\boldsymbol{X}^m$ and $\boldsymbol{X}^{m+1}$:

$$\boldsymbol{X}^h(\rho, \alpha) \coloneqq (1-\alpha)\boldsymbol{X}^m(\rho) + \alpha\boldsymbol{X}^{m+1}(\rho), \qquad 0 \leq \alpha, \rho \leq 1. \tag{2.58}$$

Let $\boldsymbol{n}^h$ be the outward unit normal to $\Gamma^h(\alpha)$, and let $A(\alpha)$ be the area enclosed by $\Gamma^h(\alpha)$. Applying the Reynolds transport theorem [123] to $A(\alpha)$ gives

$$\begin{aligned}\frac{\mathrm{d}}{\mathrm{d}\alpha}A(\alpha) &= \int_{\Gamma^h(\alpha)} \partial_\alpha \boldsymbol{X}^h \cdot \boldsymbol{n}^h \,\mathrm{d}s \\ &= \int_{\mathbb{I}} \left[\boldsymbol{X}^{m+1} - \boldsymbol{X}^m\right] \cdot \left[-(1-\alpha)\partial_\rho \boldsymbol{X}^m - \alpha\partial_\rho \boldsymbol{X}^{m+1}\right]^\perp \mathrm{d}\rho,\end{aligned} \tag{2.59}$$

Here we have used (2.58) and the identities

$$\partial_\alpha \boldsymbol{X}^h = \boldsymbol{X}^{m+1} - \boldsymbol{X}^m, \qquad \boldsymbol{n}^h = -|\partial_\rho \boldsymbol{X}^h|^{-1}(\partial_\rho \boldsymbol{X}^h)^\perp. \tag{2.60}$$

Integrating (2.59) from 0 to 1 and using the definition of $\boldsymbol{n}^{m+\frac{1}{2}}$ in (2.54), we obtain

$$\begin{aligned}A(1) - A(0) &= \int_{\mathbb{I}} \left[\boldsymbol{X}^{m+1} - \boldsymbol{X}^m\right] \cdot \left[-\frac{1}{2}\left(\partial_\rho \boldsymbol{X}^m + \partial_\rho \boldsymbol{X}^{m+1}\right)\right]^\perp \mathrm{d}\rho \\ &= \left((\boldsymbol{X}^{m+1} - \boldsymbol{X}^m) \cdot \boldsymbol{n}^{m+\frac{1}{2}}, 1\right)_{\Gamma^m}^h.\end{aligned} \tag{2.61}$$

Taking $\varphi^h \equiv 1$ in (2.52a) gives $A(1) = A(0)$, or equivalently $A^{m+1} = A^m$. This proves area conservation. □

Remark 2.6. The scheme (2.52) is designed for a sharp-interface model. Stabilization techniques for phase-field models, such as convex splitting [133, 76] and stabilized semi-implicit schemes [51, 41], therefore do not apply directly here. The scheme (2.52) preserves the original energy stability without additional correction terms.

Remark 2.7. For the $m$-fold anisotropy $\hat{\gamma}(\theta) = 1 + \beta\cos m\theta$, condition (2.56) holds for $|\beta| < 1$ when $m$ is even and for $|\beta| \leq \frac{1}{2}$ when $m$ is odd. Compared with the energy stability condition $|\beta| \leq \frac{1}{m^2+1}$ in [108], this substantially relaxes the restriction on the anisotropy strength.

Remark 2.8. For the ellipsoidal anisotropy $\hat{\gamma}(\theta) = \sqrt{a + b\cos^2\theta}$, the energy stability condition in [108] requires $-\frac{a}{2} \le b \le a$, whereas (2.56) holds for all $a > 0, a + b > 0$.

Remark 2.9. For every symmetric anisotropy satisfying $\hat{\gamma}(\theta) = \hat{\gamma}(\theta - \pi),\ \forall\theta \in 2\pi\mathbb{T}$, including Riemannian metric anisotropy, condition (2.56) holds automatically. Thus the scheme (2.52) is unconditionally energy stable.

### 2.4. Proof of unconditional energy stability

The key to proving energy dissipation for (2.52) is an estimate of the form

$$\left(\hat{\boldsymbol{G}}_k(\theta^m)\partial_s \boldsymbol{X}^{m+1}, \partial_s(\boldsymbol{X}^{m+1} - \boldsymbol{X}^m)\right)_{\Gamma^m}^h \ge W^{m+1} - W^m, \tag{2.62}$$

which controls the energy difference between successive time levels. We first establish its local version in the following lemma:

Lemma 2.2 (Local energy estimate). *Let $\boldsymbol{p}, \boldsymbol{q}$ be two nonzero vectors in $\mathbb{R}^2$, written as $\boldsymbol{p} = |\boldsymbol{p}|(\cos\varphi, \sin\varphi)^T$, $\boldsymbol{q} = |\boldsymbol{q}|(\cos\theta, \sin\theta)^T$. For sufficiently large $k(\theta)$, the following inequality holds:*

$$\frac{1}{|\boldsymbol{q}|}\left(\hat{\boldsymbol{G}}_k(\theta)\boldsymbol{p}\right)\cdot(\boldsymbol{p} - \boldsymbol{q}) \ge |\boldsymbol{p}|\hat{\gamma}(\varphi) - |\boldsymbol{q}|\hat{\gamma}(\theta). \tag{2.63}$$

Remark 2.10. Condition (2.56) is almost necessary for the local energy estimate. Taking $\boldsymbol{p} = -\boldsymbol{q}$ gives $\varphi = \theta - \pi$, and (2.63) reduces to $2|\boldsymbol{q}|\hat{\gamma}(\theta) \ge |\boldsymbol{q}|\hat{\gamma}(\theta - \pi) - |\boldsymbol{q}|\hat{\gamma}(\theta)$. Thus condition (2.56) is almost necessary for establishing this local estimate.

**2.4.1. The minimal stabilizing function and its properties.** To prove the local energy estimate (2.63), we introduce two auxiliary functions:

$$P_\alpha(\phi, \theta) := 2\sqrt{\hat{\gamma}^2(\theta) + \alpha\hat{\gamma}(\theta)\sin^2\phi}, \qquad \forall\phi \in 2\pi\mathbb{T}, \tag{2.64a}$$

$$Q(\phi, \theta) := \hat{\gamma}(\theta - \phi) + \hat{\gamma}(\theta)\cos\phi + \hat{\gamma}'(\theta)\sin\phi, \qquad \forall\phi \in 2\pi\mathbb{T}. \tag{2.64b}$$

Using the auxiliary functions $P_\alpha, Q$, we define the minimal stabilizing function by

$$k_0(\theta) := \inf\left\{\alpha \ge 0 \mid P_\alpha(\phi, \theta) - Q(\phi, \theta) \ge 0,\ \forall\phi \in 2\pi\mathbb{T}\right\}. \tag{2.65}$$

By definition, $k_0(\theta)$ is determined by the surface energy $\hat{\gamma}(\theta)$ and is therefore independent of time.

The following theorem ensures the existence of $k_0(\theta)$:

Theorem 2.3. *Suppose that $\hat{\gamma}(\theta)$ satisfies* (2.56). *Then the minimal stabilizing function $k_0(\theta)$ defined in* (2.65) *is well-defined.*

We defer the proof of Theorem 2.3 to Section 2.4.4.

A prescribed $\hat{\gamma}(\theta)$ determines the minimal stabilizing function $k_0(\theta)$, inducing a mapping from $\hat{\gamma}(\theta)$ to $k_0(\theta)$. This mapping is sublinear: it satisfies positive homogeneity and subadditivity.

Lemma 2.3 (Positive homogeneity and subadditivity). *Let $\hat{\gamma}_i(\theta)$ $(i = 1, 2, 3)$ be anisotropic surface energies satisfying* (2.56), *and let $k_i(\theta)$ be the corresponding minimal stabilizing functions.*

*(i) If $\hat{\gamma}_2(\theta) = c\hat{\gamma}_1(\theta)$ for a prescribed positive real number $c > 0$, then $k_2(\theta) = ck_1(\theta)$;*
*(ii) if $\hat{\gamma}_3(\theta) = \hat{\gamma}_1(\theta) + \hat{\gamma}_2(\theta)$, then $k_3(\theta) \le k_1(\theta) + k_2(\theta)$.*

Proof. Denote the auxiliary functions associated with $\hat{\gamma}_i(\theta)$ by $P_{\alpha,i}, Q_i$, respectively.

(i) If $\hat{\gamma}_2(\theta) = c\hat{\gamma}_1(\theta)$, then

$$\begin{aligned} P_{ck_1,2}(\phi, \theta) - Q_2(\phi, \theta) &= 2\sqrt{c^2\hat{\gamma}_1^2(\theta) + c^2k_1(\theta)\hat{\gamma}_1(\theta)\sin^2\phi} \\ &\quad - \left(c\hat{\gamma}_1(\theta - \phi) + c\hat{\gamma}_1(\theta)\cos\phi + c\hat{\gamma}_1'(\theta)\sin\phi\right) \\ &= c\left(P_{k_1,1}(\phi, \theta) - Q_1(\phi, \theta)\right) \ge 0. \end{aligned} \tag{2.66}$$

By the definition of the minimal stabilizing function, $k_2(\theta) \le ck_1(\theta)$. Since $\hat{\gamma}_1(\theta) = \frac{1}{c}\hat{\gamma}_2(\theta)$, the same argument gives $k_1(\theta) \le \frac{1}{c}k_2(\theta)$. Hence $k_2(\theta) = ck_1(\theta)$.

(ii) Suppose that $\hat{\gamma}_3(\theta) = \hat{\gamma}_1(\theta) + \hat{\gamma}_2(\theta)$. We note that

$$\begin{aligned} P^2_{k_1+k_2,3}(\phi,\theta) &= 4\left(\hat{\gamma}_1(\theta)+\hat{\gamma}_2(\theta)\right)^2 + 4\left(\hat{\gamma}_1(\theta)+\hat{\gamma}_2(\theta)\right)\left(k_1(\theta)+k_2(\theta)\right)\sin^2\phi \\ &= 4\left(\hat{\gamma}_1^2(\theta)+\hat{\gamma}_2^2(\theta)+\hat{\gamma}_1(\theta)k_1(\theta)\sin^2\phi+\hat{\gamma}_2(\theta)k_2(\theta)\sin^2\phi\right) \\ &\quad + 4\left[\hat{\gamma}_1(\theta)\left(\hat{\gamma}_2(\theta)+k_2(\theta)\sin^2\phi\right)+\hat{\gamma}_2(\theta)\left(\hat{\gamma}_1(\theta)+k_1(\theta)\sin^2\phi\right)\right] \\ &\geq 4\left(\hat{\gamma}_1^2(\theta)+\hat{\gamma}_1(\theta)k_1(\theta)\sin^2\phi+\hat{\gamma}_2^2(\theta)+\hat{\gamma}_2(\theta)k_2(\theta)\sin^2\phi\right) \\ &\quad + 8\sqrt{\left(\hat{\gamma}_1^2(\theta)+\hat{\gamma}_1(\theta)k_1(\theta)\sin^2\phi\right)\left(\hat{\gamma}_2^2(\theta)+\hat{\gamma}_2(\theta)k_2(\theta)\sin^2\phi\right)} \\ &= \left(P_{k_1,1}(\phi,\theta)+P_{k_2,2}(\phi,\theta)\right)^2, \end{aligned} \tag{2.67}$$

Thus $P_{k_1+k_2,3}(\phi,\theta) \geq P_{k_1,1}(\phi,\theta) + P_{k_2,2}(\phi,\theta)$.

Together with $Q_3(\phi,\theta) = Q_1(\phi,\theta) + Q_2(\phi,\theta)$, this gives

$$\begin{aligned} P_{k_1+k_2,3}(\phi,\theta) - Q_3(\phi,\theta) &\geq P_{k_1,1}(\phi,\theta) - Q_1(\phi,\theta) + P_{k_2,2}(\phi,\theta) - Q_2(\phi,\theta) \\ &\geq 0, \end{aligned} \tag{2.68}$$

The definition of the minimal stabilizing function therefore gives $k_3(\theta) \leq k_1(\theta) + k_2(\theta)$.

□

**2.4.2. The local energy estimate.** In this subsection, we prove the local energy estimate (2.63) assuming Theorem 2.3.

Proof. From the definition of $\hat{\boldsymbol{G}}_k(\theta)$ in (2.10), we note that

$$\begin{pmatrix} \sin^2\theta & -\cos\theta\sin\theta \\ -\cos\theta\sin\theta & \cos^2\theta \end{pmatrix} = \begin{pmatrix} -\sin\theta \\ \cos\theta \end{pmatrix}(-\sin\theta,\cos\theta) = \boldsymbol{n}\boldsymbol{n}^T, \tag{2.69}$$

where $\boldsymbol{n} = -\boldsymbol{q}^\perp/|\boldsymbol{q}|$ is the corresponding unit normal. Hence

$$\begin{aligned} \frac{1}{|\boldsymbol{q}|}\left(\hat{\boldsymbol{G}}_k(\theta)\boldsymbol{p}\right)\cdot\boldsymbol{p} &= \frac{1}{|\boldsymbol{q}|}\left[\hat{\gamma}(\theta)I_2+\hat{\gamma}'(\theta)J+k(\theta)\boldsymbol{n}\boldsymbol{n}^T\right]\boldsymbol{p}\cdot\boldsymbol{p} \\ &= \frac{1}{|\boldsymbol{q}|}\hat{\gamma}(\theta)|\boldsymbol{p}|^2 + \frac{1}{|\boldsymbol{q}|}\hat{\gamma}'(\theta)J\boldsymbol{p}\cdot\boldsymbol{p} + \frac{1}{|\boldsymbol{q}|}k(\theta)(\boldsymbol{n}\cdot\boldsymbol{p})^2 \\ &= \frac{1}{|\boldsymbol{q}|}\hat{\gamma}(\theta)|\boldsymbol{p}|^2 + \frac{1}{|\boldsymbol{q}|}k(\theta)(\boldsymbol{n}\cdot\boldsymbol{p})^2 \\ &= \frac{1}{|\boldsymbol{q}|}\left[\hat{\gamma}(\theta)+k(\theta)\sin^2(\theta-\varphi)\right]|\boldsymbol{p}|^2, \end{aligned} \tag{2.70}$$

and

$$\begin{aligned} \frac{1}{|\boldsymbol{q}|}\left(\hat{\boldsymbol{G}}_k(\theta)\boldsymbol{p}\right)\cdot\boldsymbol{q} &= \frac{1}{|\boldsymbol{q}|}\left[\hat{\gamma}(\theta)I_2+\hat{\gamma}'(\theta)J+k(\theta)\boldsymbol{n}\boldsymbol{n}^T\right]\boldsymbol{p}\cdot\boldsymbol{q} \\ &= \frac{1}{|\boldsymbol{q}|}\hat{\gamma}(\theta)(\boldsymbol{q}\cdot\boldsymbol{p}) + \frac{1}{|\boldsymbol{q}|}\hat{\gamma}'(\theta)J\boldsymbol{p}\cdot\boldsymbol{q} + \frac{1}{|\boldsymbol{q}|}k(\theta)\boldsymbol{n}\boldsymbol{n}^T\boldsymbol{p}\cdot\boldsymbol{q} \\ &= |\boldsymbol{p}|\hat{\gamma}(\theta)\begin{pmatrix}\cos\theta\\ \sin\theta\end{pmatrix}\cdot\begin{pmatrix}\cos\varphi\\ \sin\varphi\end{pmatrix} + |\boldsymbol{p}|\hat{\gamma}'(\theta)\begin{pmatrix}0 & -1\\ 1 & 0\end{pmatrix}\begin{pmatrix}\cos\varphi\\ \sin\varphi\end{pmatrix}\cdot\begin{pmatrix}\cos\theta\\ \sin\theta\end{pmatrix} \\ &\quad + |\boldsymbol{p}|k(\theta)\begin{pmatrix}\sin^2\theta & -\cos\theta\sin\theta\\ -\cos\theta\sin\theta & \cos^2\theta\end{pmatrix}\begin{pmatrix}\cos\varphi\\ \sin\varphi\end{pmatrix}\cdot\begin{pmatrix}\cos\theta\\ \sin\theta\end{pmatrix} \\ &= |\boldsymbol{p}|\hat{\gamma}(\theta)\cos(\theta-\varphi) + |\boldsymbol{p}|\hat{\gamma}'(\theta)(-\sin\varphi,\cos\varphi)\cdot(\cos\theta,\sin\theta) \\ &= |\boldsymbol{p}|\left[\hat{\gamma}(\theta)\cos(\theta-\varphi)+\hat{\gamma}'(\theta)\sin(\theta-\varphi)\right]. \end{aligned} \tag{2.71}$$

Recalling the definition of $P_\alpha(\phi,\theta), Q(\phi,\theta)$ in (2.64), we obtain

$$\frac{1}{|\boldsymbol{q}|}\left(\hat{\boldsymbol{G}}_k(\theta)\boldsymbol{p}\right)\cdot\boldsymbol{p} = \frac{|\boldsymbol{p}|^2}{4|\boldsymbol{q}|\hat{\gamma}(\theta)}P^2_{k(\theta)}(\phi,\theta), \tag{2.72a}$$

$$\frac{1}{|\boldsymbol{q}|}\left(\hat{\boldsymbol{G}}_k(\theta)\boldsymbol{p}\right)\cdot\boldsymbol{q} = |\boldsymbol{p}|(Q(\phi,\theta)-\hat{\gamma}(\theta-\phi)), \tag{2.72b}$$

where $\phi=\theta-\varphi$.

Substituting (2.72a) and (2.72b) into the local energy estimate (2.63) gives

$$\begin{aligned}
&\frac{1}{|\boldsymbol{q}|}\left(\hat{\boldsymbol{G}}_k(\theta)\boldsymbol{p}\right)\cdot(\boldsymbol{p}-\boldsymbol{q}) - \left(|\boldsymbol{p}|\hat{\gamma}(\varphi)-|\boldsymbol{q}|\hat{\gamma}(\theta)\right)\\
&\quad= \frac{|\boldsymbol{p}|^2}{4|\boldsymbol{q}|\hat{\gamma}(\theta)}P^2_{k(\theta)}(\phi,\theta) - |\boldsymbol{p}|(Q(\phi,\theta)-\hat{\gamma}(\theta-\phi))\\
&\qquad- |\boldsymbol{p}|\hat{\gamma}(\theta-\phi)+|\boldsymbol{q}|\hat{\gamma}(\theta)\\
&\quad= \frac{1}{4|\boldsymbol{q}|\hat{\gamma}(\theta)}\left[|\boldsymbol{p}|^2P^2_{k(\theta)}(\phi,\theta) - 4|\boldsymbol{p}||\boldsymbol{q}|\hat{\gamma}(\theta)Q(\phi,\theta)+4|\boldsymbol{q}|^2\hat{\gamma}^2(\theta)\right],
\end{aligned} \tag{2.73}$$

Thus the local energy estimate (2.63) is equivalent to

$$|\boldsymbol{p}|^2P^2_{k(\theta)}(\phi,\theta) - 4|\boldsymbol{p}||\boldsymbol{q}|\hat{\gamma}(\theta)Q(\phi,\theta)+4|\boldsymbol{q}|^2\hat{\gamma}^2(\theta)\geq 0, \tag{2.74}$$

or, equivalently,

$$\left(|\boldsymbol{p}|P_{k(\theta)}-2|\boldsymbol{q}|\hat{\gamma}(\theta)\right)^2 + 4|\boldsymbol{p}||\boldsymbol{q}|\hat{\gamma}(\theta)\left(P_{k(\theta)}(\phi,\theta)-Q(\phi,\theta)\right)\geq 0 \tag{2.75}$$

By (2.65), we have $P_{k(\theta)}(\phi,\theta)-Q(\phi,\theta)\geq 0,\ \forall\phi\in 2\pi\mathbb{T}$ for every $k(\theta)\geq k_0(\theta)$, which proves (2.75). Theorem 2.3 ensures that the minimal stabilizing function $k_0(\theta)<+\infty$ is well-defined. We may therefore choose $k(\theta)\geq k_0(\theta)$ sufficiently large to obtain the desired inequality (2.63). □

**2.4.3. Unconditional energy stability.** The local energy estimate (2.63) in Lemma 2.2 allows us to prove the energy dissipation statement in Theorem 2.2.

Proof. Choose $k(\theta)$ sufficiently large that $k(\theta)\geq k_0(\theta)$. Taking $\boldsymbol{q}=\boldsymbol{h}_j^m, \boldsymbol{p}=\boldsymbol{h}_j^{m+1}$ in the local energy estimate (2.63) gives

$$\frac{1}{|\boldsymbol{h}_j^m|}\left(\hat{\boldsymbol{G}}_k(\theta_j^m)\boldsymbol{h}_j^{m+1}\right)\cdot(\boldsymbol{h}_j^{m+1}-\boldsymbol{h}_j^m)\geq|\boldsymbol{h}_j^{m+1}|\hat{\gamma}(\theta_j^{m+1})-|\boldsymbol{h}_j^m|\hat{\gamma}(\theta_j^m). \tag{2.76}$$

Consequently, for every $m\geq 0$,

$$\begin{aligned}
\left(\hat{\boldsymbol{G}}_k(\theta^m)\partial_s\boldsymbol{X}^{m+1},\partial_s(\boldsymbol{X}^{m+1}-\boldsymbol{X}^m)\right)^h_{\Gamma^m} &= \sum_{j=1}^N\left[|\boldsymbol{h}_j^m|\left(\hat{\boldsymbol{G}}_k(\theta_j^m)\frac{\boldsymbol{h}_j^{m+1}}{|\boldsymbol{h}_j^m|}\right)\cdot\frac{\boldsymbol{h}_j^{m+1}-\boldsymbol{h}_j^m}{|\boldsymbol{h}_j^m|}\right]\\
&= \sum_{j=1}^N\left[\frac{1}{|\boldsymbol{h}_j^m|}\left(\hat{\boldsymbol{G}}_k(\theta_j^m)\boldsymbol{h}_j^{m+1}\right)\cdot(\boldsymbol{h}_j^{m+1}-\boldsymbol{h}_j^m)\right]\\
&\geq \sum_{j=1}^N\left[|\boldsymbol{h}_j^{m+1}|\hat{\gamma}(\theta_j^{m+1})-|\boldsymbol{h}_j^m|\hat{\gamma}(\theta_j^m)\right]\\
&= \sum_{j=1}^N|\boldsymbol{h}_j^{m+1}|\hat{\gamma}(\theta_j^{m+1})-\sum_{j=1}^N|\boldsymbol{h}_j^m|\hat{\gamma}(\theta_j^m)\\
&= W^{m+1}-W^m.
\end{aligned} \tag{2.77}$$

Taking $\varphi^h = \mu^{m+1}$, $\boldsymbol{\omega}^h = \boldsymbol{X}^{m+1} - \boldsymbol{X}^m$ in (2.52) gives

$$\begin{aligned}\left(\hat{\boldsymbol{G}}_k(\theta^m)\partial_s \boldsymbol{X}^{m+1}, \partial_s(\boldsymbol{X}^{m+1} - \boldsymbol{X}^m)\right)^h_{\Gamma^m} &= \left(\mu^{m+1}\boldsymbol{n}^{m+\frac{1}{2}}, \boldsymbol{X}^{m+1} - \boldsymbol{X}^m\right)^h_{\Gamma^m} \\ &= -\tau\left(\partial_s \mu^{m+1}, \partial_s \mu^{m+1}\right)^h_{\Gamma^m}.\end{aligned} \tag{2.78}$$

Combining this with (2.77), we obtain

$$\begin{aligned}W^{m+1} - W^m &\le \left(\hat{\boldsymbol{G}}_k(\theta^m)\partial_s \boldsymbol{X}^{m+1}, \partial_s(\boldsymbol{X}^{m+1} - \boldsymbol{X}^m)\right)^h_{\Gamma^m} \\ &\le -\tau\left(\partial_s \mu^{m+1}, \partial_s \mu^{m+1}\right)^h_{\Gamma^m} \\ &\le 0, \qquad \forall m \ge 0.\end{aligned} \tag{2.79}$$

□

**2.4.4. Existence of the minimal stabilizing function.** In this subsection, we prove the existence of $k_0(\theta)$ under condition (2.56).

Recalling the definition of $P_\alpha, Q$ in (2.64), we set

$$\begin{aligned}F_\alpha(\phi, \theta) &:= P_\alpha^2(\phi, \theta) - Q^2(\phi, \theta) \\ &= 4\hat{\gamma}(\theta)\left(\hat{\gamma}(\theta) + \alpha \sin^2\phi\right) \\ &\quad - \left(\hat{\gamma}(\theta - \phi) + \hat{\gamma}(\theta)\cos\phi + \hat{\gamma}'(\theta)\sin\phi\right)^2.\end{aligned} \tag{2.80}$$

Let $C > 0$ be a constant such that $\frac{1}{C} \le \hat{\gamma}(\theta) \le C$ and $|\hat{\gamma}'(\theta)|, |\hat{\gamma}''(\theta)| \le C,\ \forall \theta \in 2\pi\mathbb{T}$.

Lemma 2.4. *For a globally $C^1$ and piecewise $C^2$ function $\hat{\gamma}(\theta)$, there exist an open neighborhood $U_0$ of 0 and a positive constant $k_{U_0} > 0$ such that $F_\alpha(\phi, \theta) \ge 0, \forall \phi \in U_0$ for every $\alpha > k_{U_0}$.*

Proof. The regularity assumption implies that there exists $0 < \varepsilon < \frac{\pi}{2}$ such that $\hat{\gamma}(\theta)$ is 2 times continuously differentiable on both $[\theta - \varepsilon, \theta]$ and $[\theta, \theta + \varepsilon]$.

Applying the mean value theorem on $[\theta - \varepsilon, \theta]$ and $[\theta, \theta + \varepsilon]$ separately, we find that for $\phi \in U_0 := \left\{\phi \mid |\phi| < \varepsilon\right\}$ there exists $\xi$ between $\theta, \theta - \phi$ such that

$$\hat{\gamma}(\theta - \phi) = \hat{\gamma}(\theta) - \hat{\gamma}'(\theta)\phi + \frac{\hat{\gamma}''(\xi)}{2}\phi^2. \tag{2.81}$$

There also exists $\xi_1, \xi_2$ between $0, \phi$ such that

$$\cos\phi = 1 - \frac{1}{2}\phi^2 + \frac{\sin\xi_1}{6}\phi^3 \tag{2.82a}$$

$$\sin\phi = \phi - \frac{\cos\xi_2}{6}\phi^3. \tag{2.82b}$$

Substituting (2.81) and (2.82) into $2\hat{\gamma}(\theta) - Q(\phi, \theta)$ gives

$$\begin{aligned}2\hat{\gamma}(\theta) - Q(\phi, \theta) &= 2\hat{\gamma}(\theta) - \hat{\gamma}(\theta) + \hat{\gamma}'(\theta)\phi - \frac{1}{2}\hat{\gamma}''(\xi)\phi^2 \\ &\quad - \hat{\gamma}(\theta) + \frac{1}{2}\hat{\gamma}(\theta)\phi^2 - \frac{1}{6}\hat{\gamma}(\theta)\sin\xi_1\phi^3 \\ &\quad - \hat{\gamma}'(\theta)\phi + \frac{1}{6}\hat{\gamma}'(\theta)\cos\xi_2\phi^3 \\ &= \frac{1}{2}\left(\hat{\gamma}(\theta) - \hat{\gamma}''(\xi)\right)\phi^2 - \frac{1}{6}\left(\hat{\gamma}(\theta)\sin\xi_1 - \hat{\gamma}'(\theta)\cos\xi_2\right)\phi^3.\end{aligned} \tag{2.83}$$

Hence

$$\begin{aligned}|2\hat{\gamma}(\theta) - Q(\phi, \theta)| &\le \frac{1}{2}\left(|\hat{\gamma}(\theta)| + |\hat{\gamma}''(\xi)|\right)|\phi|^2 \\ &\quad + \frac{1}{6}\left(|\hat{\gamma}(\theta)\sin\xi_1| + |\hat{\gamma}'(\theta)\cos\xi_2|\right)|\phi|^3 \\ &\le C|\phi|^2 + \frac{C}{3}|\phi|^3.\end{aligned} \tag{2.84}$$

Since $|2\hat{\gamma}(\theta) + Q(\phi,\theta)| \le 2|\hat{\gamma}(\theta)| + |Q(\phi,\theta)| \le 5C$, for every $\phi \in U_0$ we have

$$\begin{aligned} |4\hat{\gamma}^2(\theta) - Q^2(\phi,\theta)| &\le |2\hat{\gamma}(\theta) + Q(\phi,\theta)||2\hat{\gamma}(\theta) - Q(\phi,\theta)| \\ &\le 5C\left(C|\phi|^2 + \frac{C}{3}|\phi|^3\right) = \frac{5C^2}{3}\left(3 + |\phi|\right)|\phi|^2 \\ &\le \frac{5(6+\pi)C^2}{6}|\phi|^2. \end{aligned} \tag{2.85}$$

For every $\phi \in U_0$, the inequality $|\sin\phi| \ge \frac{2}{\pi}|\phi|$ holds. Therefore,

$$\begin{aligned} F_\alpha(\phi,\theta) &= 4\hat{\gamma}(\theta)\alpha\sin^2\phi + 4\hat{\gamma}^2(\theta) - Q^2(\phi,\theta) \\ &\ge \frac{16}{C\pi^2}\alpha|\phi|^2 - \frac{5(6+\pi)C^2}{6}|\phi|^2 \\ &\ge \left[\frac{16}{C\pi^2}\alpha - \frac{5(6+\pi)C^2}{6}\right]|\phi|^2, \ \forall\phi \in U_0. \end{aligned} \tag{2.86}$$

Choosing $k_{U_0} := \frac{5\pi^2(6+\pi)C^3}{96}$ gives $F_\alpha(\phi,\theta) \ge 0, \forall\phi \in U_0$ for every $\alpha > k_{U_0}$. □

Lemma 2.5. *Fix $\theta \in 2\pi\mathbb{T}$ and assume* (2.56)*. There exist an open neighborhood $U_\pi$ of $\pi$ and a positive constant $k_{U_\pi} > 0$, both allowed to depend on $\theta$, such that $F_\alpha(\phi,\theta) \ge 0, \forall\phi \in U_\pi$ for every $\alpha > k_{U_\pi}$.*

Proof. (i) If $3\hat{\gamma}(\theta) > \hat{\gamma}(\theta-\pi)$, then

$$F_\alpha(\pi,\theta) = \left(3\hat{\gamma}(\theta) - \hat{\gamma}(\theta-\pi)\right)\left(\hat{\gamma}(\theta) + \hat{\gamma}(\theta-\pi)\right) > 0. \tag{2.87}$$

By the continuity of $F_\alpha(\phi,\theta)$, there exists an open neighborhood $U_\pi$ of $\pi$ such that $F_\alpha(\phi,\theta) \ge 0, \forall\phi \in U_\pi$.

(ii) Otherwise set $\theta^* = \theta$. The assumptions give $3\hat{\gamma}(\theta^*) = \hat{\gamma}(\theta^*-\pi)$ and $\hat{\gamma}'(\theta^*) = 0$. Since $\hat{\gamma}(\theta-\pi)/\hat{\gamma}(\theta) \le 3$, this function attains its maximum at $\theta^*$, and hence

$$\begin{aligned} \left.\left(\frac{\hat{\gamma}(\theta-\pi)}{\hat{\gamma}(\theta)}\right)'\right|_{\theta=\theta^*} &= \frac{\hat{\gamma}'(\theta^*-\pi)\hat{\gamma}(\theta^*) - \hat{\gamma}(\theta^*-\pi)\hat{\gamma}'(\theta^*)}{\hat{\gamma}^2(\theta^*)} \\ &= \frac{\hat{\gamma}'(\theta^*-\pi) - 3\hat{\gamma}'(\theta^*)}{\hat{\gamma}(\theta^*)} \\ &= \frac{\hat{\gamma}'(\theta^*-\pi)}{\hat{\gamma}(\theta^*)} = 0, \end{aligned} \tag{2.88}$$

Thus $\hat{\gamma}'(\theta^*-\pi) = 0$.

As in the derivation of (2.81), the mean value theorem gives a positive constant $0 < \varepsilon < \frac{\pi}{2}$ and an open neighborhood $U_\pi = \{\phi \mid |\phi-\pi| < \varepsilon\}$ such that, for every $\phi \in U_\pi$, there exists a constant $\xi$ between $\theta^*-\phi, \theta^*-\pi$ satisfying

$$\begin{aligned} \hat{\gamma}(\theta^*-\phi) &= \hat{\gamma}(\theta^*-\pi) - \hat{\gamma}'(\theta^*-\pi)(\phi-\pi) + \frac{\hat{\gamma}''(\xi)}{2}(\phi-\pi)^2 \\ &= \hat{\gamma}(\theta^*-\pi) + \frac{\hat{\gamma}''(\xi)}{2}(\phi-\pi)^2. \end{aligned} \tag{2.89}$$

There also exists a constant $\xi_1$ between $\pi, \phi$ satisfying

$$\cos\phi = -1 - \frac{\cos\xi_1}{2}(\phi-\pi)^2. \tag{2.90}$$

Substituting (2.89) and (2.90) into $2\hat{\gamma}(\theta^*) - Q(\phi,\theta^*)$ gives

$$\begin{aligned} 2\hat{\gamma}(\theta^*) - Q(\phi,\theta^*) &= 2\hat{\gamma}(\theta^*) - \hat{\gamma}(\theta^*-\pi) - \frac{\hat{\gamma}''(\xi)}{2}(\phi-\pi)^2 \\ &\quad + \hat{\gamma}(\theta^*) + \frac{\cos\xi_1}{2}\hat{\gamma}(\theta^*)(\phi-\pi)^2 - \hat{\gamma}'(\theta^*)\sin\phi \\ &= \frac{1}{2}\left(\hat{\gamma}(\theta^*)\cos\xi_1 - \hat{\gamma}''(\xi)\right)(\phi-\pi)^2. \end{aligned} \tag{2.91}$$

Hence

$$
\begin{aligned}
|2\hat{\gamma}(\theta^*) - Q(\phi,\theta^*)| &\le \frac{1}{2}\left(|\hat{\gamma}(\theta^*)\cos\xi_1| + |\hat{\gamma}''(\xi)|\right)|\phi-\pi|^2 \\
&\le C|\phi-\pi|^2.
\end{aligned} \tag{2.92}
$$

Since $|2\hat{\gamma}(\theta^*) + Q(\phi,\theta^*)| \le 5C$, we obtain

$$
\begin{aligned}
|4\hat{\gamma}^2(\theta^*) - Q^2(\phi,\theta^*)| &\le |2\hat{\gamma}(\theta^*) + Q(\phi,\theta^*)||2\hat{\gamma}(\theta^*) - Q(\phi,\theta^*)| \\
&\le 5C^2|\phi-\pi|^2.
\end{aligned} \tag{2.93}
$$

Noting that $|\sin\phi| \ge \frac{2}{\pi}|\phi-\pi|,\ \forall\phi\in U_\pi$, we have

$$
\begin{aligned}
F_\alpha(\phi,\theta^*) &= 4\hat{\gamma}(\theta^*)\alpha\sin^2\phi + 4\hat{\gamma}^2(\theta^*) - Q^2(\phi,\theta^*) \\
&\ge \frac{16}{C\pi^2}\alpha|\phi-\pi|^2 - 5C^2|\phi-\pi|^2 \\
&\ge \left[\frac{16}{C\pi^2}\alpha - 5C^2\right]|\phi-\pi|^2,\ \forall\phi\in U_\pi.
\end{aligned} \tag{2.94}
$$

Therefore, there exists a positive constant $k_{U_\pi} := \frac{5\pi^2C^3}{16}$ such that $F_\alpha(\phi,\theta^*)\ge 0, \forall\phi\in U_\pi$ for every $\alpha > k_{U_\pi}$.

□

Using these lemmas, we now prove Theorem 2.3:

Proof. *(Existence of the minimal stabilizing function)* Fix $\theta\in 2\pi\mathbb{T}$.

(i) For $\phi_0\neq 0,\pi$, there exists an open neighborhood $U_{\phi_0}$ on which $\sin^2\phi$ has a strictly positive lower bound: there is a constant $c>0$ such that $\sin^2\phi\ge c>0, \forall\phi\in U_{\phi_0}$. Thus, on this neighborhood,

$$
\begin{aligned}
F_\alpha(\phi,\theta) &= 4\hat{\gamma}(\theta)\alpha\sin^2\phi + O(1) \\
&\ge 4c\hat{\gamma}(\theta)\alpha + O(1).
\end{aligned} \tag{2.95}
$$

There exists a constant $k_{U_{\phi_0}} < +\infty$ such that $F_\alpha(\phi,\theta)\ge 0, \forall\phi\in U_{\phi_0}$ for every $\alpha > k_{U_{\phi_0}}$.

(ii) For $\phi_0 = 0$ or $\pi$, Lemmas 2.4 and 2.5 provide a neighborhood $U_{\phi_0}$ of $\phi_0$ and a constant $k_{U_{\phi_0}} < +\infty$ such that $F_\alpha(\phi,\theta)\ge 0, \forall\phi\in U_{\phi_0}$ for every $\alpha > k_{U_{\phi_0}}$.

Since $2\pi\mathbb{T}$ is compact and $\{U_{\phi_0} : \phi_0\in 2\pi\mathbb{T}\}$ is an open cover, the finite subcover theorem gives a finite subcover $\{U_i\}_{i=1}^M \subset \{U_{\phi_0} : \phi_0\in 2\pi\mathbb{T}\}$. Consequently, for every $\alpha > \max\limits_{1\le i\le M} k_{U_i}$,

$$
F_\alpha(\phi,\theta)\ge 0, \qquad \forall\phi\in 2\pi\mathbb{T}. \tag{2.96}
$$

This shows that $k_0(\theta) = \inf\left\{\alpha\ge 0 \mid P_\alpha(\phi,\theta) - Q(\phi,\theta)\ge 0,\ \forall\phi\in 2\pi\mathbb{T}\right\} < +\infty$ and completes the proof. □

### 2.5. Numerical experiments

In this section, we present numerical results for the scheme (2.52). Extensive tests examine its efficiency, accuracy, area conservation, and unconditional energy stability.

We mainly consider the following two anisotropic surface energies:

- Case I: $\hat{\gamma}(\theta) = 1 + \beta\cos 3\theta$, where $|\beta| < 1$. This energy is weakly anisotropic when $|\beta| < \frac{1}{8}$ and strongly anisotropic otherwise.
- Case II: $\hat{\gamma}(\theta) = \sqrt{1 + b\cos^2\theta}$, where $b > -1$.

To compute the minimal stabilizing function $k_0(\theta)$, we take 20 uniformly distributed nodes $\theta_j = -\pi + \frac{j\pi}{10},\ \forall 1\le j\le 20$ in $[-\pi,\pi]$ and solve the optimization problem (2.65) at each node to obtain $k_0(\theta_j)$. Values between neighboring nodes in $(\theta_j,\theta_{j+1})$ are obtained by linear interpolation, namely $k_0(\theta) = (1-\lambda)k_0(\theta_j) + \lambda k_0(\theta_{j+1})$, where $\lambda = \frac{10}{\pi}(\theta-\theta_j)$, with periodic continuation at the endpoints.

We introduce the manifold distance [151, 108]

$$M(\Gamma_1, \Gamma_2) := 2|\Omega_1 \cup \Omega_2| - |\Omega_1| - |\Omega_2|, \tag{2.97}$$

to measure the distance between two closed curves $\Gamma_1, \Gamma_2$, where $\Omega_i$ $(i = 1, 2)$ is the region enclosed by $\Gamma_i$ and $|\Omega_i|$ denotes its area. Let $\Gamma^m$ be a numerical approximation to $\Gamma^h(t = t_m := m\tau)$. We define the numerical error by

$$e^h(t)\Big|_{t=t_m} := M(\Gamma^m, \Gamma(t = t_m)). \tag{2.98}$$

To examine mesh quality, area conservation, and energy stability numerically, we introduce the following quantities: the weighted mesh ratio

$$R_\gamma^h(t) := \frac{\max\limits_{1\le j\le N} \hat{\gamma}(\theta_j)|\boldsymbol{h}_j|}{\min\limits_{1\le j\le N} \hat{\gamma}(\theta_j)|\boldsymbol{h}_j|}, \tag{2.99}$$

and the normalized area loss and normalized energy

$$\frac{\Delta A^h(t)}{A^h(0)}\Big|_{t=t_m} := \frac{A^m - A^0}{A^0}, \qquad \frac{W^h(t)}{W^h(0)}\Big|_{t=t_m} := \frac{W^m}{W^0}, \qquad \forall m \ge 0. \tag{2.100}$$

The scheme (2.52) is formally second-order accurate in space and first-order accurate in time. Unless otherwise stated, the time step $\tau$ is therefore set to $\tau = O(h^2)$; in this chapter, we use $\tau = 16h^2$. The tolerance for Newton iteration is tol $= 10^{-12}$.

**2.5.1. Convergence rates and structure preservation.** In the following tests, the initial curve is an ellipse with major axis 4 and minor axis 1. Since an analytic exact solution is unavailable, we approximate $\Gamma(t = t_m)$ numerically on the fine mesh $h = h_e, \tau = \tau_e$. In this chapter, $(h_e, \tau_e) = (2^{-8}, 2^{-12})$.

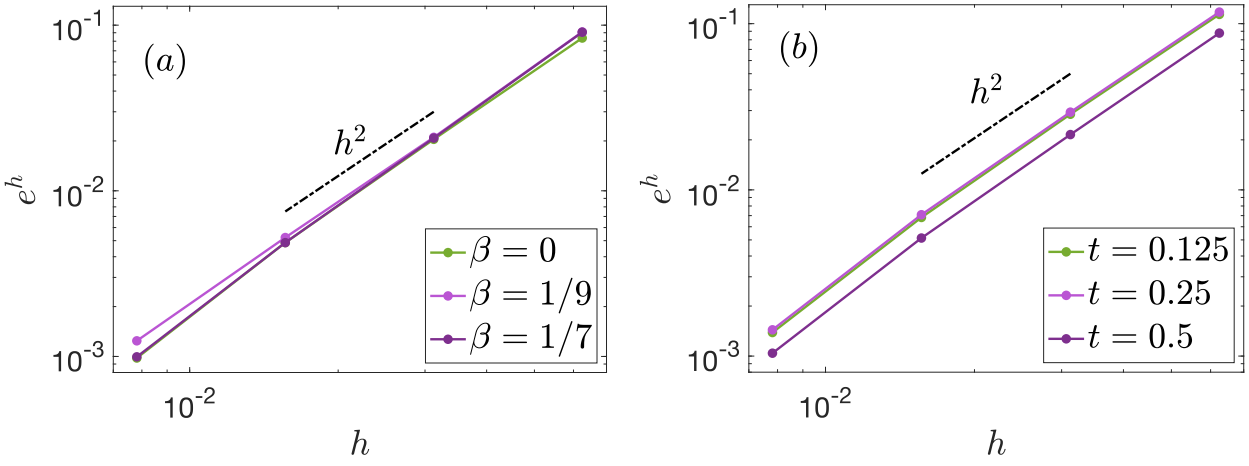



**Figure 2.1.** Convergence rates of the SPFEM (2.52) with $k(\theta) = k_0(\theta)$ for (a) anisotropy in Case I at $t = 0.5$ with different $\beta$; (b) anisotropy in Case II with $b = -0.8$ at different times $t = 0.125, 0.25, 0.5$.

Figure 2.1 shows the convergence rates of (2.52) for (a) the 3-fold anisotropy $\hat{\gamma}(\theta) = 1 + \beta\cos 3\theta$ with different strengths $\beta$ at the fixed time $t = 0.5$, and (b) the ellipsoidal anisotropy $\hat{\gamma}(\theta) = \sqrt{1 - 0.8\cos^2\theta}$ at different times. The scheme achieves second-order spatial convergence for all anisotropies and times considered, demonstrating its robustness.

Figure 2.2 shows the convergence rates of (2.52) for Case I with $\hat{\gamma}(\theta) = 1 + \beta\cos 3\theta$ and different $k(\theta)$: (a) $\beta = 0$; (b) $\beta = 1/9$. The stabilizing function $k(\theta)$ is independent of time, and its choice does not affect convergence.

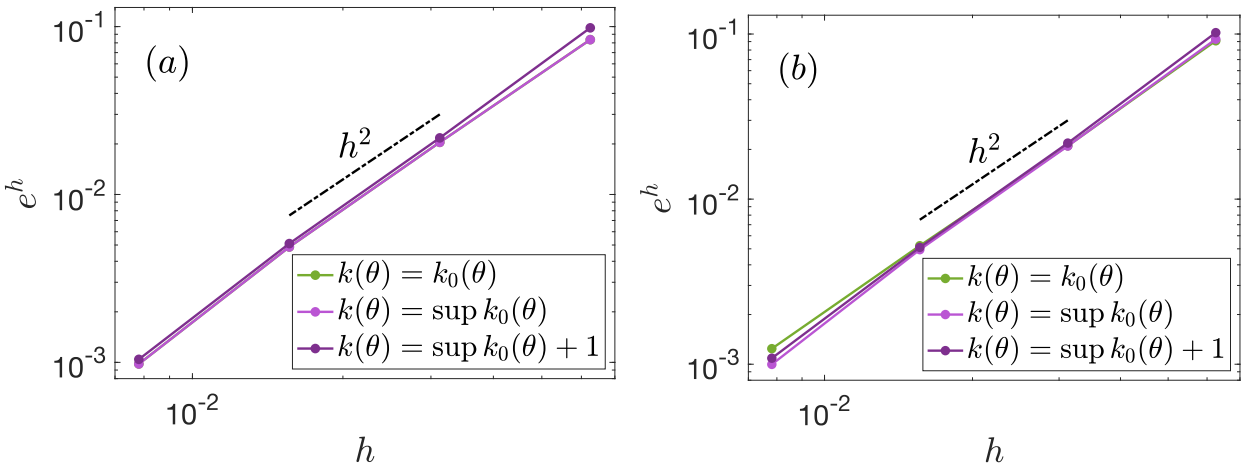



**Figure 2.2.** Convergence rates of the SPFEM (2.52) for Case I at $t = 0.5$ with different $k(\theta)$: (a) $\beta = 0$; (b) $\beta = 1/9$.

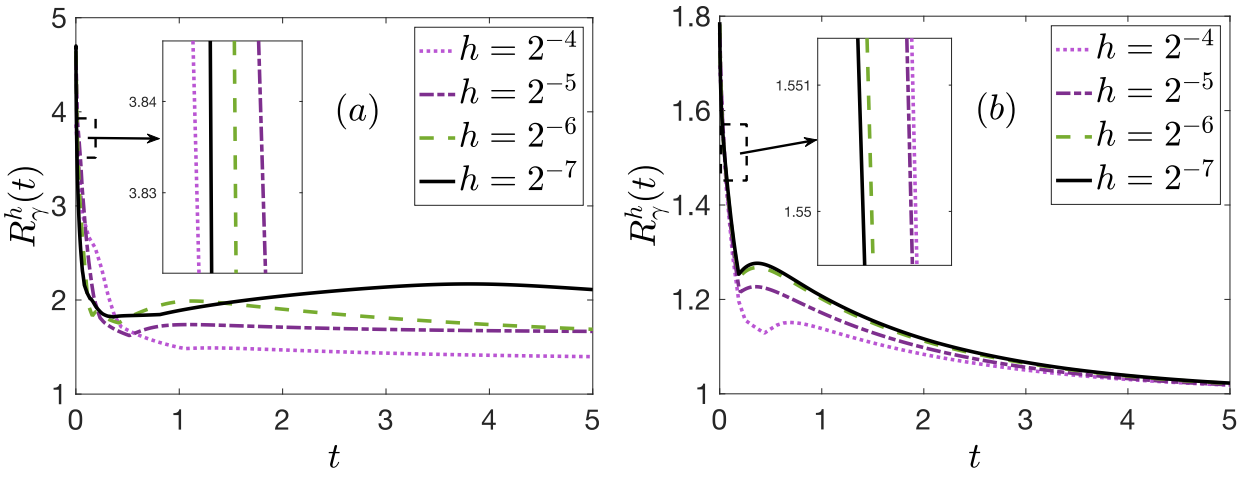



**Figure 2.3.** Weighted mesh ratio of the SPFEM (2.52) with $k(\theta) = k_0(\theta)$ for (a) anisotropy in Case I with $\beta = \frac{1}{9}$; (b) anisotropy in Case II with $b = -0.8$.

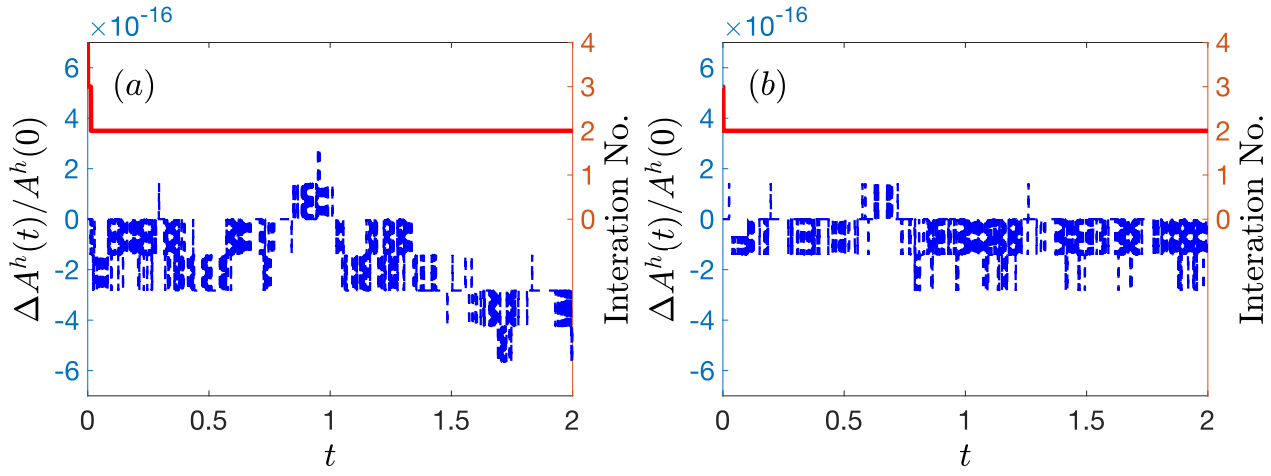



**Figure 2.4.** Normalized area loss (blue dashed line) and number of Newton iterations (red line) of the SPFEM (2.52) with $k(\theta) = k_0(\theta)$ and $h = 2^{-7}, \tau = 2^{-10}$ for (a) anisotropy in Case I with $\beta = \frac{1}{2}$; (b) anisotropy in Case II with $b = -0.8$.

Figure 2.3 shows that the weighted mesh ratio $R_\gamma^h$ converges to a constant as $t \to +\infty$. This indicates that (2.52) produces an asymptotically quasi-uniform mesh distribution.

Figure 2.4 shows the time evolution of the normalized area loss $\Delta A^h(t)/A^h(0)$ and the number of Newton iterations with $(h, \tau) = (2^{-7}, 2^{-10})$. The time evolution of the normalized energy $W^h(t)/W^h(t)$ for different mesh sizes $h$ is shown in Figure 2.5.

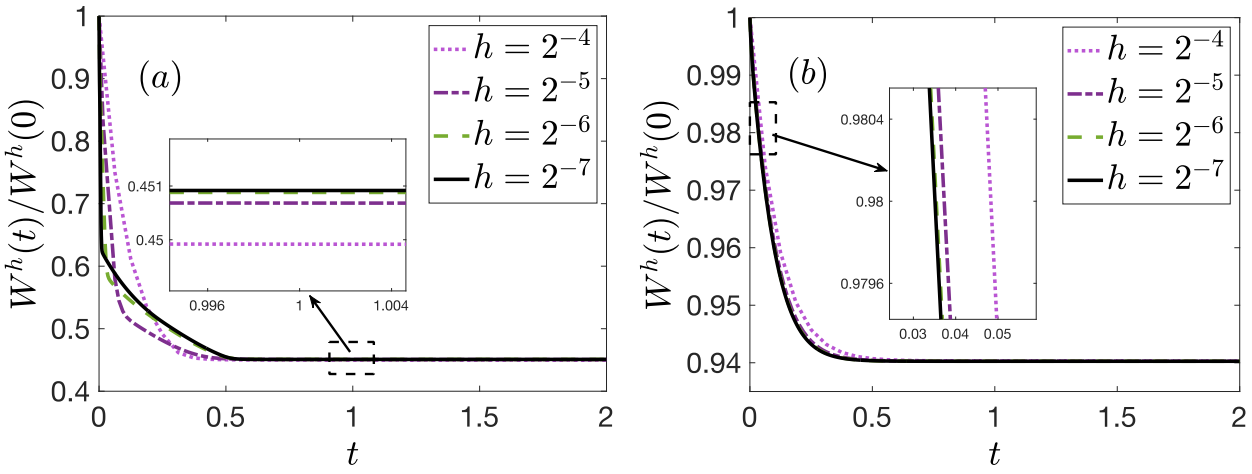



**Figure 2.5.** Normalized energy for (a) anisotropy in Case I with $\beta = \frac{1}{2}$; (b) anisotropy in Case II with $b = -0.8$.

The results in Figures 2.4–2.5 show that:

(1) The normalized area loss is of order $10^{-16}$, close to round-off error; see Figure 2.4. This verifies area conservation to machine precision.
(2) The number of Newton iterations starts at 3 or 4 and quickly decreases to 2; see Figure 2.4. Thus (2.52) can be solved efficiently in only a few iterations.
(3) When the surface energy $\hat{\gamma}(\theta)$ satisfies (2.56), the normalized energy is monotonically decreasing; see Figure 2.5. Figure 2.5(a) shows that (2.52) remains energy stable when the anisotropy strength $\beta$ reaches the maximum value 1/2 allowed by Remark 2.7. Figure 2.5(b) also shows that, unlike the *energy-stable parametric finite element method* in [108], the scheme (2.52) is unconditionally energy stable for $b < -1/2$, as stated in Remark 2.8.

**2.5.2. Morphological evolution under two-dimensional surface diffusion.** We apply (2.52) to simulate the morphological evolution of closed curves under anisotropic surface diffusion. Figures 2.6–2.7 show the evolution from the initial shapes to numerical equilibria.

Figure 2.6 shows the morphological evolution of an ellipse with major axis 4 and minor axis 1 under surface diffusion with four different surface energies: (a) Case I with $\beta = 1/2$, reaching the maximum value in Remark 2.7; (b) Case II with $b = -0.8$; (c) the 4-fold anisotropy $\hat{\gamma}(\theta) = 1 + \frac{1}{16}\cos 4\theta$ [11]; and (d) $\hat{\gamma}(\theta) = \sqrt{\left(\frac{5}{2} + \frac{3}{2}\mathrm{sgn}(n_1)\right) n_1^2 + n_2^2}$, where $\boldsymbol{n} = (n_1, n_2)^T = (-\sin\theta, \cos\theta)^T$ [44].

The results in Figure 2.6(a)–(c) show that (2.52) performs well over a broader parameter range than the *energy-stable parametric finite element method* in [108]. Figure 2.6(d) shows that (2.52) also applies to anisotropies with limited regularity, namely those that are globally $C^1$ and piecewise $C^2$.

Figure 2.7 also shows the morphological evolution of the four-fold star-shaped curve

$$\begin{cases} x = (1 + 0.5\cos 4\theta)\cos\theta, \\ y = (1 + 0.5\cos 4\theta)\sin\theta, \end{cases} \qquad \theta \in 2\pi\mathbb{T}, \tag{2.101}$$

and an ellipse rotated counterclockwise by $\frac{\pi}{10}$ under the same four surface energies.

## 2.6. Chapter summary

In this chapter, we have proposed a structure-preserving *stabilized parametric finite element method* for anisotropic surface diffusion. The method requires only the mild condition (2.56) on $\hat{\gamma}(\theta)$ and

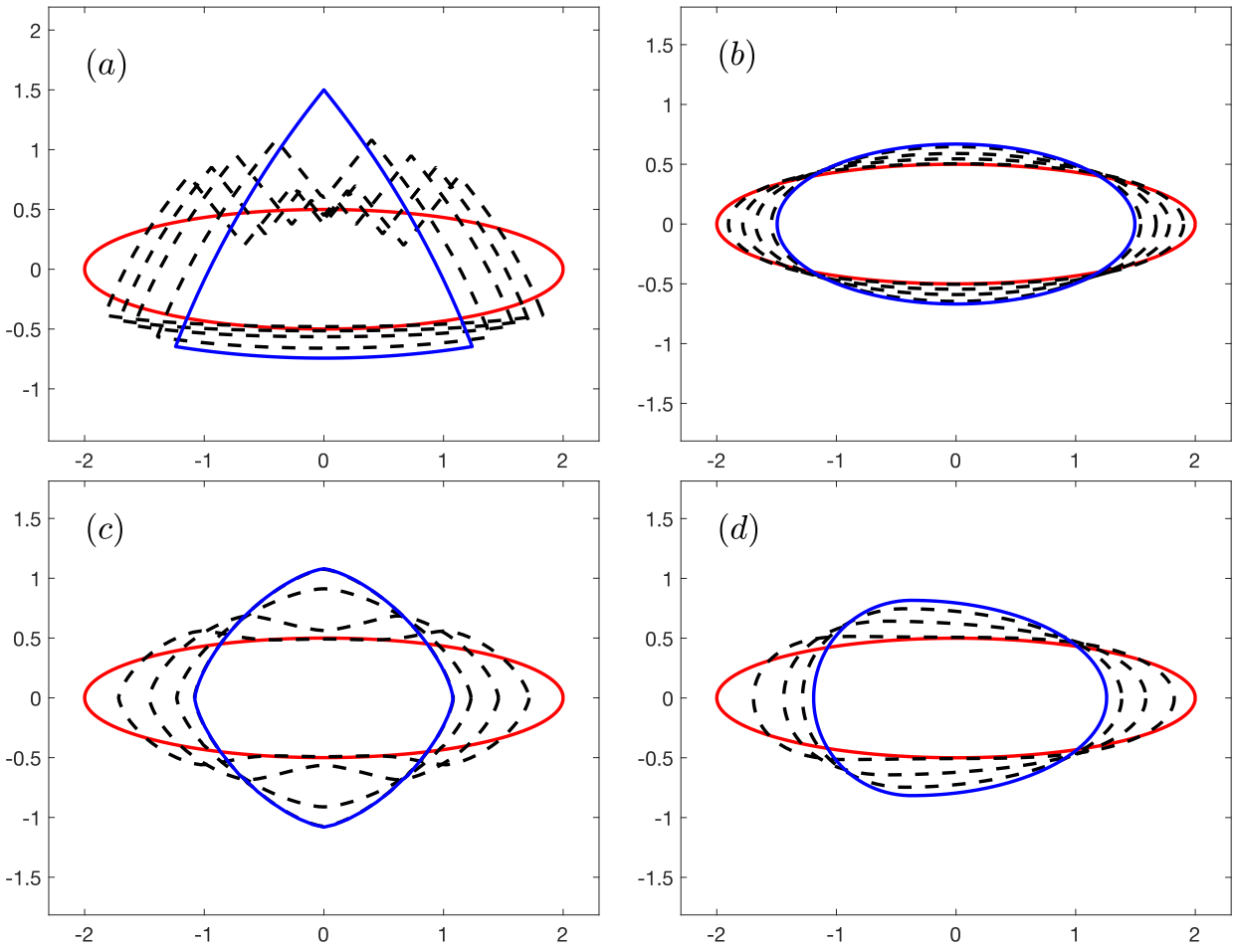



**Figure 2.6.** Morphological evolution of an ellipse with major axis 4 and minor axis 1 under anisotropic surface diffusion with different surface energies: (a) anisotropy in Case I with $\beta = \frac{1}{2}$; (b) anisotropy in Case II with $b = -0.8$; (c) $\hat{\gamma}(\theta) = 1 + \frac{1}{16}\cos 4\theta$; (d) $\hat{\gamma}(\theta) = \sqrt{\left(\frac{5}{2} + \frac{3}{2}\mathrm{sgn}(n_1)\right) n_1^2 + n_2^2}$ with $\boldsymbol{n} = (n_1, n_2)^T = (-\sin\theta, \cos\theta)^T$. The red and blue lines represent the initial shape and the numerical equilibrium, respectively. The black dashed lines represent the intermediate curves. The mesh size and the time step are taken as $h = 2^{-7}, \tau = 2^{-10}$.

applies effectively to anisotropic evolution of closed curves. Introducing a new stabilized surface energy matrix gives a conservative form and a weak formulation for anisotropic surface diffusion. Combining parametric finite element discretization in space with the semi-implicit Euler method in time yields a new stabilized scheme. To analyze unconditional energy stability, we extend the framework of Bao and Li to the $\hat{\gamma}(\theta)$ formulation. We define the minimal stabilizing function, prove its existence, derive a local energy estimate, and establish unconditional energy stability. The mild requirements on $\hat{\gamma}(\theta)$ include the critical case and allow simulations for a broader range of anisotropies. The scheme also applies to globally $C^1$ and piecewise $C^2$ anisotropies, a capability not available in the other parametric finite element methods considered here.

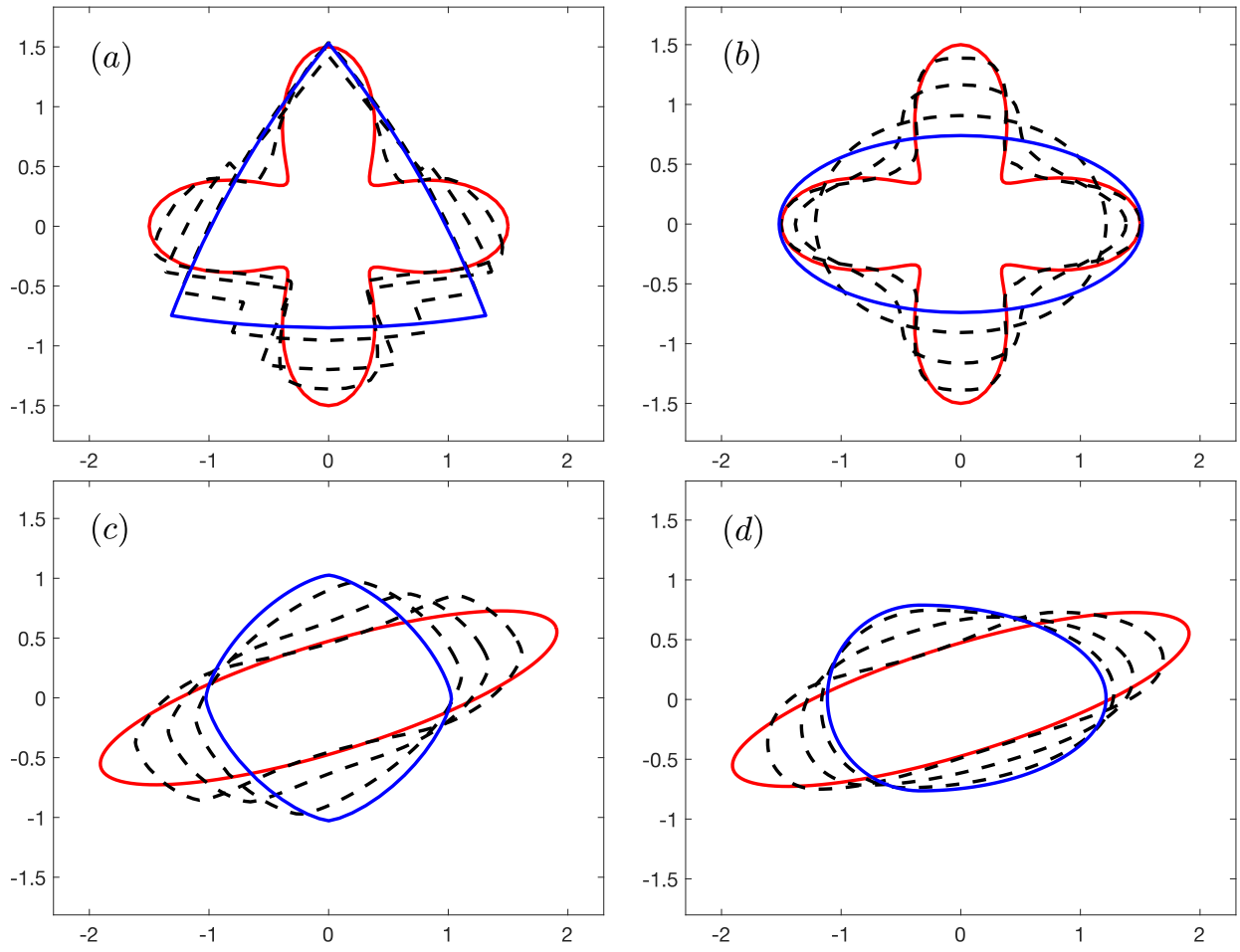



**Figure 2.7.** Morphological evolution of a four-fold star-shaped curve and a rotated ellipse under anisotropic surface diffusion with different surface energies: (a) anisotropy in Case I with $\beta = \frac{1}{2}$; (b) anisotropy in Case II with $b = -0.8$; (c) $\hat{\gamma}(\theta) = 1 + \frac{1}{16}\cos 4\theta$; (d) $\hat{\gamma}(\theta) = \sqrt{\left(\frac{5}{2} + \frac{3}{2}\mathrm{sgn}(n_1)\right) n_1^2 + n_2^2}$ with $\boldsymbol{n} = (n_1, n_2)^T = (-\sin\theta, \cos\theta)^T$. The red and blue lines represent the initial shape and the numerical equilibrium, respectively. The black dashed lines represent the intermediate curves. The mesh size and the time step are taken as $h = 2^{-7}, \tau = 2^{-10}$.

CHAPTER 3

# A structure-preserving parametric finite element method with an optimal energy stability condition

An important advance in structure-preserving methods for anisotropic geometric flows is the introduction of a stabilizing function $k(\theta)$ into the surface energy matrix. Building on this idea, [13] established a unified analytical framework in which energy stability follows from a local energy estimate, provided that the stabilizing function $k(\theta)$ exceeds a bounded minimal stabilizing function $k_0(\theta)$. The energy stability proofs for all existing *structure-preserving or energy-stable parametric finite element methods* [14, 149, 108, 18, 107], including the method in Chapter 2, can be recast within this framework. Thus the energy stability conditions on $\hat{\gamma}(\theta)$ depend on the chosen surface energy matrix and the analytical techniques used to establish the local energy estimate.

For example, the *symmetrized structure-preserving parametric finite element method* [9, 12] uses a symmetric surface energy matrix $\boldsymbol{Z}_k$. Applying the Cauchy inequality yields the stability condition $\hat{\gamma}(\theta) = \hat{\gamma}(\theta - \pi)$, and estimates of the minimal stabilizing function $k_0(\theta)$ are available for several surface energies $\hat{\gamma}(\theta)$. Subsequently, the works in [13, 14, 18, 107] introduced a nonsymmetric surface energy matrix $\boldsymbol{G}_k$ and refined the analysis to obtain the condition $3\hat{\gamma}(\theta) - \hat{\gamma}(\theta - \pi) > 0$. In Chapter 2, we further relaxed the condition to $3\hat{\gamma}(\theta) - \hat{\gamma}(\theta - \pi) \geq 0$, with the additional requirement $\hat{\gamma}'(\theta^*) = 0$ whenever $3\hat{\gamma}(\theta^*) - \hat{\gamma}(\theta^* - \pi) = 0$. However, an explicit characterization of the minimal stabilizing function $k_0(\theta)$ remained unavailable.

On the other hand, the analysis of the surface energy matrix $\boldsymbol{G}_k$ in [14] first established that

$$3\hat{\gamma}(\theta) - \hat{\gamma}(\theta - \pi) \geq 0, \qquad \forall \theta \in 2\pi\mathbb{T} \tag{3.1}$$

is a necessary condition for the local energy estimate. Inspired by that proof, we show in Remark 3.5 that this condition is independent of the particular construction of $\boldsymbol{G}_k$ or $\boldsymbol{Z}_k$. Hence the energy stability condition in Chapter 2 is almost optimal, apart from the additional requirement $\hat{\gamma}'(\theta^*) = 0$. This leads to three questions:

(i) Is this necessary condition also sufficient for energy stability?
(ii) If so, which surface energy matrix and analytical techniques yield this optimal condition?
(iii) How can we obtain an explicit estimate of the minimal stabilizing function $k_0(\theta)$?

In this chapter, we propose and analyze a *structure-preserving parametric finite element method* (SP-PFEM) for two-dimensional anisotropic surface diffusion. Under the energy stability condition (3.1), it preserves area conservation and unconditional energy stability without any additional constraints. We thereby prove that the necessary condition (3.1) is also sufficient, establishing its optimality within the framework of local energy estimates.

The chapter is organized as follows. Section 3.1 introduces a conservative form using the symmetric surface energy matrix $\hat{\boldsymbol{Z}}_k(\theta)$ and derives a weak formulation for anisotropic surface diffusion. Section 3.2 presents a fully discrete parametric finite element scheme and states its structure-preserving properties. In Section 3.3, we define the minimal stabilizing function $k_0(\theta)$ and, assuming its existence, establish a local energy estimate and prove energy stability. Section 3.3.3 proves the existence of $k_0(\theta)$ and derives a global upper bound for $k_0(\theta)$ using a sharp estimate lemma. Finally, Section 3.4 presents numerical experiments examining accuracy, efficiency, and structure preservation.

### 3.1. A symmetric surface energy matrix and a symmetrized conservative form

We introduce the following symmetric surface energy matrix:

Definition 3.1 (Symmetric surface energy matrix).

$$\begin{aligned}\hat{\boldsymbol{Z}}_k(\theta) \coloneqq &\begin{pmatrix} \hat{\gamma}(\theta) - \hat{\gamma}'(\theta)\sin 2\theta & \hat{\gamma}'(\theta)\cos 2\theta \\ \hat{\gamma}'(\theta)\cos 2\theta & \hat{\gamma}(\theta) + \hat{\gamma}'(\theta)\sin 2\theta \end{pmatrix} \\ &+ k(\theta)\begin{pmatrix} \sin^2\theta & -\cos\theta\sin\theta \\ -\cos\theta\sin\theta & \cos^2\theta \end{pmatrix}, \qquad \forall \theta \in 2\pi\mathbb{T}.\end{aligned} \tag{3.2}$$

Here $k\colon 2\pi\mathbb{T} \to \mathbb{R}_{\geq 0}$ is a prescribed stabilizing function.

Theorem 3.1. *The surface energy matrix* (3.2) *satisfies the geometric identity*

$$\mu \boldsymbol{n} + \partial_s\left(\hat{\boldsymbol{Z}}_k(\theta)\partial_s \boldsymbol{X}\right) = \boldsymbol{0}. \tag{3.3}$$

Proof. We note that $\boldsymbol{n} = (-\sin\theta, \cos\theta)^T$ and $\boldsymbol{\tau} \coloneqq \partial_s \boldsymbol{X} = (\cos\theta, \sin\theta)^T$. An argument analogous to (2.17) gives

$$\mu \boldsymbol{n} = -\partial_s\left(\hat{\gamma}(\theta)\partial_s \boldsymbol{X} + \hat{\gamma}'(\theta)\boldsymbol{n}\right). \tag{3.4}$$

Since $\boldsymbol{n}^T \partial_s \boldsymbol{X} = \boldsymbol{n} \cdot \boldsymbol{\tau} \equiv 0$, the term $\partial_s\left(k(\theta)\boldsymbol{n}\boldsymbol{n}^T \partial_s \boldsymbol{X}\right)$ vanishes identically. We may therefore rewrite (3.4) as

$$\mu \boldsymbol{n} = -\partial_s\left(\hat{\gamma}(\theta)\partial_s \boldsymbol{X} + \hat{\gamma}'(\theta)\boldsymbol{n} + k(\theta)\boldsymbol{n}\boldsymbol{n}^T \partial_s \boldsymbol{X}\right). \tag{3.5}$$

Set

$$L_\theta \coloneqq \begin{pmatrix} -\sin 2\theta & \cos 2\theta \\ \cos 2\theta & \sin 2\theta \end{pmatrix}, \tag{3.6}$$

Applying this matrix to the tangent vector $\partial_s \boldsymbol{X} = \boldsymbol{\tau}$ gives

$$L_\theta \partial_s \boldsymbol{X} = \begin{pmatrix} -\sin 2\theta & \cos 2\theta \\ \cos 2\theta & \sin 2\theta \end{pmatrix}\begin{pmatrix} \cos\theta \\ \sin\theta \end{pmatrix} = \begin{pmatrix} -\sin\theta \\ \cos\theta \end{pmatrix} = \boldsymbol{n}. \tag{3.7}$$

Hence

$$\begin{aligned}\hat{\boldsymbol{Z}}_k(\theta)\partial_s \boldsymbol{X} &= \left(\hat{\gamma}(\theta) I_2 + \hat{\gamma}'(\theta) L_\theta + k(\theta)\boldsymbol{n}\boldsymbol{n}^T\right)\partial_s \boldsymbol{X} \\ &= \hat{\gamma}(\theta)\partial_s \boldsymbol{X} + \hat{\gamma}'(\theta)\boldsymbol{n} + k(\theta)\boldsymbol{n}\boldsymbol{n}^T \partial_s \boldsymbol{X},\end{aligned} \tag{3.8}$$

Substitution of (3.8) into (3.5) proves the desired identity. □

Using the geometric identity (3.3), we rewrite the two-dimensional anisotropic surface diffusion equations (2.8) in the following symmetrized conservative form:

$$\partial_t \boldsymbol{X} \cdot \boldsymbol{n} - \partial_{ss}\mu = 0, \qquad 0 < s < L(t), \qquad t > 0, \tag{3.9a}$$

$$\mu \boldsymbol{n} + \partial_s\left(\hat{\boldsymbol{Z}}_k(\theta)\partial_s \boldsymbol{X}\right) = \boldsymbol{0}, \tag{3.9b}$$

where $L(t) = \int_{\Gamma(t)} \mathrm{d}s$ is the length of $\Gamma(t)$.

### 3.2. A symmetrized structure-preserving parametric finite element scheme

In this section, we introduce a parametric finite element scheme based on the conservative form (3.9) and describe its structure-preserving properties.

**3.2.1. Weak formulation.** As in the derivation of (2.27), multiplying (3.9) by the test functions $\varphi \in H_p^1(\mathbb{I})$, $\boldsymbol{\omega} \in [H_p^1(\mathbb{I})]^2$ and integrating by parts yields the following weak formulation of (3.9): given an initial closed curve $\Gamma(0) = \boldsymbol{X}(\cdot,0) = \boldsymbol{X}_0 \in [H_p^1(\mathbb{I})]^2$, find $\big(\boldsymbol{X}(\cdot,t), \mu(\cdot,t)\big) \in [H_p^1(\mathbb{I})]^2 \times H_p^1(\mathbb{I})$ satisfying

$$\Big(\boldsymbol{n}\cdot\partial_t\boldsymbol{X}, \varphi\Big)_{\Gamma(t)} + \Big(\partial_s\mu, \partial_s\varphi\Big)_{\Gamma(t)} = 0, \qquad \forall \varphi \in H_p^1(\mathbb{I}), \tag{3.10a}$$

$$\Big(\mu\boldsymbol{n}, \boldsymbol{\omega}\Big)_{\Gamma(t)} - \Big(\hat{\boldsymbol{Z}}_k(\theta)\partial_s\boldsymbol{X}, \partial_s\boldsymbol{\omega}\Big)_{\Gamma(t)} = 0, \qquad \forall \boldsymbol{\omega} \in [H_p^1(\mathbb{I})]^2. \tag{3.10b}$$

Remark 3.1. Under the one-to-one correspondence $\boldsymbol{n} := \boldsymbol{n}(\theta) = (-\sin\theta, \cos\theta)^T$, the surface energy matrix $\hat{\boldsymbol{Z}}_k(\theta)$ becomes the matrix $\boldsymbol{Z}_k(\boldsymbol{n})$ in [9].

Proposition 3.1 (Area conservation and energy dissipation). *Let $\Gamma(t)$ be determined by a solution $(\boldsymbol{X}(\cdot,t), \mu(\cdot,t))$ of* (3.10). *Its enclosed area $A(t)$ is conserved, and its total free energy $W(t)$ is dissipated, namely*

$$A(t) \equiv A(0), \qquad W(t) \le W(t_1) \le W(0), \qquad \forall t \ge t_1 \ge 0. \tag{3.11}$$

*The quantities $A(t), W(t)$ are defined in* (2.28).

The proof of Proposition 3.1 is analogous to that of Proposition 2.1, so we omit the details.

**3.2.2. Fully discrete scheme.** Let $\tau$ be a uniform time step, and let $\Gamma^m = \boldsymbol{X}^m(\cdot)$ approximate $\Gamma(t_m = m\tau)$. Based on the weak formulation (3.10), the symmetrized *fully discrete structure-preserving parametric finite element scheme* for (2.8) reads as follows: given an initial curve $\Gamma^0 = \boldsymbol{X}^0(\cdot) \in [\mathbb{K}_p^h]^2$, find $\big(\boldsymbol{X}^{m+1}(\cdot), \mu^{m+1}(\cdot)\big) \in [\mathbb{K}_p^h]^2 \times \mathbb{K}_p^h$, $m = 0, 1, 2, \dots$ such that

$$\Big(\boldsymbol{n}^{m+\frac{1}{2}} \cdot \frac{\boldsymbol{X}^{m+1} - \boldsymbol{X}^m}{\tau}, \varphi^h\Big)_{\Gamma^m}^h + \Big(\partial_s\mu^{m+1}, \partial_s\varphi^h\Big)_{\Gamma^m}^h = 0, \qquad \forall \varphi^h \in \mathbb{K}_p^h, \tag{3.12a}$$

$$\Big(\mu^{m+1}\boldsymbol{n}^{m+\frac{1}{2}}, \boldsymbol{\omega}^h\Big)_{\Gamma^m}^h - \Big(\hat{\boldsymbol{Z}}_k(\theta^m)\partial_s\boldsymbol{X}^{m+1}, \partial_s\boldsymbol{\omega}^h\Big)_{\Gamma^m}^h = 0, \qquad \forall \boldsymbol{\omega}^h \in [\mathbb{K}_p^h]^2, \tag{3.12b}$$

where

$$\boldsymbol{n}^{m+\frac{1}{2}} = -\frac{1}{2}\left(\partial_s\boldsymbol{X}^m + \partial_s\boldsymbol{X}^{m+1}\right)^\perp = -\frac{1}{2|\partial_\rho\boldsymbol{X}^m|}\left(\partial_\rho\boldsymbol{X}^m + \partial_\rho\boldsymbol{X}^{m+1}\right)^\perp. \tag{3.13}$$

The discrete geometric quantities and operators are defined in (2.43)–(2.47).

Remark 3.2. The spatial semidiscretization of (3.9) is analogous to (2.48), with only the surface energy matrix replaced. It also preserves area conservation and energy dissipation.

**3.2.3. Structure preservation.** Let $A^m, W^m$ denote the enclosed area and total free energy of the discrete curve $\Gamma^m$, respectively, as defined in (2.55).

Theorem 3.2 (Structure preservation). *Suppose that $\hat{\gamma} \in C^2(2\pi\mathbb{T})$ is strictly positive and satisfies the optimal energy stability condition* (3.1). *The scheme* (3.12) *preserves area conservation and, for sufficiently large $k(\theta)$, unconditional energy dissipation, namely*

$$A^{m+1} = A^m = \cdots = A^0, \qquad W^{m+1} \le W^m \le \cdots \le W^0, \qquad \forall m \ge 0. \tag{3.14}$$

Area conservation is proved as in Theorem 2.2. The detailed proof of energy dissipation is given in the next section.

Remark 3.3. In the $\gamma(\boldsymbol{n})$ formulation, the scheme (3.12) becomes the structure-preserving parametric finite element method in [9]. Theorem 3.2 substantially improves the energy stability condition $\gamma(\boldsymbol{n}) = \gamma(-\boldsymbol{n})$, or equivalently $\hat{\gamma}(\theta) = \hat{\gamma}(\theta - \pi)$, in [9]. The analysis in the $\hat{\gamma}(\theta)$ formulation shows that the symmetry condition $\hat{\gamma}(\theta) = \hat{\gamma}(\theta - \pi)$ for the symmetrized structure-preserving scheme can be relaxed to the optimal condition (3.1) without additional assumptions.

### 3.3. Proof of unconditional energy stability

We introduce the auxiliary functions

$$P_\alpha(\phi,\theta) \coloneqq \hat\gamma(\theta) - \hat\gamma'(\theta)\sin 2\phi + \alpha\sin^2\phi, \tag{3.15a}$$

$$Q(\phi,\theta) \coloneqq \hat\gamma(\theta-\phi) + \hat\gamma(\theta)\cos\phi - \hat\gamma'(\theta)\sin\phi, \tag{3.15b}$$

and define the minimal stabilizing function by

$$k_0(\theta) \coloneqq \inf\left\{\alpha \geq 0 \mid 4\hat\gamma(\theta)P_\alpha(\phi,\theta) \geq Q^2(\phi,\theta),\ \forall\phi\in 2\pi\mathbb{T}\right\}. \tag{3.16}$$

The following theorem ensures the existence of $k_0(\theta)$ and provides a global upper bound:

Theorem 3.3. *Suppose that $\hat\gamma \in C^2(2\pi\mathbb{T})$ is strictly positive and satisfies* (3.1)*. Then the minimal stabilizing function $k_0(\theta)$ defined in* (3.16) *is well-defined. Moreover,*

$$k_0(\theta) \leq \frac{1}{4\hat\gamma(\theta)}\left[A^2(\theta) + 4\hat\gamma(\theta)A(\theta) + 4|\hat\gamma'(\theta)|^2\right] < \infty, \tag{3.17}$$

*where*

$$A(\theta) \coloneqq \frac{\pi^2}{8}\left(5\sup_{2\pi\mathbb{T}}|\hat\gamma''| + 5|\hat\gamma'(\theta)| + \hat\gamma(\theta)\right). \tag{3.18}$$

The proof of Theorem 3.3 is given in Section 3.3.3.

Remark 3.4. Earlier existence proofs for the minimal stabilizing function relied on the finite subcover theorem [13, 14, 149] and did not provide a global estimate. Numerical computations therefore typically required solving an optimization problem to approximate $k_0(\theta)$. Theorem 3.3 provides the first global estimate of $k_0(\theta)$, eliminating the need for this preliminary computation in applications.

#### 3.3.1. The local energy estimate revisited.

Lemma 3.1 (Local energy estimate). *For any $\boldsymbol{p},\boldsymbol{q} \in \mathbb{R}^2\backslash\{\mathbf{0}\}$, write $\boldsymbol{p} = |\boldsymbol{p}|(\cos\varphi,\sin\varphi)^T$, $\boldsymbol{q} = |\boldsymbol{q}|(\cos\theta,\sin\theta)^T$. For sufficiently large $k(\theta)$,*

$$\frac{1}{|\boldsymbol{q}|}\left(\hat{\boldsymbol{Z}}_k(\theta)\boldsymbol{p}\right)\cdot(\boldsymbol{p}-\boldsymbol{q}) \geq \hat\gamma(\varphi)|\boldsymbol{p}| - \hat\gamma(\theta)|\boldsymbol{q}|. \tag{3.19}$$

Proof. Recalling the definition of $\hat{\boldsymbol{Z}}_k(\theta)$ in (3.2), we have

$$\begin{aligned}\frac{1}{|\boldsymbol{q}|}\left(\hat{\boldsymbol{Z}}_k(\theta)\boldsymbol{p}\right)\cdot\boldsymbol{p} &= \frac{|\boldsymbol{p}|^2}{|\boldsymbol{q}|}\hat{\boldsymbol{Z}}_k(\theta)\begin{pmatrix}\cos\varphi\\ \sin\varphi\end{pmatrix}\cdot\begin{pmatrix}\cos\varphi\\ \sin\varphi\end{pmatrix}\\ &= \frac{|\boldsymbol{p}|^2}{|\boldsymbol{q}|}\left(\hat\gamma(\theta) - \hat\gamma'(\theta)\sin 2(\theta-\varphi) + k(\theta)\sin^2(\theta-\varphi)\right)\\ &= \frac{|\boldsymbol{p}|^2}{|\boldsymbol{q}|}P_k(\theta-\varphi,\theta).\end{aligned} \tag{3.20}$$

and

$$\begin{aligned}\frac{1}{|\boldsymbol{q}|}\left(\hat{\boldsymbol{Z}}_k(\theta)\boldsymbol{p}\right)\cdot\boldsymbol{q} &= |\boldsymbol{p}|\hat{\boldsymbol{Z}}_k(\theta)\begin{pmatrix}\cos\varphi\\ \sin\varphi\end{pmatrix}\cdot\begin{pmatrix}\cos\theta\\ \sin\theta\end{pmatrix}\\ &= |\boldsymbol{p}|\left(\hat\gamma(\theta)\cos(\theta-\varphi) - \hat\gamma'(\theta)\sin(\theta-\varphi)\right)\\ &= |\boldsymbol{p}|\left(Q(\theta-\varphi,\theta) - \hat\gamma(\varphi)\right).\end{aligned} \tag{3.21}$$

Theorem 3.3 gives $4\hat\gamma(\theta)P_k(\theta-\varphi,\theta) \geq Q^2(\theta-\varphi,\theta)$ for every $k(\theta) \geq k_0(\theta)$. Hence

$$\begin{aligned}\frac{1}{|\boldsymbol{q}|}\left(\hat{\boldsymbol{Z}}_k(\theta)\boldsymbol{p}\right)\cdot(\boldsymbol{p}-\boldsymbol{q}) &\geq \frac{|\boldsymbol{p}|^2}{4\hat\gamma(\theta)|\boldsymbol{q}|}Q^2(\theta-\varphi,\theta) - |\boldsymbol{p}|Q(\theta-\varphi,\theta) + |\boldsymbol{p}|\hat\gamma(\varphi)\\ &\geq |\boldsymbol{p}|\hat\gamma(\varphi) - |\boldsymbol{q}|\hat\gamma(\theta).\end{aligned} \tag{3.22}$$

The last inequality follows from $\frac{1}{4a}t^2 - t \geq -a,\ \forall t\in\mathbb{R}, a>0$. □

Remark 3.5. Taking $\boldsymbol{p} = -\boldsymbol{q}$ in (3.19) gives $\theta = \varphi + \pi, |\boldsymbol{p}| = |\boldsymbol{q}|$. The local energy estimate (3.19) then yields $2\hat{\gamma}(\theta) \geq \hat{\gamma}(\theta - \pi) - \hat{\gamma}(\theta)$, which is precisely (3.1). This conclusion extends to any surface energy matrix $\hat{\boldsymbol{Z}}(\theta)$ satisfying $\begin{pmatrix}\cos\theta & \sin\theta\end{pmatrix} \hat{\boldsymbol{Z}}(\theta) \begin{pmatrix}\cos\theta \\ \sin\theta\end{pmatrix} = \hat{\gamma}(\theta)$, including $\hat{\boldsymbol{G}}_k(\theta)$ as stated in Remark 2.10. Thus, within the framework of local energy estimates, the energy stability condition (3.1) is optimal and cannot be further relaxed.

**3.3.2. Unconditional energy stability.**

Proof. Choose $k(\theta)$ sufficiently large that $k(\theta) \geq k_0(\theta)$.

For every $m \geq 0$, we have

$$\begin{aligned} &\left(\hat{\boldsymbol{Z}}_k(\theta^m)\partial_s \boldsymbol{X}^{m+1}, \partial_s(\boldsymbol{X}^{m+1} - \boldsymbol{X}^m)\right)_{\Gamma^m}^h \\ &= \sum_{j=1}^N \left[ |\boldsymbol{h}_j^m| \left( \hat{\boldsymbol{Z}}_k(\theta_j^m) \frac{\boldsymbol{h}_j^{m+1}}{|\boldsymbol{h}_j^m|} \right) \cdot \frac{\boldsymbol{h}_j^{m+1} - \boldsymbol{h}_j^m}{|\boldsymbol{h}_j^m|} \right] \\ &= \sum_{j=1}^N \left[ \frac{1}{|\boldsymbol{h}_j^m|} \left( \hat{\boldsymbol{Z}}_k(\theta_j^m) \boldsymbol{h}_j^{m+1} \right) \cdot (\boldsymbol{h}_j^{m+1} - \boldsymbol{h}_j^m) \right]. \end{aligned} \tag{3.23}$$

Combining the local energy estimate (3.19) with (3.23) gives

$$\begin{aligned} &\left(\hat{\boldsymbol{Z}}_k(\theta^m)\partial_s \boldsymbol{X}^{m+1}, \partial_s(\boldsymbol{X}^{m+1} - \boldsymbol{X}^m)\right)_{\Gamma^m}^h \\ &\geq \sum_{j=1}^N \left[ |\boldsymbol{h}_j^{m+1}| \hat{\gamma}(\theta_j^{m+1}) - |\boldsymbol{h}_j^m| \hat{\gamma}(\theta_j^m) \right] \\ &= \sum_{j=1}^N |\boldsymbol{h}_j^{m+1}| \hat{\gamma}(\theta_j^{m+1}) - \sum_{j=1}^N |\boldsymbol{h}_j^m| \hat{\gamma}(\theta_j^m) = W^{m+1} - W^m. \end{aligned} \tag{3.24}$$

Taking $\varphi^h = \mu^{m+1}, \boldsymbol{\omega}^h = \boldsymbol{X}^{m+1} - \boldsymbol{X}^m$ in (3.12) gives

$$\begin{aligned} \left(\hat{\boldsymbol{Z}}_k(\theta^m)\partial_s \boldsymbol{X}^{m+1}, \partial_s(\boldsymbol{X}^{m+1} - \boldsymbol{X}^m)\right)_{\Gamma^m}^h &= \left(\mu^{m+1}\boldsymbol{n}^{m+\frac{1}{2}}, \boldsymbol{X}^{m+1} - \boldsymbol{X}^m\right)_{\Gamma^m}^h \\ &= -\tau \left(\partial_s \mu^{m+1}, \partial_s \mu^{m+1}\right)_{\Gamma^m}^h. \end{aligned} \tag{3.25}$$

Combining this with (3.24) yields

$$W^{m+1} - W^m \leq -\tau \left(\partial_s \mu^{m+1}, \partial_s \mu^{m+1}\right)_{\Gamma^m}^h \leq 0, \qquad \forall m \geq 0. \tag{3.26}$$

This completes the proof. □

**3.3.3. A global estimate for the minimal stabilizing function.** To prove the existence of $k_0(\theta)$ under the optimal condition (3.1), we need a sharp estimate of $Q(\phi, \theta)$. Unlike the estimates in [13, 149], this estimate explicitly uses both $P_\alpha(\phi, \theta)$ and $\hat{\gamma}(\theta)$. Lemma 3.2 provides the estimate that is central to the existence proof.

Remark 3.6. In [149] and Section 2.4.4, $Q(\phi, \theta)$ is controlled only by $\hat{\gamma}(\theta)$. In [13], the authors couple $P_\alpha(\phi, \theta)$ separately with $Q(\phi, \theta)$, $\hat{\gamma}(\theta)$ to obtain the required estimates. These estimates are therefore less precise. Here we explicitly combine $P_\alpha(\phi, \theta)$, $\hat{\gamma}(\theta)$ with $Q(\phi, \theta)$ to obtain a sharper bound.

Lemma 3.2. *Let $f$ be a nonnegative $C^2$ function on $2\pi\mathbb{T}$. For every positive constant $C \geq \sup_{2\pi\mathbb{T}} |f''|$,*

$$|f'(x)y| \leq f(x) + \frac{1}{2} \sup_{2\pi\mathbb{T}} |f''|\, y^2 \leq f(x) + \frac{C}{2} y^2, \qquad \forall x, y \in 2\pi\mathbb{T}. \tag{3.27}$$

Proof. The mean value theorem and the nonnegativity of $f$ give, for every $C \geq \sup_{2\pi\mathbb{T}} |f''|$,

$$0 \leq f(x+y) \leq f(x) + f'(x)y + \frac{C}{2}y^2, \qquad \forall x, y \in 2\pi\mathbb{T}, \tag{3.28}$$

That is, $-f'(x)y \leq f(x) + \frac{C}{2}y^2$. Replacing $y$ by $-y$ gives $f'(x)y \leq f(x) + \frac{C}{2}y^2$ by the same argument. □

Remark 3.7. Lemma 3.2 is essential for controlling $Q(\phi, \theta)$ and analyzing the critical case $\phi = \pi$. An analogous inequality is difficult to obtain in the $\gamma(\boldsymbol{n})$ formulation.

Remark 3.8. Establishing an analogue of Lemma 3.2 in the $\gamma(\boldsymbol{n})$ formulation presents several difficulties. Expanding $\gamma(\boldsymbol{n})$ at a point $\boldsymbol{n}_0$ introduces the Hessian $\boldsymbol{H}_\gamma$, which is undefined at $\mathbf{0}$. If the line joining $\boldsymbol{n}, \boldsymbol{n}_0$ passes through the origin, $\boldsymbol{H}_\gamma$ becomes unbounded, preventing effective control of the gradient $\nabla\gamma(\boldsymbol{n})$. Even if a comparable estimate could be obtained, its coefficient would depend on $\boldsymbol{n}_0$, whereas the $\hat{\gamma}(\theta)$ formulation permits an absolute constant.

Lemma 3.3 (Estimate of $Q(\phi, \theta)$). *Suppose that the optimal energy stability condition* (3.1) *holds. Then* $Q(\phi, \theta)$*, defined in* (3.15b)*, satisfies*

$$|Q(\phi, \theta)| \leq |P_{A(\theta)}(\phi, \theta) + \hat{\gamma}(\theta)|, \qquad \forall \phi \in 2\pi\mathbb{T}, \tag{3.29}$$

*The quantity* $A(\theta)$ *is defined in* (3.18)*.*

Proof. We first obtain a lower bound for $Q(\phi, \theta)$ as follows:

$$\begin{aligned} Q(\phi, \theta) + P_0(\phi, \theta) + \hat{\gamma}(\theta) &= \hat{\gamma}(\theta - \phi) + \hat{\gamma}(\theta)(2 + \cos\phi) - \hat{\gamma}'(\theta)(\sin\phi + \sin 2\phi) \\ &\geq \hat{\gamma}(\theta - \phi) + \hat{\gamma}(\theta) - \hat{\gamma}'(\theta)(1 + 2\cos\phi)\sin\phi \\ &\geq \hat{\gamma}(\theta) - 3|\hat{\gamma}'(\theta)||\sin\phi| \\ &\geq -\frac{9}{2}\sup_{2\pi\mathbb{T}}|\hat{\gamma}''|\,\sin^2\phi, \end{aligned}$$

The last inequality follows from (3.28). Moreover, using $A(\theta) \geq \frac{9}{2}\sup_{2\pi\mathbb{T}}|\hat{\gamma}''|$ and $P_{A(\theta)}(\phi, \theta) = P_0(\phi, \theta) + A(\theta)\sin^2\phi$ gives

$$Q(\phi, \theta) \geq -P_{A(\theta)}(\phi, \theta) - \hat{\gamma}(\theta), \qquad \forall \phi \in 2\pi\mathbb{T}. \tag{3.30}$$

For the opposite inequality, we first note that $Q(0, \theta) - P_0(0, \theta) - \hat{\gamma}(\theta) = 0$ and $Q(\pi, \theta) - P_0(\pi, \theta) - \hat{\gamma}(\theta) = -(3\hat{\gamma}(\theta) - \hat{\gamma}(\theta - \pi)) \leq 0$. We consider two cases.

Case 1: $|\phi| \leq \frac{\pi}{2}$. Applying the mean value theorem to $Q(\cdot, \theta) - P_0(\cdot, \theta) - \hat{\gamma}(\theta)$ on $[\phi, 0]$ gives $\xi \in [\phi, 0], |\xi| \leq \frac{\pi}{2}$ such that

$$\begin{aligned} &Q(\phi, \theta) - P_0(\phi, \theta) - \hat{\gamma}(\theta) \\ &= \frac{1}{2}\left(\hat{\gamma}''(\theta - \xi) - \hat{\gamma}(\theta)\cos\xi + \hat{\gamma}'(\theta)\sin\xi - 4\hat{\gamma}'(\theta)\sin 2\xi\right)\phi^2 \\ &\leq \frac{1}{2}\left(\sup_{2\pi\mathbb{T}}|\hat{\gamma}''| + 5|\hat{\gamma}'(\theta)| + \hat{\gamma}(\theta)\right)\left(\frac{\pi^2}{4}\sin^2\phi\right) \\ &\leq A(\theta)\sin^2\phi. \end{aligned} \tag{3.31}$$

Case 2: $|\phi - \pi| < \frac{\pi}{2}$. By (3.1), $3\hat{\gamma}(\theta) - \hat{\gamma}(\theta - \pi)$ is a nonnegative $C^2$ function. Applying Lemma 3.2 gives

$$\begin{aligned} &\left|(3\hat{\gamma}'(\theta) - \hat{\gamma}'(\theta - \pi))\,(\phi - \pi)\right| \\ &\leq (3\hat{\gamma}(\theta) - \hat{\gamma}(\theta - \pi)) + \frac{\sup_{\theta\in 2\pi\mathbb{T}}|3\hat{\gamma}''(\theta) - \hat{\gamma}''(\theta - \pi)|}{2}(\phi - \pi)^2 \\ &\leq (3\hat{\gamma}(\theta) - \hat{\gamma}(\theta - \pi)) + 2\sup_{2\pi\mathbb{T}}|\hat{\gamma}''|(\phi - \pi)^2, \quad \forall |\phi - \pi| < \frac{\pi}{2}. \end{aligned} \tag{3.32}$$

Applying the mean value theorem to $Q(\cdot,\theta)-P_0(\cdot,\theta)-\hat{\gamma}(\theta)$ on $[\phi,\pi]$ gives $\xi\in[\phi,\pi], |\xi-\pi|<\frac{\pi}{2}$ such that

$$\begin{aligned}
&Q(\phi,\theta)-P_0(\phi,\theta)-\hat{\gamma}(\theta)\\
&=-\left(3\hat{\gamma}(\theta)-\hat{\gamma}(\theta-\pi)\right)+\left(3\hat{\gamma}'(\theta)-\hat{\gamma}'(\theta-\pi)\right)(\phi-\pi)\\
&\quad+\frac{1}{2}\left(\hat{\gamma}''(\theta-\xi)-\hat{\gamma}(\theta)\cos\xi+\hat{\gamma}'(\theta)\sin\xi-4\hat{\gamma}'(\theta)\sin 2\xi\right)(\phi-\pi)^2\\
&\le-\left(3\hat{\gamma}(\theta)-\hat{\gamma}(\theta-\pi)\right)+\left(3\hat{\gamma}(\theta)-\hat{\gamma}(\theta-\pi)\right)\\
&\quad+\frac{1}{2}\left(\sup_{2\pi\mathbb{T}}|\hat{\gamma}''|+5|\hat{\gamma}'(\theta)|+\hat{\gamma}(\theta)+4\sup_{2\pi\mathbb{T}}|\hat{\gamma}''|\right)(\phi-\pi)^2\\
&\le\frac{\pi^2}{8}\left(5\sup_{2\pi\mathbb{T}}|\hat{\gamma}''|+5|\hat{\gamma}'(\theta)|+\hat{\gamma}(\theta)\right)\sin^2\left(\phi-\pi\right)=A(\theta)\sin^2\phi.
\end{aligned}$$

Combining (3.31) and (3.33) yields

$$Q(\phi,\theta)\le P_0(\phi,\theta)+\hat{\gamma}(\theta)+A(\theta)\sin^2\phi=P_{A(\theta)}(\phi,\theta)+\hat{\gamma}(\theta),\quad\forall\phi\in 2\pi\mathbb{T}. \tag{3.33}$$

This completes the proof. □

We now use the sharp estimate in Lemma 3.3 to prove Theorem 3.3.

Proof. *(Existence of the minimal stabilizing function)*
By Lemma 3.3,

$$Q^2(\phi,\theta)\le\left(P_{A(\theta)}(\phi,\theta)+\hat{\gamma}(\theta)\right)^2. \tag{3.34}$$

Recalling the definition of $P_\alpha(\phi,\theta)$ in (3.15a), we have $P_\alpha(\phi,\theta)=P_0(\phi,\theta)+\alpha\sin^2\phi$, and hence

$$\begin{aligned}
&4\hat{\gamma}(\theta)P_\alpha(\phi,\theta)-Q^2(\phi,\theta)\\
&\ge 4\hat{\gamma}(\theta)P_{A(\theta)}(\phi,\theta)-\left(P_{A(\theta)}(\phi,\theta)+\hat{\gamma}(\theta)\right)^2+4\hat{\gamma}(\theta)\left(\alpha-A(\theta)\right)\sin^2\phi\\
&=-\left(P_{A(\theta)}(\phi,\theta)-\hat{\gamma}(\theta)\right)^2+4\hat{\gamma}(\theta)\left(\alpha-A(\theta)\right)\sin^2\phi\\
&=\left(-\left(-2\hat{\gamma}'(\theta)\cos\phi+A(\theta)\sin\phi\right)^2+4\hat{\gamma}(\theta)\left(\alpha-A(\theta)\right)\right)\sin^2\phi\\
&\ge\left[4\hat{\gamma}(\theta)\alpha-A^2(\theta)-4|\hat{\gamma}'(\theta)|^2-4\hat{\gamma}(\theta)A(\theta)\right]\sin^2\phi.
\end{aligned} \tag{3.35}$$

The last inequality follows from $|a\cos\phi+b\sin\phi|\le\sqrt{a^2+b^2}$.

Therefore, for every $\alpha\ge\frac{1}{4\hat{\gamma}(\theta)}\left[A^2(\theta)+4\hat{\gamma}(\theta)A(\theta)+4|\hat{\gamma}'(\theta)|^2\right]$, we have

$$4\hat{\gamma}(\theta)P_\alpha(\phi,\theta)-Q^2(\phi,\theta)\ge 0,\qquad\forall\phi\in 2\pi\mathbb{T}. \tag{3.36}$$

Consequently,

$$k_0(\theta)\le\frac{1}{4\hat{\gamma}(\theta)}\left[A^2(\theta)+4\hat{\gamma}(\theta)A(\theta)+4|\hat{\gamma}'(\theta)|^2\right]<\infty. \tag{3.37}$$

□

### 3.4. Numerical experiments

In this section, we present numerical experiments for (3.12). We first examine efficiency and accuracy through convergence tests, then verify its structure-preserving properties: area conservation and unconditional energy stability.

We mainly consider the following two anisotropic surface energies:

- Case I: $\hat{\gamma}(\theta)=1+\beta\cos 3\theta$, where $|\beta|<1$. This energy is weakly anisotropic when $|\beta|<\frac{1}{8}$ and strongly anisotropic otherwise.
- Case II: $\hat{\gamma}(\theta)=\sqrt{\left(\frac{5}{2}+\frac{3}{2}\operatorname{sgn}(n_1)\right)n_1^2+n_2^2}$, where $\boldsymbol{n}=(n_1,n_2)^T=(-\sin\theta,\cos\theta)^T$.

The scheme (3.12) is formally second-order accurate in space and first-order accurate in time. Unless otherwise stated, we therefore use the time step $\tau = h^2$. The definitions of the numerical error $e^h$, weighted mesh ratio $R^h_\gamma$, and normalized area loss and energy are given in (2.97)–(2.100). Since an analytic exact solution is unavailable, we approximate $\Gamma(t = t_m)$ using (3.12) on the fine mesh $h_e = 2^{-8}, \tau_e = 2^{-16}$.

We solve the nonlinear scheme (3.12) by a Newton method analogous to that in Appendix A, with tolerance tol $= 10^{-12}$.

We first verify the upper bound for $k_0(\theta)$ in Theorem 3.3; see Figure 3.1. Here $K(\theta)$ denotes the bound given in (3.17).

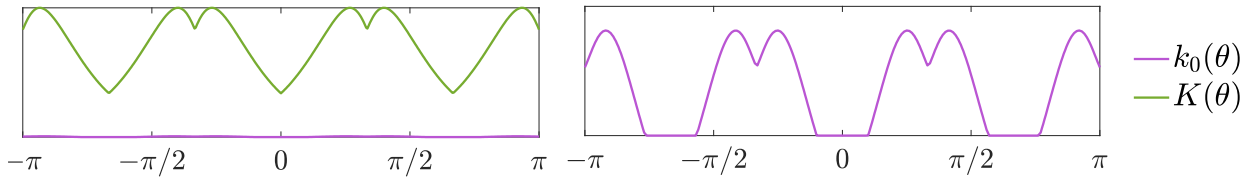



**Figure 3.1.** Minimal stabilizing function $k_0(\theta)$ and upper bound $K(\theta)$ in (3.17) for Case I with $\beta = \frac{1}{2}$.

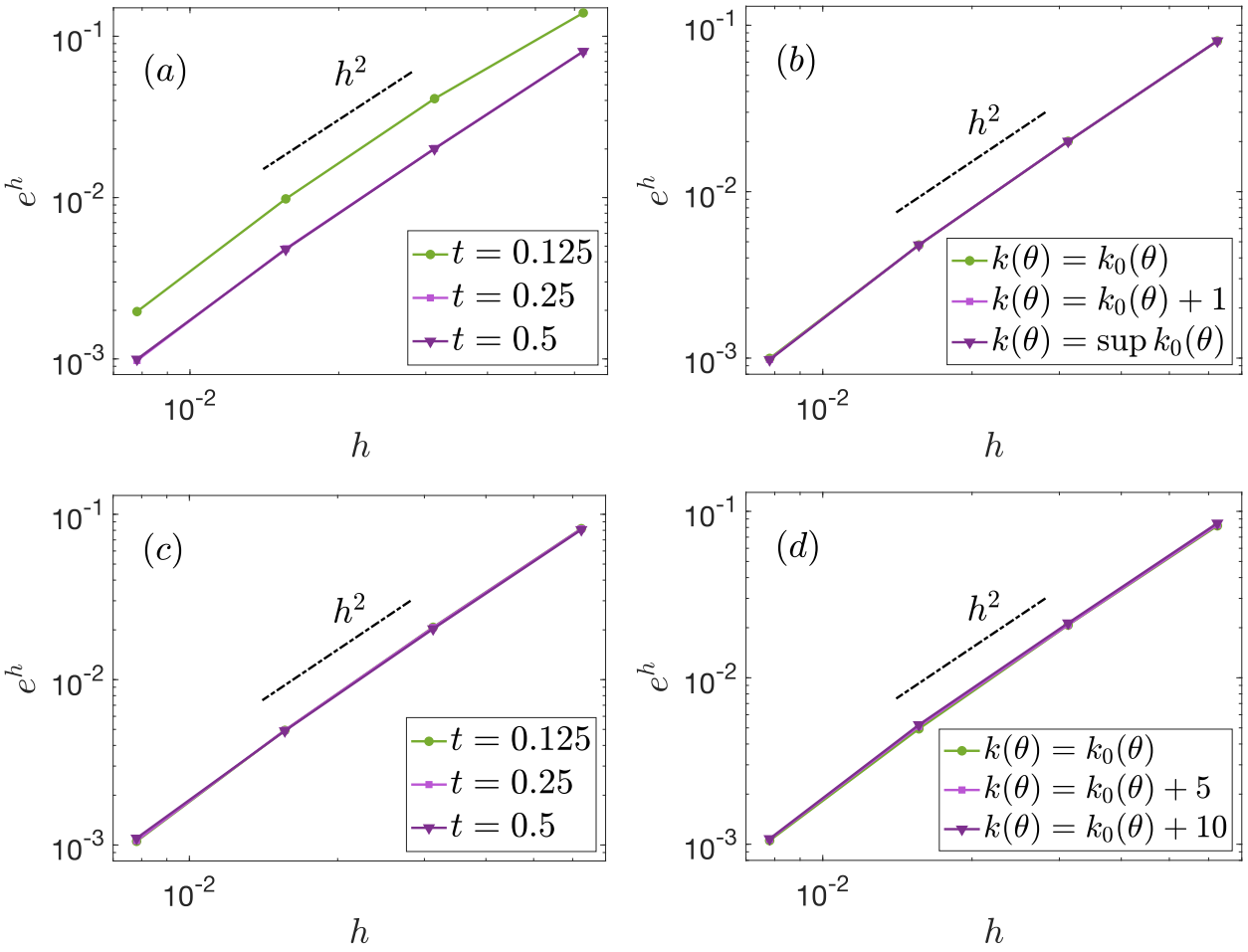



**Figure 3.2.** Convergence rates of the SP-PFEM (3.12) for Case I with $\beta = 1/9$ (a) at different times with $k(\theta) = k_0(\theta)$, and (b) at $t = 0.5$ with different $k(\theta)$; and for Case II (c) at different times with $k(\theta) = k_0(\theta)$, and (d) at $t = 0.5$ with different $k(\theta)$.

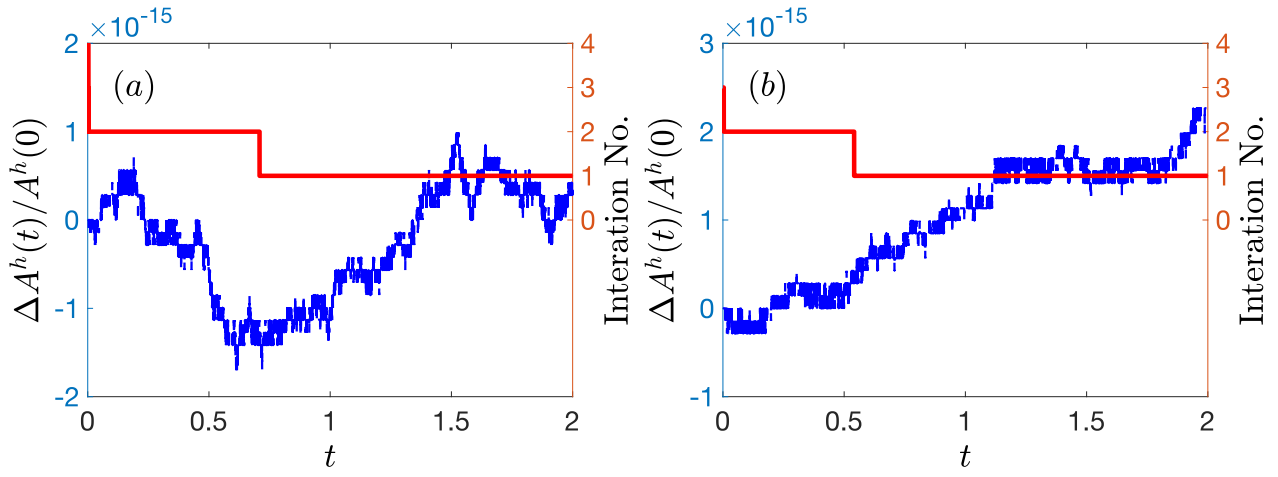



**Figure 3.3.** Normalized area loss (blue dashed line) and number of Newton iterations (red line) of the SP-PFEM (3.12) with $k(\theta) = k_0(\theta)$ and $h = 2^{-6}$, $\tau = 2^{-12}$ for (a) Case I with $\beta = 1/2$; (b) Case II.

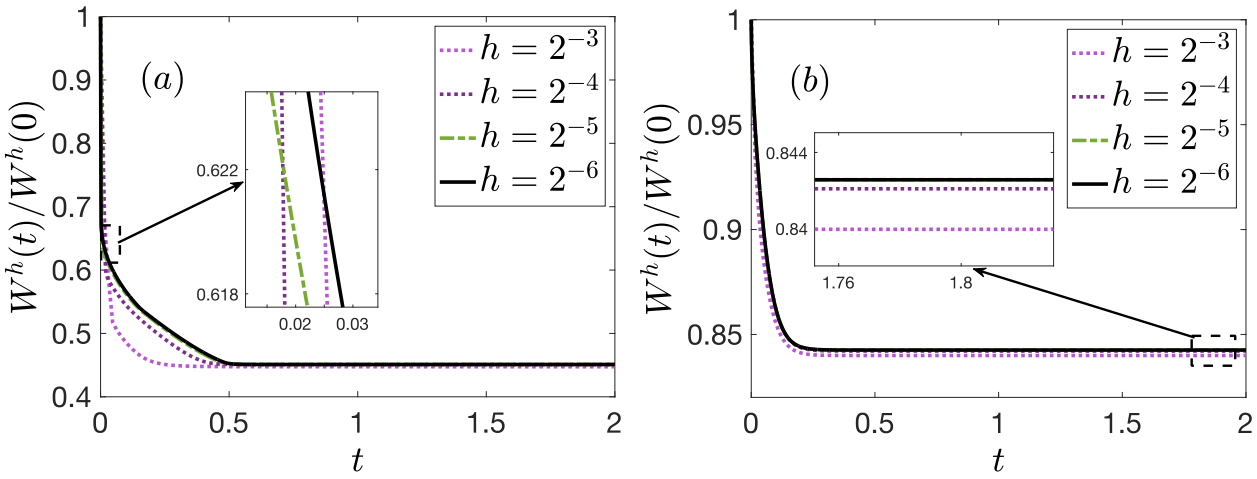



**Figure 3.4.** Normalized energy of the SP-PFEM (3.12) with $k(\theta) = k_0(\theta)$ for (a) Case I with $\beta = 1/2$; (b) Case II.

**3.4.1. Convergence rates and structure preservation.** Figures 3.2–3.5 show the following results:

- The scheme (3.12) is second-order accurate in space and first-order accurate in time; see Figure 3.2.
- The normalized area loss is approximately $10^{-15}$, on the order of round-off error; see Figure 3.3. Thus the enclosed area is preserved to machine precision.
- The number of Newton iterations quickly decreases to 2 and eventually to 1. Thus this semi-implicit scheme can be solved efficiently; see Figure 3.3.
- When $\hat{\gamma}(\theta)$ satisfies (3.1), the normalized energy is monotonically decreasing; see Figure 3.4. For Case I, (3.1) requires $0 < \beta \le \frac{1}{2}$. Figure 3.4(a) shows that (3.12) still dissipates energy when $\beta$ takes its maximum value, confirming Theorem 3.2. Unlike the method in [9], the scheme (3.12) is also unconditionally energy stable for asymmetric surface energies.
- The weighted mesh ratio $R^h_\gamma(t)$ approaches a constant as $t \to +\infty$, indicating an asymptotically quasi-uniform mesh distribution for (3.12); see Figure 3.5.

**3.4.2. Morphological evolution under two-dimensional surface diffusion.** We now apply (3.12) to simulate the morphological evolution of closed curves under anisotropic surface diffusion, using the mesh size $h = 2^{-6}$ and time step $\tau = h^2$.

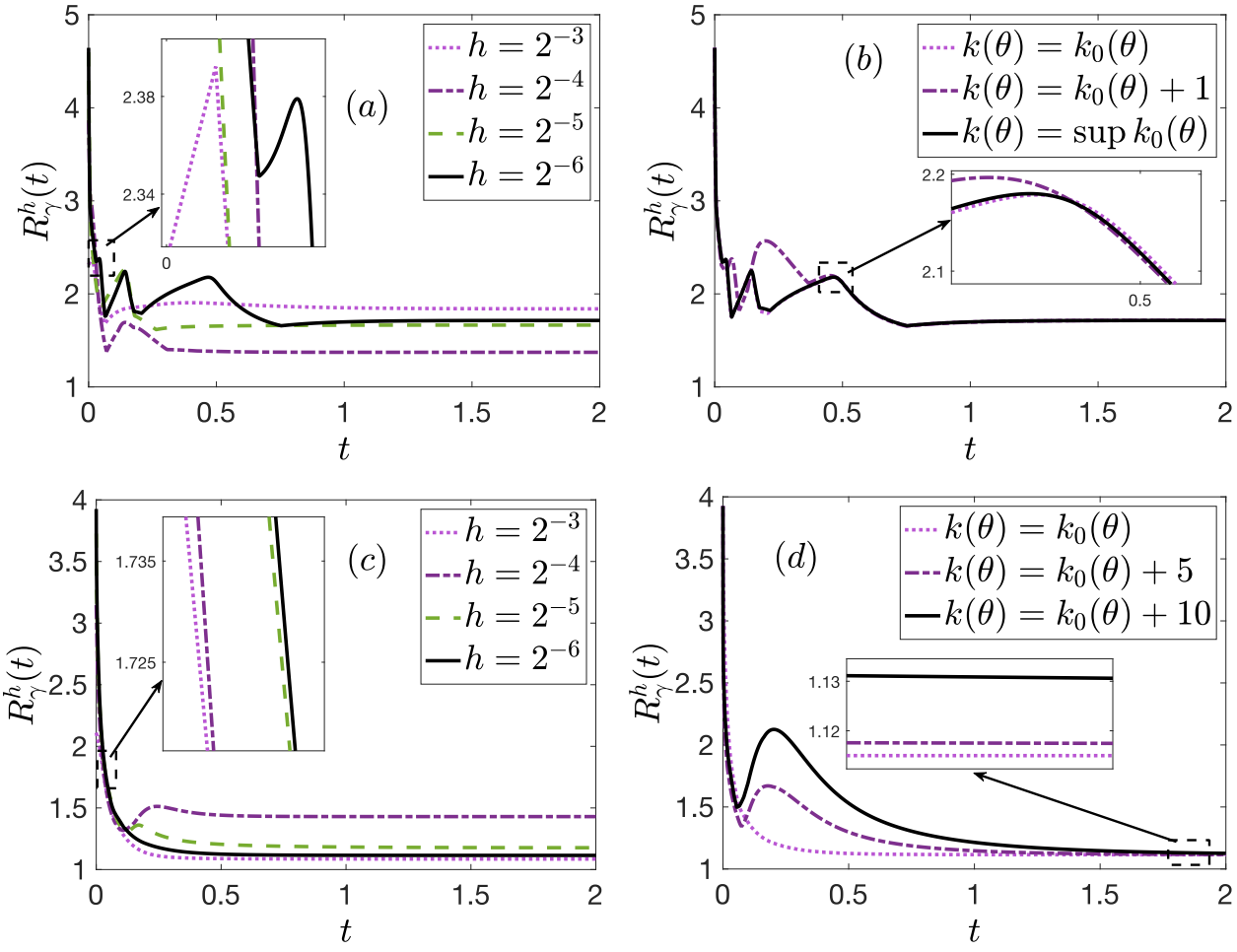



**Figure 3.5.** Weighted mesh ratio of the SP-PFEM (3.12) for Case I with $\beta = 1/9$ is illustrated in (a) for $k(\theta) = k_0(\theta)$ with different $h$, and in (b) for different $k(\theta)$ with $h = 2^{-6}$; and for Case II is presented in (c) for $k(\theta) = k_0(\theta)$ with different $h$, and in (d) for different $k(\theta)$ with $h = 2^{-6}$.

Figure 3.6 shows the evolution of an ellipse with major axis 4 and minor axis 1 under anisotropic surface diffusion with four surface energies:

(a) three-fold symmetric anisotropy [11]: $\hat{\gamma}(\theta) = 1 + \frac{1}{2}\cos 3\theta$;

(b) piecewise ellipsoidal anisotropy [44]: $\hat{\gamma}(\theta) = \sqrt{\left(\frac{5}{2} + \frac{3}{2}\,\mathrm{sgn}(n_1)\right) n_1^2 + n_2^2}$, where $\boldsymbol{n} = (n_1, n_2)^T := (-\sin\theta, \cos\theta)^T$;

(c) four-fold symmetric anisotropy [11, 147]: $\hat{\gamma}(\theta) = 1 + \frac{1}{10}\cos 4\theta$;

(d) regularized crystalline anisotropy [119]: $\hat{\gamma}(\theta) = 1 + \sqrt{\varepsilon^2 + (1-\varepsilon^2)\sin^2\frac{m}{2}\theta}$, where $\varepsilon = 0.1, m = 7$.

Among these surface energies, anisotropy (c) is symmetric, whereas the others are asymmetric. Figure 3.6 shows that, compared with the *symmetrized structure-preserving parametric finite element method* in [9], the scheme (3.12) applies to both symmetric and asymmetric surface energies. Figure 3.6(b) also shows that the method works for $\hat{\gamma}(\theta)$ with limited regularity, namely globally $C^1$ and piecewise $C^2$ anisotropies. This extends its applicability to a broader class of surface energies.

### 3.5. Chapter summary

We have proposed a structure-preserving parametric finite element method for two-dimensional anisotropic surface diffusion with the optimal energy stability condition $3\hat{\gamma}(\theta) - \hat{\gamma}(\theta - \pi) \geq 0$. Introducing the symmetric surface energy matrix $\hat{\boldsymbol{Z}}_k(\theta)$ gives a conservative weak formulation of

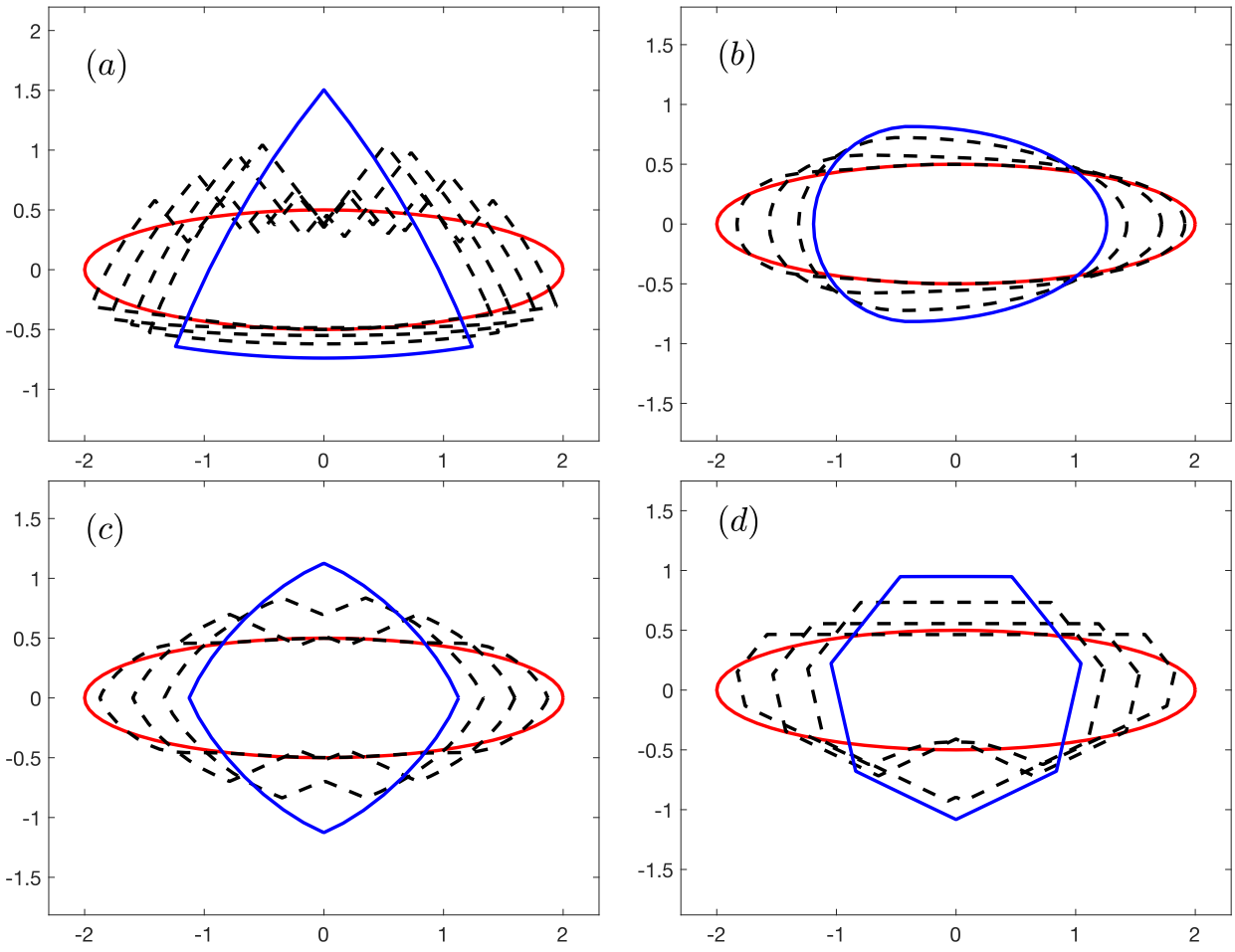



**Figure 3.6.** Morphological evolution of an ellipse with major axis 4 and minor axis 1 under anisotropic surface diffusion with different surface energies: (a) Case I with $\beta = 1/2$; (b) Case II; (c) the 4-fold anisotropy $\hat{\gamma}(\theta) = 1 + \frac{1}{10}\cos 4\theta$; (d) the regularized crystalline anisotropy $\hat{\gamma}(\theta) = 1 + \sqrt{\varepsilon^2 + (1-\varepsilon^2)\sin^2 \frac{m}{2}\theta}$, with $\varepsilon = 0.1, m = 7$. The red and blue lines represent the initial shape and the numerical equilibrium, respectively. The black dashed lines represent the intermediate curves.

anisotropic surface diffusion. We discretize this formulation using a parametric finite element method with piecewise linear functions in space and the semi-implicit Euler method in time. The scheme is second-order accurate in space and first-order accurate in time, and it preserves area conservation at the fully discrete level. A sharp estimate lemma provides a global upper bound for the minimal stabilizing function $k_0(\theta)$ under condition $3\hat{\gamma}(\theta) - \hat{\gamma}(\theta - \pi) \geq 0$, explicitly characterizing and proving the existence of $k_0(\theta)$ without additional assumptions. We then establish the required local energy estimate and prove unconditional energy stability for sufficiently large $k(\theta) \geq k_0(\theta)$. Since this condition is also necessary for the local energy estimate, it is optimal within this framework. Numerical experiments verify the efficiency, accuracy, and structure-preserving properties of the method. In the $\gamma(\boldsymbol{n})$ formulation, the method becomes the symmetrized parametric finite element scheme in [9, 103]. Our analysis further relaxes the symmetry condition in [9, 103] to $3\gamma(\boldsymbol{n}) - \gamma(-\boldsymbol{n}) \geq 0$.

CHAPTER 4

# Applications: two-dimensional crystalline film evolution and solid-state dewetting

This chapter studies the morphological evolution of two-dimensional crystalline films and islands in the solid state. We use a sharp-interface model in which the film boundary is represented by a moving curve. Interface motion is driven by a reduction in interfacial energy, and mass transport occurs primarily through diffusion along the free surface. Crystalline surface energies are typically anisotropic, leading to phenomena such as faceting and pinch-off. The conservative mass transport of surface diffusion also produces substantial geometric rearrangements and topological changes as the energy decreases.

In Section 4.1, we use the preceding methods to simulate crystalline film evolution under anisotropic surface diffusion. We study film stability, pinch-off, and island formation, and examine how geometric scales and anisotropy strength affect topological changes. In Section 4.2, we extend the *structure-preserving parametric finite element method* to open curves in solid-state dewetting and discuss the evolution toward multiple equilibria under strong anisotropy.

## 4.1. Two-dimensional crystalline film evolution

The morphological evolution of crystalline films driven by anisotropic surface diffusion has long attracted attention in materials science and solid-state physics [136]. Theoretical and experimental studies have advanced the understanding of interface dynamics, with applications to heterogeneous catalysis [122], quantum dot fabrication [64], and solid-state dewetting [143, 136]. Previous studies [49, 90] show that an island becomes unstable when its aspect ratio exceeds a critical value. It then undergoes pinch-off and separates into several smaller islands.

In this section, we apply the scheme (3.12) to simulate pinch-off of long thin films under anisotropic surface diffusion and examine the evolution and associated topological changes.

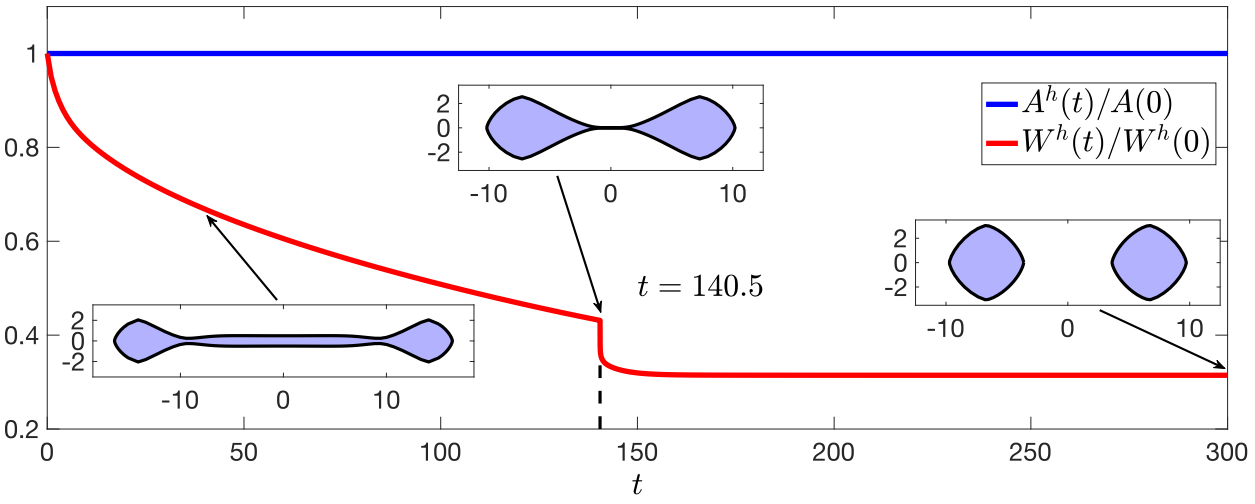



**Figure 4.1.** Normalized area and energy of a long thin film (aspect ratio of 50) governed by anisotropic surface diffusion with the 4-fold anisotropy $\hat{\gamma}(\theta) = 1 + \frac{1}{16}\cos 4\theta$.

We first simulate a long thin film with aspect ratio 50 under the four-fold symmetric anisotropy $\hat{\gamma}(\theta) = 1 + \frac{1}{16}\cos 4\theta$. Figure 4.1 shows the evolution of the normalized area and energy. Pinch-off occurs at $t = 140.5$, accompanied by a sudden decrease in energy, while the area remains conserved.

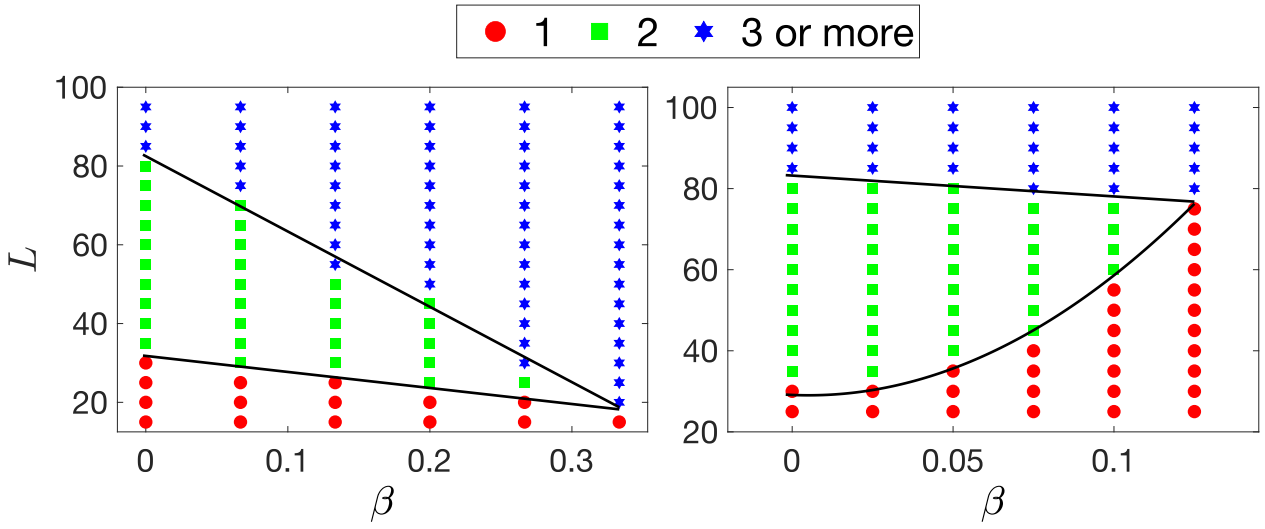



**Figure 4.2.** The number of islands formed from the pinch-off of a $2L \times 1$ long thin film as a function of $L$ and anisotropy strength $\beta$ for: (left) the 2-fold anisotropy $\hat{\gamma}(\theta) = 1 + \beta\cos 2\theta$; (right) the 3-fold anisotropy $\hat{\gamma}(\theta) = 1 + \beta\cos 3\theta$. The solid curves separate regions producing one and two islands, and regions producing two and three islands.

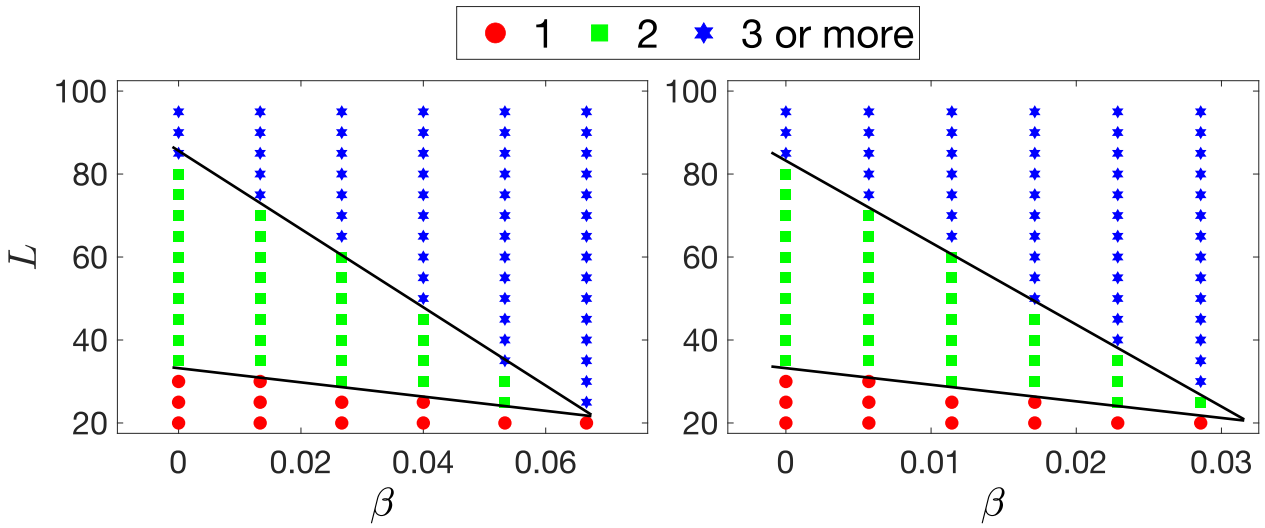



**Figure 4.3.** The number of islands formed from the pinch-off of a $2L \times 1$ long thin film as a function of $L$ and anisotropy strength $\beta$ for: (left) the 4-fold anisotropy $\hat{\gamma}(\theta) = 1 + \beta\cos 4\theta$; (right) the 6-fold anisotropy $\hat{\gamma}(\theta) = 1 + \beta\cos 6\theta$. The solid curves separate regions producing one and two islands, and regions producing two and three islands.

Both the film aspect ratio and the anisotropy strength influence island formation. To examine their effects, we perform numerical experiments with different aspect ratios and anisotropy strengths. Figures 4.2–4.3 summarize the results for the common $m$-fold symmetric anisotropy $\hat{\gamma}(\theta) = 1 + \beta\cos m\theta$, $m = 2, 3, 4, 6$.

For symmetric anisotropy $\hat{\gamma}(\theta) = 1 + \beta\cos m\theta$, $m = 2, 4, 6$, the boundaries between regions producing one and two islands, and between those producing two and three islands, are approximated by the following linear fits $L = p(m)\beta + q(m)$:

- Boundary between one and two islands: $p(m) = -12.23m^2 + 8.04m - 7.86$, $q(m) = 0.36m + 31.31$;
- boundary between two and three islands: $p(m) = -35.07m^2 - 165.40m + 279.82$, $q(m) = 0.18m + 83.06$.

These results indicate that, at a fixed aspect ratio, increasing the strength of a symmetric anisotropy promotes the formation of more islands.

For asymmetric anisotropy $\hat{\gamma}(\theta) = 1 + \beta \cos 3\theta$, we use a quadratic fit $L = 3285.70\beta^2 - 33.57\beta + 29.11$ for the boundary between one and two islands, and a linear fit $L = -51.43\beta + 83.21$ for the boundary between two and three islands. At small aspect ratios, increasing the anisotropy strength instead favors fewer islands. This behavior can be attributed to the asymmetry of the surface energy. The two sets of simulations show that symmetric and asymmetric anisotropies can produce markedly different morphological evolution of long thin films.

Finally, Figures 4.4 and 4.5 show the evolution of very thin films. In Figure 4.4, the asymmetry of the surface energy produces different behavior on the upper and lower surfaces: pronounced peaks and valleys form on the upper surface, whereas the lower surface remains relatively smooth and nearly flat. Figure 4.5 shows that, at the same aspect ratio, a symmetric anisotropy favors more islands than the isotropic surface energy.

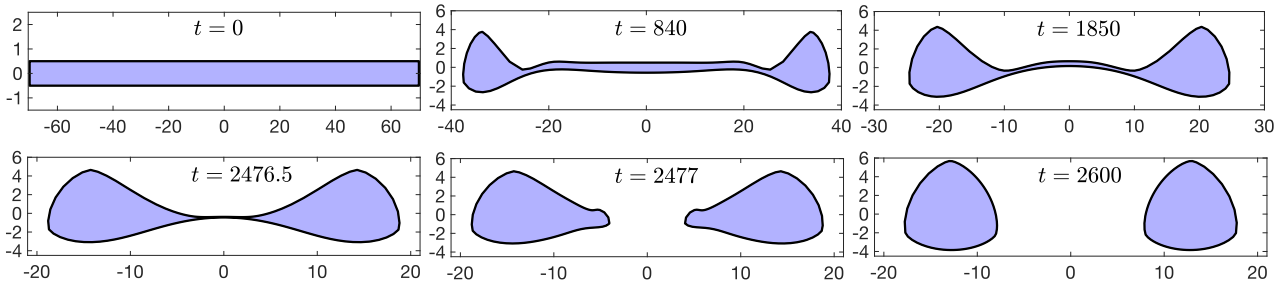



**Figure 4.4.** Snapshots of the evolution of a $140 \times 1$ thin film under anisotropic surface diffusion with 3-fold anisotropy $\hat{\gamma}(\theta) = 1 + \frac{1}{9}\cos 3\theta$.

## 4.2. Two-dimensional solid-state dewetting

When a solid film is heated above a critical temperature that remains below its melting point, it may undergo complex morphological changes. This phenomenon is called solid-state dewetting [136, 92, 139]. It has applications in thin film technology, including catalysts for semiconductor nanowire growth [125] and optical and magnetic devices [4, 112]. In two dimensions, solid-state dewetting can be viewed as open curve evolution governed by surface diffusion and moving contact lines; see Figure 4.6. In this section, we extend the conservative formulation (2.20) and the structure-preserving parametric finite element scheme (2.52) for closed curves to two-dimensional solid-state dewetting [11, 92, 139].

**4.2.1. The sharp-interface model and a stabilized formulation.** As illustrated in Figure 4.6, two-dimensional solid-state dewetting describes the evolution of an open curve

$$\Gamma(t) := \boldsymbol{X}(s,t) = (x(s,t), y(s,t))^T, \qquad 0 \le s \le L, \tag{4.1}$$

under *anisotropic surface diffusion* and *contact line migration*. Here $s$ and $t$ denote arc length and time, respectively, and $L := L(t) = |\Gamma(t)|$ is the total length of $\Gamma(t)$. As derived in [11, 92, 139], the dewetting of a film with a weakly anisotropic surface energy is described by the following dimensionless sharp-interface model:

The open curve $\boldsymbol{X}(s,t)$ satisfies the anisotropic surface diffusion equations (2.6)–(2.7) with the boundary conditions:

(i) *Contact point condition*

$$y(0,t) = 0, \qquad y(L,t) = 0, \qquad t \ge 0; \tag{4.2}$$

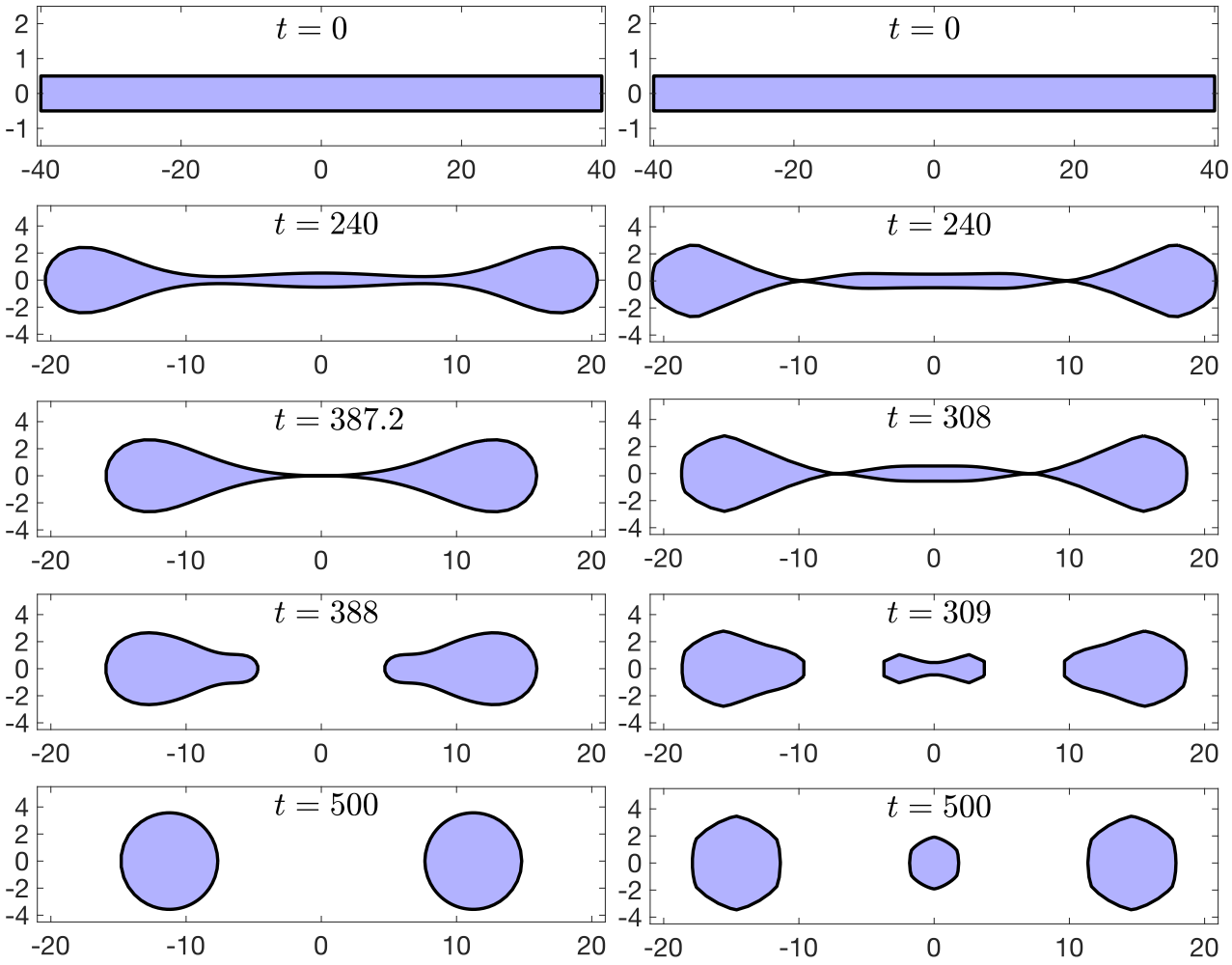



**Figure 4.5.** Morphological evolution of a thin film with aspect ratio 80 under surface diffusion: (left) isotropic; (right) 6-fold anisotropy $\hat{\gamma}(\theta) = 1 + \frac{1}{35.1}\cos 6\theta$.

(ii) *Relaxed contact angle condition*

$$\frac{\mathrm{d}x_c^l(t)}{\mathrm{d}t} = \eta f(\theta_d^l;\sigma), \qquad \frac{\mathrm{d}x_c^r(t)}{\mathrm{d}t} = -\eta f(\theta_d^r;\sigma), \qquad t \geq 0; \tag{4.3}$$

(iii) *Zero mass flux condition*

$$\partial_s \mu(0,t) = 0, \qquad \partial_s \mu(L,t) = 0, \qquad t \geq 0; \tag{4.4}$$

Here $x_c^l(t) = x(0,t) \leq x_c^r(t) = x(L,t)$ denote the left and right contact points, respectively, and $\theta_d^l := \theta_d^l(t), \theta_d^r := \theta_d^r(t)$ are the corresponding contact angles. The function $f(\theta;\sigma)$ is defined by

$$f(\theta;\sigma) := \hat{\gamma}(\theta)\cos\theta - \hat{\gamma}'(\theta)\sin\theta - \sigma, \qquad \theta \in 2\pi\mathbb{T}. \tag{4.5}$$

where $\sigma := \cos\theta_Y = \frac{\gamma_{VS}-\gamma_{FS}}{\gamma_{FV}}$, $\theta_Y$ is the isotropic Young contact angle, and $0 < \eta < +\infty$ is the contact line mobility [11, 92, 139].

As in (2.20), we derive the stabilized conservative form for solid-state dewetting:

$$\boldsymbol{n}\cdot\partial_t \boldsymbol{X} - \partial_{ss}\mu = 0, \qquad 0 < s < L(t), \qquad t > 0, \tag{4.6a}$$

$$\mu\boldsymbol{n} + \partial_s\left(\hat{\boldsymbol{G}}_k(\theta)\partial_s \boldsymbol{X}\right) = \boldsymbol{0}, \tag{4.6b}$$

with boundary conditions (4.2)–(4.4), where $\hat{\boldsymbol{G}}_k(\theta)$ is the stabilized surface energy matrix defined in (2.10).

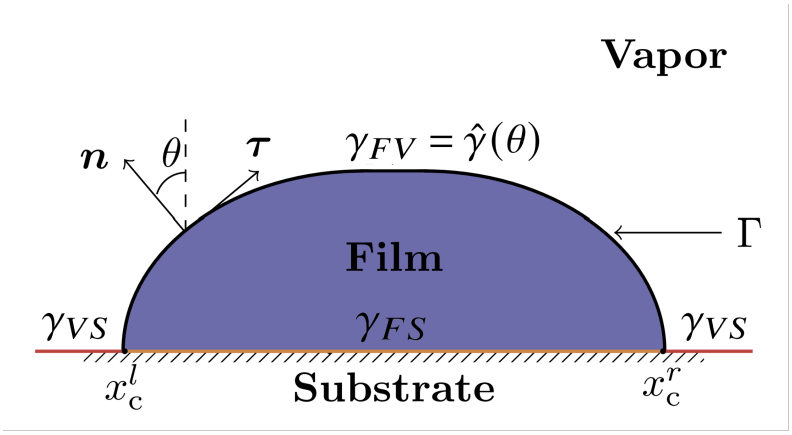



**Figure 4.6.** An illustration of solid-state dewetting of a thin film on a flat rigid substrate in 2D, where $\gamma_{FV} = \hat{\gamma}(\theta), \gamma_{VS}, \gamma_{FS}$ denote the surface energy densities of the film/vapor, vapor/substrate, and film/substrate interfaces, respectively, and $x_c^l, x_c^r$ are the left and right contact points.

**4.2.2. Weak formulation.** Let $\Gamma(t)$ be parameterized by a time-independent parameter $\rho$ on the fixed interval $\rho \in \mathbb{I} = [0, 1]$, namely

$$\Gamma(t) := \boldsymbol{X}(\rho, t) = (x(\rho, t), y(\rho, t))^T : \mathbb{I} \times \mathbb{R}^+ \to \mathbb{R}^2, \tag{4.7}$$

The arc length parameter $s$ is then given by $s = \int_0^\rho |\partial_q \boldsymbol{X}(q, t)| \, \mathrm{d}q$. Again, we use $\boldsymbol{X}(s, t)$ and $\boldsymbol{X}(\rho, t)$ interchangeably.

We introduce the function space

$$H_0^1(\mathbb{I}) := \left\{ u \in H^1(\mathbb{I}) \mid u(0) = u(1) = 0 \right\}, \qquad \mathbb{X} := H^1(\mathbb{I}) \times H_0^1(\mathbb{I}). \tag{4.8}$$

Following the derivation in Section 2.3, the weak formulation of (4.6) with boundary conditions (4.2)–(4.4) reads as follows: given an initial open curve $\Gamma(0) = \boldsymbol{X}(\cdot, 0) = \boldsymbol{X}_0 \in \mathbb{X}$, find $(\boldsymbol{X}(\cdot, t), \mu(\cdot, t)) \in \mathbb{X} \times H^1(\mathbb{I})$ such that

$$\left(\boldsymbol{n} \cdot \partial_t \boldsymbol{X}, \varphi\right)_{\Gamma(t)} + \left(\partial_s \mu, \partial_s \varphi\right)_{\Gamma(t)} = 0, \qquad \forall \varphi \in H^1(\mathbb{I}), \tag{4.9a}$$

$$\begin{aligned} &\left(\mu \boldsymbol{n}, \boldsymbol{\omega}\right)_{\Gamma(t)} - \left(\hat{\boldsymbol{G}}_k(\theta) \partial_s \boldsymbol{X}, \partial_s \boldsymbol{\omega}\right)_{\Gamma(t)} - \frac{1}{\eta} \left[ \frac{\mathrm{d}x_c^l(t)}{\mathrm{d}t} \omega_1(0) + \frac{\mathrm{d}x_c^r(t)}{\mathrm{d}t} \omega_1(1) \right] \\ &\qquad + \sigma \left[ \omega_1(1) - \omega_1(0) \right] = 0, \qquad \forall \boldsymbol{\omega} = (\omega_1, \omega_2)^T \in \mathbb{X}. \end{aligned} \tag{4.9b}$$

The area $A_o(t)$ enclosed by $\Gamma(t)$ and the substrate, and its total energy $W_o(t)$, are defined by

$$A_o(t) := \int_{\Gamma(t)} y(s, t) \partial_s x(s, t) \, \mathrm{d}s, \quad W_o(t) := \int_{\Gamma(t)} \hat{\gamma}(\theta) \, \mathrm{d}s - \sigma \left( x_c^r(t) - x_c^l(t) \right). \tag{4.10}$$

As in the closed curve case, the weak formulation (4.9) preserves area conservation and energy dissipation.

Proposition 4.1 (Area conservation and energy dissipation). *Let $\Gamma(t)$ be determined by a solution $(\boldsymbol{X}(\cdot, t), \mu(\cdot, t))$ of the weak formulation* (4.9)*. Then*

$$A_o(t) \equiv A_o(0), \qquad W_o(t) \le W_o(t_1) \le W_o(0), \qquad \forall t \ge t_1 \ge 0. \tag{4.11}$$

*More precisely,*

$$\frac{\mathrm{d}}{\mathrm{d}t} A_o(t) = 0, \quad \frac{\mathrm{d}}{\mathrm{d}t} W_o(t) = -\int_{\Gamma(t)} |\partial_s \mu|^2 \, \mathrm{d}s - \frac{1}{\eta} \left[ \left( \frac{\mathrm{d}x_c^r}{\mathrm{d}t} \right)^2 + \left( \frac{\mathrm{d}x_c^l}{\mathrm{d}t} \right)^2 \right] \le 0, \quad t \ge 0. \tag{4.12}$$

The proof is analogous to that of Proposition 2.1, so we omit the details.

**4.2.3. A stabilized parametric finite element scheme and its properties.** We introduce the finite element space

$$\mathbb{K}_0^h := \left\{u^h \in \mathbb{K}^h \mid u^h(0) = u^h(1) = 0\right\}, \qquad \mathbb{X}^h := \mathbb{K}^h \times \mathbb{K}_0^h. \tag{4.13}$$

The spatial semidiscretization of (4.9) and the proofs of its area conservation and energy dissipation follow the same arguments as in Section 2.3; we omit the details.

Let $\tau$ be a uniform time step, and approximate $\Gamma(t) = \boldsymbol{X}(\cdot,t)$ at $t_m = m\tau, m = 0,1,\dots$ by $\Gamma^m = \boldsymbol{X}^m(\cdot) = \cup_{j=1}^N \boldsymbol{h}_j^m$, where $\boldsymbol{h}_j^m := \boldsymbol{X}^m(\rho_j) - \boldsymbol{X}^m(\rho_{j-1})$. The *structure-preserving stabilized parametric finite element scheme* for solid-state dewetting (4.6) reads as follows: let the initial approximation $\Gamma^0(\cdot) \in \mathbb{X}^h$ be given by $\boldsymbol{X}^0(\rho_j) = \boldsymbol{X}_0(\rho_j), \forall 0 \le j \le N$. For every $m = 0,1,2,\dots$, find $(\boldsymbol{X}^{m+1}(\cdot) = (x^{m+1}(\cdot), y^{m+1}(\cdot))^T, \mu^{m+1}(\cdot)) \in \mathbb{X}^h \times \mathbb{K}^h$ such that

$$\left(\boldsymbol{n}^{m+\frac{1}{2}} \cdot \frac{\boldsymbol{X}^{m+1} - \boldsymbol{X}^m}{\tau}, \varphi^h\right)_{\Gamma^m}^h + \left(\partial_s \mu^{m+1}, \partial_s \varphi^h\right)_{\Gamma^m}^h = 0, \qquad \forall \varphi^h \in \mathbb{K}^h, \tag{4.14a}$$

$$\begin{aligned}\left(\mu^{m+1}\boldsymbol{n}^{m+\frac{1}{2}}, \boldsymbol{\omega}^h\right)_{\Gamma^m}^h - \left(\hat{\boldsymbol{G}}_k(\theta^m)\partial_s \boldsymbol{X}^{m+1}, \partial_s \boldsymbol{\omega}^h\right)_{\Gamma^m}^h - \frac{1}{\eta}\left[\frac{x_l^{m+1} - x_l^m}{\tau}\omega_1^h(0) + \frac{x_r^{m+1} - x_r^m}{\tau}\omega_1^h(1)\right] \\ + \sigma\left[\omega_1^h(1) - \omega_1^h(0)\right] = 0, \qquad \forall \boldsymbol{\omega}^h = (\omega_1^h, \omega_2^h) \in \mathbb{X}^h,\end{aligned} \tag{4.14b}$$

with $x_l^{m+1} = x^{m+1}(0) \le x_r^{m+1} = x^{m+1}(1)$. The matrix $\hat{\boldsymbol{G}}_k(\theta^m)$ is defined analogously to (2.54).

Let $A_o^m$ be the area enclosed by the open polygonal curve $\Gamma^m$ and the substrate, and let $W_o^m$ be the total surface energy, defined by

$$A_o^m := \frac{1}{2}\sum_{j=1}^N \left(x^m(\rho_j) - x^m(\rho_{j-1})\right)\left(y^m(\rho_j) + y^m(\rho_{j-1})\right), \tag{4.15a}$$

$$W_o^m := \sum_{j=1}^N |\boldsymbol{h}_j^m|\hat{\gamma}(\theta_j^m) - \sigma\left(x_r^m - x_l^m\right). \tag{4.15b}$$

We then obtain the following structure-preserving properties of (4.14).

Theorem 4.1 (Structure preservation). *For any $\hat{\gamma}(\theta)$ satisfying* (2.56) *and sufficiently large $k(\theta)$, the scheme* (4.14) *preserves area conservation and unconditional energy dissipation, namely*

$$A_o^{m+1} = A_o^m = \cdots = A_o^0, \qquad W_o^{m+1} \le W_o^m \le \cdots \le W_o^0, \qquad \forall m \ge 0. \tag{4.16}$$

Proof. Area conservation follows by an argument analogous to that of Theorem 2.2; we omit the details.

For energy dissipation, taking $\varphi^h = \mu^{m+1}$, $\boldsymbol{\omega}^h = \boldsymbol{X}^{m+1} - \boldsymbol{X}^m$ in (4.14) gives

$$\begin{aligned}&\tau\left(\partial_s \mu^{m+1}, \partial_s \mu^{m+1}\right)_{\Gamma^m}^h + \left(\hat{\boldsymbol{G}}_k(\theta^m)\partial_s \boldsymbol{X}^{m+1}, \partial_s(\boldsymbol{X}^{m+1} - \boldsymbol{X}^m)\right)_{\Gamma^m}^h \\ &\quad + \frac{1}{\eta}\left[\frac{(x_l^{m+1} - x_l^m)^2}{\tau} + \frac{(x_r^{m+1} - x_r^m)^2}{\tau}\right] - \sigma\left[(x_r^{m+1} - x_r^m) - (x_l^{m+1} - x_l^m)\right] = 0.\end{aligned} \tag{4.17}$$

When $\hat{\gamma}(\theta)$ satisfies (2.56), Lemma 2.2 also applies to open polygonal curves. Following the derivation of (2.77), we obtain

$$\left(\hat{\boldsymbol{G}}_k(\theta^m)\partial_s \boldsymbol{X}^{m+1}, \partial_s(\boldsymbol{X}^{m+1} - \boldsymbol{X}^m)\right)_{\Gamma^m}^h \ge \sum_{j=1}^N |\boldsymbol{h}_j^{m+1}|\hat{\gamma}(\theta_j^{m+1}) - \sum_{j=1}^N |\boldsymbol{h}_j^m|\hat{\gamma}(\theta_j^m). \tag{4.18}$$

Therefore, using (4.17) and (4.18), we have

$$
\begin{aligned}
W_o^{m+1} - W_o^m &= \sum_{j=1}^{N} |\boldsymbol{h}_j^{m+1}| \hat{\gamma}(\theta_j^{m+1}) - \sum_{j=1}^{N} |\boldsymbol{h}_j^m| \hat{\gamma}(\theta_j^m) \\
&\quad - \sigma \left[ \left( x_r^{m+1} - x_r^m \right) - \left( x_l^{m+1} - x_l^m \right) \right] \\
&\le \left( \hat{\boldsymbol{G}}_k(\theta^m) \partial_s \boldsymbol{X}^{m+1}, \partial_s (\boldsymbol{X}^{m+1} - \boldsymbol{X}^m) \right)_{\Gamma^m}^h \\
&\quad - \sigma \left[ \left( x_r^{m+1} - x_r^m \right) - \left( x_l^{m+1} - x_l^m \right) \right] \\
&\le -\tau \left( \partial_s \mu^{m+1}, \partial_s \mu^{m+1} \right)_{\Gamma^m}^h \\
&\quad - \frac{1}{\eta} \left[ \frac{(x_l^{m+1} - x_l^m)^2}{\tau} + \frac{(x_r^{m+1} - x_r^m)^2}{\tau} \right] \\
&\le 0, \qquad \forall m \ge 0,
\end{aligned}
\tag{4.19}
$$

This proves the energy dissipation stated in (4.16). □

Remark 4.1. Since the local energy estimate (2.63) depends only on $\hat{\gamma}(\theta)$, the energy dissipation results for the closed curve scheme (2.52) extend to the open curve scheme (4.14) for solid-state dewetting, including the conclusions in Remarks 2.7–2.9.

Remark 4.2. The local energy estimate implies energy dissipation for the discrete scheme. Replacing $\hat{\boldsymbol{G}}_k(\theta)$ by the symmetric surface energy matrix $\hat{\boldsymbol{Z}}_k(\theta)$ from Chapter 3 therefore relaxes the energy stability condition to $3\hat{\gamma}(\theta) \ge \hat{\gamma}(\theta - \pi)$ without additional requirements.

**4.2.4. Convergence rates and structure preservation.** In this subsection, we present numerical results for the evolution of open curves in solid-state dewetting using (4.14).

We mainly consider the following two anisotropic surface energies:

- Case I: $\hat{\gamma}(\theta) = 1 + \beta \cos 3\theta$, where $|\beta| < 1$. This energy is weakly anisotropic when $|\beta| < \frac{1}{8}$ and strongly anisotropic otherwise.
- Case II: $\hat{\gamma}(\theta) = \sqrt{1 + b \cos^2 \theta}$, where $b > -1$.

To examine mesh quality, area conservation, and energy stability, we introduce the weighted mesh ratio

$$
R_\gamma^h(t) := \frac{\max\limits_{1 \le j \le N} \hat{\gamma}(\theta_j) |\boldsymbol{h}_j|}{\min\limits_{1 \le j \le N} \hat{\gamma}(\theta_j) |\boldsymbol{h}_j|},
\tag{4.20}
$$

and the normalized area loss and energy

$$
\left. \frac{\Delta A_o^h(t)}{A_o^h(0)} \right|_{t=t_m} := \frac{A_o^m - A_o^0}{A_o^0}, \qquad \left. \frac{W_o^h(t)}{W_o^h(0)} \right|_{t=t_m} := \frac{W_o^m}{W_o^0}.
\tag{4.21}
$$

The scheme (4.14) is formally second-order accurate in space and first-order accurate in time; we therefore use $\tau = 16h^2$. The Newton iteration tolerance is tol $= 10^{-12}$. Unless otherwise stated, the initial shape is a half-ellipse with major axis 4 and minor axis 1. We approximate the exact solution $\Gamma(t)$ using (4.14) with $k(\theta) = k_0(\theta)$, the fine mesh $h_e = 2^{-8}$, and the small time step $\tau_e = 2^{-12}$. The contact line mobility is $\eta = 100$ throughout.

Figure 4.7 shows the numerical errors of (4.14) for (a) the three-fold symmetric anisotropy $\hat{\gamma}(\theta) = 1 + \beta \cos 3\theta$ with different strengths $\beta$ at the fixed time $t = 0.5$, and (b) the ellipsoidal anisotropy $\hat{\gamma}(\theta) = \sqrt{1 + 2\cos^2 \theta}$ at different times. The results confirm second-order convergence of (4.14).

As shown in Figure 4.8, the weighted mesh ratio $R_\gamma^h$ approaches a constant as $t \to +\infty$, indicating an asymptotically quasi-uniform mesh distribution for (4.14).

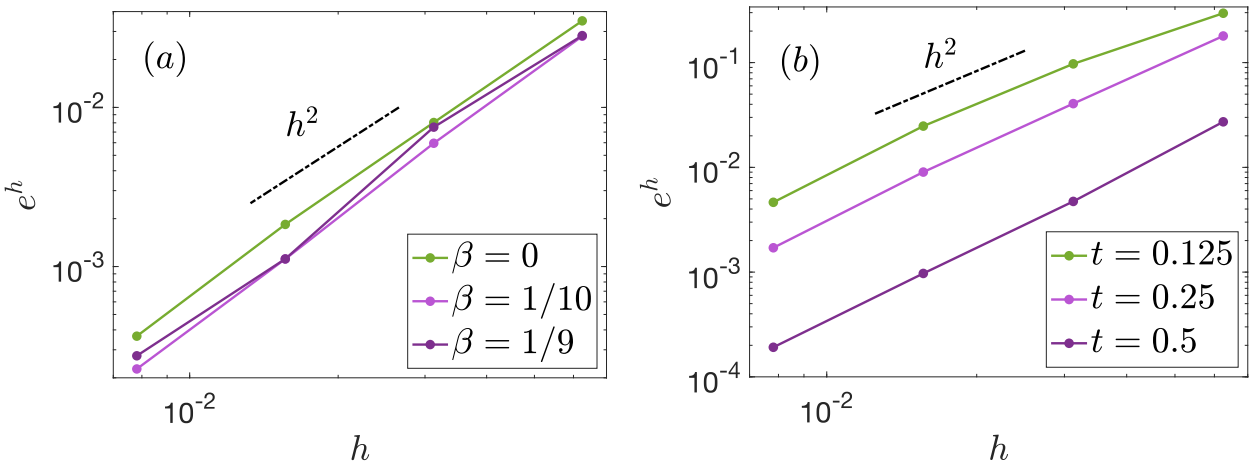



**Figure 4.7.** Convergence rates of the SPFEM (4.14) with $k(\theta) = k_0(\theta)$ and $\sigma = -\frac{\sqrt{2}}{2}$ for (a) anisotropy in Case I at $t = 0.5$ with different $\beta$; (b) anisotropy in Case II with $b = 2$ at different times $t = 0.125, 0.25, 0.5$.

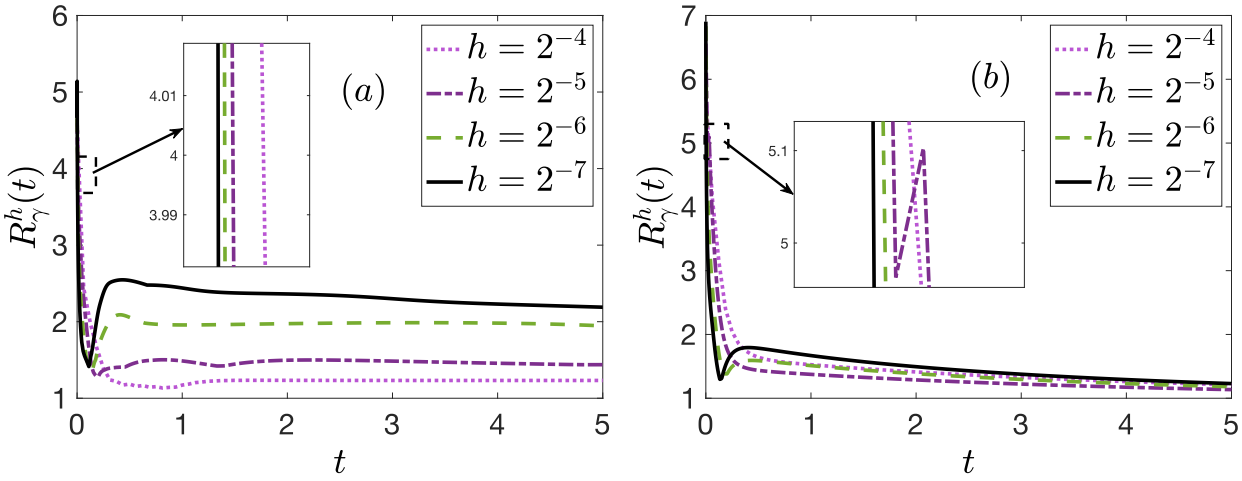



**Figure 4.8.** Weighted mesh ratio of the SPFEM (4.14) with $k(\theta) = k_0(\theta)$ and $\sigma = -\frac{\sqrt{2}}{2}$ for (a) anisotropy in Case I with $\beta = \frac{1}{9}$; (b) anisotropy in Case II with $b = 2$.

Figure 4.9 shows the time evolution of the normalized area loss $\frac{\Delta A_o^h(t)}{A_o^h(0)}$ and the number of Newton iterations with $h = 2^{-7}, \tau = 2^{-10}$. The normalized energy $\frac{W_o^h(t)}{W_o^h(t)}$ for different mesh sizes $h$ is shown in Figure 4.10.

Figures 4.9–4.10 show that:

(1) The normalized area loss is approximately $10^{-16}$, on the order of round-off error; see Figure 4.9. This verifies that area is conserved to machine precision.
(2) The number of Newton iterations starts at 3 and eventually decreases to 2; see Figure 4.9. Thus the semi-implicit scheme (4.14) can be solved efficiently.
(3) When $\hat{\gamma}(\theta)$ satisfies (2.56), the normalized energy is monotonically decreasing; see Figure 4.10. Unlike the *energy-stable parametric finite element method* in [108], the scheme (4.14) remains energy stable for Case I with $\beta < \frac{1}{10}$ and Case II with $b > 1$, consistent with Remarks 2.7 and 2.8.

**4.2.5. Morphological evolution in two-dimensional solid-state dewetting.** We now apply (4.14) to simulate the morphological evolution in two-dimensional anisotropic solid-state dewetting.

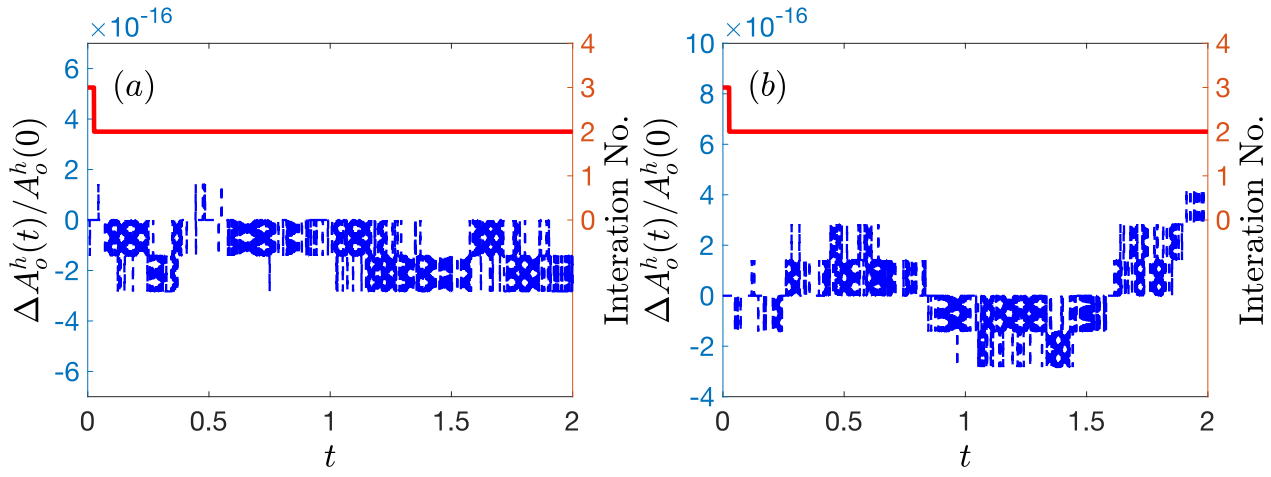



**Figure 4.9.** Normalized area loss (blue dashed line) and number of Newton iterations (red line) of the SPFEM (4.14) with $k(\theta) = k_0(\theta)$, $\sigma = -\frac{\sqrt{2}}{2}$ and $h = 2^{-7}, \tau = 2^{-10}$ for (a) anisotropy in Case I with $\beta = \frac{1}{9}$; (b) anisotropy in Case II with $b = 2$.

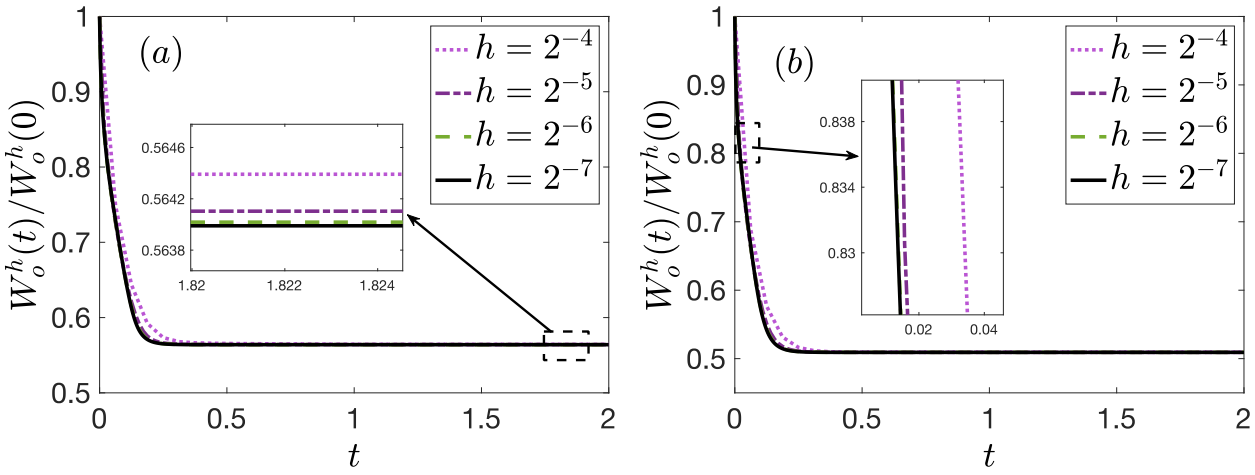



**Figure 4.10.** Normalized energy of the SPFEM (4.14) with $k(\theta) = k_0(\theta)$ and $\sigma = -\frac{\sqrt{2}}{2}$ for (a) anisotropy in Case I with $\beta = \frac{1}{9}$; (b) anisotropy in Case II with $b = 2$.

Figure 4.11 shows the evolution from the initial shape to the numerical equilibrium for an open $4 \times 1$ rectangular curve with four surface energies: (a) Case I with $\beta = \frac{1}{9}$; (b) Case II with $b = 2$; (c) four-fold symmetric anisotropy $\hat{\gamma}(\theta) = 1 + \frac{1}{16}\cos 4\theta$; and (d) $\hat{\gamma}(\theta) = \sqrt{\left(\frac{5}{2} + \frac{3}{2}\mathrm{sgn}(n_1)\right) n_1^2 + n_2^2}$, where $\boldsymbol{n} = (n_1, n_2)^T = (-\sin\theta, \cos\theta)^T$.

As in the closed curve case, the scheme (4.14) extends the range of surface energies available for solid-state dewetting simulations; see Figure 4.11(a)–Figure 4.11(c). Figure 4.11(d) also shows that the method applies to $\hat{\gamma}(\theta)$ with limited regularity.

**4.2.6. Multiple equilibria of open curves in solid-state dewetting.** Following the derivations in [108, 103, 149] and Section 4.2.3, the symmetrized scheme (3.12) also extends to the evolution of open curves in solid-state dewetting. Its discrete formulation is analogous to (4.14), and we omit the details. As in Theorem 3.2, the method preserves area conservation and is unconditionally energy stable under (3.1).

As described in [10], stable equilibrium shapes in two-dimensional solid-state dewetting with anisotropic surface energies can be predicted by the generalized Winterbottom construction. For strongly anisotropic surface energies, multiple stable island shapes may exist.

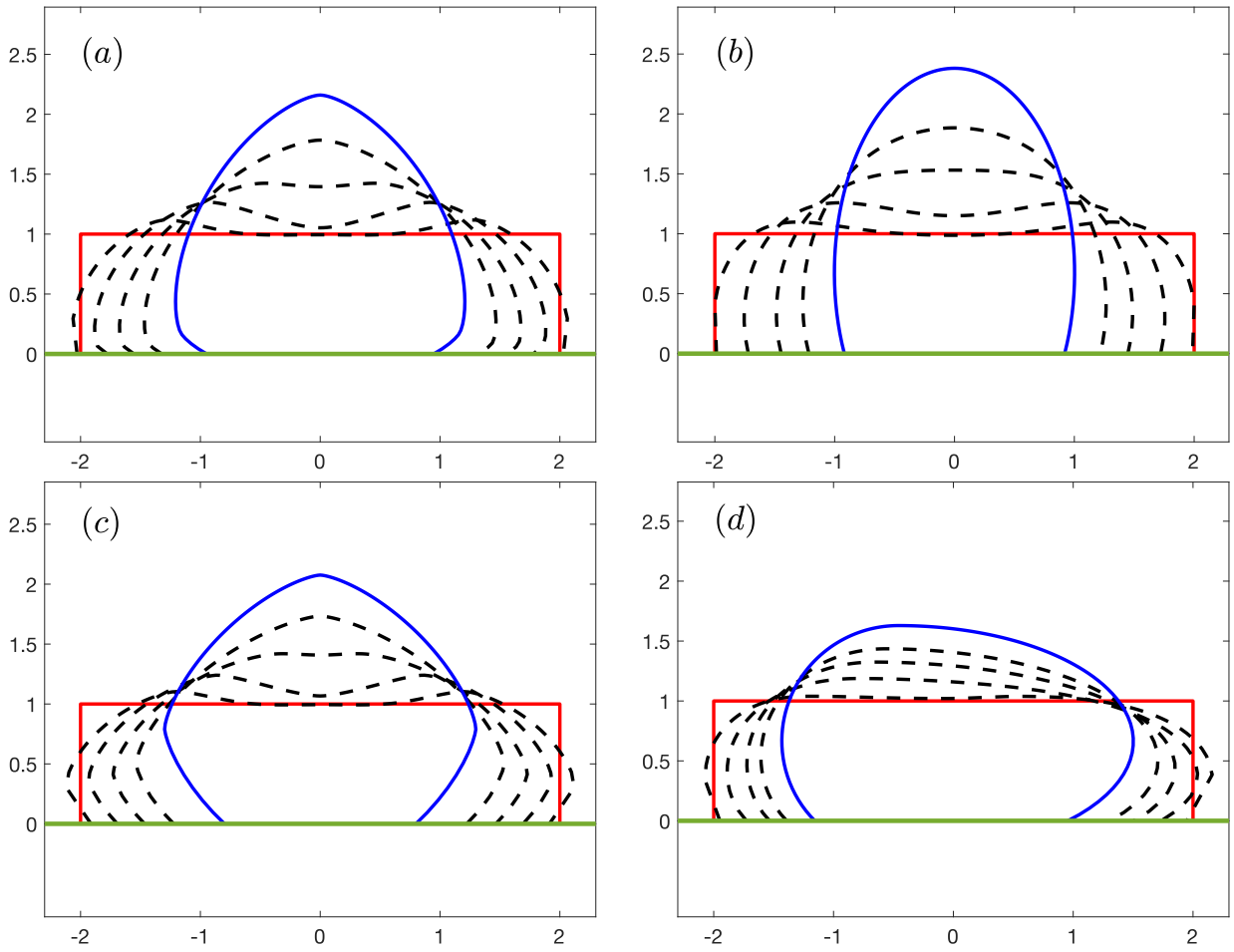



**Figure 4.11.** Morphological evolution of an open $4 \times 1$ rectangle under anisotropic surface diffusion with different surface energies: (a) anisotropy in Case I with $\beta = \frac{1}{9}$; (b) anisotropy in Case II with $b = 2$; (c) $\hat{\gamma}(\theta) = 1 + \frac{1}{16}\cos 4\theta$; (d) $\hat{\gamma}(\theta) = \sqrt{\left(\frac{5}{2} + \frac{3}{2}\mathrm{sgn}(n_1)\right) n_1^2 + n_2^2}$ with $\boldsymbol{n} = (n_1, n_2)^T = (-\sin\theta, \cos\theta)^T$. The red and blue lines represent the initial shape and the numerical equilibrium, respectively. The black dashed lines represent the intermediate curves. The parameters are $\sigma = -\frac{\sqrt{2}}{2}$, $h = 2^{-7}$, $\tau = 2^{-10}$.

(i) *Construct the Wulff envelope.* For a given anisotropy $\hat{\gamma}(\theta)$, first plot its $\gamma$-plot, shown as the blue curve in Figure 4.12(a). Construct the Wulff envelope from the $\gamma$-plot using [119, 10], as shown by the black curve in Figure 4.12(a):

$$\begin{cases} x(\theta) = -\hat{\gamma}(\theta)\sin\theta - \hat{\gamma}'(\theta)\cos\theta, \\ y(\theta) = \hat{\gamma}(\theta)\cos\theta - \hat{\gamma}'(\theta)\sin\theta, \end{cases} \qquad \theta \in 2\pi\mathbb{T}. \tag{4.22}$$

(ii) *Remove unstable orientations.* Remove orientations satisfying $\hat{\gamma}(\theta) + \hat{\gamma}''(\theta) < 0$ from the Wulff envelope; see the black dashed segments in Figure 4.12(b). The "ears" of the Wulff envelope are unstable regions, as illustrated in Figure 4.12.

(iii) *Truncate the Wulff envelope.* Intersect the Wulff envelope with the flat substrate line $y = \sigma$, shown as the red dashed line in Figure 4.12(b)–Figure 4.12(f). The regions enclosed by the remaining Wulff envelope and the substrate are stable equilibrium shapes; see the green shaded regions in Figure 4.12(c)–Figure 4.12(e) and the blue shaded region in Figure 4.12(f).

We apply the proposed method to simulate equilibrium shapes obtained from different initial films in solid-state dewetting, using the $m$-fold symmetric anisotropy $\hat{\gamma}(\theta) = 1 + \beta\cos m(\theta - \theta_0)$. It is strongly anisotropic when $|\beta| > \frac{1}{m^2-1}$. The results are shown in Figures 4.13–4.17.

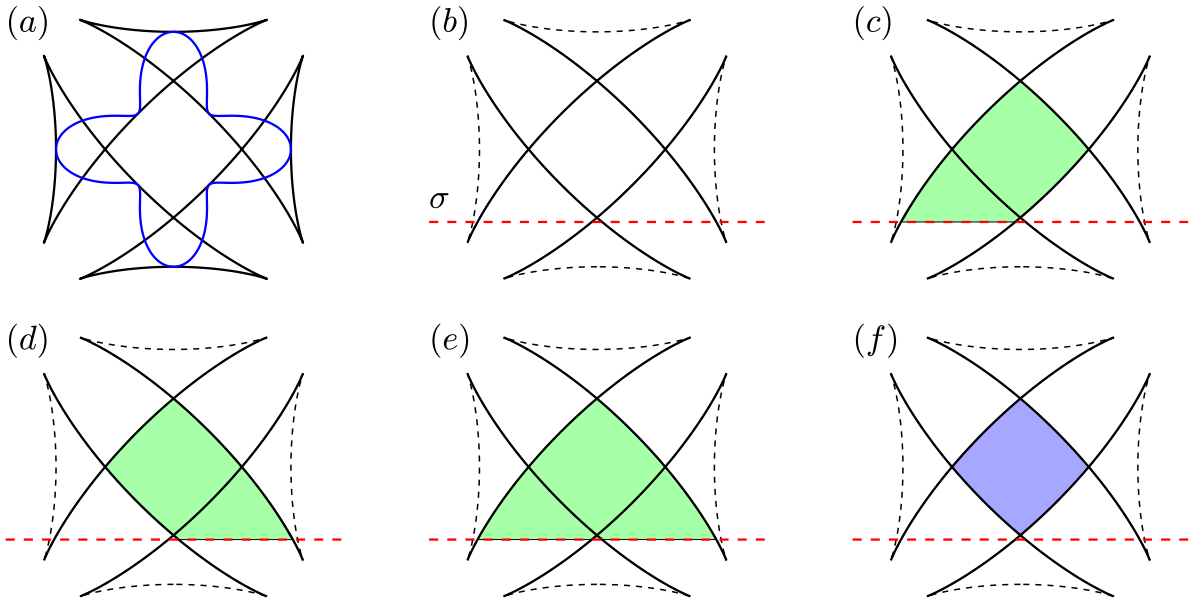



**Figure 4.12.** Generalized Winterbottom construction for surface energy $\hat{\gamma}(\theta) = 1 + 0.4\cos 4\theta$ and $\sigma = \cos\frac{5\pi}{6}$. The green and blue shaded regions are stable equilibrium shapes.

In Figure 4.13, the parameters are $\beta = 0.4$, $\theta_0 = 0$ and $\sigma = \cos\frac{5\pi}{6}$. The simulations produce four possible stable equilibria. The numerical shapes in Figure 4.13 agree closely with the generalized Winterbottom construction in Figure 4.12, also shown by the black dashed curves in Figure 4.13.

Figures 4.14 and 4.16 compare the numerical equilibria for two anisotropies with the stable shapes predicted by the generalized Winterbottom construction. Numerical equilibria are shown as blue solid curves, initial curves as red solid curves, and the corresponding Wulff envelopes as black dashed curves. The numerical and theoretical shapes agree closely. Unlike the *symmetrized structure-preserving parametric finite element method* in [103], the proposed method applies stably to both symmetric and asymmetric surface energies.

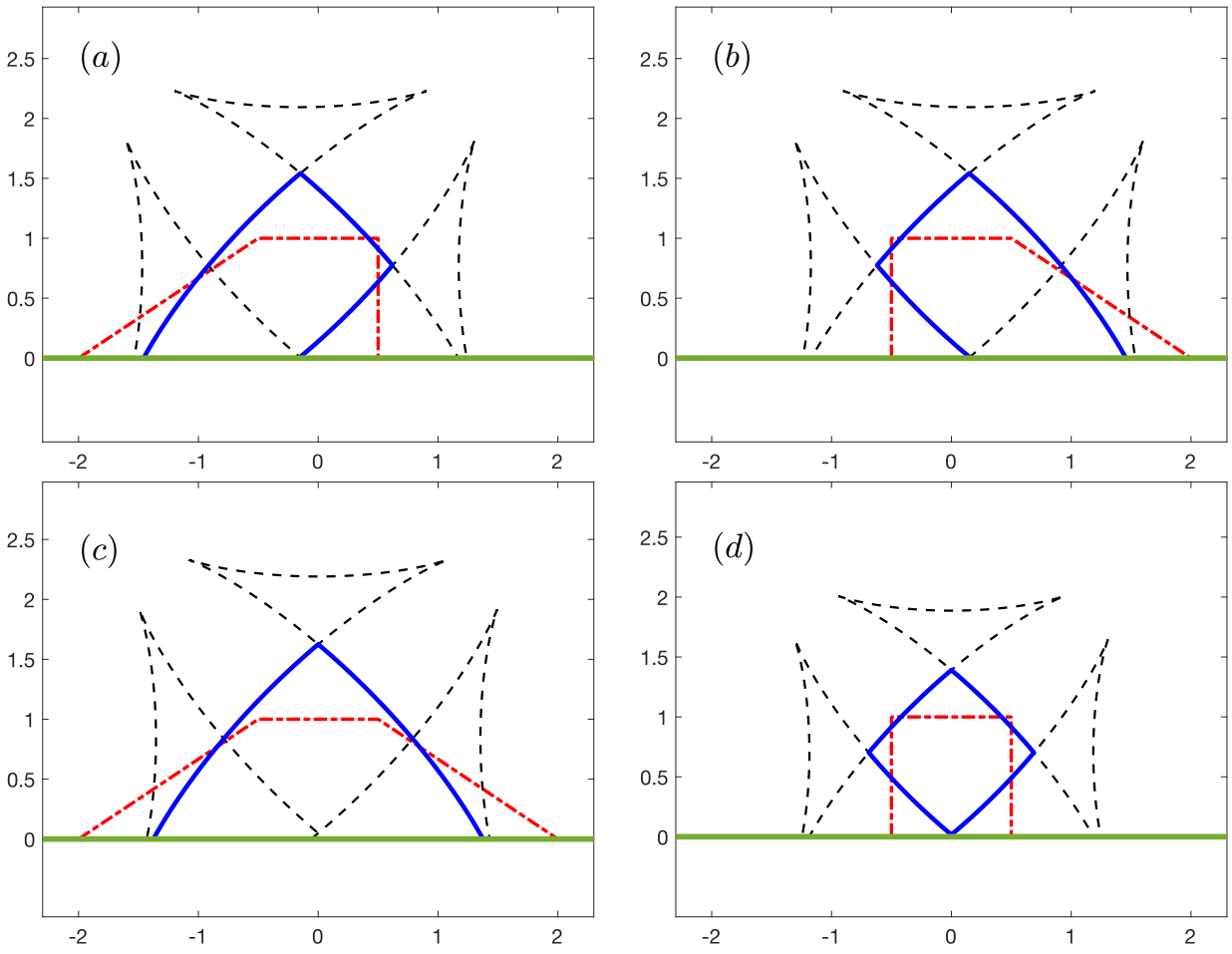



**Figure 4.13.** Multiple equilibrium shapes for the 4-fold surface energy $\hat{\gamma}(\theta) = 1 + \beta \cos 4\theta$ starting with different initial curves (shown in red dash-dotted line). The corresponding Wulff envelope is shown as a black dashed curve. The parameters are $\beta = 0.4$, $\sigma = \cos \frac{5\pi}{6}$ and $\eta = 100$.

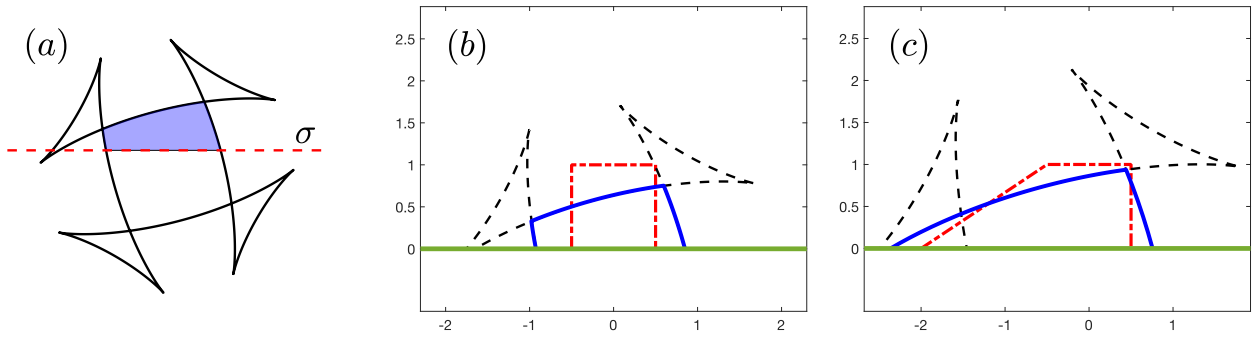



**Figure 4.14.** Illustration of the generalized Winterbottom construction (a) and numerical equilibrium shapes (b)–(c) starting with different initial curves for the 4-fold surface energy $\hat{\gamma}(\theta) = 1 + 0.3 \cos 4(\theta + \frac{\pi}{6})$ and $\sigma = 0.2$.

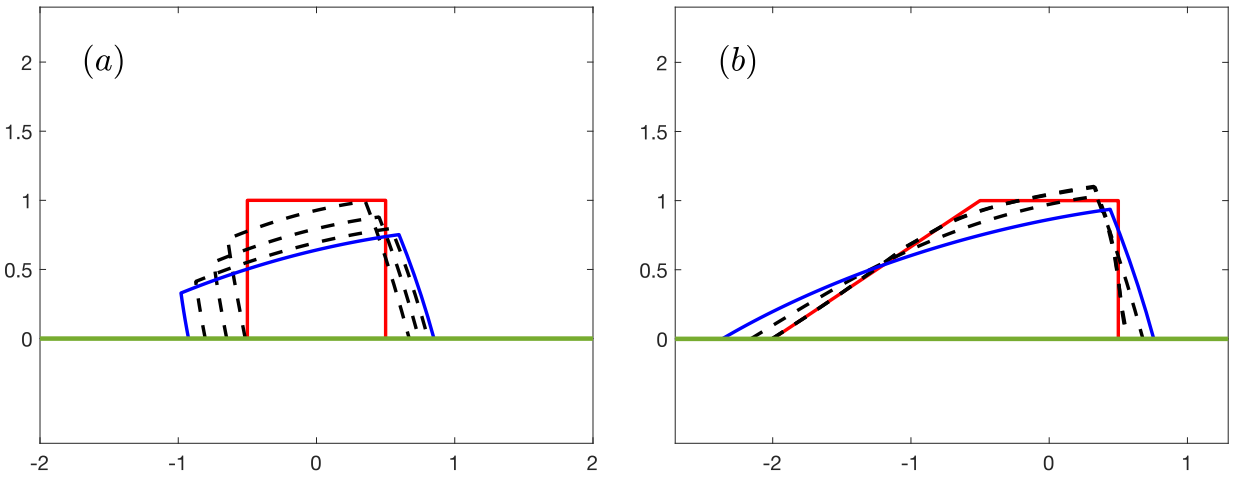



**Figure 4.15.** Morphological evolution of different initial shapes with the 4-fold anisotropy $\hat{\gamma}(\theta) = 1 + 0.3\cos 4\left(\theta + \frac{\pi}{6}\right)$, $\sigma = 0.2$: (a) a unit square; (b) a right trapezoid. The red and blue lines represent the initial shape and the numerical equilibrium, respectively. The black dashed lines represent the intermediate curves.

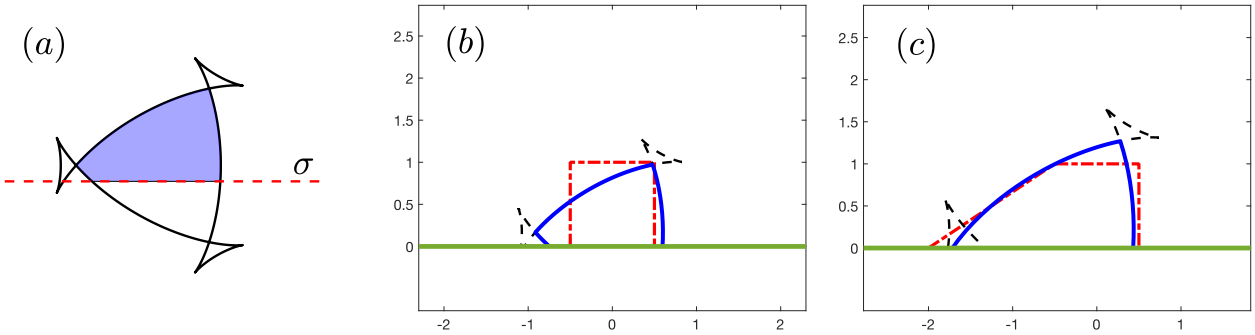



**Figure 4.16.** Illustration of the generalized Winterbottom construction (a) and numerical equilibrium shapes (b)–(c) starting with different initial curves for the 3-fold surface energy $\hat{\gamma}(\theta) = 1 + 0.3\cos 3(\theta + \frac{\pi}{6})$ and $\sigma = -0.2$.

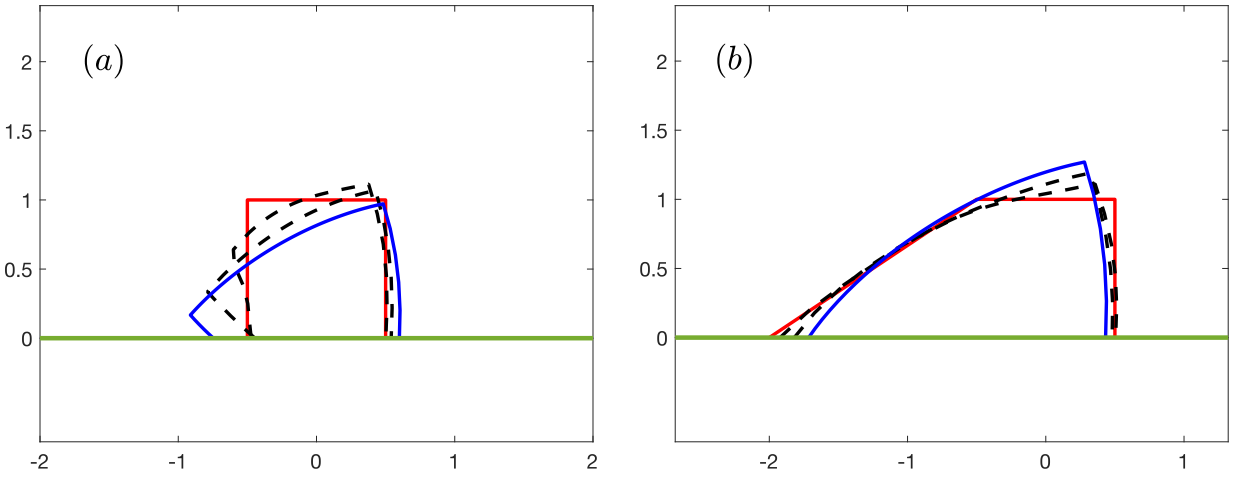



**Figure 4.17.** Morphological evolution of different initial shapes with the 3-fold anisotropy $\hat{\gamma}(\theta) = 1 + 0.3\cos 3\left(\theta + \frac{\pi}{6}\right)$, $\sigma = -0.2$: (a) a unit square; (b) a right trapezoid. The red and blue lines represent the initial shape and the numerical equilibrium, respectively. The black dashed lines represent the intermediate curves.

CHAPTER 5

# Structure-preserving parametric approximation via an $\alpha$-surface energy matrix: anisotropic curve evolution

The *energy-stable parametric finite element method* developed by Barrett, Garcke, and Nürnberg [22, 25], commonly called the BGN method, has attracted considerable attention in structure-preserving numerical methods for geometric flows because of its unconditional energy stability and favorable mesh quality. It has been successfully applied to many isotropic curvature-driven problems, including mean curvature flow [25, 102], surface diffusion [21], multiphase flow [67, 69], the Stefan problem [63], the *Mullins–Sekerka problem* [27], and the evolution of open curves and surfaces in solid-state dewetting [151, 20]. These applications demonstrate the robustness and efficiency of the method.

A key feature of BGN methods is that they approximate the curvature vector $\kappa\boldsymbol{n}$ through the geometric identity

$$\kappa\boldsymbol{n} = -\partial_{ss}\boldsymbol{X} = -\partial_s\Big(\boldsymbol{I}_d\partial_s\boldsymbol{X}\Big), \tag{5.1}$$

where $\boldsymbol{I}_d$ denotes the $d$-dimensional identity matrix, instead of directly approximating the curvature $\kappa$. This approach provides a natural framework consistent with the geometric structure for establishing energy stability in isotropic curvature-driven problems. For a detailed account of the theory and numerical behavior of BGN methods, see the survey monograph by Barrett et al. [29].

Many studies have extended BGN methods to anisotropic problems. Their common feature is to replace $\boldsymbol{I}_d$ in (5.1) with a suitably constructed surface energy matrix, yielding an analogous identity for the weighted curvature vector $\mu\boldsymbol{n}$. Barrett et al. first developed such an extension for surface energies of the Riemannian metric form $\hat{\gamma}(\theta) = (\boldsymbol{n}(\theta)\cdot G\boldsymbol{n}(\theta))^{1/2}$, by introducing the matrix $\frac{1}{\hat{\gamma}(\theta)}\det(G)\,G^{-1}$ [24, 28]. In [108], a surface energy matrix $\hat{\boldsymbol{G}}(\theta) = \hat{\gamma}(\theta)I_2 - \boldsymbol{n}(\theta)\boldsymbol{\xi}(\theta)^T + \boldsymbol{\xi}(\theta)\boldsymbol{n}(\theta)^T$ was constructed using the Cahn–Hoffman $\boldsymbol{\xi}$-vector. This gave the first extension of the framework to general surface energies, although some restrictions on $\hat{\gamma}(\theta)$ remained necessary. Subsequently, a stabilizing function $k(\theta)$ was introduced in [9] to construct the symmetric surface energy matrix $\hat{\boldsymbol{Z}}_k(\theta) = \hat{\gamma}(\theta)I_2 - \boldsymbol{n}\boldsymbol{\xi}^T - \boldsymbol{\xi}\boldsymbol{n}^T + k(\theta)\boldsymbol{n}\boldsymbol{n}^T$. The resulting scheme was proved to be unconditionally energy stable under the symmetry condition $\hat{\gamma}(\theta) = \hat{\gamma}(\theta-\pi)$.

In Chapters 2–3, refined analysis substantially improved the energy stability conditions for the proposed methods and yielded optimal results within the local energy estimate framework. The analytical techniques differed somewhat between schemes. These studies show that different surface energy matrices require different analytical tools and lead to substantially different energy stability conditions, motivating further refinement and a unified treatment.

The main objective of this chapter is to establish a unified framework for analyzing the energy stability of *structure-preserving parametric finite element schemes* associated with the constant-$\alpha$ family of surface energy matrices introduced below. Within the local energy estimate framework, we derive optimal energy stability conditions and systematically compare the computational performance of the resulting schemes. The main contributions are as follows.

- **A unified construction of the surface energy matrix.** We introduce a hyperparameter $\alpha\in\mathbb{R}$ and construct the unified $\alpha$-surface energy matrix

$$\hat{\boldsymbol{G}}_k^{\alpha}(\theta) \coloneqq \hat{\gamma}(\theta)I_2 - \boldsymbol{n}\boldsymbol{\xi}^T + \alpha\boldsymbol{\xi}\boldsymbol{n}^T + k(\theta)\boldsymbol{n}\boldsymbol{n}^T, \tag{5.2}$$

  This construction includes all existing forms [14, 149, 9, 107] and those in Chapters 3–2 as special cases. It characterizes the normal-column modifications with the prescribed tangential component and constant $\alpha$; see Remark 5.3.

- **Optimal energy stability conditions within the local energy estimate framework.** We prove that the symmetric case $\alpha = -1$ is the unique member of this family that achieves unconditional energy stability under the following necessary and sufficient condition for the local energy estimate (see Remark 5.5):

$$3\hat{\gamma}(\theta) - \hat{\gamma}(\theta - \pi) \geq 0, \qquad \forall \theta \in 2\pi\mathbb{T}. \tag{5.3}$$

  For other values of $\alpha$, the stricter condition $3\hat{\gamma}(\theta) - \hat{\gamma}(\theta - \pi) > 0$ is required unless additional constraints, such as $\hat{\gamma}'(\theta^*) = 0$, are imposed.
- **A unified framework for discretizing velocity laws.** We extend the *structure-preserving parametric finite element method* to general anisotropic curvature-driven problems with normal velocities of the form

$$V_n = \mathfrak{F}(\mu), \tag{5.4}$$

  where $\mathfrak{F}$ is a mapping that depends on the weighted curvature $\mu$. This formulation naturally encompasses all velocity laws in (1.13) and provides a unified discretization framework that ensures energy stability.

The chapter is organized as follows. Section 5.1 introduces the hyperparameter $\alpha$ to construct a unified representation of this family of surface energy matrices and derives a conservative variational formulation for anisotropic curvature flow. Section 5.2 presents the corresponding fully discrete structure-preserving parametric finite element scheme and states its structure-preserving properties. Section 5.3 proves energy stability. Section 5.5 discusses extensions to other anisotropic curvature-driven problems. Section 5.6 reports extensive numerical experiments that assess accuracy, efficiency, structure preservation, and robustness.

### 5.1. A unified $\alpha$-surface energy matrix

To study general anisotropic curvature-driven problems, we first turn from the *anisotropic surface diffusion* considered in the preceding chapters to the simpler *anisotropic curvature flow*:

$$V_n = -\mu, \tag{5.5}$$

where $\mu = [\hat{\gamma}(\theta) + \hat{\gamma}''(\theta)]\,\kappa$ is the weighted curvature. Equivalently,

$$\partial_t \boldsymbol{X} = -\mu \boldsymbol{n}, \qquad 0 < s < L(t), \qquad 0 \leq t \leq T, \tag{5.6a}$$

$$\mu = [\hat{\gamma}(\theta) + \hat{\gamma}''(\theta)]\,\kappa. \tag{5.6b}$$

Here $L(t) = |\Gamma(t)|$ is the length of the curve $\Gamma(t)$ at time $t$, and $T$ is the maximal existence time of the solution.

During curve evolution, tangential velocity affects only the parametrization and leaves the geometry of the curve unchanged. Its geometric evolution is therefore determined by the normal velocity $V_n = \boldsymbol{n} \cdot \partial_t \boldsymbol{X}$. Allowing suitable tangential motion, we can rewrite the anisotropic curvature flow (5.6) equivalently as the geometric PDE

$$\boldsymbol{n} \cdot \partial_t \boldsymbol{X} = -\mu, \qquad 0 < s < L(t) \qquad 0 \leq t \leq T, \tag{5.7a}$$

$$\mu = [\hat{\gamma}(\theta) + \hat{\gamma}''(\theta)]\,\kappa. \tag{5.7b}$$

as we did for surface diffusion in Chapters 2–3.

To derive a conservative formulation of the anisotropic curvature flow (5.7), we introduce the unified $\alpha$-surface energy matrix

$$\hat{\boldsymbol{G}}_k^{\alpha}(\theta) := \hat{\gamma}(\theta) I_2 - \boldsymbol{n}(\theta)\boldsymbol{\xi}(\theta)^T + \alpha \boldsymbol{\xi}(\theta)\boldsymbol{n}(\theta)^T + k(\theta)\boldsymbol{n}(\theta)\boldsymbol{n}(\theta)^T, \tag{5.8}$$

where $\boldsymbol{\xi}(\theta) = \hat{\gamma}(\theta)\boldsymbol{n}(\theta) - \hat{\gamma}'(\theta)\boldsymbol{\tau}(\theta)$ is the *Cahn–Hoffman $\boldsymbol{\xi}$-vector*, $\alpha \in \mathbb{R}$, and $k\colon 2\pi\mathbb{T} \to \mathbb{R}$ is a prescribed stabilizing function.

Lemma 5.1. *The weighted curvature $\mu$ defined in* (5.7b) *satisfies the geometric identity*

$$\mu \boldsymbol{n} + \partial_s \left( \hat{\boldsymbol{G}}_k^{\alpha}(\theta) \partial_s \boldsymbol{X} \right) = \boldsymbol{0}, \qquad \forall \alpha \in \mathbb{R}. \tag{5.9}$$

Proof. By [93] or (3.4),

$$\mu \boldsymbol{n} = -\partial_s \Big( \hat{\gamma}(\theta) \partial_s \boldsymbol{X} + \hat{\gamma}'(\theta) \boldsymbol{n} \Big). \tag{5.10}$$

It therefore suffices to prove that

$$\hat{\boldsymbol{G}}_k^\alpha(\theta) \partial_s \boldsymbol{X} = \hat{\gamma}(\theta) \partial_s \boldsymbol{X} + \hat{\gamma}'(\theta) \boldsymbol{n}. \tag{5.11}$$

Since $\boldsymbol{n} = (-\sin\theta, \cos\theta)^T$, $\boldsymbol{\tau} = (\cos\theta, \sin\theta)^T$, we have

$$\hat{\boldsymbol{G}}_k^\alpha(\theta) = \hat{\gamma}(\theta) I_2 + \hat{\gamma}'(\theta)(\boldsymbol{n}\boldsymbol{\tau}^T - \alpha \boldsymbol{\tau}\boldsymbol{n}^T) + (k(\theta) + (\alpha - 1)\hat{\gamma}(\theta))\, \boldsymbol{n}\boldsymbol{n}^T. \tag{5.12}$$

Combining (5.12) with $\partial_s \boldsymbol{X} = \boldsymbol{\tau}$ and $\boldsymbol{n}^T \partial_s \boldsymbol{X} \equiv 0$ gives

$$\begin{aligned} \hat{\boldsymbol{G}}_k^\alpha(\theta) \partial_s \boldsymbol{X} &= \hat{\gamma}(\theta) \partial_s \boldsymbol{X} + \hat{\gamma}'(\theta) \boldsymbol{n} + \left( -\alpha \hat{\gamma}'(\theta) \boldsymbol{\tau}\boldsymbol{n}^T + (k(\theta) + (\alpha - 1)\hat{\gamma}(\theta))\, \boldsymbol{n}\boldsymbol{n}^T \right) \partial_s \boldsymbol{X} \\ &= \hat{\gamma}(\theta) \partial_s \boldsymbol{X} + \hat{\gamma}'(\theta) \boldsymbol{n}. \end{aligned} \tag{5.13}$$

This proves the lemma. □

Using (5.9), we obtain the following strong formulation of the geometric PDE (5.7a)–(5.7b):

$$\boldsymbol{n} \cdot \partial_t \boldsymbol{X} + \mu = 0, \qquad 0 < s < L(t), \qquad \forall 0 \le t \le T, \tag{5.14a}$$

$$\mu \boldsymbol{n} + \partial_s \Big( \hat{\boldsymbol{G}}_k^\alpha(\theta) \partial_s \boldsymbol{X} \Big) = \boldsymbol{0}, \tag{5.14b}$$

where $L(t)$ is the length of the evolving curve $\Gamma(t)$.

Remark 5.1. When $\hat{\gamma}(\theta) \equiv 1$, the weighted curvature $\mu$ reduces to the usual curvature $\kappa$. Taking $k(\theta) \equiv 1 - \alpha$ then gives $\hat{\boldsymbol{G}}_k^\alpha(\theta) \equiv I_2$. Thus (5.14) reduces to the standard BGN formulation of mean curvature flow [22].

Remark 5.2. Different values of $\alpha$ yield different representations of the weighted curvature vector $\mu\boldsymbol{n}$ in (5.14). For $\alpha = -1$, we recover the symmetrized formulations in [9, 107] and Chapter 3. The choice $\alpha = 0, k(\theta) \equiv 0$ gives the formulation proposed in [23]. For $\alpha = 1$, we recover the formulations in [108, 13, 149] and Chapter 2.

Remark 5.3. The family (5.8) includes the cited symmetric and nonsymmetric surface energy matrices as particular choices of the constant parameter $\alpha$ and the function $k$. Its algebraic scope can be stated precisely in terms of its action on the orthonormal basis $(\boldsymbol{\tau}, \boldsymbol{n})$. Fix $\alpha \in \mathbb{R}$ and require a matrix $\hat{\boldsymbol{G}}(\theta)$ to satisfy $\hat{\boldsymbol{G}}(\theta)\boldsymbol{\tau} = \hat{\gamma}(\theta)\boldsymbol{\tau} + \hat{\gamma}'(\theta)\boldsymbol{n}$ and $\boldsymbol{\tau}^T \hat{\boldsymbol{G}}(\theta)\boldsymbol{n} = -\alpha\hat{\gamma}'(\theta)$. Then $\hat{\boldsymbol{G}}(\theta) = \hat{\boldsymbol{G}}_k^\alpha(\theta)$ for a scalar function $k(\theta)$.

Indeed, $K(\boldsymbol{\tau}) := \{\boldsymbol{A} \in \mathbb{R}^{2\times 2} \mid \boldsymbol{A}\boldsymbol{\tau} = \boldsymbol{0}\} = \{\boldsymbol{b}\boldsymbol{n}^T \mid \boldsymbol{b} \in \mathbb{R}^2\}$ has dimension 2. The prescribed tangential action gives $\hat{\boldsymbol{G}} - \hat{\boldsymbol{G}}_0^0 = \boldsymbol{b}\boldsymbol{n}^T \in K(\boldsymbol{\tau})$. Since $\hat{\boldsymbol{G}}_0^0 \boldsymbol{n} = \boldsymbol{0}$, the second prescribed action gives $\boldsymbol{\tau} \cdot \boldsymbol{b} = -\alpha\hat{\gamma}'(\theta)$. Using $\boldsymbol{\xi} = \hat{\gamma}\boldsymbol{n} - \hat{\gamma}'\boldsymbol{\tau}$, we obtain $\boldsymbol{b} = \alpha\boldsymbol{\xi} + k\boldsymbol{n}$ with $k = \boldsymbol{n} \cdot \boldsymbol{b} - \alpha\hat{\gamma}$. Hence $\hat{\boldsymbol{G}} = \hat{\boldsymbol{G}}_0^0 + \alpha\boldsymbol{\xi}\boldsymbol{n}^T + k\boldsymbol{n}\boldsymbol{n}^T$, as claimed. This argument remains valid when $\hat{\gamma}'(\theta) = 0$. The characterization concerns the constant-$\alpha$ family with the two explicitly prescribed matrix actions.

### 5.2. Structure-preserving parametric finite element discretization via the $\alpha$-surface energy matrix

**5.2.1. Weak formulation.** To derive the weak formulation from (5.14), we parametrize the evolving curve $\Gamma(t)$ by a time-independent parameter $\rho$ on the fixed domain $\mathbb{I} := [0, 1]$:

$$\Gamma(t) \colon \boldsymbol{X}(\rho, t) = (x(\rho, t), y(\rho, t))^T, \qquad \forall \rho \in \mathbb{I},\ t \in [0, T]. \tag{5.15}$$

The arc length is then given by $s(\rho, t) = \int_0^\rho |\partial_r \boldsymbol{X}(r, t)|\, \mathrm{d}r$ We do not distinguish between $\boldsymbol{X}(s, t)$ and $\boldsymbol{X}(\rho, t)$, and assume that the $\rho$-parametrization remains regular: there exists a constant $C > 1$ such that $\frac{1}{C} \le |\partial_r s(\rho, t)| \le C,\ \forall \rho \in \mathbb{I}$.

For the evolving curve $\Gamma(t)$, define the $L^2$ space

$$L^2(\mathbb{I}) := \left\{ u \colon \mathbb{I} \to \mathbb{R} \mid \int_{\Gamma(t)} |u(s)|^2\, \mathrm{d}s = \int_{\mathbb{I}} |u(s(\rho, t))|^2 \partial_\rho s\, \mathrm{d}\rho < +\infty \right\}, \tag{5.16}$$

with the inner product

$$\Big(u, v\Big)_{\Gamma(t)} \coloneqq \int_{\Gamma(t)} u(s)v(s)\,\mathrm{d}s = \int_{\mathbb{I}} u(s(\rho,t))v(s(\rho,t))\partial_\rho s\,\mathrm{d}\rho, \qquad \forall u, v \in L^2(\mathbb{I}). \tag{5.17}$$

The corresponding Sobolev spaces are

$$H^1(\mathbb{I}) \coloneqq \left\{u \in L^2(\mathbb{I}) \mid \partial_\rho u \in L^2(\mathbb{I})\right\}, \qquad H^1_p(\mathbb{I}) \coloneqq \left\{u \in H^1(\mathbb{I}) \mid u(0) = u(1)\right\}. \tag{5.18a}$$

As in the derivations of (3.10) and (2.27), we multiply (5.14a) by a test function $\varphi \in H^1_p(\mathbb{I})$ and (5.14b) by $\boldsymbol{\omega} = (\omega_1, \omega_2)^T \in [H^1_p(\mathbb{I})]^2$, integrate over $\Gamma(t)$, and integrate by parts. The resulting weak formulation of (5.14) is as follows. Given the initial closed curve $\Gamma(0) \coloneqq \boldsymbol{X}(\cdot,0) = (x(\cdot,0), y(\cdot,0))^T \in [H^1_p(\mathbb{I})]^2$ and initial weighted curvature $\mu(\cdot,0) \coloneqq \mu_0(\cdot) \in H^1_p(\mathbb{I})$, find, for every $t > 0$, $\big(\boldsymbol{X}(\cdot,t), \mu(\cdot,t)\big) \in [H^1_p(\mathbb{I})]^2 \times H^1_p(\mathbb{I})$ such that

$$\Big(\boldsymbol{n}\cdot\partial_t\boldsymbol{X}, \varphi\Big)_{\Gamma(t)} + \Big(\mu, \varphi\Big)_{\Gamma(t)} = 0, \qquad \forall \varphi \in H^1_p(\mathbb{I}), \tag{5.19a}$$

$$\Big(\mu\boldsymbol{n}, \boldsymbol{\omega}\Big)_{\Gamma(t)} - \Big(\hat{\boldsymbol{G}}^\alpha_k(\theta)\partial_s\boldsymbol{X}, \partial_s\boldsymbol{\omega}\Big)_{\Gamma(t)} = 0, \qquad \forall \boldsymbol{\omega} \in [H^1_p(\mathbb{I})]^2. \tag{5.19b}$$

Let $A(t)$ be the total area enclosed by $\Gamma(t)$ and $W(t)$ its total energy, as defined in (2.28).

To derive the area decay rate and energy dissipation, we need an identity for the time derivative $\partial_t\theta$ of the inclination angle, together with the transport lemma (2.31).

Lemma 5.2. *The time derivative of the inclination angle $\theta$ satisfies*

$$\partial_t\theta = \partial_s(\partial_t\boldsymbol{X})\cdot\boldsymbol{n}. \tag{5.20}$$

Proof. Differentiating $|\partial_\rho\boldsymbol{X}| = \sqrt{(\partial_\rho x)^2 + (\partial_\rho y)^2}$ with respect to time gives

$$\partial_t|\partial_\rho\boldsymbol{X}| = \frac{\partial_\rho x\partial_t(\partial_\rho x) + \partial_\rho y\partial_t(\partial_\rho y)}{\sqrt{(\partial_\rho x)^2 + (\partial_\rho y)^2}} = \frac{\partial_\rho\boldsymbol{X}}{|\partial_\rho\boldsymbol{X}|}\cdot\frac{\partial_\rho(\partial_t\boldsymbol{X})}{|\partial_\rho\boldsymbol{X}|}|\partial_\rho\boldsymbol{X}| = \partial_s\boldsymbol{X}\cdot\partial_s(\partial_t\boldsymbol{X})|\partial_\rho\boldsymbol{X}|. \tag{5.21}$$

Therefore, by (5.21),

$$\begin{aligned}\partial_s(\partial_t\boldsymbol{X}) &= \frac{1}{|\partial_\rho\boldsymbol{X}|}\partial_\rho(\partial_t\boldsymbol{X}) = \frac{1}{|\partial_\rho\boldsymbol{X}|}\partial_t\left(|\partial_\rho\boldsymbol{X}|(\cos\theta, \sin\theta)^T\right)\\ &= \partial_s\boldsymbol{X}\cdot\partial_s(\partial_t\boldsymbol{X})(\cos\theta, \sin\theta)^T + (-\sin\theta, \cos\theta)^T\partial_t\theta.\end{aligned} \tag{5.22}$$

The result follows from $\boldsymbol{n} = (-\sin\theta, \cos\theta)^T$. □

Proposition 5.1 (Area decay rate and energy dissipation). *Let $(\boldsymbol{X}(\cdot,t), \mu(\cdot,t))$ solve the weak formulation (5.19). Then the total area $A(t)$ satisfies the following decay rate, and the total interfacial energy $W(t)$ dissipates over time:*

$$\frac{\mathrm{d}A}{\mathrm{d}t} = -\Big(\mu, 1\Big)_{\Gamma(t)}, \qquad W(t) \le W(t') \le W(0), \qquad \forall\, t \ge t' \ge 0. \tag{5.23}$$

Proof. Let $\Omega(t)$ be the region enclosed by $\Gamma(t)$. Reynolds' transport theorem [123] and the choice $\varphi = 1$ in (5.19a) give

$$\begin{aligned}\frac{\mathrm{d}}{\mathrm{d}t}A(t) = \frac{\mathrm{d}}{\mathrm{d}t}\int_{\Omega(t)}\mathrm{d}x\,\mathrm{d}y &= \int_{\Gamma(t)}\boldsymbol{n}\cdot\partial_t\boldsymbol{X}\,\mathrm{d}s\\ &= \Big(\boldsymbol{n}\cdot\partial_t\boldsymbol{X}, 1\Big)_{\Gamma(t)} = -\Big(\mu, 1\Big)_{\Gamma(t)}.\end{aligned} \tag{5.24}$$

For energy dissipation, differentiating $W(t)$ with respect to $t$ using Lemma 2.1 gives

$$\frac{\mathrm{d}}{\mathrm{d}t}W(t) = \int_{\Gamma(t)}\Big[\hat\gamma'(\theta)\,\partial_t\theta + \hat\gamma(\theta)\,\partial_s(\partial_t\boldsymbol{X})\cdot\partial_s\boldsymbol{X}\Big]\,\mathrm{d}s. \tag{5.25}$$

Combining this with the geometric identity (5.20) for $\theta$, we obtain

$$\begin{aligned}\frac{\mathrm{d}}{\mathrm{d}t}W(t) &= \int_{\Gamma(t)}\Big[\hat{\gamma}(\theta)\,\partial_s\boldsymbol{X} + \hat{\gamma}'(\theta)\,\boldsymbol{n}\Big]\cdot\partial_s(\partial_t\boldsymbol{X})\,\mathrm{d}s\\ &= \int_{\Gamma(t)}\hat{\boldsymbol{G}}^{\alpha}_{k}(\theta)\,\partial_s\boldsymbol{X}\cdot\partial_s(\partial_t\boldsymbol{X})\,\mathrm{d}s.\end{aligned}\tag{5.26}$$

Taking $\varphi = \mu$ in (5.19a) and $\boldsymbol{\omega} = \partial_t\boldsymbol{X}$ in (5.19b), and using (5.26), gives

$$\begin{aligned}\frac{\mathrm{d}}{\mathrm{d}t}W(t) &= \Big(\hat{\boldsymbol{G}}^{\alpha}_{k}(\theta)\,\partial_s\boldsymbol{X},\,\partial_s(\partial_t\boldsymbol{X})\Big)_{\Gamma(t)} = \Big(\mu\,\boldsymbol{n},\,\partial_t\boldsymbol{X}\Big)_{\Gamma(t)}\\ &= -\Big(\mu,\mu\Big)_{\Gamma(t)} \le 0.\end{aligned}\tag{5.27}$$

□

**5.2.2. Fully discrete scheme.** Based on the weak formulation (5.19), we propose a fully discrete parametric finite element scheme that preserves both the area decay rate and energy dissipation.

Let $N > 2$ be a positive integer and $h = 1/N$ the mesh size. Consider the uniform partition $\mathbb{I} = [0,1] \coloneqq \cup_{j=1}^{N} I_j$, where $I_j = [\rho_{j-1}, \rho_j]$, $\rho_j \coloneqq jh$, and $j = 0, 1, \ldots, N$. Define the piecewise linear finite element spaces

$$\mathbb{K}^h \coloneqq \big\{u^h \in C(\mathbb{I}) \mid u^h|_{I_j} \in \mathcal{P}^1(I_j),\ \forall j = 1, 2, \ldots, N\big\} \subseteq H^1(\mathbb{I}),\tag{5.28a}$$

$$\mathbb{K}^h_p \coloneqq \big\{u^h \in \mathbb{K}^h \mid u^h(0) = u^h(1)\big\} \subseteq H^1_p(\mathbb{I}),\tag{5.28b}$$

where $\mathcal{P}^1(I_j)$ is the space of polynomials of degree at most 1 on $I_j$. Let $0 = t_0 < t_1 < \cdots < t_M = T$ be a uniform partition of $[0,T]$, with $t_m = m\tau$, $\tau \coloneqq T/M$.

Let $\Gamma^m \coloneqq \boldsymbol{X}^m(\cdot) \in [\mathbb{K}^h_p]^2$ approximate $\Gamma(t_m) = \boldsymbol{X}(\cdot, t_m = m\tau)$ and satisfy the nondegeneracy condition

$$\min_{1\le j\le N} |\boldsymbol{h}^m_j| > 0, \qquad \forall m = 0, 1, \ldots, M,\tag{5.29}$$

where $\boldsymbol{h}^m_j \coloneqq \boldsymbol{X}^m(\rho_j) - \boldsymbol{X}^m(\rho_{j-1})$. Similarly, $\mu^m \in \mathbb{K}^h_p$ approximates $\mu(\cdot, t_m)$. The mass-lumped inner product $(\cdot,\cdot)^h_{\Gamma^m}$, discrete differential operator $\partial_s$, and discrete geometric quantities are defined in (2.43)–(2.47).

The *structure-preserving parametric finite element approximation* of anisotropic curvature flow (5.7a)–(5.7b) is now stated as follows. Let $\Gamma^0 \in [\mathbb{K}^h_p]^2$ be the initial approximation obtained by interpolation, $\boldsymbol{X}^0(\rho_j) = \boldsymbol{X}(\rho_j, 0), j = 1, 2, \cdots, N$. For $m = 0, 1, \cdots, M-1$, find $\big(\boldsymbol{X}^{m+1}(\cdot), \mu^{m+1}(\cdot)\big) \in [\mathbb{K}^h_p]^2 \times \mathbb{K}^h_p$ such that

$$\Big(\boldsymbol{n}^{m+\frac{1}{2}}\cdot\frac{\boldsymbol{X}^{m+1}-\boldsymbol{X}^m}{\tau},\varphi^h\Big)^h_{\Gamma^m} + \Big(\mu^{m+1},\varphi^h\Big)^h_{\Gamma^m} = 0, \qquad \forall\varphi^h \in \mathbb{K}^h_p,\tag{5.30a}$$

$$\Big(\mu^{m+1}\boldsymbol{n}^{m+\frac{1}{2}},\boldsymbol{\omega}^h\Big)^h_{\Gamma^m} - \Big(\hat{\boldsymbol{G}}^{\alpha}_{k}(\theta^m)\partial_s\boldsymbol{X}^{m+1},\partial_s\boldsymbol{\omega}^h\Big)^h_{\Gamma^m} = 0, \qquad \forall\boldsymbol{\omega}^h \in [\mathbb{K}^h_p]^2,\tag{5.30b}$$

where

$$\boldsymbol{n}^{m+\frac{1}{2}} \coloneqq -\frac{1}{2}\left(\partial_s\boldsymbol{X}^m + \partial_s\boldsymbol{X}^{m+1}\right)^{\perp} = -\frac{1}{2|\partial_\rho\boldsymbol{X}^m|}\left(\partial_\rho\boldsymbol{X}^m + \partial_\rho\boldsymbol{X}^{m+1}\right)^{\perp}.\tag{5.31}$$

Remark 5.4. The choice of $\boldsymbol{n}^{m+\frac{1}{2}}$ is motivated by the area-preserving parametric finite element method for surface diffusion proposed in [19], which was also used in Chapters 2 and 3. This construction exactly represents the area difference between successive discrete time levels of the evolving polygonal curve and is therefore essential for preserving the area decay rate.

**5.2.3. Structure preservation.** Let $A^m$ denote the area enclosed by the polygonal curve $\Gamma^m$ and $W^m$ its total interfacial energy, as defined in (2.55). The main result of this chapter is as follows.

THEOREM 5.1 (Structure preservation). *The numerical scheme* (5.30) *preserves the area decay rate:*

$$\frac{A^{m+1}-A^m}{\tau} = -\left(\mu^{m+1}, 1\right)_{\Gamma^m}^h, \qquad \forall 0 \le m \le M-1. \tag{5.32}$$

*Moreover, if* $\alpha = -1$ *and* $\hat{\gamma}(\theta) \in C^2(2\pi\mathbb{T})$ *satisfies*

$$3\hat{\gamma}(\theta) - \hat{\gamma}(\theta-\pi) \ge 0, \qquad \forall \theta \in 2\pi\mathbb{T}, \tag{5.33}$$

*then, for sufficiently large* $k(\theta)$*, the numerical scheme* (5.30) *is unconditionally energy stable:*

$$W^{m+1} \le W^m \le \cdots \le W^0, \qquad \forall 0 \le m \le M-1. \tag{5.34}$$

*For* $\alpha \ne -1$*, the energy stability condition* (5.33) *must instead be strengthened to*

$$3\hat{\gamma}(\theta) - \hat{\gamma}(\theta-\pi) > 0, \qquad \forall \theta \in 2\pi\mathbb{T}. \tag{5.35}$$

We prove the preservation of the area decay rate here and defer the proof of energy dissipation to the next section.

PROOF. Following the argument in Theorem 2.2, we obtain

$$A^{m+1} - A^m = \left(\boldsymbol{n}^{m+\frac{1}{2}} \cdot (\boldsymbol{X}^{m+1} - \boldsymbol{X}^m), 1\right)_{\Gamma^m}^h. \tag{5.36}$$

Taking $\varphi^h \equiv 1$ in (5.30a) then gives

$$A^{m+1} - A^m = -\tau\left(\mu^{m+1}, 1\right)_{\Gamma^m}^h. \tag{5.37}$$

This proves the area decay rate formula. □

### 5.3. Proof of unconditional energy stability

To prove unconditional energy stability of the fully discrete scheme (5.30), we introduce the minimal stabilizing function $k_{\min}^{\alpha}(\theta)$, defined by

$$k_{\min}^{\alpha}(\theta) := k_0^{\alpha}(\theta) - (\alpha-1)\hat{\gamma}(\theta), \qquad \forall \theta \in 2\pi\mathbb{T}, \tag{5.38}$$

where $k_0^{\alpha}(\theta)$ is defined by

$$k_0^{\alpha}(\theta) := \inf\left\{a \ge 0 \mid 4\hat{\gamma}(\theta)P_{\alpha,a}(\phi,\theta) \ge Q_{\alpha}^2(\phi,\theta),\ \forall \phi \in 2\pi\mathbb{T}\right\}. \tag{5.39}$$

Here $P_{\alpha,a}$ and $Q_{\alpha}$ are the auxiliary functions

$$P_{\alpha,a}(\phi,\theta) := \hat{\gamma}(\theta) + \frac{\alpha-1}{2}\hat{\gamma}'(\theta)\sin 2\phi + a\sin^2\phi, \tag{5.40a}$$

$$Q_{\alpha}(\phi,\theta) := \hat{\gamma}(\theta-\phi) + \hat{\gamma}(\theta)\cos\phi + \alpha\hat{\gamma}'(\theta)\sin\phi. \tag{5.40b}$$

ASSUMPTION 5.1. For a given $\hat{\gamma}(\theta) \in C^2(2\pi\mathbb{T})$ and $\alpha \in \mathbb{R}$, assume that the minimal stabilizing function $k_{\min}^{\alpha}(\theta)$ exists, that is,

$$k_{\min}^{\alpha}(\theta) < +\infty, \qquad \forall \theta \in 2\pi\mathbb{T}. \tag{5.41}$$

Under Assumption 5.1, we establish the following local energy estimate.

LEMMA 5.3 (Local energy estimate). *Assume that* (5.41) *holds. For arbitrary* $\boldsymbol{p}, \boldsymbol{q} \in \mathbb{R}^2\backslash\{\boldsymbol{0}\}$*, write* $\boldsymbol{p} = |\boldsymbol{p}|(\cos\varphi, \sin\varphi)^T$, $\boldsymbol{q} = |\boldsymbol{q}|(\cos\theta, \sin\theta)^T$*. Then, for sufficiently large* $k(\theta)$*,*

$$\frac{1}{|\boldsymbol{q}|}\left(\hat{\boldsymbol{G}}_k^{\alpha}(\theta)\boldsymbol{p}\right) \cdot (\boldsymbol{p}-\boldsymbol{q}) \ge \hat{\gamma}(\varphi)|\boldsymbol{p}| - \hat{\gamma}(\theta)|\boldsymbol{q}|. \tag{5.42}$$

Proof. Recalling the definition (5.8) of $\hat{\boldsymbol{G}}_k^\alpha(\theta)$, we have

$$\begin{aligned}
\frac{1}{|\boldsymbol{q}|}\Big(\hat{\boldsymbol{G}}_k^\alpha(\theta)\boldsymbol{p}\Big)\cdot\boldsymbol{p} &= \frac{|\boldsymbol{p}|^2}{|\boldsymbol{q}|}\left(\hat{\boldsymbol{G}}_k^\alpha(\theta)\begin{pmatrix}\cos\varphi\\ \sin\varphi\end{pmatrix}\right)\cdot\begin{pmatrix}\cos\varphi\\ \sin\varphi\end{pmatrix}\\
&= \frac{|\boldsymbol{p}|^2}{|\boldsymbol{q}|}\left(\hat\gamma(\theta)+(\alpha-1)\hat\gamma'(\theta)\sin(\theta-\varphi)\cos(\theta-\varphi)+(k(\theta)+(\alpha-1)\hat\gamma(\theta))\sin^2(\theta-\varphi)\right)\\
&= \frac{|\boldsymbol{p}|^2}{|\boldsymbol{q}|}\left(\hat\gamma(\theta)+\frac{\alpha-1}{2}\hat\gamma'(\theta)\sin\big(2(\theta-\varphi)\big)+(k(\theta)+(\alpha-1)\hat\gamma(\theta))\sin^2(\theta-\varphi)\right)\\
&= \frac{|\boldsymbol{p}|^2}{|\boldsymbol{q}|}P_{\alpha,k+(\alpha-1)\hat\gamma}(\theta-\varphi,\theta), \qquad (5.43)
\end{aligned}$$

and

$$\begin{aligned}
\frac{1}{|\boldsymbol{q}|}\Big(\hat{\boldsymbol{G}}_k^\alpha(\theta)\boldsymbol{p}\Big)\cdot\boldsymbol{q} &= |\boldsymbol{p}|\left(\hat{\boldsymbol{G}}_k^\alpha(\theta)\begin{pmatrix}\cos\varphi\\ \sin\varphi\end{pmatrix}\right)\cdot\begin{pmatrix}\cos\theta\\ \sin\theta\end{pmatrix}\\
&= |\boldsymbol{p}|\left(\hat\gamma(\theta)\cos(\theta-\varphi)+\alpha\hat\gamma'(\theta)\sin(\theta-\varphi)\right)\\
&= |\boldsymbol{p}|\left(Q_\alpha(\theta-\varphi,\theta)-\hat\gamma(\varphi)\right). \qquad (5.44)
\end{aligned}$$

Suppose that (5.41) holds. For sufficiently large $k(\theta)$ satisfying $k(\theta)\ge k_{\min}^\alpha(\theta)$, we have $k(\theta)+(\alpha-1)\hat\gamma(\theta)\ge k_{\min}^\alpha(\theta)+(\alpha-1)\hat\gamma(\theta)=k_0^\alpha(\theta)$. Thus, by (5.39),

$$\begin{aligned}
4\hat\gamma(\theta)P_{\alpha,k+(\alpha-1)\hat\gamma}(\theta-\varphi,\theta) &= 4\hat\gamma(\theta)P_{\alpha,k_0^\alpha}(\theta-\varphi,\theta)+4\hat\gamma(\theta)\left(k(\theta)-k_{\min}^\alpha(\theta)\right)\sin^2(\theta-\varphi)\\
&\ge 4\hat\gamma(\theta)P_{\alpha,k_0^\alpha}(\theta-\varphi,\theta)\ge Q_\alpha^2(\theta-\varphi,\theta), \qquad \forall\varphi\in 2\pi\mathbb{T}. \qquad (5.45)
\end{aligned}$$

Combining this with $\frac{1}{4c}x^2-x\ge -c,\ \forall x\in\mathbb{R},\ c>0$, gives

$$\begin{aligned}
\frac{1}{|\boldsymbol{q}|}\Big(\hat{\boldsymbol{G}}_k^\alpha(\theta)\boldsymbol{p}\Big)\cdot(\boldsymbol{p}-\boldsymbol{q}) &= \frac{|\boldsymbol{p}|^2}{|\boldsymbol{q}|}P_{\alpha,k+(\alpha-1)\hat\gamma}(\theta-\varphi,\theta)-|\boldsymbol{p}|\left(Q_\alpha(\theta-\varphi,\theta)-\hat\gamma(\varphi)\right)\\
&\ge \hat\gamma(\varphi)|\boldsymbol{p}|+\left(\frac{1}{4\hat\gamma(\theta)|\boldsymbol{q}|}\left(|\boldsymbol{p}|Q_\alpha(\theta-\varphi,\theta)\right)^2-|\boldsymbol{p}|Q_\alpha(\theta-\varphi,\theta)\right)\\
&\ge \hat\gamma(\varphi)|\boldsymbol{p}|-\hat\gamma(\theta)|\boldsymbol{q}|, \qquad (5.46)
\end{aligned}$$

This proves the desired estimate. □

Remark 5.5. Following the analysis in Remark 2.10 or Remark 3.5, we set $\boldsymbol{p}=-\boldsymbol{q}$, that is, $\varphi=\theta-\pi$, in (5.42). This yields the necessary condition $3\hat\gamma(\theta)\ge\hat\gamma(\theta-\pi)$ for the local energy estimate. Comparing this condition with (5.33) for $\alpha=-1$ shows that (5.33) is both necessary and sufficient for the local energy estimate when $\alpha=-1$. It is therefore optimal within this framework, as discussed in Chapter 3.

Remark 5.6. In the isotropic case $\hat\gamma(\theta)\equiv 1$, it is straightforward to verify that $k_0^\alpha(\theta)\equiv 0$ for every $\alpha\in\mathbb{R}$. Thus the minimal stabilizing function is $k_{\min}^\alpha(\theta)\equiv 1-\alpha$.

Using the local energy estimate (5.42), we can prove unconditional energy stability of the fully discrete scheme (5.30) under Assumption 5.1.

Proof. Let $k(\theta)$ be sufficiently large and satisfy $k(\theta)\ge k_{\min}^\alpha(\theta)$. For each time step ($\forall 0\le m\le M-1$),

$$\begin{aligned}
\left(\hat{\boldsymbol{G}}_k^\alpha(\theta^m)\partial_s\boldsymbol{X}^{m+1},\partial_s(\boldsymbol{X}^{m+1}-\boldsymbol{X}^m)\right)_{\Gamma^m}^h &= \sum_{j=1}^N\left[|\boldsymbol{h}_j^m|\Big(\hat{\boldsymbol{G}}_k^\alpha(\theta^m)\frac{\boldsymbol{h}_j^{m+1}}{|\boldsymbol{h}_j^m|}\Big)\cdot\frac{\boldsymbol{h}_j^{m+1}-\boldsymbol{h}_j^m}{|\boldsymbol{h}_j^m|}\right]\\
&= \sum_{j=1}^N\left[\frac{1}{|\boldsymbol{h}_j^m|}\Big(\hat{\boldsymbol{G}}_k^\alpha(\theta^m)\boldsymbol{h}_j^{m+1}\Big)\cdot(\boldsymbol{h}_j^{m+1}-\boldsymbol{h}_j^m)\right]. \qquad (5.47)
\end{aligned}$$

Taking $\boldsymbol{p} = \boldsymbol{h}_j^{m+1} = |\boldsymbol{h}_j^{m+1}|(\cos\theta_j^{m+1}, \sin\theta_j^{m+1})^T$ and $\boldsymbol{q} = \boldsymbol{h}_j^m = |\boldsymbol{h}_j^m|(\cos\theta_j^m, \sin\theta_j^m)^T$ in (5.42) gives

$$\begin{aligned}\left(\hat{\boldsymbol{G}}_k^\alpha(\theta^m)\partial_s\boldsymbol{X}^{m+1}, \partial_s(\boldsymbol{X}^{m+1}-\boldsymbol{X}^m)\right)_{\Gamma^m}^h &\geq \sum_{j=1}^N\left[\hat\gamma(\theta_j^{m+1})|\boldsymbol{h}_j^{m+1}| - \hat\gamma(\theta_j^m)|\boldsymbol{h}_j^m|\right]\\ &= \sum_{j=1}^N \hat\gamma(\theta_j^{m+1})|\boldsymbol{h}_j^{m+1}| - \sum_{j=1}^N\hat\gamma(\theta_j^m)|\boldsymbol{h}_j^m|\\ &= W^{m+1}-W^m. \end{aligned}\tag{5.48}$$

Taking $\varphi^h = \mu^{m+1}$ and $\boldsymbol{\omega}^h = \boldsymbol{X}^{m+1}-\boldsymbol{X}^m$ in (5.30), we obtain

$$\begin{aligned} W^{m+1}-W^m &\leq \left(\hat{\boldsymbol{G}}_k^\alpha(\theta^m)\partial_s\boldsymbol{X}^{m+1}, \partial_s(\boldsymbol{X}^{m+1}-\boldsymbol{X}^m)\right)_{\Gamma^m}^h\\ &= \left(\mu^{m+1}\boldsymbol{n}^{m+\frac12}, \boldsymbol{X}^{m+1}-\boldsymbol{X}^m\right)_{\Gamma^m}^h = -\tau\left(\mu^{m+1},\mu^{m+1}\right)_{\Gamma^m}^h \leq 0. \end{aligned}\tag{5.49}$$

This proves unconditional energy stability of the fully discrete scheme (5.30). □

## 5.4. Existence of the minimal stabilizing function

We now analyze the existence of the minimal stabilizing function $k_{\min}^\alpha(\theta)$.

Suppose that $\hat\gamma(\theta) \in C^2(2\pi\mathbb{T})$ satisfies

$$3\hat\gamma(\theta) - \hat\gamma(\theta-\pi) \geq 0, \qquad \forall\theta\in 2\pi\mathbb{T},\tag{5.50}$$

and let $c := \inf_{\theta\in2\pi\mathbb{T}}\left[3\hat\gamma(\theta)-\hat\gamma(\theta-\pi)\right]$. Since $k_{\min}^\alpha(\theta) = k_0^\alpha(\theta) - (\alpha-1)\hat\gamma(\theta)$, the existence of $k_{\min}^\alpha(\theta)$ is equivalent to the boundedness of $k_0^\alpha(\theta)$. We therefore focus on the latter. For the critical case $c = 0$, we establish necessary and sufficient conditions for boundedness of $k_0^\alpha(\theta)$. For $c > 0$, we derive an upper bound for $k_0^\alpha(\theta)$.

### 5.4.1. Boundedness of $k_0^\alpha(\theta)$.

Theorem 5.2. *If $c = 0$, then $k_0^\alpha(\theta)$ exists if and only if at least one of the following conditions holds:*

*(1) $\alpha = -1$;*

*(2) Whenever $3\hat\gamma(\theta^*) = \hat\gamma(\theta^*-\pi)$, we have $\hat\gamma'(\theta^*) = 0$.*

Proof. (*Sufficiency*) The proofs under conditions (1) and (2) follow the arguments in Sections 3.3.3 and 2.4.4, respectively, and are omitted here.

(*Necessity*) Suppose that there exists $\theta^* \in 2\pi\mathbb{T}$ such that $3\hat\gamma(\theta^*) = \hat\gamma(\theta^*-\pi)$. The function $\hat\gamma(\theta-\pi)/\hat\gamma(\theta)$ attains its maximum at $\theta = \theta^*$, and hence

$$\begin{aligned}\frac{d}{d\theta}\left(\frac{\hat\gamma(\theta-\pi)}{\hat\gamma(\theta)}\right)\Big|_{\theta=\theta^*} &= \frac{\hat\gamma'(\theta^*-\pi)\hat\gamma(\theta^*) - \hat\gamma(\theta^*-\pi)\hat\gamma'(\theta^*)}{\hat\gamma^2(\theta^*)}\\ &= \frac{\hat\gamma'(\theta^*-\pi) - 3\hat\gamma'(\theta^*)}{\hat\gamma(\theta^*)} = 0.\end{aligned}\tag{5.51}$$

Therefore,

$$3\hat\gamma'(\theta^*) = \hat\gamma'(\theta^*-\pi), \quad \text{whenever } 3\hat\gamma(\theta^*) = \hat\gamma(\theta^*-\pi)\ .\tag{5.52}$$

Define $F_\alpha(\phi,\theta) := 4\hat\gamma(\theta)P_{\alpha,k_0^\alpha}(\phi,\theta) - Q_\alpha^2(\phi,\theta)$. Then

$$F_\alpha(\phi,\theta) \geq 0, \qquad \forall\phi,\theta\in 2\pi\mathbb{T}.\tag{5.53}$$

Applying the mean value theorem to $F_\alpha(\phi,\theta^*)$ at $\phi = \pi$ gives

$$\begin{aligned}F_\alpha(\phi,\theta^*) &= \left(3\hat\gamma(\theta^*) - \hat\gamma(\theta^*-\pi)\right)\left(\hat\gamma(\theta^*)+\hat\gamma(\theta^*-\pi)\right)\\ &\quad + \left[4(\alpha-1)\hat\gamma(\theta^*)\hat\gamma'(\theta^*) + 2\left(\hat\gamma(\theta^*-\pi)-\hat\gamma(\theta^*)\right)\left(\hat\gamma'(\theta^*-\pi)+\alpha\hat\gamma'(\theta^*)\right)\right](\phi-\pi)\\ &\quad + O((\phi-\pi)^2).\end{aligned}\tag{5.54}$$

Substituting $3\hat{\gamma}(\theta^*) = \hat{\gamma}(\theta^* - \pi)$ and (5.52) into (5.54) yields

$$\begin{aligned} F_\alpha(\phi, \theta^*) &= [4(\alpha-1)\hat{\gamma}(\theta^*)\hat{\gamma}'(\theta^*) + 2\,(3\hat{\gamma}(\theta^*) - \hat{\gamma}(\theta^*))\,(3\hat{\gamma}'(\theta^*) + \alpha\hat{\gamma}'(\theta^*))]\,(\phi-\pi) \\ &\quad + O((\phi-\pi)^2) \\ &= 8(\alpha+1)\hat{\gamma}(\theta^*)\hat{\gamma}'(\theta^*)(\phi-\pi) + O((\phi-\pi)^2). \end{aligned} \tag{5.55}$$

Consequently, $(\alpha+1)\hat{\gamma}'(\theta^*) = 0$, so either $\alpha = -1$ or $\hat{\gamma}'(\theta^*) = 0$. □

Remark 5.7. Theorem 5.2 unifies the main results of Chapters 2 and 3 and identifies $\alpha = -1$ as the optimal choice within the local energy estimate framework. Indeed, as stated in Remark 5.5, condition (5.33), $3\hat{\gamma}(\theta) - \hat{\gamma}(\theta - \pi) \geq 0$, is both necessary and sufficient for the local energy estimate when $\alpha = -1$. For $\alpha \neq -1$, ensuring energy stability under (5.33) requires an additional condition such as $\hat{\gamma}'(\theta^*) = 0$, or the stronger condition (5.35), $3\hat{\gamma}(\theta) - \hat{\gamma}(\theta - \pi) > 0$.

**5.4.2. A global upper bound for $k_0^\alpha(\theta)$.** We first establish several lemmas to derive a global upper bound for $k_0^\alpha(\theta)$.

Lemma 5.4. *Let $f$ be a nonnegative $C^2$ function on $2\pi\mathbb{T}$. For any constant $C \geq \sup_{2\pi\mathbb{T}} |f''|$, we have*

$$-f(x) \leq f'(x)y + \frac{C}{2}y^2, \qquad \forall x, y \in 2\pi\mathbb{T}. \tag{5.56}$$

This is Lemma 3.2; its proof was given earlier.

Lemma 5.5 (Estimate for $Q_\alpha(\phi, \theta)$). *Suppose that $c > 0$. For $Q_\alpha(\phi, \theta)$ defined in* (5.40b)*, we have*

$$|Q_\alpha(\phi, \theta)| \leq |P_{\alpha,A}(\phi, \theta) + \hat{\gamma}(\theta)|, \qquad \forall \phi \in 2\pi\mathbb{T}, \tag{5.57}$$

*where $A(\theta)$ is defined by*

$$A(\theta) := \frac{\pi^2}{8}\left(C_\alpha \sup_{2\pi\mathbb{T}} |\hat{\gamma}''| + (3|\alpha|+2)|\hat{\gamma}'(\theta)| + \hat{\gamma}(\theta) + B(\theta)\right), \tag{5.58a}$$

$$B(\theta) := \frac{2}{c}(\alpha+1)^2|\hat{\gamma}'(\theta)|^2, \qquad C_\alpha = \max\{5, \frac{4}{\pi^2}(2|\alpha|+1)^2\}. \tag{5.58b}$$

Proof. We first prove the lower bound for $Q_\alpha(\phi, \theta)$. Lemma 5.4 gives

$$\begin{aligned} &Q_\alpha(\phi,\theta) + P_{\alpha,0}(\phi,\theta) + \hat{\gamma}(\theta) \\ &\quad = \hat{\gamma}(\theta-\phi) + \hat{\gamma}(\theta)(2+\cos\phi) + \hat{\gamma}'(\theta)(\alpha\sin\phi + \frac{\alpha-1}{2}\sin 2\phi) \\ &\quad \geq \hat{\gamma}(\theta) + \hat{\gamma}'(\theta)(\alpha + (\alpha-1)\cos\phi)\sin\phi \\ &\quad \geq \hat{\gamma}(\theta) - (2|\alpha|+1)|\hat{\gamma}'(\theta)||\sin\phi| \\ &\quad \geq -\frac{(2|\alpha|+1)^2}{2}\sup_{2\pi\mathbb{T}}|\hat{\gamma}''|\sin^2\phi. \end{aligned} \tag{5.59}$$

Using $A(\theta) \geq \frac{(2|\alpha|+1)^2}{2}\sup_{2\pi\mathbb{T}}|\hat{\gamma}''|$ and $P_{\alpha,A}(\phi,\theta) = P_{\alpha,0}(\phi,\theta) + A(\theta)\sin^2\phi$, we obtain

$$Q_\alpha(\phi,\theta) \geq -P_{\alpha,0}(\phi,\theta) - \hat{\gamma}(\theta) - A(\theta)\sin^2\phi = -P_{\alpha,A}(\phi,\theta) - \hat{\gamma}(\theta), \qquad \forall\phi \in 2\pi\mathbb{T}. \tag{5.60}$$

It remains to establish the upper bound for $Q_\alpha(\phi, \theta)$. We consider two cases.

*Case 1*: $|\phi| \leq \frac{\pi}{2}$. Applying the mean value theorem to $Q_\alpha(\cdot,\theta) - P_{\alpha,0}(\cdot,\theta) - \hat{\gamma}(\theta)$ on $[0,\phi]$, we obtain $\xi \in [0,\phi]$ such that

$$\begin{aligned} &Q_\alpha(\phi,\theta) - P_{\alpha,0}(\phi,\theta) - \hat{\gamma}(\theta) \\ &\quad = \frac{1}{2}\left(\hat{\gamma}''(\theta-\xi) - \hat{\gamma}(\theta)\cos\xi - \alpha\hat{\gamma}'(\theta)\sin\xi + 2(\alpha-1)\hat{\gamma}'(\theta)\sin 2\xi\right)\phi^2 \\ &\quad \leq \frac{1}{2}\left(\sup_{2\pi\mathbb{T}}|\hat{\gamma}''| + (3|\alpha|+2)|\hat{\gamma}'(\theta)| + \hat{\gamma}(\theta)\right)\left(\frac{\pi^2}{4}\sin^2\phi\right) \\ &\quad \leq A(\theta)\sin^2\phi. \end{aligned} \tag{5.61}$$

The penultimate inequality follows from $|\phi| \le \frac{\pi}{2}|\sin\phi|$ whenever $|\phi| \le \frac{\pi}{2}$.

*Case 2*: $|\phi - \pi| < \frac{\pi}{2}$. Similarly, applying the mean value theorem to $Q_\alpha(\cdot,\theta) - P_{\alpha,0}(\cdot,\theta) - \hat\gamma(\theta)$ on $[\phi,\pi]$, we obtain $\xi \in [\phi,\pi]$ such that

$$\begin{aligned} &Q_\alpha(\phi,\theta) - P_{\alpha,0}(\phi,\theta) - \hat\gamma(\theta) \\ &\quad= (\hat\gamma(\theta-\pi) - 3\hat\gamma(\theta)) - (\hat\gamma'(\theta-\pi) + (2\alpha-1)\hat\gamma'(\theta))(\phi-\pi) \\ &\qquad+ \frac{1}{2}(\hat\gamma''(\theta-\xi) - \hat\gamma(\theta)\cos\xi - \alpha\hat\gamma'(\theta)\sin\xi + 2(\alpha-1)\hat\gamma'(\theta)\sin 2\xi)(\phi-\pi)^2. \end{aligned} \tag{5.62}$$

By the definition of $c$, we have $3\hat\gamma(\theta) - \hat\gamma(\theta-\pi) \ge c$. Applying Lemma 5.4 to $3\hat\gamma(\theta) - \hat\gamma(\theta-\pi) - c$ gives

$$\begin{aligned} \hat\gamma(\theta-\pi) - 3\hat\gamma(\theta) &= -c - (3\hat\gamma(\theta) - \hat\gamma(\theta-\pi) - c) \\ &\le -c + (\hat\gamma'(\theta-\pi) - 3\hat\gamma'(\theta))(\phi-\pi) + \frac{1}{2}\sup_{2\pi\mathbb{T}}|3\hat\gamma''(\theta) - \hat\gamma''(\theta-\pi)|(\phi-\pi)^2 \\ &\le -c + (\hat\gamma'(\theta-\pi) - 3\hat\gamma'(\theta))(\phi-\pi) + 2\sup_{2\pi\mathbb{T}}|\hat\gamma''|(\phi-\pi)^2. \end{aligned} \tag{5.63}$$

Therefore,

$$\begin{aligned} &Q_\alpha(\phi,\theta) - P_{\alpha,0}(\phi,\theta) - \hat\gamma(\theta) \\ &\quad\le -c + (\hat\gamma'(\theta-\pi) - 3\hat\gamma'(\theta))(\phi-\pi) + 2\sup_{2\pi\mathbb{T}}|\hat\gamma''|(\phi-\pi)^2 \\ &\qquad- (\hat\gamma'(\theta-\pi) + (2\alpha-1)\hat\gamma'(\theta))(\phi-\pi) \\ &\qquad+ \frac{1}{2}(\hat\gamma''(\theta-\xi) - \hat\gamma(\theta)\cos\xi - \alpha\hat\gamma'(\theta)\sin\xi + 2(\alpha-1)\hat\gamma'(\theta)\sin 2\xi)(\phi-\pi)^2 \\ &\quad\le -c - 2(\alpha+1)\hat\gamma'(\theta)(\phi-\pi) + \frac{1}{2}\left(5\sup_{2\pi\mathbb{T}}|\hat\gamma''| + (3|\alpha|+2)|\hat\gamma'(\theta)| + \hat\gamma(\theta)\right)(\phi-\pi)^2. \end{aligned} \tag{5.64}$$

Since $c > 0$, the lower-order terms on the right-hand side of (5.64) can be bounded by a quadratic term:

$$-c - 2(\alpha+1)\hat\gamma'(\theta)(\phi-\pi) \le \frac{1}{c}(\alpha+1)^2|\hat\gamma'(\theta)|^2(\phi-\pi)^2. \tag{5.65}$$

Using $|\phi-\pi| \le \frac{\pi}{2}|\sin\phi|$ whenever $|\phi-\pi| \le \frac{\pi}{2}$, we obtain the desired inequality

$$Q_\alpha(\phi,\theta) \le P_{\alpha,A}(\phi,\theta) + \hat\gamma(\theta), \qquad \forall\phi \in 2\pi\mathbb{T}. \tag{5.66}$$

□

Theorem 5.3. *If $c > 0$, then for any $\alpha \in \mathbb{R}$, the function $k_0^\alpha(\theta)$ defined in* (5.39) *satisfies the upper bound*

$$k_0^\alpha(\theta) \le \frac{1}{4\hat\gamma(\theta)}\left[A^2(\theta) + 4\hat\gamma(\theta)A(\theta) + (\alpha-1)^2|\hat\gamma'(\theta)|^2\right] < +\infty, \qquad \forall\theta \in 2\pi\mathbb{T}. \tag{5.67}$$

Proof. Lemma 5.5 gives

$$Q_\alpha^2(\phi,\theta) \le \left(P_{\alpha,A}(\phi,\theta) + \hat\gamma(\theta)\right)^2, \qquad \forall\phi \in 2\pi\mathbb{T}. \tag{5.68}$$

Recalling the definition of $P_{\alpha,a}(\phi,\theta)$ in (5.40a), we have $P_{\alpha,a}(\phi,\theta) = P_{\alpha,0}(\phi,\theta) + a(\theta)\sin^2\phi$. Hence

$$\begin{aligned} &4\hat\gamma(\theta)P_{\alpha,a}(\phi,\theta) - Q_\alpha^2(\phi,\theta) \\ &\quad\ge 4\hat\gamma(\theta)(a(\theta) - A(\theta))\sin^2\phi + 4\hat\gamma(\theta)P_{\alpha,A}(\phi,\theta) - \left(P_{\alpha,A}(\phi,\theta) + \hat\gamma(\theta)\right)^2 \\ &\quad= 4\hat\gamma(\theta)(a(\theta) - A(\theta))\sin^2\phi - \left(P_{\alpha,A}(\phi,\theta) - \hat\gamma(\theta)\right)^2 \\ &\quad= \left(4\hat\gamma(\theta)(a(\theta) - A(\theta)) - ((\alpha-1)\hat\gamma'(\theta)\cos\phi + A(\theta)\sin\phi)^2\right)\sin^2\phi \\ &\quad\ge \left(4\hat\gamma(\theta)a(\theta) - A^2(\theta) - (\alpha-1)^2|\hat\gamma'(\theta)|^2 - 4\hat\gamma(\theta)A(\theta)\right)\sin^2\phi. \end{aligned} \tag{5.69}$$

The last inequality follows directly from $|a\cos\phi + b\sin\phi| \le \sqrt{a^2+b^2}$, $\forall\phi \in 2\pi\mathbb{T}$.

Therefore, for any $a(\theta)$ satisfying

$$a(\theta) \geq \frac{1}{4\hat{\gamma}(\theta)}\left[A^2(\theta) + 4\hat{\gamma}(\theta)A(\theta) + (\alpha-1)^2|\hat{\gamma}'(\theta)|^2\right]$$

we have

$$4\hat{\gamma}(\theta)P_{\alpha,a}(\phi,\theta) - Q_\alpha^2(\phi,\theta) \geq 0, \qquad \forall \phi \in 2\pi\mathbb{T}. \tag{5.70}$$

By the definition (5.39) of $k_0^\alpha(\theta)$, this proves (5.67). □

### 5.5. Extensions to other geometric flows

We consider two specific geometric flows, *area-preserving anisotropic curvature flow* and *anisotropic surface diffusion*, and construct their *structure-preserving parametric finite element schemes*. We then use the preceding analytical framework to discuss the design of structure-preserving algorithms for general normal velocity laws.

**5.5.1. Area-preserving anisotropic curvature flow.** As stated in (1.13), *area-preserving anisotropic curvature flow* is governed by

$$V_n = -\mu + \lambda, \tag{5.71}$$

where $\lambda := \int_\Gamma \mu \,\mathrm{d}s/|\Gamma|$ is a Lagrange multiplier that ensures conservation of the area enclosed by $\Gamma$.

As in (5.14), we obtain the following conservative strong formulation of area-preserving anisotropic curvature flow (5.71):

$$\boldsymbol{n}\cdot\partial_t \boldsymbol{X} + \mu - \lambda(t) = 0, \tag{5.72a}$$

$$\mu\boldsymbol{n} + \partial_s\left(\hat{\boldsymbol{G}}_k^\alpha(\theta)\partial_s \boldsymbol{X}\right) = \boldsymbol{0}, \tag{5.72b}$$

where $\lambda(t) := \int_{\Gamma(t)} \mu \,\mathrm{d}s/|\Gamma(t)|$ is the Lagrange multiplier.

Given the initial closed curve $\Gamma(0) = \boldsymbol{X}(\cdot,0) \in [H_p^1(\mathbb{I})]^2$ and initial weighted curvature $\mu(\cdot,0) = \mu_0(\cdot) \in H_p^1(\mathbb{I})$, the weak formulation of (5.72) is as follows: for every $t > 0$, find $\big(\boldsymbol{X}(\cdot,t), \mu(\cdot,t)\big) \in [H_p^1(\mathbb{I})]^2 \times H_p^1(\mathbb{I})$ such that

$$\Big(\boldsymbol{n}\cdot\partial_t\boldsymbol{X}, \varphi\Big)_{\Gamma(t)} + \Big(\mu - \lambda(t), \varphi\Big)_{\Gamma(t)} = 0, \qquad \forall \varphi \in H_p^1(\mathbb{I}), \tag{5.73a}$$

$$\Big(\mu\boldsymbol{n}, \boldsymbol{\omega}\Big)_{\Gamma(t)} - \Big(\hat{\boldsymbol{G}}_k^\alpha(\theta)\partial_s\boldsymbol{X}, \partial_s\boldsymbol{\omega}\Big)_{\Gamma(t)} = 0, \qquad \forall \boldsymbol{\omega} \in [H_p^1(\mathbb{I})]^2. \tag{5.73b}$$

The *structure-preserving parametric finite element method* for area-preserving anisotropic curvature flow (5.71) is then given as follows. Let the initial curve $\Gamma^0$ be specified by $\boldsymbol{X}^0(\rho_j) = \boldsymbol{X}(\rho_j, 0)$, $j = 1, 2, \cdots, N$. For every $m \geq 0$, find $\big(\boldsymbol{X}^{m+1}(\cdot), \mu^{m+1}(\cdot)\big) \in [\mathbb{K}_p^h]^2 \times \mathbb{K}_p^h$ such that

$$\left(\boldsymbol{n}^{m+\frac{1}{2}}\cdot\frac{\boldsymbol{X}^{m+1}-\boldsymbol{X}^m}{\tau}, \varphi^h\right)_{\Gamma^m}^h + \left(\mu^{m+1} - \lambda^{m,*}, \varphi^h\right)_{\Gamma^m}^h = 0, \qquad \forall \varphi^h \in \mathbb{K}_p^h, \tag{5.74a}$$

$$\left(\mu^{m+1}\boldsymbol{n}^{m+\frac{1}{2}}, \boldsymbol{\omega}^h\right)_{\Gamma^m}^h - \left(\hat{\boldsymbol{G}}_k^\alpha(\theta^m)\partial_s\boldsymbol{X}^{m+1}, \partial_s\boldsymbol{\omega}^h\right)_{\Gamma^m}^h = 0, \qquad \forall \boldsymbol{\omega}^h \in [\mathbb{K}_p^h]^2, \tag{5.74b}$$

where $\lambda^{m,*} := \big(\mu^{m+1}, 1\big)_{\Gamma^m}^h / |\Gamma^m|$.

The scheme (5.74) has the following structure-preserving properties.

Theorem 5.4. *Suppose that $\hat{\gamma}(\theta)$ satisfies* (5.35)*, or* (5.33) *when $\alpha = -1$. Then, for sufficiently large $k(\theta)$, the fully discrete scheme* (5.74) *is structure-preserving:*

$$A^{m+1} = A^m = \cdots = A^0, \qquad W^{m+1} \leq W^m \leq \cdots \leq W^0, \qquad \forall m \geq 0. \tag{5.75}$$

The proof follows [107], and its details are omitted for brevity.

**5.5.2. Anisotropic surface diffusion.** Similarly, the evolution equation for *anisotropic surface diffusion* is

$$V_n = \partial_{ss}\mu, \tag{5.76}$$

Its conservative strong formulation is

$$\boldsymbol{n}\cdot\partial_t\boldsymbol{X} - \partial_{ss}\mu = 0, \tag{5.77a}$$

$$\mu\boldsymbol{n} + \partial_s\left(\hat{\boldsymbol{G}}_k^{\alpha}(\theta)\partial_s\boldsymbol{X}\right) = \boldsymbol{0}. \tag{5.77b}$$

The corresponding weak formulation follows by the same procedure.

Let the initial closed curve $\Gamma^0$ be specified by $\boldsymbol{X}^0(\rho_j) = \boldsymbol{X}(\rho_j, 0)$, $j = 1, 2, \cdots, N$. The *structure-preserving parametric finite element scheme* for anisotropic surface diffusion (5.76) is as follows: for every $m \geq 0$, find $\left(\boldsymbol{X}^{m+1}(\cdot), \mu^{m+1}(\cdot)\right) \in [\mathbb{K}_p^h]^2 \times \mathbb{K}_p^h$ such that

$$\left(\boldsymbol{n}^{m+\frac{1}{2}}\cdot\frac{\boldsymbol{X}^{m+1}-\boldsymbol{X}^m}{\tau}, \varphi^h\right)_{\Gamma^m}^h + \left(\partial_s\mu^{m+1}, \partial_s\varphi^h\right)_{\Gamma^m}^h = 0, \qquad \forall\varphi^h \in \mathbb{K}_p^h, \tag{5.78a}$$

$$\left(\mu^{m+1}\boldsymbol{n}^{m+\frac{1}{2}}, \boldsymbol{\omega}^h\right)_{\Gamma^m}^h - \left(\hat{\boldsymbol{G}}_k^{\alpha}(\theta^m)\partial_s\boldsymbol{X}^{m+1}, \partial_s\boldsymbol{\omega}^h\right)_{\Gamma^m}^h = 0, \qquad \forall\boldsymbol{\omega}^h \in [\mathbb{K}_p^h]^2. \tag{5.78b}$$

The scheme (5.78) has the following structure-preserving properties.

Theorem 5.5. *Suppose that $\hat{\gamma}(\theta)$ satisfies* (5.35)*, or* (5.33) *when $\alpha = -1$. Then, for sufficiently large $k(\theta)$, the scheme* (5.78) *is structure-preserving:*

$$A^{m+1} = A^m = \cdots = A^0, \qquad W^{m+1} \leq W^m \leq \cdots \leq W^0, \qquad \forall m \geq 0. \tag{5.79}$$

The proof is analogous to those of Theorems 2.2 and 5.1 and is omitted.

**5.5.3. General normal velocity laws.** The surface energy matrix allows us to treat anisotropic problems using a framework and strategies analogous to those of *Barrett–Garcke–Nürnberg methods* for isotropic problems [29, 27].

Consider an evolution equation of the form

$$V_n = \mathfrak{F}(\mu), \qquad \text{on } \Gamma(t), \tag{5.80}$$

where $\mathfrak{F}(\cdot)$ maps functions on the closed evolving curve $\Gamma(t)$ to functions on $\Gamma(t)$.

If $\mathfrak{F}$ satisfies

$$\left(\mathfrak{F}(\mu), \mu\right)_{\Gamma(t)} \leq 0, \tag{5.81}$$

then (5.80) satisfies the following area decay rate and energy dissipation identities:

$$\frac{\mathrm{d}}{\mathrm{d}t}A(t) = \left(\mathfrak{F}(\mu), 1\right)_{\Gamma(t)}, \qquad \frac{\mathrm{d}}{\mathrm{d}t}W(t) = \left(V_n, \mu\right)_{\Gamma(t)} = \left(\mathfrak{F}(\mu), \mu\right)_{\Gamma(t)} \leq 0. \tag{5.82}$$

The preceding evolution laws all fit within this framework. For example, integration by parts for anisotropic surface diffusion $V_n = \partial_{ss}\mu$ gives

$$\left(\mathfrak{F}(\mu), \mu\right)_{\Gamma(t)} = \left(\partial_{ss}\mu, \mu\right)_{\Gamma(t)} = -\left(\partial_s\mu, \partial_s\mu\right)_{\Gamma(t)} \leq 0. \tag{5.83}$$

As above, to construct a *structure-preserving numerical scheme* for (5.80), we formally consider the strong formulation

$$\boldsymbol{n}\cdot\partial_t\boldsymbol{X} - \mathfrak{F}(\mu) = 0, \tag{5.84a}$$

$$\mu\boldsymbol{n} + \partial_s\left(\hat{\boldsymbol{G}}_k^{\alpha}(\theta)\partial_s\boldsymbol{X}\right) = \boldsymbol{0}. \tag{5.84b}$$

Although $\mathfrak{F}(\mu)$ is conventional notation, constructing a structure-preserving fully discrete scheme requires careful treatment of its dependence on the underlying curve $\Gamma(t)$. To make this dependence explicit, we write $\mathfrak{F}(\mu, \Gamma) = \mathfrak{F}(\mu)$. This suggests a semi-implicit discretization that treats $\mu$ implicitly at time level $m+1$ and $\Gamma$ explicitly at time level $m$. The resulting framework yields *structure-preserving fully discrete schemes* as follows.

Given the initial data $\Gamma^0$, find, for every $m \geq 0$, $\big(\boldsymbol{X}^{m+1}(\cdot), \mu^{m+1}(\cdot)\big) \in [\mathbb{K}_p^h]^2 \times \mathbb{K}_p^h$ such that

$$\left(\boldsymbol{n}^{m+\frac{1}{2}} \cdot \frac{\boldsymbol{X}^{m+1} - \boldsymbol{X}^m}{\tau}, \varphi^h\right)_{\Gamma^m}^h - \left(\mathfrak{F}(\mu^{m+1}, \Gamma^m), \varphi^h\right)_{\Gamma^m}^h = 0, \qquad \forall \varphi^h \in \mathbb{K}_p^h, \tag{5.85a}$$

$$\left(\mu^{m+1}\boldsymbol{n}^{m+\frac{1}{2}}, \boldsymbol{\omega}^h\right)_{\Gamma^m}^h - \left(\hat{\boldsymbol{G}}_k^\alpha(\theta^m)\partial_s \boldsymbol{X}^{m+1}, \partial_s \boldsymbol{\omega}^h\right)_{\Gamma^m}^h = 0, \qquad \forall \boldsymbol{\omega}^h \in [\mathbb{K}_p^h]^2. \tag{5.85b}$$

For the following result, assume that the chosen discrete realization of $\mathfrak{F}$ preserves the dissipation property, that is, $\big(\mathfrak{F}(\mu^{m+1}, \Gamma^m), \mu^{m+1}\big)_{\Gamma^m}^h \leq 0$. The scheme (5.85) then has the following structure-preserving properties.

Theorem 5.6. *Suppose that $\hat{\gamma} \in C^2(2\pi\mathbb{T})$ is strictly positive and satisfies* (5.35)*, or* (5.33) *when $\alpha = -1$. Then, for sufficiently large $k(\theta)$, the scheme* (5.85) *is structure-preserving:*

$$\frac{A^{m+1} - A^m}{\tau} = \left(\mathfrak{F}(\mu^{m+1}, \Gamma^m), 1\right)_{\Gamma^m}^h, \qquad W^{m+1} \leq W^m \leq \cdots \leq W^0, \qquad \forall m \geq 0. \tag{5.86}$$

Proof. For the area decay rate, following (5.36), we have

$$A^{m+1} - A^m = \left(\boldsymbol{n}^{m+\frac{1}{2}} \cdot (\boldsymbol{X}^{m+1} - \boldsymbol{X}^m), 1\right)_{\Gamma^m}^h = \tau\left(\mathfrak{F}(\mu^{m+1}, \Gamma^m), 1\right)_{\Gamma^m}^h. \tag{5.87}$$

For energy dissipation, (5.48) continues to hold, giving

$$\begin{aligned} W^{m+1} - W^m &\leq \left(\hat{\boldsymbol{G}}_k^\alpha(\theta^m)\partial_s \boldsymbol{X}^{m+1}, \partial_s(\boldsymbol{X}^{m+1} - \boldsymbol{X}^m)\right)_{\Gamma^m}^h \\ &= \left(\mu^{m+1}\boldsymbol{n}^{m+\frac{1}{2}}, \boldsymbol{X}^{m+1} - \boldsymbol{X}^m\right)_{\Gamma^m}^h = \tau\left(\mathfrak{F}(\mu^{m+1}, \Gamma^m), \mu^{m+1}\right)_{\Gamma^m}^h \leq 0. \end{aligned} \tag{5.88}$$

The final inequality follows from the discrete dissipation assumption corresponding to (5.81). □

We give three examples to illustrate this construction. Further examples and numerical discussions can be found in the survey by Barrett et al. [29] and the references therein.

Example 5.1. Take $\mathfrak{F}(f, \Gamma) = -f + \int_\Gamma f \, \mathrm{d}s/|\Gamma|$, where $f$ is a function on $\Gamma$. Then $\mathfrak{F}(\mu^{m+1}, \Gamma^m) = -\mu^{m+1} + \int_{\Gamma^m} \mu^{m+1} \, \mathrm{d}s/|\Gamma^m|$. This recovers the structure-preserving parametric finite element discretization (5.74) of *area-preserving anisotropic curvature flow*.

Example 5.2. For surface diffusion, take $\mathfrak{F}(f, \Gamma) = \partial_{ss} f$, where $\partial_s$ denotes differentiation with respect to arc length along $\Gamma$. Integration by parts yields $\big(\mathfrak{F}(\mu, \Gamma), \mu\big)_\Gamma = -(\partial_s \mu, \partial_s \mu)_\Gamma \leq 0$, recovering the structure-preserving scheme (5.78) and Theorem 5.5 for *anisotropic surface diffusion*.

Example 5.3. An intermediate evolution law between area-preserving anisotropic curvature flow and surface diffusion is

$$V_n = \partial_{ss}\eta, \qquad \text{where } \left(-\frac{1}{\xi}\partial_{ss} + \frac{1}{\nu}\right)\eta = \mu, \tag{5.89}$$

where $\xi, \nu \in \mathbb{R}^+$ are constants. We define the mapping $\mathfrak{F}(\cdot, \Gamma^m)$ by

$$\left(\mathfrak{F}(f, \Gamma^m), \varphi^h\right)_{\Gamma^m}^h = -\left(\partial_s \eta(f), \partial_s \varphi^h\right)_{\Gamma^m}^h, \qquad \forall \varphi^h \in \mathbb{K}_p^h, \tag{5.90}$$

where $\eta(f)$ solves

$$\frac{1}{\xi}\left(\partial_s \eta(f), \partial_s \psi^h\right)_{\Gamma^m}^h + \frac{1}{\nu}\left(\eta(f), \psi^h\right)_{\Gamma^m}^h = \left(f, \psi^h\right)_{\Gamma^m}^h, \qquad \forall \psi^h \in \mathbb{K}_p^h. \tag{5.91}$$

Taking $f = \varphi^h = \mu^{m+1}, \psi^h = \mu^{m+1} - \frac{1}{\nu}\eta(\mu^{m+1})$ gives

$$\left(\mathfrak{F}(\mu^{m+1}, \Gamma^m), \mu^{m+1}\right)_{\Gamma^m}^h = -\frac{1}{\nu}\left(\partial_s \eta, \partial_s \eta\right)_{\Gamma^m}^h - \xi\left(\mu^{m+1} - \frac{1}{\nu}\eta, \mu^{m+1} - \frac{1}{\nu}\eta\right)_{\Gamma^m}^h \leq 0. \tag{5.92}$$

Thus we obtain a structure-preserving discretization of the intermediate flow (5.89) under (5.35) or (5.33). For further discussion of this flow, see [135, 59, 60] for theoretical results and [7, 22] for numerical methods.

### 5.6. Numerical experiments

We report extensive numerical experiments to assess the performance of the proposed *structure-preserving parametric finite element schemes*.

**5.6.1. Numerical errors and convergence rates.** To measure the distance between two closed curves $\Gamma_1$ and $\Gamma_2$, we use the manifold distance $M(\Gamma_1, \Gamma_2)$ [151, 108], defined by

$$M(\Gamma_1, \Gamma_2) := |(\Omega_1 \backslash \Omega_2) \cup (\Omega_2 \backslash \Omega_1)| = 2|\Omega_1 \cup \Omega_2| - |\Omega_1| - |\Omega_2|, \tag{5.93}$$

where $\Omega_i$ $(i = 1, 2)$ is the interior region enclosed by $\Gamma_i$, and $|\Omega|$ denotes the area of $\Omega$.

Define the intermediate curve $\Gamma_{h,\tau}(t)$ between $\Gamma^m$ and $\Gamma^{m+1}$ by

$$\Gamma_{h,\tau}(t) := \frac{t_{m+1} - t}{\tau}\,\Gamma^m + \frac{t - t_m}{\tau}\,\Gamma^{m+1}, \qquad t \in [t_m, t_{m+1}],\ m \geq 0. \tag{5.94}$$

The numerical error $e^h(t)$ is formally defined by

$$e^h(t) := M(\Gamma_{h,\tau}(t), \Gamma(t)). \tag{5.95}$$

We approximate the exact solution $\Gamma(t)$ by $\Gamma_{h_e,\tau_e}(t)$ computed on the fine grid $h_e = 2^{-8}$, $\tau_e = h_e^2$.

| $\alpha$ | $(h, \tau)$ | $e^h(t = 0.1)$ | order | $e^h(t = 0.2)$ | order | $e^h(t = 0.3)$ | order |
|---|---|---|---|---|---|---|---|
| -1 | $(h_0, \tau_0)$ | 1.30e-1 | - | 1.63e-1 | - | 1.84e-1 | - |
| | $(\frac{h_0}{2}, \frac{\tau_0}{4})$ | 3.12e-2 | 2.06 | 4.03e-2 | 2.01 | 4.64e-2 | 1.98 |
| | $(\frac{h_0}{2^2}, \frac{\tau_0}{4^2})$ | 8.02e-3 | 1.96 | 1.05e-2 | 1.94 | 1.21e-2 | 1.94 |
| 0 | $(h_0, \tau_0)$ | 1.30e-1 | - | 1.56e-1 | - | 1.73e-1 | - |
| | $(\frac{h_0}{2}, \frac{\tau_0}{4})$ | 3.14e-2 | 2.05 | 4.04e-2 | 1.95 | 4.65e-2 | 1.90 |
| | $(\frac{h_0}{2^2}, \frac{\tau_0}{4^2})$ | 8.00e-3 | 1.97 | 1.04e-2 | 1.95 | 1.20e-2 | 1.94 |
| 1 | $(h_0, \tau_0)$ | 1.31e-1 | - | 1.58e-1 | - | 1.76e-1 | - |
| | $(\frac{h_0}{2}, \frac{\tau_0}{4})$ | 3.15e-2 | 2.05 | 4.05e-2 | 1.97 | 4.66e-2 | 1.92 |
| | $(\frac{h_0}{2^2}, \frac{\tau_0}{4^2})$ | 7.98e-3 | 1.98 | 1.04e-2 | 1.97 | 1.20e-2 | 1.96 |

**Table 5.1.** Numerical errors $e^h(t)$ and convergence rates for the fully discrete scheme (5.30) with $\alpha = 0, \pm 1$. The anisotropy is Case I with $\beta = 1/9$. The remaining parameters are $h_0 = 2^{-4}$, $\tau_0 = h_0^2$.

We consider the following two surface energies in the convergence tests:

- Case I: $\hat{\gamma}(\theta) = 1 + \beta \cos 3\theta$, where $|\beta| < 1$.
- Case II: $\hat{\gamma}(\theta) = \sqrt{\left(\frac{5}{2} + \frac{3}{2}\mathrm{sgn}(n_1)\right) n_1^2 + n_2^2}$, where $\boldsymbol{n} = (n_1, n_2)^T = (-\sin\theta, \cos\theta)^T$.

We compute the minimal stabilizing function $k^\alpha_{\min}(\theta)$ as follows. For a given $\hat{\gamma}(\theta)$ and $\alpha \in \mathbb{R}$, solve the optimization problem (5.39) at the nodes $\theta_j = -\pi + \frac{j\pi}{10}$, $\forall 0 \leq j \leq 20$ to obtain $k^\alpha_0(\theta_j)$. Then use linear interpolation to approximate $k^\alpha_0(\theta)$ between nodes and obtain $k^\alpha_{\min}(\theta)$ from (5.38). In the following convergence tests, we take $k(\theta) = k^\alpha_{\min}(\theta)$ unless otherwise stated.

The scheme formally has second-order spatial accuracy and first-order temporal accuracy. We therefore take $\tau = h^2$ unless otherwise stated. The initial curve is an ellipse with major axis 4 and minor axis 1, and the Newton iteration tolerance is tol $= 10^{-11}$.

Table 5.1 and Figure 5.1 report the numerical errors. They show second-order spatial convergence and first-order temporal convergence for (5.30).

Figure 5.2 compares the errors at $t = 0.25$ for Cases I and II with several values of $\alpha$. The tests include the reference values $\alpha = 0, \pm 1$, nearby values $\alpha = \pm 0.9, \pm 1.1$, fractional values $\alpha = \pm 0.5$, and values with larger magnitudes $\alpha = \pm 3, \pm 6, \pm 10$. The results demonstrate that the accuracy of (5.30) is robust with respect to $\alpha$: the relative differences between errors are less than 5% in most cases.

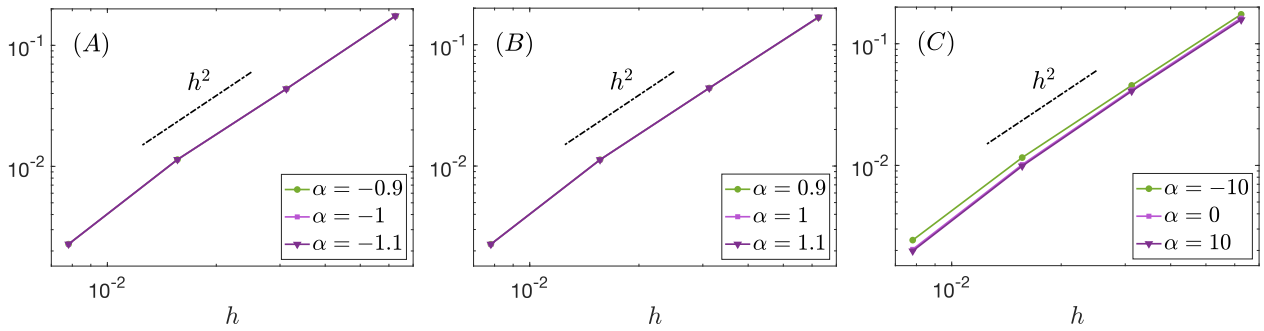



**Figure 5.1.** Convergence rates for (5.30) at $t = 0.25$ for different values of $\alpha$: (A)–(B) Case I with $\beta = 1/9$; (C) Case II.

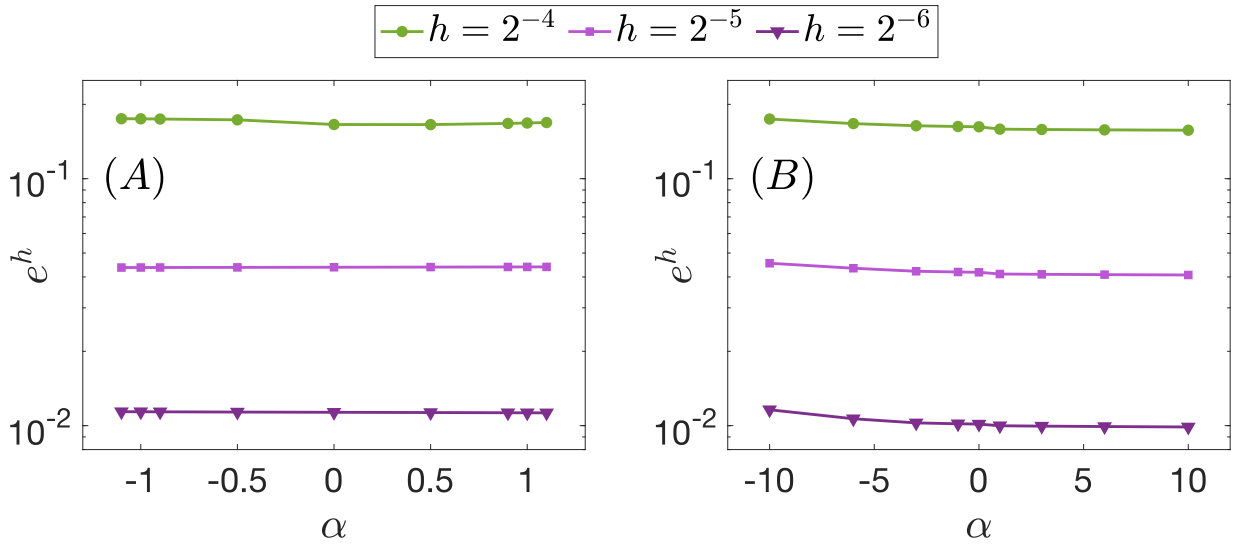



**Figure 5.2.** Error comparison for (5.30) at $t = 0.25$: (A) Case I with $\beta = 1/7$ and $\alpha = 0, \pm 0.5, \pm 0.9, \pm 1, \pm 1.1$; (B) Case II with $\alpha = 0, \pm 1, \pm 3, \pm 6, \pm 10$.

**5.6.2. Iteration counts and CPU time.** Table 5.2 lists the total iteration counts and average CPU times for (5.30) at $t = 0.1$ with different values of $\alpha$. The CPU times are arithmetic averages over five independent runs. All computations were performed on a laptop with an Apple M1 Pro chip and 16 GB of memory running macOS Sequoia 15.3.2. The average number of Newton iterations per time step is approximately 2, indicating that the scheme can be solved efficiently. The average CPU time is approximately 18 seconds on the grid $(h, \tau) = (2^{-7}, 4^{-7})$ and 150 seconds on the finer grid $(h_e, \tau_e) = (2^{-8}, 4^{-8})$. These results indicate consistent computational efficiency across the tested values of $\alpha$.

**5.6.3. Minimal stabilizing function and mesh quality.**

5.6.3.1. *Minimal stabilizing function.* Figure 5.3 shows the minimal stabilizing functions for the threefold anisotropy $\hat{\gamma}(\theta) = 1 + \beta \cos 3\theta$ and the ratios of their $L^\infty$ norms to the $L^\infty$ norm of $\hat{\gamma}(\theta)$ as functions of $\alpha$. The right panel plots $k_0^\alpha$ for $\alpha = -1$. The values of $k_{\min}^\alpha(\theta)$ increase with the anisotropy strength $\beta$. Moreover, $k_{\min}^\alpha(\theta)$ remains bounded in the critical case $\beta = \frac{1}{2}$ associated with (5.35) or (5.33), consistent with Theorem 5.2. The left panel shows that the supremum of $k_{\min}^\alpha$ grows rapidly as $|\alpha|$ increases. Growth is moderate for $-1 \le \alpha \le 1$, whereas for $|\alpha| > 1$, the stabilizing term $k_{\min}^\alpha(\theta)\boldsymbol{n}(\theta)\boldsymbol{n}(\theta)^T$ in $\hat{\boldsymbol{G}}_k^\alpha(\theta)$ becomes substantially larger than the other components.

Figure 5.4 plots $k_{\min}^\alpha(\theta)$ and $k_{\min}^\alpha(\theta) + \alpha$ for different values of $\alpha$. The left panel shows an approximately linear dependence of $k_{\min}^\alpha(\theta)$ on $\alpha$ for small values of $\alpha$. For large $|\alpha|$, we use $k_{\min}^\alpha + \alpha$

| | $(h,\tau)=(2^{-7},4^{-7})$ | | $(h,\tau)=(2^{-8},4^{-8})$ | |
|---|---|---|---|---|
| $\alpha$ | Iteration count | CPU time (s) | Iteration count | CPU time (s) |
| -10 | 3278 | 17.9999 | 15856 | 162.2915 |
| -5 | 3278 | 18.0083 | 13265 | 148.6691 |
| -1 | 3278 | 18.5907 | 13294 | 151.7395 |
| 0 | 3278 | 18.6436 | 13304 | 152.5232 |
| 1 | 3278 | 18.3653 | 13313 | 151.2127 |
| 5 | 3278 | 18.6596 | 13496 | 151.3283 |
| 10 | 3278 | 17.1996 | 18070 | 166.7016 |

**Table 5.2.** Total iteration counts and average CPU times for (5.30) at $t = 0.1$ for Case I with $\beta = 1/7$.

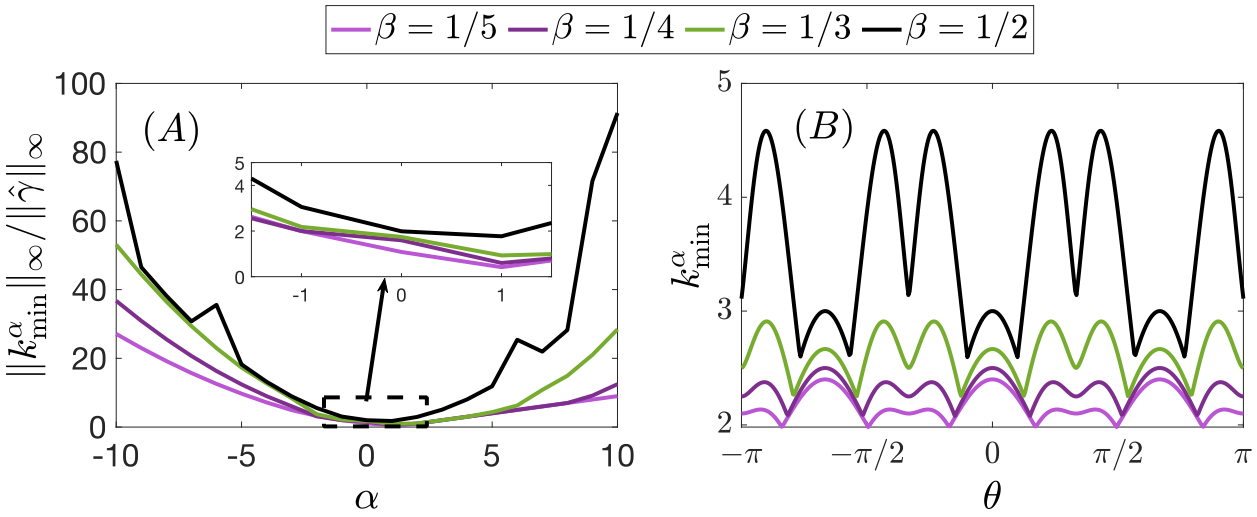



**Figure 5.3.** Minimal stabilizing functions in Case I and the ratios of their $L^\infty$ norms to the $L^\infty$ norm of the anisotropy.

to measure the magnitude of the regularizing term in $\hat{\boldsymbol{G}}_k^\alpha(\theta)$. As shown in the right panel of Figure 5.4, this term is substantially larger than $\hat{\gamma}(\theta)$, consistent with Figure 5.3.

5.6.3.2. *Weighted mesh ratio.* To assess mesh quality, we introduce the weighted mesh ratio $R_\gamma^h(t)$,

$$R_\gamma^h(t)\Big|_{t=t_m} := \frac{\max\limits_{1\le j\le N} \hat{\gamma}(\theta_j)|\boldsymbol{h}_j^m|}{\min\limits_{1\le j\le N} \hat{\gamma}(\theta_j)|\boldsymbol{h}_j^m|}, \qquad m \ge 0. \tag{5.96}$$

Since anisotropic curvature flow causes the curve to shrink and eventually develop a singularity, we use *anisotropic surface diffusion* to examine mesh properties over long evolution times.

Figure 5.5 shows the weighted mesh ratio $R_\gamma^h(t)$ for an ellipse with major axis 4 and minor axis 1 evolving by anisotropic surface diffusion under the fully discrete scheme (5.78), with $\hat{\gamma}(\theta) = 1 + \frac{1}{16}\cos 4\theta$. As $t \to \infty$, the weighted mesh ratio $R_\gamma^h$ approaches a constant, indicating an asymptotically quasi-uniform mesh distribution. For small $|\alpha|$, the evolutions of $R_\gamma^h$ are nearly identical. For large $|\alpha|$, however, $R_\gamma^h$ may increase substantially during the initial stage. Small values of $|\alpha|$ are therefore preferable for mesh quality in practice.

**5.6.4. Area decay rate and energy dissipation.** Figure 5.6 shows the area of an ellipse with major axis 4 and minor axis 1 evolving by *anisotropic curvature flow* under (5.30). We consider two surface

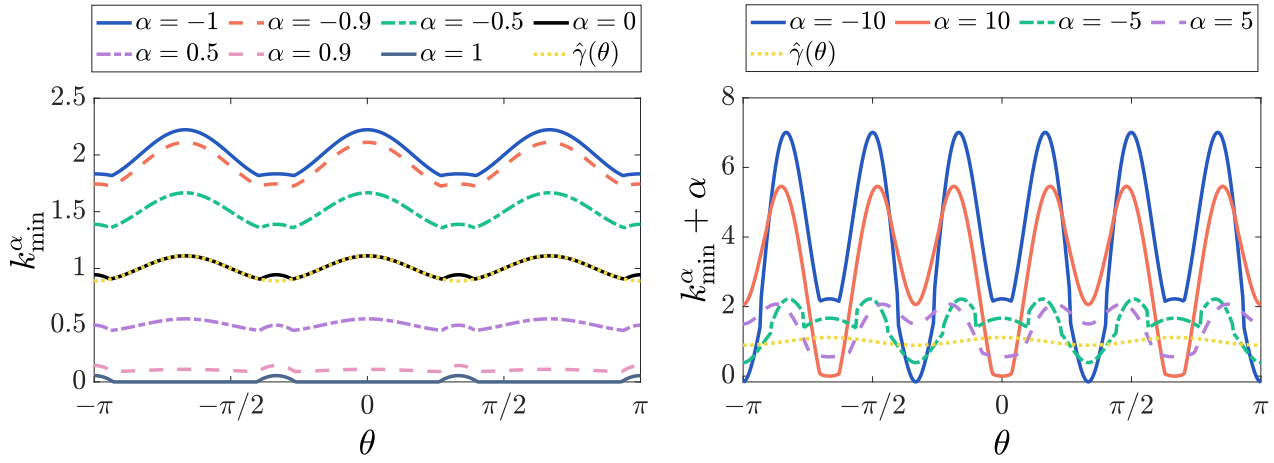



**Figure 5.4.** Minimal stabilizing functions for different values of $\alpha$ in Case I with $\beta = 1/9$.

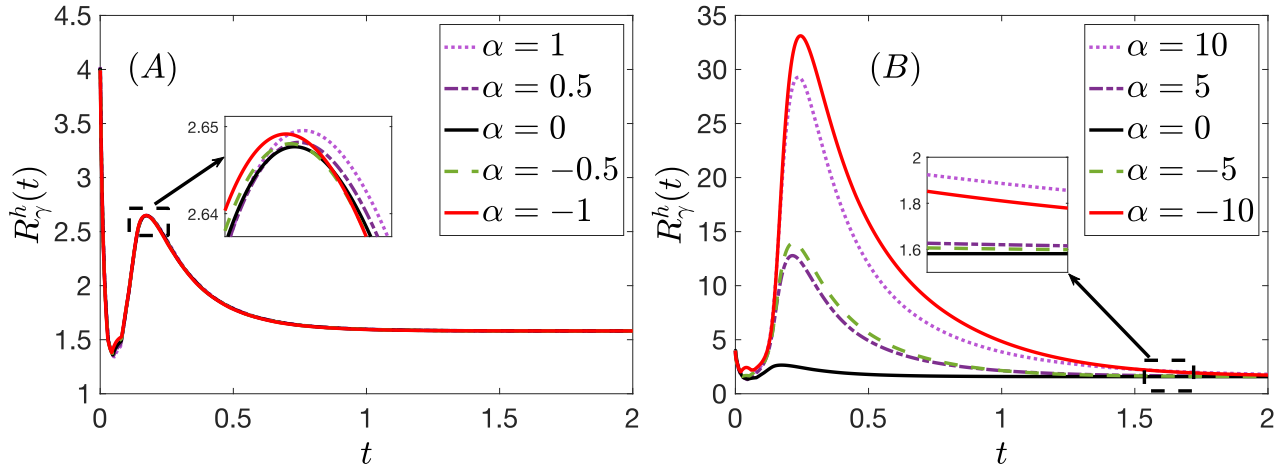



**Figure 5.5.** Weighted mesh ratios for (5.78) with different values of $\alpha$. The initial curve is an ellipse with major axis 4 and minor axis 1, evolving by anisotropic surface diffusion with $\hat{\gamma}(\theta) = 1 + \frac{1}{16}\cos 4\theta$. The mesh sizes are $(h, \tau) = (2^{-6}, 4^{-6})$.

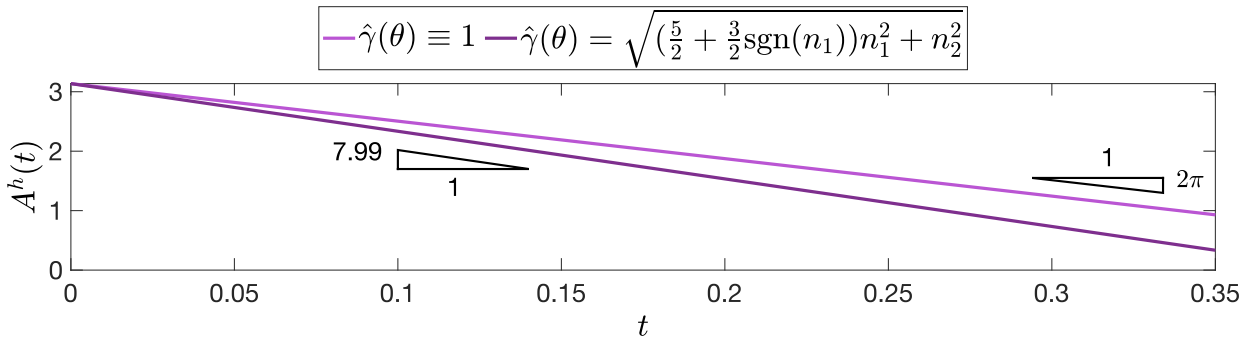



**Figure 5.6.** Area and area decay rate of an ellipse with major axis 4 and minor axis 1 evolving by anisotropic curvature flow under (5.30), with $\alpha = 0$.

energy densities: (i) the isotropic energy $\hat{\gamma}(\theta) \equiv 1$ and (ii) the energy in Case II. The area decreases approximately linearly with time.

For a simple closed curve evolving by isotropic curvature flow, the area decay rate satisfies $\frac{dA(t)}{dt} = -\int_\Gamma \kappa \, ds = -2\pi$ and remains constant. For anisotropic surface energies, the area decay rate approaches the constant $-\int_\Gamma \mu \, ds$. Here $\Gamma$ denotes the *Wulff shape* determined by $\hat{\gamma}(\theta)$ [118], rescaled to enclose the same area as the initial curve. For the surface energy density in Case II, we have $-\int_\Gamma \mu \, ds \approx -7.9858$ [13].

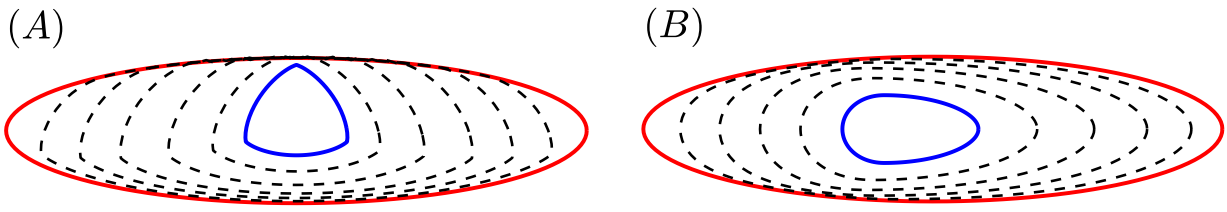



**Figure 5.7.** Morphological evolution of an ellipse with major axis 4 and minor axis 1 under anisotropic curvature flow computed with (5.30): (A) Case I with $\beta = 1/7$; (B) Case II. Red curves show the initial shapes, blue curves show the numerical solutions at (A) $t = 0.45$ and (B) $t = 0.35$, and black dashed curves show intermediate stages. The parameters are $\alpha = 0, (h, \tau) = (2^{-7}, 4^{-7})$.

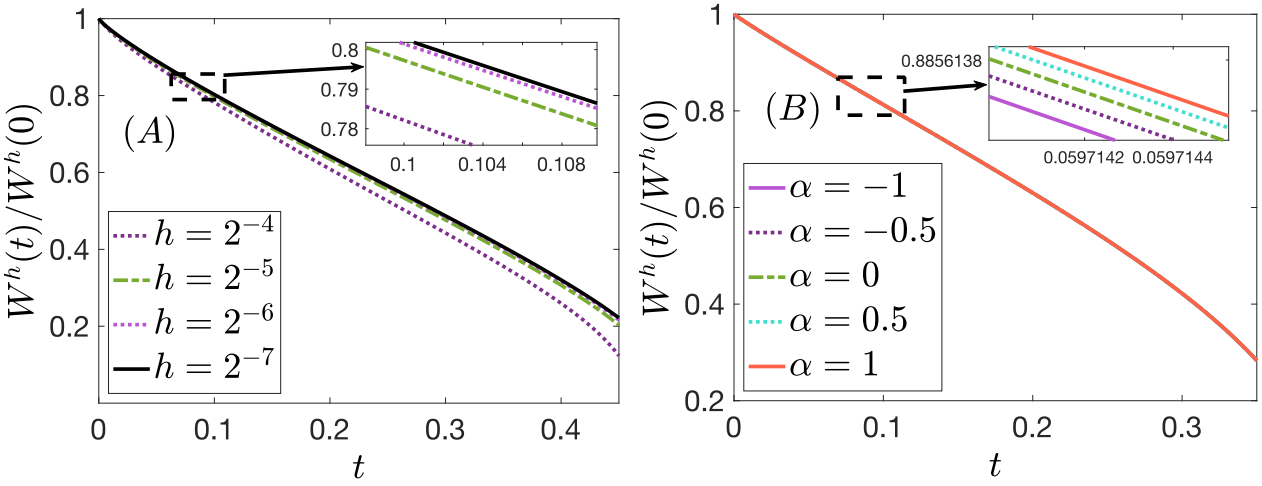



**Figure 5.8.** Normalized energy for (5.30): (A) Case I with $\beta = 1/7, \alpha = 0$; (B) Case II with different values of $\alpha$. The mesh sizes in panel (B) are $(h, \tau) = (2^{-7}, 4^{-7})$.

Figures 5.7–5.8 show the morphological evolution and normalized energy of an ellipse with major axis 4 and minor axis 1 evolving by *anisotropic curvature flow* under (5.30). The anisotropies are (A) Case I with $\beta = 1/7$ and (B) Case II. Figures 5.7–5.8 show that

- the normalized energy decreases monotonically when $\hat{\gamma}(\theta)$ satisfies the energy stability condition (5.35);
- the energy decay curves for (5.30) are very similar for different values of $\alpha$, indicating robustness with respect to this parameter.

**5.6.5. Morphological evolution under anisotropic curvature flow.** We now use (5.30) to simulate the morphological evolution of closed curves driven by *anisotropic curvature flow*. Unless otherwise stated, the mesh sizes are $(h, \tau) = (2^{-7}, 4^{-7})$.

We first consider the following nonconvex initial curve with large curvature variations [127]:

$$\begin{cases} x = \cos(2\pi\rho), & \rho \in [0, 1], \\ y = \frac{1}{2}\sin(2\pi\rho) + \sin(\cos(2\pi\rho)) + \sin(2\pi\rho)\left(\frac{1}{5} + \sin(2\pi\rho)\sin^2(6\pi\rho)\right), \end{cases} \tag{5.97}$$

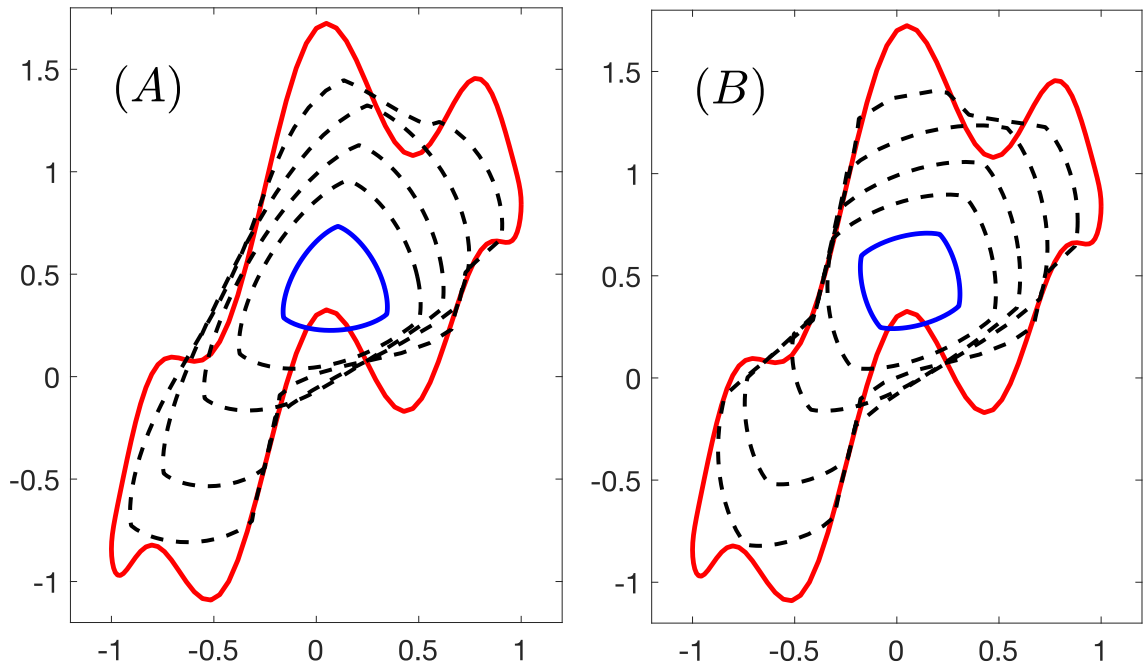



**Figure 5.9.** Morphological evolution of a nonconvex initial curve with large curvature variations under anisotropic curvature flow computed with (5.30), with $\alpha = 2$. Red curves show the initial shapes, blue curves show the numerical solutions at $t = 0.32$, and black dashed curves show intermediate stages.

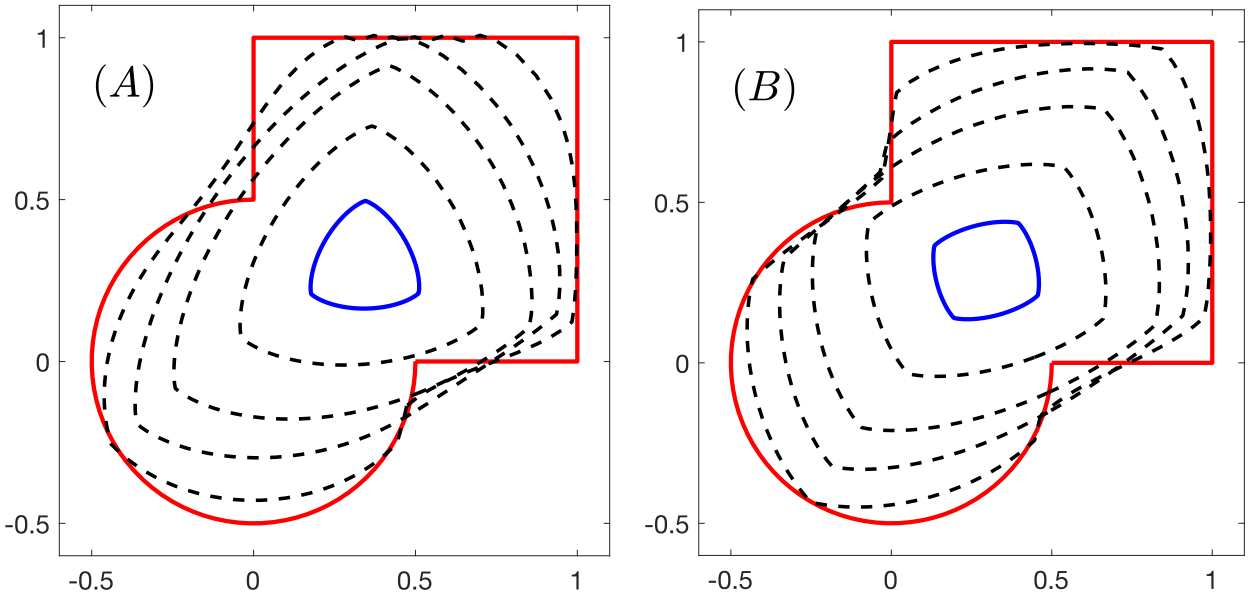



**Figure 5.10.** Morphological evolution of an initial curve with $C^0$ regularity under anisotropic curvature flow computed with (5.30), with $\alpha = -2$. Red curves show the initial shapes, blue curves show the numerical solutions at $t = 0.24$, and black dashed curves show intermediate stages.

We also consider an initial curve with only $C^0$ regularity, containing corners and indentations. The corresponding numerical results are shown in Figures 5.9 and 5.10, respectively.

The simulations in Figures 5.9–5.10 use two surface energy densities: (A) $\hat{\gamma}(\theta) = 1 + \frac{1}{7}\cos 3\theta$ and (B) $\hat{\gamma}(\theta) = 1 + \frac{1}{12}\cos 4(\theta + \frac{\pi}{6})$. The curves gradually shrink under anisotropic curvature flow, and

different initial curves approach the same limiting shape for a given anisotropy, namely the *Wulff shape* determined by $\hat{\gamma}(\theta)$ [118].

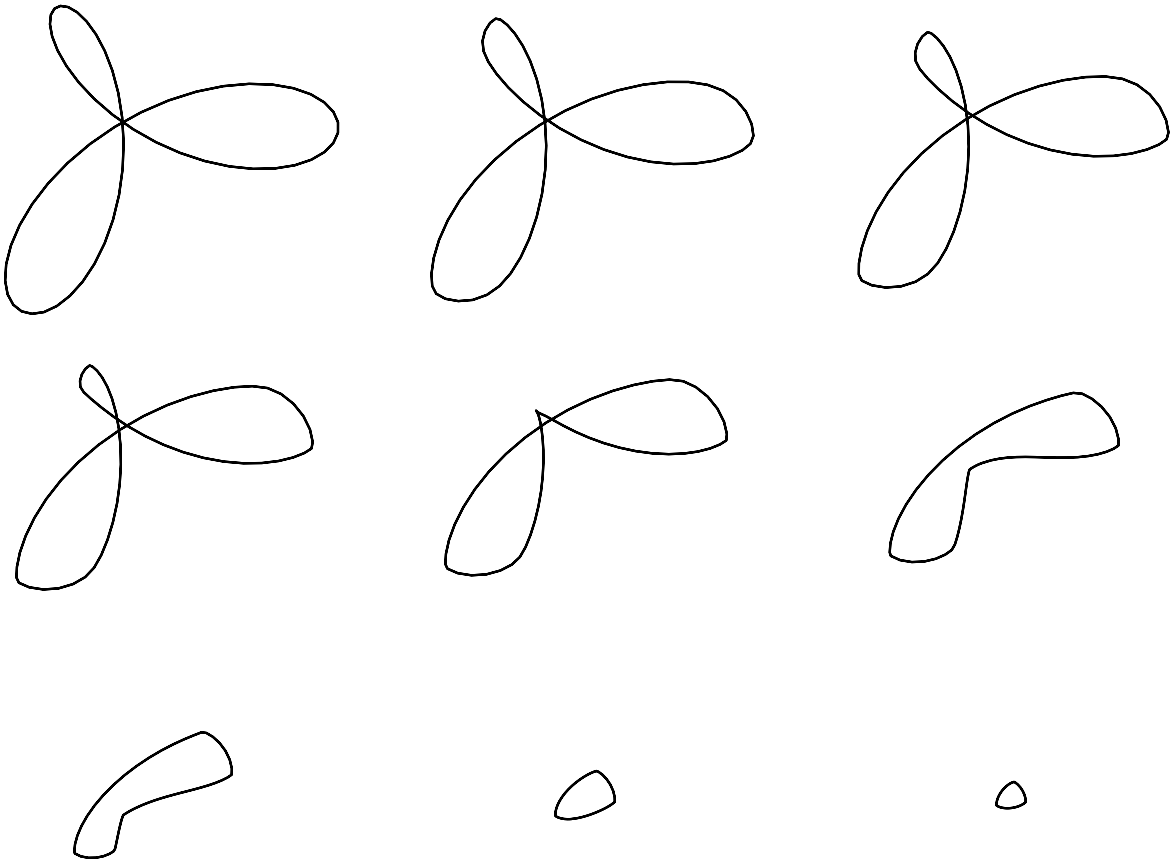


**Figure 5.11.** Anisotropic evolution of a self-intersecting initial curve at $t = 0, 0.028, 0.056, 0.084, 0.112, 0.2, 0.3, 0.4, 0.42$. The surface energy density is the threefold anisotropy $\hat{\gamma}(\theta) = 1 + \frac{1}{9}\cos 3\theta$. The remaining parameters are $\alpha = -1$, $h = 2^{-7}$, $\tau = 0.005$.

Self-intersecting curves can develop singularities during curvature-driven evolution. The complicated local geometry near these points presents substantial numerical challenges. Figure 5.11 shows the evolution under *anisotropic curvature flow* of an initial curve with a triple self-intersection point. A similar isotropic example appears in Figure 7.2 of [55]. The numerical results demonstrate that the method can capture the formation and development of cusp singularities in the anisotropic setting.

**5.6.6. Numerical results for other anisotropic geometric flows.** We perform numerical experiments for two area-preserving anisotropic geometric flows: *area-preserving anisotropic curvature flow* and *anisotropic surface diffusion*. To assess area conservation numerically, we define the normalized area loss

$$\left.\frac{\Delta A^h(t)}{A^h(0)}\right|_{t=t_m} := \frac{A^m - A^0}{A^0}, \qquad \forall m \geq 0. \tag{5.98}$$

5.6.6.1. *Area-preserving anisotropic curvature flow.* Figure 5.12 shows the morphological evolution of an ellipse with major axis 8 and minor axis 1 under *area-preserving anisotropic curvature flow*. We use the *$l^4$-norm metric anisotropy* $\hat{\gamma}(\theta) = \sqrt[4]{n_1^4 + n_2^4}$, where $\boldsymbol{n} = (n_1, n_2)^T = (-\sin\theta, \cos\theta)^T$ [9]. Figure 5.13(A) plots the normalized area loss and Newton iteration count. The area loss is of order $10^{-15}$, close to roundoff error, demonstrating area conservation to machine precision. The Newton iteration count

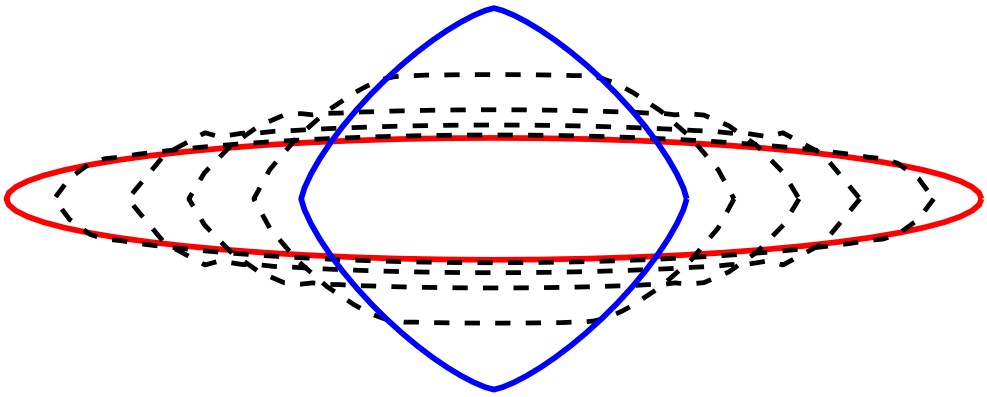


**Figure 5.12.** Morphological evolution of an ellipse with major axis 8 and minor axis 1 under area-preserving anisotropic curvature flow computed with (5.74). The surface energy density is the $l^4$-norm metric anisotropy $\hat{\gamma}(\theta) = \sqrt[4]{n_1^4 + n_2^4}$, where $\boldsymbol{n} = (n_1, n_2)^T = (-\sin\theta, \cos\theta)^T$. Red and blue curves show the initial shape and numerical equilibrium, respectively, and black dashed curves show intermediate stages. The parameters are $\alpha = 2.5, (h, \tau) = (2^{-6}, 4^{-6})$.

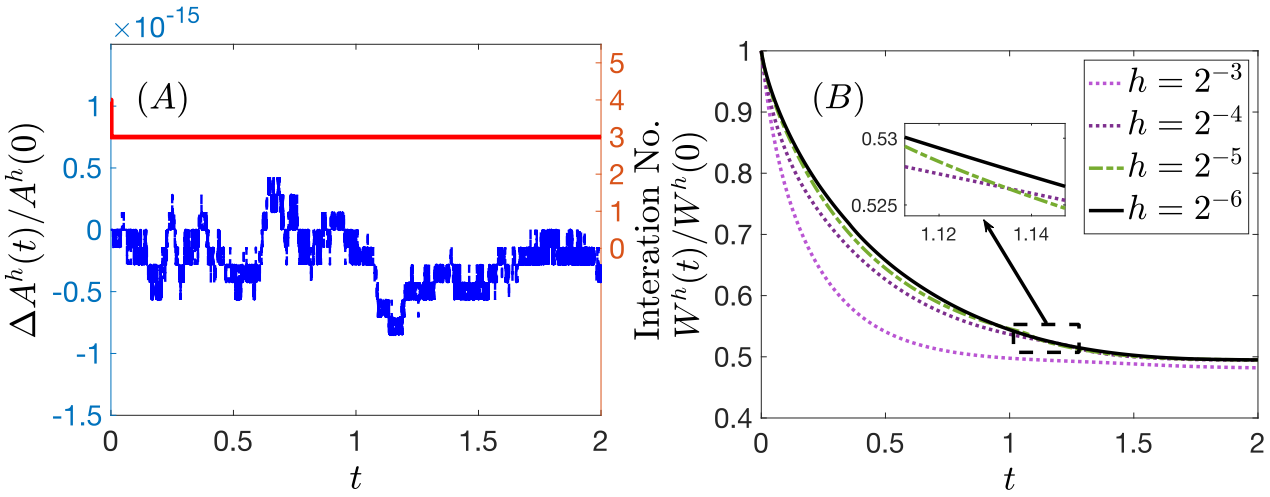



**Figure 5.13.** Time evolution for the simulation in Figure 5.12: (A) normalized area loss (blue dashed curve) and iteration count (red curve); (B) normalized energy. The scheme is (5.74).

quickly decreases from 4 to 3. Meanwhile, the normalized energy decreases monotonically, as shown in Figure 5.13(B).

We also use (5.74) to simulate the morphological evolution of more complex initial curves under area-preserving anisotropic curvature flow. Figures 5.14–5.15 show the results for the following two curves:

- A *bowtie-shaped curve*:

$$\begin{cases} x = \cos(2\pi\rho), \\ y = 2\sin(2\pi\rho) - 1.9\sin^3(2\pi\rho), \end{cases} \qquad \rho \in [0, 1]; \tag{5.99}$$

- A *flower-shaped curve*:

$$\begin{cases} x = \big(2 + \cos(12\pi\rho)\big)\cos(2\pi\rho), \\ y = \big(2 + \cos(12\pi\rho)\big)\sin(2\pi\rho), \end{cases} \qquad \rho \in [0, 1]. \tag{5.100}$$

Both curves gradually approach the Wulff shape associated with the prescribed anisotropy, consistent with the theoretical prediction [144].

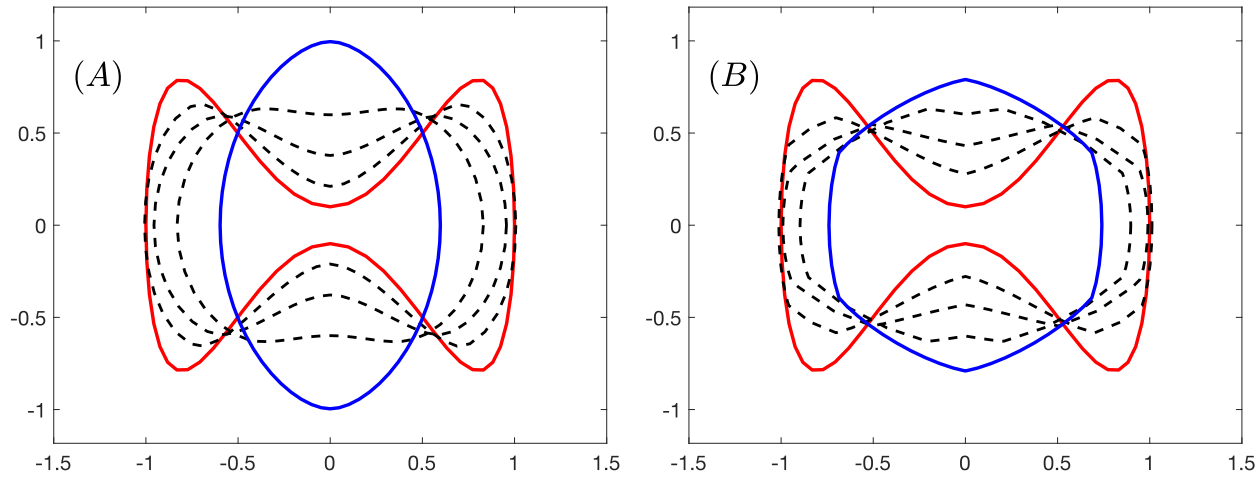



**Figure 5.14.** Morphological evolution of a bowtie-shaped initial curve under area-preserving anisotropic curvature flow with (A) $\hat{\gamma}(\theta) = 1 + \frac{1}{28}\cos 2\theta$ and (B) $\hat{\gamma}(\theta) = 1 + \frac{1}{30}\cos 6\theta$. Red and blue curves show the initial shapes and numerical equilibria, respectively, and black dashed curves show intermediate stages. The remaining parameters are $\alpha = 0.5, (h, \tau) = (2^{-6}, 4^{-6})$.

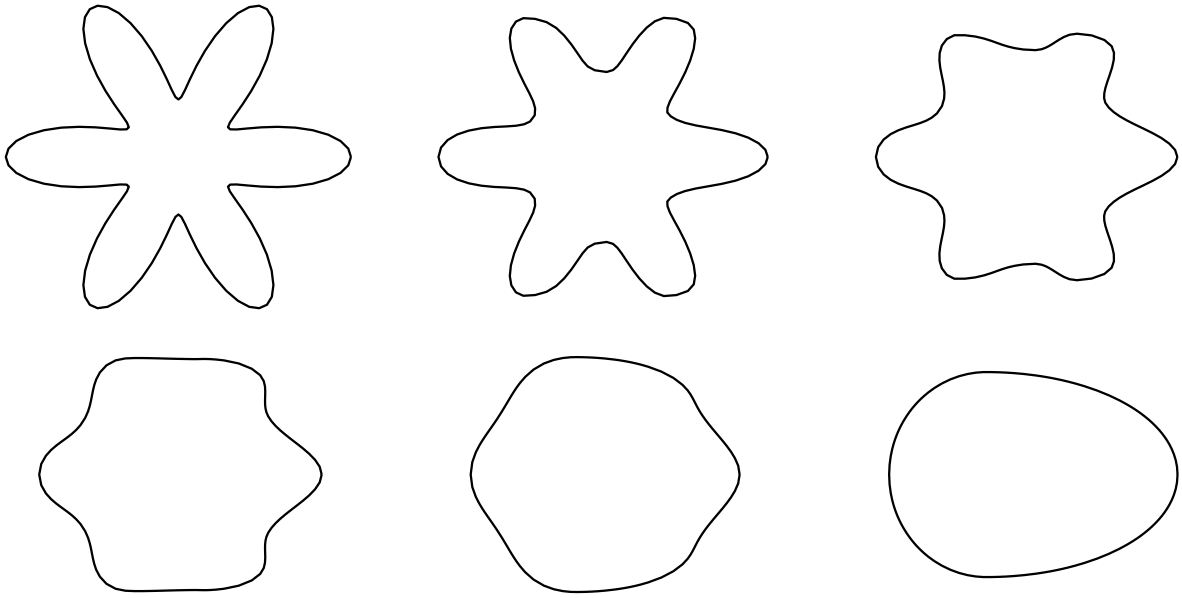


**Figure 5.15.** Snapshots of a flower-shaped initial curve evolving by area-preserving anisotropic curvature flow with the anisotropy in Case II, at $t = 0, 0.05, 0.15, 0.25, 0.4, 2.5$. The remaining parameters are $\alpha = -0.5, h = 2^{-7}, \tau = 0.005$.

5.6.6.2. *Anisotropic surface diffusion.* Figures 5.16–5.17 show the evolution of an ellipse with major-to-minor axis ratio 8 : 1 under *anisotropic surface diffusion*, together with the normalized area loss, iteration count, and normalized energy. The surface energy density is Case I with $\beta = 1/9$. The results in Figure 5.17 verify area conservation and energy dissipation when (5.35) holds.

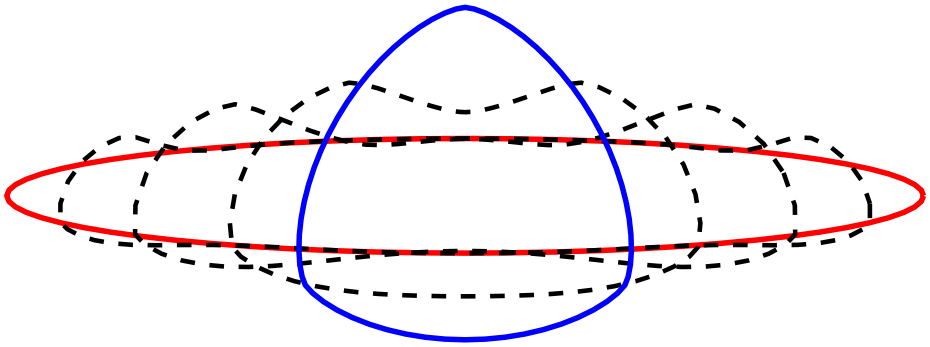


**Figure 5.16.** Morphological evolution of an ellipse with major axis 8 and minor axis 1 under anisotropic surface diffusion with Case I and $\beta = 1/9$. Red and blue curves show the initial shape and numerical equilibrium, respectively, and black dashed curves show intermediate stages. The mesh sizes are $(h, \tau) = (2^{-6}, 4^{-6})$.

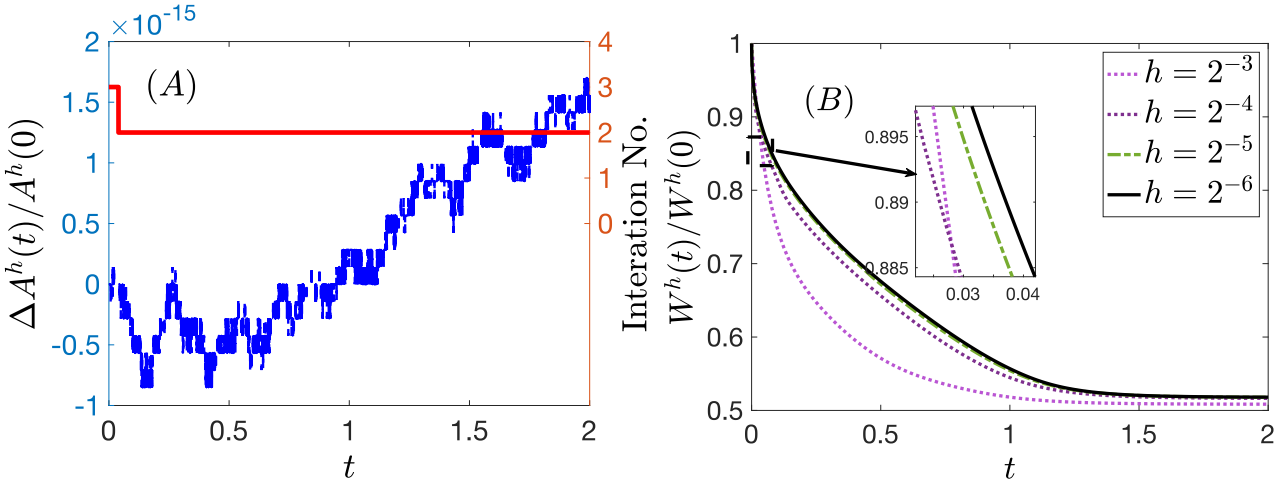



**Figure 5.17.** Time evolution for the anisotropic surface diffusion simulation in Figure 5.16: (A) normalized area loss (blue dashed curve) and iteration count (red curve); (B) normalized energy. The scheme is (5.78).

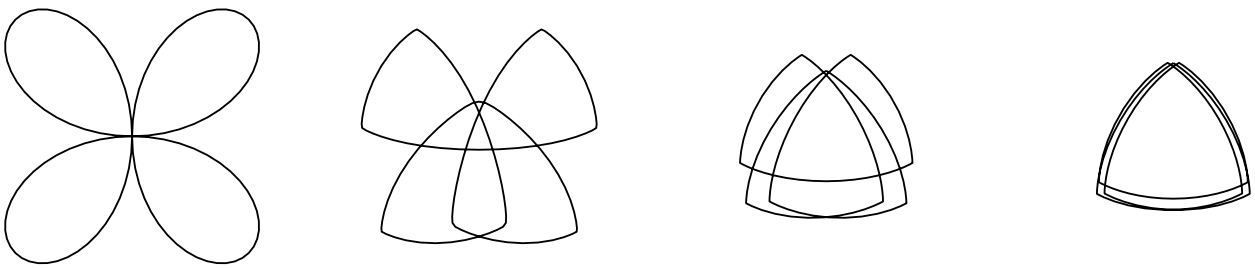


**Figure 5.18.** Anisotropic surface diffusion of a quadrifolium with Case I at $t = 0, 0.15, 0.5, 0.9$. The parameters are $\alpha = 0.5, \beta = 1/5, h = 2^{-7}, \tau = 0.001$.

Figure 5.18 shows the evolution of a quadrifolium under surface diffusion. Escher et al. [61] and Barrett et al. [21] studied this curve under isotropic surface diffusion and observed a limiting shape consisting of a triply covered circle. Our results show qualitatively similar behavior under anisotropic surface diffusion: for positive times, the winding number about the origin remains unchanged, and the limiting curve approaches a triply covered Wulff shape associated with the prescribed anisotropy; see Figure 5.18.

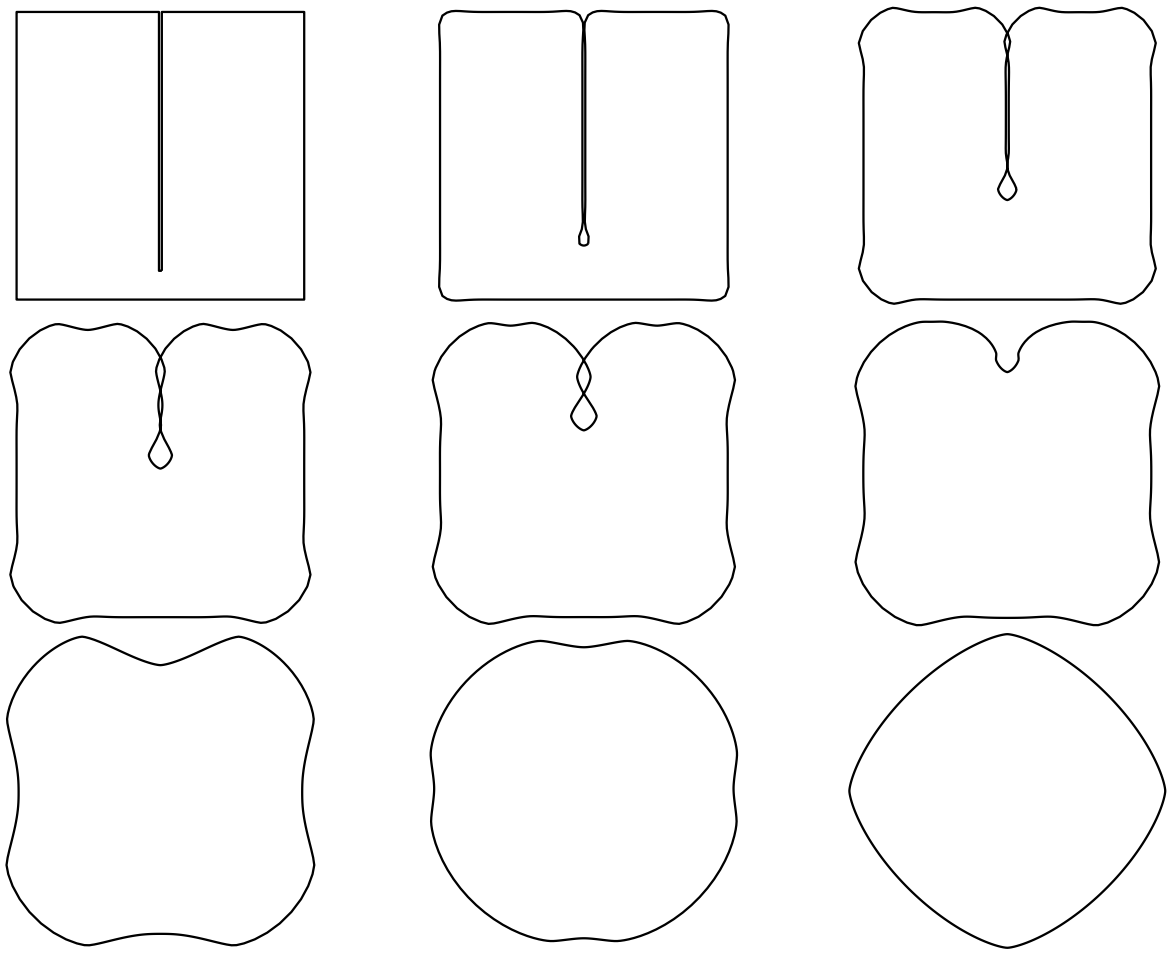


**Figure 5.19.** Anisotropic surface diffusion of an almost slit domain with the fourfold anisotropy $\hat{\gamma}(\theta) = 1 + \frac{1}{16}\cos 4\theta$, at $t = 0, 5\times10^{-6}, 7\times10^{-5}, 2.5\times10^{-4}, 5\times10^{-4}, 7.5\times10^{-4}, 0.002, 0.02, 0.1$. The parameters are $\alpha = 1, h = 1/288, \tau = 1\times10^{-6}$.

The initial curve in Figure 5.19 is obtained by removing a thin rectangular region ($0.02 \times 1.8$) from a square of side length 2. Bänsch [6] calls this an *almost slit domain*. Previous studies [6, 21] showed that the evolving curve crosses itself and undergoes pinch-off under isotropic surface diffusion. Our numerical results exhibit the same behavior under anisotropic surface diffusion. The proposed algorithm also ensures exact area conservation throughout the evolution, improving on the methods used in [6, 21].

We also simulate Bernoulli's lemniscate, as shown in Figure 5.20. Its signed area is zero. Since *anisotropic surface diffusion* preserves area while decreasing the total energy, or weighted perimeter, we expect this curve to shrink to a point. The numerical results support this expectation: the enclosed signed area remains of order $10^{-16}$ throughout the simulation and is therefore zero to machine precision. Before the final collapse, the two lobes gradually approach Wulff shapes associated with the prescribed anisotropy. The anisotropy also induces a slow overall rotation during evolution. This differs from the isotropic case, in which the curve shrinks in place without changing its orientation; see [61].

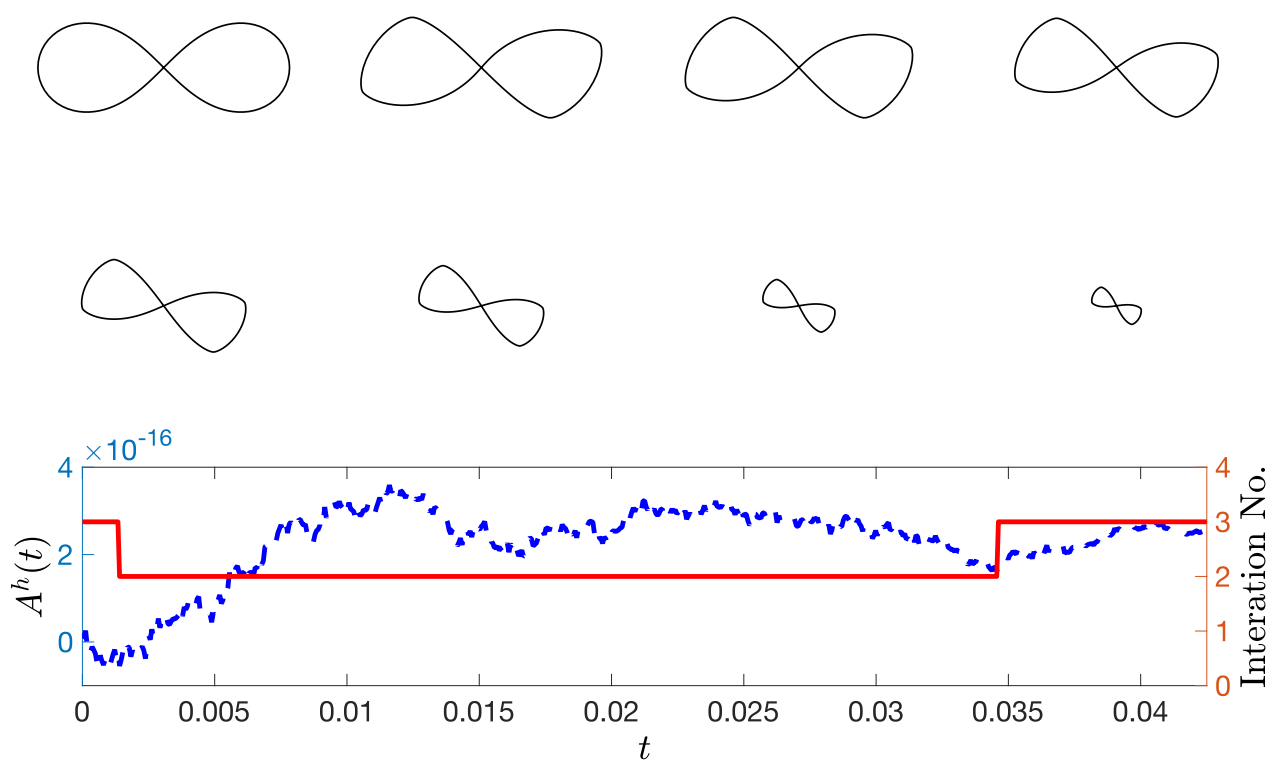



**Figure 5.20.** Evolution of Bernoulli's lemniscate under anisotropic surface diffusion with Case I, at $t = 0, 0.008, 0.015, 0.025, 0.035, 0.04, 0.0425$. The parameters are $\beta = 1/9, (h, \tau) = (2^{-7}, 4^{-7})$.

## 5.7. Chapter summary

We have analyzed and compared structure-preserving parametric finite element methods for anisotropic geometric flows. The hyperparameter $\alpha$ gives a unified representation of this family of surface energy matrices and places the associated schemes within a common analytical framework. We proved that $3\hat{\gamma}(\theta) - \hat{\gamma}(\theta - \pi) > 0$ is a common energy stability condition for all these matrices. For the symmetric surface energy matrix, this condition can be relaxed to $3\hat{\gamma}(\theta) - \hat{\gamma}(\theta - \pi) \geq 0$, which is necessary and sufficient for the local energy estimate and thus optimal within that framework. Apart from mesh quality, the methods exhibit consistent accuracy, computational efficiency, and structure-preserving behavior across the tested values of $\alpha$. The approach extends naturally to general anisotropic geometric flows, including area-preserving anisotropic curvature flow and anisotropic surface diffusion, and provides a framework for constructing structure-preserving numerical schemes for general anisotropic curvature-driven problems.

CHAPTER 6

# Structure-preserving parametric approximation based on the $\alpha$-surface energy matrix: anisotropic surface evolution

The main objective of this chapter is to extend the *structure-preserving parametric finite element scheme* (5.30) *based on the $\alpha$-surface energy matrix* for planar curve evolution to surface evolution in three dimensions. As in the two-dimensional setting, we consider an anisotropic surface energy density of the form $\hat{\gamma}(\theta, \phi)$, where $(\theta, \phi)$ are the spherical coordinates of the outward unit normal $\boldsymbol{n}$. We propose and analyze a *structure-preserving parametric finite element method* for *anisotropic surface diffusion*. The method preserves volume and is unconditionally energy stable under mild conditions on $\hat{\gamma}(\theta, \phi)$. Although extending $\hat{\boldsymbol{G}}_k^\alpha$ to three dimensions through the Cahn–Hoffman $\boldsymbol{\xi}$-vector is straightforward, several technical difficulties remain.

First, the arc-length derivative $\partial_s$ must be replaced by the surface gradient $\nabla_\Gamma$, whose mathematical properties are more complex. Second, the conservative formulations of the weighted curvature vector $\mu\boldsymbol{n}$ in the preceding chapters depend on $\partial_s$, so an appropriate extension involving $\nabla_\Gamma$ is needed. Finally, and most importantly, the minimal stabilizing function in two dimensions can be expressed in terms of the normal angle $\theta$. This representation is specific to two dimensions. We must therefore extend its definition to three dimensions and establish its existence, which requires new proof techniques.

This chapter is organized as follows. We first present the geometric evolution equations for *anisotropic surface diffusion* in three dimensions. We then define the extended $\alpha$-surface energy matrix and use it to derive a conservative strong formulation of $\mu\boldsymbol{n}$. Based on this formulation, we develop the corresponding weak formulation and fully discrete parametric finite element scheme, and analyze its energy stability in detail. Finally, we present a range of numerical examples to demonstrate the efficiency and structure-preserving properties of the method.

## 6.1. Geometric evolution equations

Let $\Gamma(t)$ be a closed, orientable, time-dependent $C^2$-surface in $\mathbb{R}^3$, parameterized by the position vector $\boldsymbol{X}(\boldsymbol{\rho}, t)$ as follows:

$$\begin{aligned} &\boldsymbol{X}(\cdot, t)\colon \Gamma_0 \to \mathbb{R}^3, \qquad \forall t > 0, \\ &\qquad \boldsymbol{\rho} \mapsto \boldsymbol{X}(\boldsymbol{\rho}, t) \coloneqq (X_1(\boldsymbol{\rho}, t), X_2(\boldsymbol{\rho}, t), X_3(\boldsymbol{\rho}, t))^T, \end{aligned} \tag{6.1}$$

where $\boldsymbol{\rho} \in \Gamma_0 \subset \mathbb{R}^3$ and $\Gamma_0$ is the initial closed, orientable surface.

For a differentiable scalar function $f$ on $\Gamma(t)$, the surface gradient $\nabla_\Gamma$ is defined by

$$\nabla_\Gamma f = \nabla_{\Gamma(t)} f \coloneqq \nabla \bar{f} - (\nabla \bar{f} \cdot \boldsymbol{n})\boldsymbol{n}, \tag{6.2}$$

where $\bar{f}$ is a smooth extension of $f$ to a neighborhood of $\Gamma(t)$ in $\mathbb{R}^3$, $\boldsymbol{n}$ is the outward unit normal to $\Gamma(t)$, and $\nabla$ denotes the Euclidean gradient in $\mathbb{R}^3$ [29, 94].

For convenience, write $\nabla_\Gamma f = (\underline{D}_1 f, \underline{D}_2 f, \underline{D}_3 f)^T$. For a differentiable vector field $\boldsymbol{f} = (f_1, f_2, f_3)^T$, its surface Jacobian matrix and surface divergence are defined by

$$\nabla_\Gamma \boldsymbol{f} = \nabla_{\Gamma(t)} \boldsymbol{f} \coloneqq \begin{bmatrix} (\nabla_\Gamma f_1)^T \\ (\nabla_\Gamma f_2)^T \\ (\nabla_\Gamma f_3)^T \end{bmatrix} = \begin{bmatrix} \underline{D}_1 f_1 & \underline{D}_2 f_1 & \underline{D}_3 f_1 \\ \underline{D}_1 f_2 & \underline{D}_2 f_2 & \underline{D}_3 f_2 \\ \underline{D}_1 f_3 & \underline{D}_2 f_3 & \underline{D}_3 f_3 \end{bmatrix}, \tag{6.3a}$$

$$\nabla_\Gamma \cdot \boldsymbol{f} = \nabla_{\Gamma(t)} \cdot \boldsymbol{f} \coloneqq \underline{D}_1 f_1 + \underline{D}_2 f_2 + \underline{D}_3 f_3. \tag{6.3b}$$

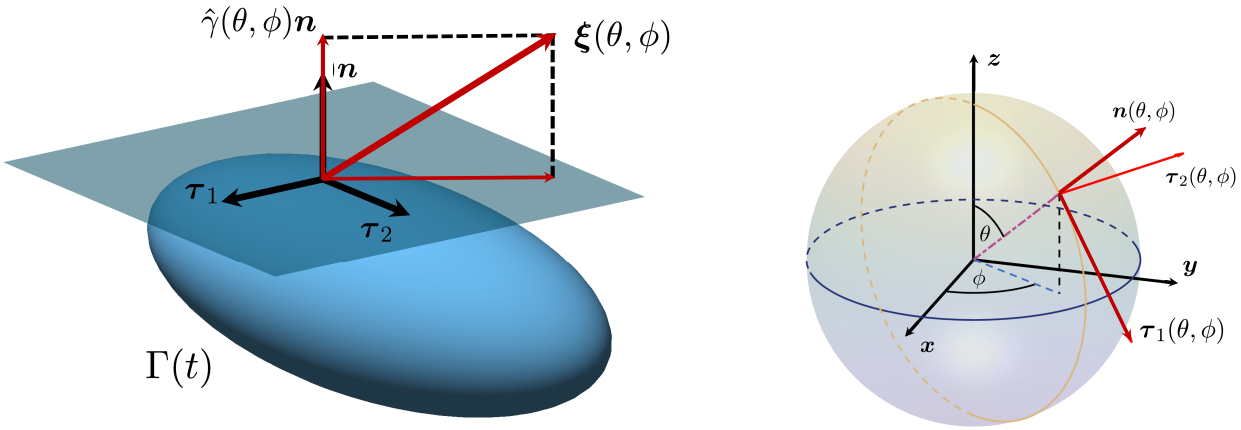



**Figure 6.1.** Anisotropic surface diffusion of a closed, orientable surface $\Gamma(t)$ in $\mathbb{R}^3$ with anisotropic surface energy $\hat{\gamma}(\theta,\phi)$ (left), and the spherical-coordinate representation of the local orthonormal frame $\{\boldsymbol{n},\boldsymbol{\tau}_1,\boldsymbol{\tau}_2\}$ (right). Here $\boldsymbol{\xi}(\theta,\phi)$ denotes the Cahn–Hoffman $\boldsymbol{\xi}$-vector.

For a matrix field $\boldsymbol{F} = (F_{ij})$, we take its surface divergence row by row, so that $(\nabla_\Gamma \cdot \boldsymbol{F})_i = \sum_j \underline{D}_j F_{ij}$. For a scalar function $f$ on $\Gamma(t)$, the Laplace–Beltrami operator $\Delta_\Gamma$ is defined by

$$\Delta_\Gamma f = \Delta_{\Gamma(t)} f := \nabla_\Gamma \cdot (\nabla_\Gamma f) = \underline{D}_1(\underline{D}_1 f) + \underline{D}_2(\underline{D}_2 f) + \underline{D}_3(\underline{D}_3 f). \tag{6.4}$$

As illustrated in Figure 6.1, we consider the evolution of $\Gamma(t)$ under *anisotropic surface diffusion*, governed by

$$V_n = \Delta_\Gamma \mu, \tag{6.5}$$

where $\mu$ is the weighted curvature. To characterize $\mu$, we introduce the Cahn–Hoffman $\boldsymbol{\xi}$-vector associated with the anisotropic surface energy density $\hat{\gamma}(\theta,\phi)$. For the analysis, assume that $\hat{\gamma}$ is the angular representation of a strictly positive $C^2$ density on $\mathbb{S}^2$. We first define its positively homogeneous extension of degree one:

$$\gamma(\boldsymbol{p}) := \begin{cases} |\boldsymbol{p}|\hat{\gamma}(\theta,\phi), & \forall \boldsymbol{p} \in \mathbb{R}^3 \backslash \{\boldsymbol{0}\}, \\ 0, & \boldsymbol{p} = \boldsymbol{0}, \end{cases} \tag{6.6}$$

where $(|\boldsymbol{p}|,\theta,\phi)$ are the spherical coordinates of $\boldsymbol{p}$. The Cahn–Hoffman $\boldsymbol{\xi}$-vector is then defined by

$$\boldsymbol{\xi} = (\xi_1,\xi_2,\xi_3)^T = \boldsymbol{\xi}(\theta,\phi) := \nabla\gamma(\boldsymbol{p})\Big|_{\boldsymbol{p}=\boldsymbol{n}(\theta,\phi)}, \qquad (\theta,\phi) \in [0,\pi] \times 2\pi\mathbb{T}. \tag{6.7}$$

To obtain an explicit expression for $\boldsymbol{\xi}$, we introduce the local orthonormal frame $\{\boldsymbol{n},\boldsymbol{\tau}_1,\boldsymbol{\tau}_2\}$ shown in the right panel of Figure 6.1:

$$\boldsymbol{n}(\theta,\phi) = (\sin\theta\cos\phi, \sin\theta\sin\phi, \cos\theta)^T, \tag{6.8a}$$

$$\boldsymbol{\tau}_1(\theta,\phi) = (\cos\theta\cos\phi, \cos\theta\sin\phi, -\sin\theta)^T, \tag{6.8b}$$

$$\boldsymbol{\tau}_2(\theta,\phi) = (-\sin\phi, \cos\phi, 0)^T, \tag{6.8c}$$

where $(\theta,\phi) \in [0,\pi] \times 2\pi\mathbb{T}$ and $\{\boldsymbol{\tau}_1,\boldsymbol{\tau}_2\}$ is an orthonormal basis of the tangent space. The angular frame is nonunique at the poles $\theta = 0,\pi$; intrinsic quantities and formulas containing $1/\sin\theta$ are understood in a regular local chart or by continuous extension. At a pole, a condition of the form $\nabla\hat{\gamma} = \boldsymbol{0}$ means that the intrinsic gradient of the density vanishes. In this frame, the Cahn–Hoffman $\boldsymbol{\xi}$-vector has the decomposition [94]

$$\boldsymbol{\xi}(\theta,\phi) := \hat{\gamma}(\theta,\phi)\boldsymbol{n}(\theta,\phi) + \frac{\partial\hat{\gamma}(\theta,\phi)}{\partial\theta}\boldsymbol{\tau}_1(\theta,\phi) + \frac{1}{\sin\theta}\frac{\partial\hat{\gamma}(\theta,\phi)}{\partial\phi}\boldsymbol{\tau}_2(\theta,\phi). \tag{6.9}$$

According to [84], the weighted curvature $\mu$ can be expressed in terms of $\boldsymbol{\xi}$ as

$$\mu = \nabla_\Gamma \cdot \boldsymbol{\xi}, \tag{6.10}$$

where $\nabla_\Gamma\cdot$ denotes the surface divergence on $\Gamma$. Thus, the anisotropic surface diffusion equation (6.5) can be rewritten as the geometric partial differential equations

$$\boldsymbol{n}\cdot\partial_t\boldsymbol{X} = \Delta_\Gamma\mu, \qquad \forall t>0, \tag{6.11a}$$

$$\mu = \nabla_\Gamma\cdot\boldsymbol{\xi}, \tag{6.11b}$$

where $\boldsymbol{\xi}$ is the Cahn–Hoffman $\boldsymbol{\xi}$-vector given in (6.9).

### 6.2. The $\alpha$-surface energy matrix and a conservative formulation

To derive a conservative formulation of anisotropic surface diffusion (6.11), we introduce the following $\alpha$-surface energy matrix:

$$\hat{\boldsymbol{G}}_k^\alpha(\theta,\phi) = \hat\gamma(\theta,\phi)I_3 - \boldsymbol{n}(\theta,\phi)\boldsymbol{\xi}(\theta,\phi)^T + \alpha\boldsymbol{\xi}(\theta,\phi)\boldsymbol{n}(\theta,\phi)^T + k(\theta,\phi)\boldsymbol{n}(\theta,\phi)\boldsymbol{n}(\theta,\phi)^T, \tag{6.12}$$

where $\alpha\in\mathbb{R}$, $k(\theta,\phi)\colon[0,\pi]\times 2\pi\mathbb{T}\to\mathbb{R}_{\geq 0}$ is a prescribed nonnegative stabilizing function, and $\boldsymbol{\xi}(\theta,\phi)$ is the Cahn–Hoffman $\boldsymbol{\xi}$-vector in (6.9).

Lemma 6.1 (Product rule, [29]). *Let $\Gamma\subset\mathbb{R}^d$ $(d\geq 2)$ be a closed, orientable $C^2$-manifold of codimension one. Let $\boldsymbol{f},\boldsymbol{g}\colon\Gamma\to\mathbb{R}^d$, $\boldsymbol{F}\colon\Gamma\to\mathbb{R}^{d\times d}$ be $C^1$ functions. Then the following product rules hold:*

$$\nabla_\Gamma(\boldsymbol{f}\cdot\boldsymbol{g}) = (\nabla_\Gamma\boldsymbol{f})^T\boldsymbol{g} + (\nabla_\Gamma\boldsymbol{g})^T\boldsymbol{f}, \tag{6.13a}$$

$$\nabla_\Gamma\cdot\left(\boldsymbol{F}^T\boldsymbol{g}\right) = (\nabla_\Gamma\cdot\boldsymbol{F})\cdot\boldsymbol{g} + \boldsymbol{F}:\nabla_\Gamma\boldsymbol{g}. \tag{6.13b}$$

Theorem 6.1. *The weighted curvature $\mu$ satisfies the geometric identity*

$$\mu\boldsymbol{n} = -\nabla_\Gamma\cdot\left(\hat{\boldsymbol{G}}_k^\alpha(\theta,\phi)\nabla_\Gamma\boldsymbol{X}\right), \qquad \forall\alpha\in\mathbb{R}. \tag{6.14}$$

Proof. Combining the identity $\hat\gamma(\theta,\phi) = \boldsymbol{\xi}\cdot\boldsymbol{n}$ with the geometric identity

$$\nabla_\Gamma\boldsymbol{X} = I_3 - \boldsymbol{n}\boldsymbol{n}^T, \tag{6.15}$$

we obtain

$$\begin{aligned}\hat{\boldsymbol{G}}_k^\alpha(\theta,\phi)\nabla_\Gamma\boldsymbol{X} &= \left(\hat\gamma(\theta,\phi)I_3 - \boldsymbol{n}\boldsymbol{\xi}^T + \alpha\boldsymbol{\xi}\boldsymbol{n}^T + k(\theta,\phi)\boldsymbol{n}\boldsymbol{n}^T\right)\left(I_3-\boldsymbol{n}\boldsymbol{n}^T\right)\\ &= \hat\gamma(\theta,\phi)I_3 - \boldsymbol{n}\boldsymbol{\xi}^T - \hat\gamma(\theta,\phi)\boldsymbol{n}\boldsymbol{n}^T + (\boldsymbol{\xi}\cdot\boldsymbol{n})\boldsymbol{n}\boldsymbol{n}^T\\ &= \hat\gamma(\theta,\phi)I_3 - \boldsymbol{n}\boldsymbol{\xi}^T.\end{aligned} \tag{6.16}$$

It therefore suffices to prove

$$\mu\boldsymbol{n} = -\nabla_\Gamma\cdot\left(\hat\gamma(\theta,\phi)I_3 - \boldsymbol{n}\boldsymbol{\xi}^T\right). \tag{6.17}$$

Applying the product rule (6.13) gives

$$\begin{aligned}\nabla_\Gamma\cdot\left(\hat\gamma(\theta,\phi)I_3\right) &= \nabla_\Gamma\hat\gamma(\theta,\phi) = \nabla_\Gamma(\boldsymbol{\xi}\cdot\boldsymbol{n})\\ &= (\nabla_\Gamma\boldsymbol{\xi})^T\boldsymbol{n} + (\nabla_\Gamma\boldsymbol{n})^T\boldsymbol{\xi}\\ &= (\nabla_\Gamma\boldsymbol{n})^T\boldsymbol{\xi}\end{aligned} \tag{6.18}$$

Consequently,

$$\begin{aligned}\nabla_\Gamma\cdot\left(\hat\gamma(\theta,\phi)I_3 - \boldsymbol{n}\boldsymbol{\xi}^T\right) &= \nabla_\Gamma\cdot\left(\hat\gamma(\theta,\phi)I_3\right) - \nabla_\Gamma\cdot\left(\boldsymbol{n}\boldsymbol{\xi}^T\right)\\ &= (\nabla_\Gamma\boldsymbol{n})^T\boldsymbol{\xi} - (\nabla_\Gamma\boldsymbol{n})\boldsymbol{\xi} - (\nabla_\Gamma\cdot\boldsymbol{\xi})\boldsymbol{n}\\ &= -\mu\boldsymbol{n}.\end{aligned} \tag{6.19}$$

The last equality follows from $\mu = \nabla_\Gamma\cdot\boldsymbol{\xi}$ and the symmetry of $\nabla_\Gamma\boldsymbol{n}$. □

Using the geometric identity (6.14), we can express the geometric evolution equations (6.11) in the following conservative strong formulation:

$$\boldsymbol{n}\cdot\partial_t\boldsymbol{X} - \Delta_\Gamma\mu = 0, \qquad \forall t>0, \tag{6.20a}$$

$$\mu\boldsymbol{n} + \nabla_\Gamma\cdot\left(\hat{\boldsymbol{G}}_k^\alpha(\theta,\phi)\nabla_\Gamma\boldsymbol{X}\right) = \boldsymbol{0}. \tag{6.20b}$$

Remark 6.1. In the isotropic case $\hat{\gamma}(\theta, \phi) \equiv 1$, the weighted curvature $\mu$ reduces to the classical mean curvature $H$, defined here as the sum of the principal curvatures. As in two dimensions, for $\alpha \leq 1$, choosing $k(\theta, \phi) \equiv 1 - \alpha \geq 0$ gives $\hat{\boldsymbol{G}}_k^\alpha(\theta, \phi) \equiv I_3$, recovering the classical BGN formulation of surface diffusion [22].

Remark 6.2. In two dimensions, every surface energy matrix $\boldsymbol{G}$ satisfying $\mu \boldsymbol{n} = -\nabla_\Gamma \cdot (\boldsymbol{G} \nabla_\Gamma \boldsymbol{X})$ can be written in the form $\boldsymbol{G}_k^\alpha$ (see Remark 5.3 in Chapter 5). This conclusion no longer holds in three dimensions, so other formulations may be possible in addition to the one proposed above.

### 6.3. Structure-preserving parametric finite element discretization

**6.3.1. The weak formulation and its properties.** To derive a weak formulation of (6.20), we introduce the following $L^2$-space on the evolving surface $\Gamma(t)$:

$$L^2(\Gamma(t)) \coloneqq \left\{ u : \Gamma(t) \to \mathbb{R} \;\middle|\; \int_{\Gamma(t)} |u|^2 \,\mathrm{d}A < +\infty \right\}, \tag{6.21}$$

equipped with the inner product

$$\Big(u, v\Big)_{\Gamma(t)} \coloneqq \int_{\Gamma(t)} uv \,\mathrm{d}A, \qquad \forall u, v \in L^2(\Gamma(t)). \tag{6.22}$$

The extensions to vector-valued and matrix-valued functions in $[L^2(\Gamma(t))]^3$ and $[L^2(\Gamma(t))]^{3\times 3}$ are straightforward. In particular, for matrix fields $\boldsymbol{U}, \boldsymbol{V} \in [L^2(\Gamma(t))]^{3\times 3}$, we define

$$\Big\langle \boldsymbol{U}, \boldsymbol{V} \Big\rangle_{\Gamma(t)} \coloneqq \int_{\Gamma(t)} \boldsymbol{U} : \boldsymbol{V} \,\mathrm{d}A, \tag{6.23}$$

where $\boldsymbol{U} : \boldsymbol{V} = \mathrm{Tr}(\boldsymbol{V}^T \boldsymbol{U})$ is the Frobenius inner product. The Sobolev spaces on $\Gamma(t)$ are defined by

$$H^1(\Gamma(t)) \coloneqq \left\{ u \in L^2(\Gamma(t)) \;\middle|\; \nabla_\Gamma u \in [L^2(\Gamma(t))]^3 \right\}, \tag{6.24a}$$

$$[H^1(\Gamma(t))]^3 \coloneqq \left\{ \boldsymbol{u} \in [L^2(\Gamma(t))]^3 \;\middle|\; \nabla_\Gamma \boldsymbol{u} \in [L^2(\Gamma(t))]^{3\times 3} \right\}. \tag{6.24b}$$

Lemma 6.2 (Divergence theorem for matrix fields). *Let $\Gamma \subset \mathbb{R}^d$ ($d \geq 2$) be a compact, orientable $C^2$-manifold of codimension one, let $\boldsymbol{F} : \Gamma \to \mathbb{R}^{d\times d}$ be a $C^1$ matrix field, and let $\boldsymbol{n}$ be the normal to $\Gamma$. If $\boldsymbol{F}\boldsymbol{n} \equiv \boldsymbol{0}$, then, for every $\boldsymbol{\omega} \in [C^1(\Gamma)]^d$, we have*

$$\int_\Gamma (\nabla_\Gamma \cdot \boldsymbol{F}) \cdot \boldsymbol{\omega} \,\mathrm{d}A = -\int_\Gamma \boldsymbol{F} : \nabla_\Gamma \boldsymbol{\omega} \,\mathrm{d}A + \int_{\partial\Gamma} (\boldsymbol{F}\boldsymbol{\nu}) \cdot \boldsymbol{\omega} \,\mathrm{d}s, \tag{6.25}$$

*where $\boldsymbol{\nu}$ is the outward unit conormal to $\partial\Gamma$.*

Proof. Applying Lemma 6.1 with $\boldsymbol{g} = \boldsymbol{\omega}$ and integrating over $\Gamma$, we obtain

$$\int_\Gamma (\nabla_\Gamma \cdot \boldsymbol{F}) \cdot \boldsymbol{\omega} \,\mathrm{d}A = -\int_\Gamma \boldsymbol{F} : \nabla_\Gamma \boldsymbol{\omega} \,\mathrm{d}A + \int_\Gamma \nabla_\Gamma \cdot \left(\boldsymbol{F}^T \boldsymbol{\omega}\right) \,\mathrm{d}A. \tag{6.26}$$

By the divergence theorem on manifolds,

$$\int_\Gamma \nabla_\Gamma \cdot \left(\boldsymbol{F}^T \boldsymbol{\omega}\right) \,\mathrm{d}A = \int_\Gamma (\boldsymbol{F}^T \boldsymbol{\omega}) \cdot H\boldsymbol{n} \,\mathrm{d}A + \int_{\partial\Gamma} (\boldsymbol{F}^T \boldsymbol{\omega}) \cdot \boldsymbol{\nu} \,\mathrm{d}s. \tag{6.27}$$

Therefore,

$$\begin{aligned} \int_\Gamma (\nabla_\Gamma \cdot \boldsymbol{F}) \cdot \boldsymbol{\omega} \,\mathrm{d}A &= -\int_\Gamma \boldsymbol{F} : \nabla_\Gamma \boldsymbol{\omega} \,\mathrm{d}A + \int_\Gamma (\boldsymbol{F}^T \boldsymbol{\omega}) \cdot H\boldsymbol{n} \,\mathrm{d}A + \int_{\partial\Gamma} (\boldsymbol{F}^T \boldsymbol{\omega}) \cdot \boldsymbol{\nu} \,\mathrm{d}s \\ &= -\int_\Gamma \boldsymbol{F} : \nabla_\Gamma \boldsymbol{\omega} \,\mathrm{d}A + \int_\Gamma H(\boldsymbol{F}\boldsymbol{n})^T \boldsymbol{\omega} \,\mathrm{d}A + \int_{\partial\Gamma} \boldsymbol{\nu}^T \boldsymbol{F}^T \boldsymbol{\omega} \,\mathrm{d}s \\ &= -\int_\Gamma \boldsymbol{F} : \nabla_\Gamma \boldsymbol{\omega} \,\mathrm{d}A + \int_{\partial\Gamma} (\boldsymbol{F}\boldsymbol{\nu}) \cdot \boldsymbol{\omega} \,\mathrm{d}s. \end{aligned} \tag{6.28}$$

□

Multiplying (6.20a) and (6.20b) by the test functions $\varphi \in H^1(\Gamma(t))$ and $\boldsymbol{\omega} \in [H^1(\Gamma(t))]^3$, respectively, and integrating over $\Gamma(t)$, we apply integration by parts and Lemma 6.2 to obtain the following weak formulation. Let the initial surface $\Gamma_0$ be closed and orientable, with $\boldsymbol{X}(\cdot,0) \coloneqq \boldsymbol{X}_0(\boldsymbol{\rho}) = \boldsymbol{\rho},\ \forall \boldsymbol{\rho} \in \Gamma_0$. Find $\big(\boldsymbol{X}(\cdot,t), \mu(\cdot,t)\big) \in [H^1(\Gamma(t))]^3 \times [H^1(\Gamma(t))]$ such that

$$\Big(\boldsymbol{n}\cdot\partial_t\boldsymbol{X}, \varphi\Big)_{\Gamma(t)} + \Big(\nabla_\Gamma\mu, \nabla_\Gamma\varphi\Big)_{\Gamma(t)} = 0, \qquad \forall \varphi \in H^1(\Gamma(t)), \tag{6.29a}$$

$$\Big(\mu\boldsymbol{n}, \boldsymbol{\omega}\Big)_{\Gamma(t)} - \Big\langle \hat{\boldsymbol{G}}^\alpha_k(\theta,\phi)\nabla_\Gamma\boldsymbol{X}, \nabla_\Gamma\boldsymbol{\omega}\Big\rangle_{\Gamma(t)} = 0, \qquad \forall \boldsymbol{\omega} \in [H^1(\Gamma(t))]^3. \tag{6.29b}$$

Proposition 6.1. *Let $\Gamma(t)$ solve the weak formulation (6.29). Denote the enclosed volume by $V(t)$ and the total surface free energy by $W(t)$, defined by*

$$V(t) \coloneqq \frac{1}{3}\int_{\Gamma(t)} \boldsymbol{X}\cdot\boldsymbol{n}\,\mathrm{d}A, \qquad W(t) \coloneqq \int_{\Gamma(t)} \hat{\gamma}(\theta,\phi)\,\mathrm{d}A. \tag{6.30}$$

*Then the enclosed volume is conserved and the total free energy is nonincreasing, namely,*

$$V(t) \equiv V(0), \qquad W(t) \le W(t') \le W(0), \qquad \forall t \ge t' \ge 0. \tag{6.31}$$

**6.3.2. The fully discrete scheme.** Let $\tau > 0$ be a uniform time step, and let $\Gamma^m$ approximate $\Gamma(t) = \boldsymbol{X}(\cdot,t)$ at the $m$th time level $t_m = m\tau,\ m \ge 0$. The polyhedral surface $\Gamma^m$ consists of a family of mutually disjoint triangular elements $\{\sigma_j^m\}_{j=1}^J$, that is,

$$\Gamma^m \coloneqq \bigcup_{j=1}^J \overline{\sigma_j^m}, \qquad \sigma_i^m \cap \sigma_j^m = \emptyset, \qquad \forall i \ne j, \tag{6.32}$$

where each triangle $\sigma_j^m = [\boldsymbol{q}_{j_1}^m, \boldsymbol{q}_{j_2}^m, \boldsymbol{q}_{j_3}^m]$ is determined by three vertices ordered counterclockwise. We denote the set of mesh vertices by $\{\boldsymbol{q}_k^m\}_{k=1}^K$.

The outward unit normal $\boldsymbol{n}^m$ on $\Gamma^m$ is a piecewise constant vector field defined by

$$\boldsymbol{n}^m|_{\sigma_j^m} = \frac{\mathcal{J}\{\sigma_j^m\}}{|\mathcal{J}\{\sigma_j^m\}|} \coloneqq \boldsymbol{n}_j^m, \qquad \forall 1 \le j \le J, \tag{6.33}$$

where $\mathcal{J}\{\sigma_j^m\}$ is the orientation vector associated with $\sigma_j^m$, given by

$$\mathcal{J}\{\sigma_j^m\} \coloneqq \Big(\boldsymbol{q}_{j_2}^m - \boldsymbol{q}_{j_1}^m\Big) \times \Big(\boldsymbol{q}_{j_3}^m - \boldsymbol{q}_{j_1}^m\Big) \tag{6.34}$$

The inclination $\theta^m$ and azimuth $\phi^m$ of $\boldsymbol{n}^m$ are determined by (6.8a).

We introduce the piecewise linear finite element space on $\Gamma^m$:

$$\mathbb{K}^m = \mathbb{K}(\Gamma^m) \coloneqq \Big\{ u \in C(\Gamma^m) \,\Big|\, u|_{\sigma_j^m} \in \mathcal{P}^1(\sigma_j^m),\ \forall 1 \le j \le J \Big\}, \tag{6.35}$$

where $\mathcal{P}^1(\sigma_j^m)$ is the space of polynomials of degree $\le 1$ on $\sigma_j^m$.

For scalar-valued and vector-valued functions in $\mathbb{K}^m/[\mathbb{K}^m]^3$, the mass-lumped inner product $(\cdot,\cdot)^h_{\Gamma^m}$ is defined by

$$\Big(u, v\Big)^h_{\Gamma^m} \coloneqq \frac{1}{3}\sum_{j=1}^J\sum_{i=1}^3 |\sigma_j^m| u((\boldsymbol{q}_{j_i}^m)^-) v((\boldsymbol{q}_{j_i}^m)^-), \tag{6.36}$$

where $u((\boldsymbol{q}_{j_i}^m)^-) \coloneqq \lim\limits_{\substack{\boldsymbol{q}\to\boldsymbol{q}_{j_i}^m \\ \boldsymbol{q}\in\sigma_j^m}} u(\boldsymbol{q})$ and $|\sigma_j^m| = \frac{1}{2}|\mathcal{J}\{\sigma_j^m\}|$ is the area of $\sigma_j^m$. For matrix-valued functions, we define $\langle\cdot,\cdot\rangle^h_{\Gamma^m}$ analogously to the continuous setting:

$$\Big\langle \boldsymbol{U}, \boldsymbol{V}\Big\rangle^h_{\Gamma^m} \coloneqq \frac{1}{3}\sum_{j=1}^J\sum_{i=1}^3 |\sigma_j^m| \boldsymbol{U}((\boldsymbol{q}_{j_i}^m)^-) : \boldsymbol{V}((\boldsymbol{q}_{j_i}^m)^-), \qquad \forall \boldsymbol{U}, \boldsymbol{V} \in [\mathbb{K}^m]^{3\times 3}. \tag{6.37}$$

Finally, on an element $\sigma = [\boldsymbol{q}_1, \boldsymbol{q}_2, \boldsymbol{q}_3]$, the discrete surface gradient $\nabla_\Gamma$ can be computed as

$$\nabla_\Gamma f|_\sigma \coloneqq f(\boldsymbol{q}_1)\frac{(\boldsymbol{q}_2-\boldsymbol{q}_3)\times\boldsymbol{n}}{|\mathcal{J}\{\sigma\}|} + f(\boldsymbol{q}_2)\frac{(\boldsymbol{q}_3-\boldsymbol{q}_1)\times\boldsymbol{n}}{|\mathcal{J}\{\sigma\}|} + f(\boldsymbol{q}_3)\frac{(\boldsymbol{q}_1-\boldsymbol{q}_2)\times\boldsymbol{n}}{|\mathcal{J}\{\sigma\}|}, \tag{6.38}$$

where $\boldsymbol{n} = \mathcal{J}\{\sigma\}/|\mathcal{J}\{\sigma\}|$ is the normal to $\sigma$. For a vector field $\boldsymbol{f} = (f_1, f_2, f_3)^T$, its discrete surface Jacobian matrix is defined by

$$\nabla_\Gamma \boldsymbol{f}|_\sigma \coloneqq \begin{bmatrix} (\nabla_\Gamma f_1)^T \\ (\nabla_\Gamma f_2)^T \\ (\nabla_\Gamma f_3)^T \end{bmatrix}, \qquad \forall \boldsymbol{f} \in [\mathcal{P}^1(\sigma)]^3. \tag{6.39}$$

The *structure-preserving parametric finite element discretization* of anisotropic surface diffusion (6.11) is given by

$$\left(\boldsymbol{n}^{m+\frac{1}{2}} \cdot \frac{\boldsymbol{X}^{m+1}-\boldsymbol{X}^m}{\tau}, \varphi^h\right)^h_{\Gamma^m} + \left(\nabla_\Gamma \mu^{m+1}, \nabla_\Gamma \varphi^h\right)^h_{\Gamma^m} = 0, \qquad \forall \varphi^h \in \mathbb{K}^m, \tag{6.40a}$$

$$\left(\mu^{m+1}\boldsymbol{n}^{m+\frac{1}{2}}, \boldsymbol{\omega}^h\right)^h_{\Gamma^m} - \left\langle \hat{\boldsymbol{G}}^\alpha_k(\theta^m, \phi^m)\nabla_\Gamma \boldsymbol{X}^{m+1}, \nabla_\Gamma \boldsymbol{\omega}^h\right\rangle^h_{\Gamma^m} = 0, \qquad \forall \boldsymbol{\omega}^h \in [\mathbb{K}^m]^3. \tag{6.40b}$$

Here the vector $\boldsymbol{n}^{m+\frac{1}{2}}$ is defined by

$$\boldsymbol{n}^{m+\frac{1}{2}} \coloneqq \frac{\mathcal{J}\{\sigma_j^m\} + 4\mathcal{J}\{\sigma_j^{m+\frac{1}{2}}\} + \mathcal{J}\{\sigma_j^{m+1}\}}{6|\mathcal{J}\{\sigma_j^m\}|}, \tag{6.41}$$

where $\sigma_j^{m+\frac{1}{2}} \coloneqq \frac{1}{2}(\sigma_j^m + \sigma_j^{m+1}) = \left[\frac{\boldsymbol{q}_{j_1}^m+\boldsymbol{q}_{j_1}^{m+1}}{2}, \frac{\boldsymbol{q}_{j_2}^m+\boldsymbol{q}_{j_2}^{m+1}}{2}, \frac{\boldsymbol{q}_{j_3}^m+\boldsymbol{q}_{j_3}^{m+1}}{2}\right]$.

Remark 6.3. The nonlinear system (6.40) is weakly implicit: its integration domain is determined explicitly, and the averaged normal is quadratic in $\boldsymbol{X}^{m+1}$, and the residuals have polynomial degree at most three in the joint unknowns $\boldsymbol{X}^{m+1}, \mu^{m+1}$. It can therefore be solved efficiently by Newton's method. The iteration is given in Appendix A.2.2.

**6.3.3. Structure preservation.** Let $V^m$ be the volume enclosed by the polyhedral surface $\Gamma^m$, and let $W^m$ be its total free energy, defined by

$$V^m \coloneqq \frac{1}{3}\left(\boldsymbol{X}^m, \boldsymbol{n}^m\right)^h_{\Gamma^m} = \frac{1}{9}\sum_{j=1}^{J}\sum_{i=1}^{3}|\sigma_j^m|\boldsymbol{q}_{j_i}^m \cdot \boldsymbol{n}_j^m, \tag{6.42a}$$

$$W^m \coloneqq \left(\hat{\gamma}(\theta^m, \phi^m), 1\right)^h_{\Gamma^m} = \sum_{j=1}^{J}|\sigma_j^m|\hat{\gamma}(\theta_j^m, \phi_j^m). \tag{6.42b}$$

The fully discrete scheme (6.40) has the following structure-preserving properties.

Theorem 6.2 (Volume conservation and energy dissipation). *The scheme* (6.40) *preserves volume, namely,*

$$V^{m+1} = V^m = \cdots = V^0, \qquad \forall m \geq 0. \tag{6.43}$$

*Moreover, if* $\alpha = -1$ *and the anisotropy* $\hat{\gamma}(\theta, \phi)$ *satisfies*

$$2\hat{\gamma}(\theta, \phi) - \hat{\gamma}(\pi - \theta, \pi + \phi) \geq 0, \qquad \forall (\theta, \phi) \in [0, \pi] \times 2\pi\mathbb{T}, \tag{6.44}$$

*then, for sufficiently large* $k(\theta, \phi)$*, the scheme* (6.40) *is unconditionally energy stable, namely,*

$$W^{m+1} \leq W^m \leq \cdots \leq W^0, \qquad \forall m \geq 0. \tag{6.45}$$

*For* $\alpha \neq -1$*, a sufficient energy stability condition is the strict form of* (6.44)*, namely,*

$$2\hat{\gamma}(\theta, \phi) - \hat{\gamma}(\pi - \theta, \pi + \phi) > 0, \qquad \forall (\theta, \phi) \in [0, \pi] \times 2\pi\mathbb{T}. \tag{6.46}$$

The proof of volume conservation is identical to that of Theorem 3.1 in [19], so we omit the details. A detailed proof of energy dissipation is given in the next section.

Remark 6.4. Using the formulation in terms of $\gamma(\boldsymbol{n})$ and taking $\alpha = -1$ recovers the symmetrized structure-preserving parametric finite element method in [12]. Compared with the symmetry assumption $\gamma(\boldsymbol{n}) = \gamma(-\boldsymbol{n})$, or equivalently $\hat{\gamma}(\theta, \phi) = \hat{\gamma}(\pi - \theta, \pi + \phi)$, required in [12], condition (6.44) is substantially weaker.

Remark 6.5. As discussed in Section 5.5, extending the scheme (6.40) to a general normal velocity law $V_n = \mathfrak{F}(\mu)$ is also straightforward. Formally, we consider $V_n = \mathfrak{F}(\mu, \Gamma)$ and treat the underlying surface $\Gamma$ explicitly at time level $m$ and the weighted curvature $\mu$ implicitly at time level $m + 1$. The construction follows the same principles, so we omit further details.

### 6.4. Proof of unconditional energy stability

**6.4.1. The minimal stabilizing function.** For a given normal $\boldsymbol{n} = \boldsymbol{n}(\theta, \phi) \in \mathbb{S}^2$, let $\boldsymbol{\tau}_1, \boldsymbol{\tau}_2$ be the associated tangent vectors defined in (6.8). For $U \in SO(3)$ and $\lambda \in \mathbb{R}_{\geq 0}$, we introduce the symmetric auxiliary matrix

$$M^{\alpha}(U, \lambda; \boldsymbol{n}) = \begin{bmatrix} \hat{\gamma}(\theta, \phi) & * & * & * \\ M_{21} & M_{22} & * & * \\ M_{31} & 0 & M_{33} & * \\ M_{41} & M_{42} & -\frac{1}{2}\hat{\gamma}(\bar{\theta}, \bar{\phi}) & M_{44} \end{bmatrix}, \tag{6.47}$$

where $(\bar{\theta}, \bar{\phi})$ are the spherical coordinates of $U\boldsymbol{n}$. Its entries $M_{ij}$ are defined by

$$M_{22} := \hat{\gamma}(\theta, \phi) + (\alpha - 1)(U\boldsymbol{\tau}_2 \cdot \boldsymbol{\xi})(U\boldsymbol{\tau}_2 \cdot \boldsymbol{n}) + \lambda(U\boldsymbol{\tau}_2 \cdot \boldsymbol{n})^2, \tag{6.48a}$$

$$M_{33} := \hat{\gamma}(\theta, \phi) + (\alpha - 1)(U\boldsymbol{\tau}_2 \cdot \boldsymbol{\xi})(U\boldsymbol{\tau}_2 \cdot \boldsymbol{n}) + \lambda(U\boldsymbol{\tau}_2 \cdot \boldsymbol{n})^2, \tag{6.48b}$$

$$M_{44} := \hat{\gamma}(\theta, \phi) + (\alpha - 1)(U\boldsymbol{\tau}_1 \cdot \boldsymbol{\xi})(U\boldsymbol{\tau}_1 \cdot \boldsymbol{n}) + \lambda(U\boldsymbol{\tau}_1 \cdot \boldsymbol{n})^2, \tag{6.48c}$$

and

$$M_{21} := -\frac{1}{2}\Big[\hat{\gamma}(\theta, \phi)(U\boldsymbol{\tau}_2 \cdot \boldsymbol{\tau}_1) + \alpha(U\boldsymbol{\tau}_2 \cdot \boldsymbol{n})(\boldsymbol{\tau}_1 \cdot \boldsymbol{\xi})\Big], \tag{6.49a}$$

$$M_{31} := -\frac{1}{2}\Big[\hat{\gamma}(\theta, \phi)(U\boldsymbol{\tau}_2 \cdot \boldsymbol{\tau}_2) + \alpha(U\boldsymbol{\tau}_2 \cdot \boldsymbol{n})(\boldsymbol{\tau}_2 \cdot \boldsymbol{\xi})\Big], \tag{6.49b}$$

$$M_{41} := -\frac{1}{2}\Big[\hat{\gamma}(\theta, \phi)(U\boldsymbol{\tau}_1 \cdot \boldsymbol{\tau}_1) + \alpha(U\boldsymbol{\tau}_1 \cdot \boldsymbol{n})(\boldsymbol{\tau}_1 \cdot \boldsymbol{\xi})\Big], \tag{6.49c}$$

$$M_{42} := \frac{\alpha - 1}{2}\Big[(U\boldsymbol{\tau}_1 \cdot \boldsymbol{\xi})(U\boldsymbol{\tau}_2 \cdot \boldsymbol{n}) + (U\boldsymbol{\tau}_2 \cdot \boldsymbol{\xi})(U\boldsymbol{\tau}_1 \cdot \boldsymbol{n})\Big] + \lambda(U\boldsymbol{\tau}_1 \cdot \boldsymbol{n})(U\boldsymbol{\tau}_2 \cdot \boldsymbol{n}). \tag{6.49d}$$

To simplify notation, we write $U\boldsymbol{\tau}_i \cdot \boldsymbol{v} := (U\boldsymbol{\tau}_i) \cdot \boldsymbol{v}$ whenever no ambiguity arises. Since $M^{\alpha}(U, \lambda; \boldsymbol{n})$ is symmetric, entries above the main diagonal are denoted by asterisks $*$.

Using this auxiliary matrix, we define the minimal stabilizing function by

$$k^{\alpha}_{\min}(\theta, \phi) = \inf\Big\{\lambda \geq 0 \;\Big|\; M^{\alpha}(U, \lambda; \boldsymbol{n}) \text{ is positive semidefinite, } \forall U \in SO(3)\Big\}. \tag{6.50}$$

The existence of $k^{\alpha}_{\min}(\theta, \phi)$ is guaranteed by the following theorem.

Theorem 6.3. *Suppose that $\hat{\gamma}(\theta, \phi)$ satisfies* (6.44)*. Then $k^{\alpha}_{\min}(\theta, \phi)$ is well defined if and only if at least one of the following conditions holds:*

*(1) $\alpha = -1$;*
*(2) Whenever $2\hat{\gamma}(\theta^*, \phi^*) = \hat{\gamma}(\pi - \theta^*, \pi + \phi^*)$, we have $\nabla\hat{\gamma}(\theta^*, \phi^*) = \boldsymbol{0}$.*

A detailed proof of Theorem 6.3 is given in Section 6.5. For now, we assume that $k^{\alpha}_{\min}(\theta, \phi)$ is well defined, that is, $k^{\alpha}_{\min}(\theta, \phi) < +\infty$.

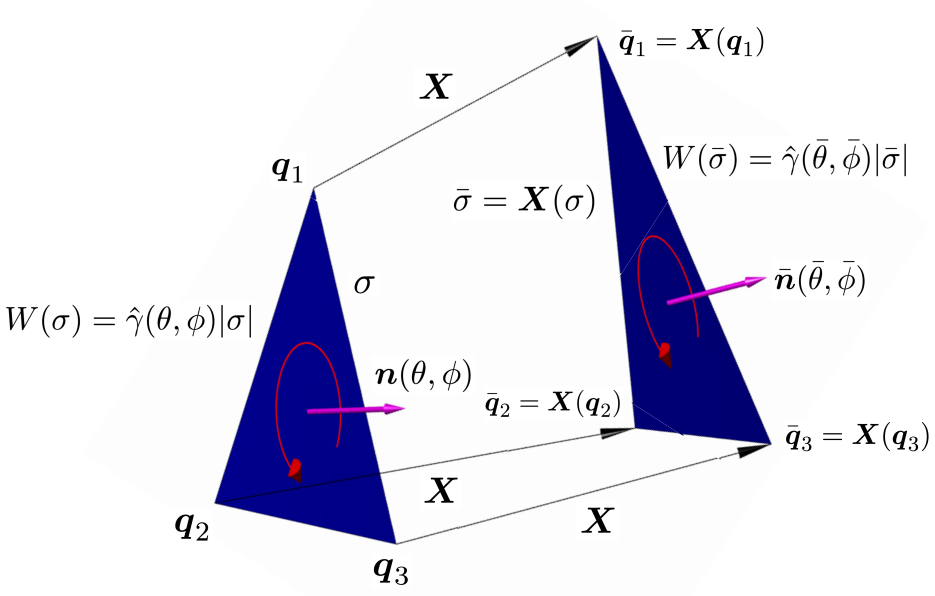



**Figure 6.2.** Schematic illustration of the local energy estimate in Lemma 6.4.

### 6.4.2. The local energy estimate.

LEMMA 6.3. *[14] Let $\sigma = [q_1, q_2, q_3]$ and $\bar{\sigma} = [\bar{q}_1, \bar{q}_2, \bar{q}_3]$ be two nondegenerate triangular elements. If a continuously differentiable map $X : \mathbb{R}^3 \to \mathbb{R}^3$ satisfies*

$$X(q_i) = \bar{q}_i, \ \forall 1 \le i \le 3, \qquad X|_\sigma \in [\mathcal{P}^1(\sigma)]^3, \tag{6.51}$$

*then there exist an orthogonal matrix $U \in SO(3)$ and a lower triangular matrix $L = \begin{pmatrix} l_{11} & 0 \\ l_{21} & l_{22} \end{pmatrix}$, with $l_{11}, l_{22} > 0$, such that*

$$\nabla_\Gamma X|_\sigma = l_{11}(U\tau_1)\tau_1^T + l_{21}(U\tau_2)\tau_1^T + l_{22}(U\tau_2)\tau_2^T, \qquad \bar{n} = Un, \qquad |\bar{\sigma}| = |\sigma| l_{11} l_{22}, \tag{6.52}$$

*where $\bar{n}, n$ are the unit normals to $\bar{\sigma}, \sigma$, respectively, and the tangent vectors $\tau_1, \tau_2$ of $\sigma$, together with $n$, form an orthonormal basis of $\mathbb{R}^3$.*

LEMMA 6.4 (Local energy estimate). *Let $\sigma = [q_1, q_2, q_3]$ and $\bar{\sigma} = [\bar{q}_1, \bar{q}_2, \bar{q}_3]$ be two nondegenerate triangular elements. Suppose that a continuously differentiable map $X : \mathbb{R}^3 \to \mathbb{R}^3$ satisfies*

$$X(q_i) = \bar{q}_i, \ \forall 1 \le i \le 3, \qquad X|_\sigma \in [\mathcal{P}^1(\sigma)]^3. \tag{6.53}$$

*Then, for sufficiently large $k(\theta, \phi)$, we have*

$$|\sigma| \left( \hat{G}_k^\alpha(\theta, \phi) \nabla_\Gamma X|_\sigma \right) : \left( \nabla_\Gamma X|_\sigma - \nabla_\Gamma \mathbf{id}|_\sigma \right) \ge \hat{\gamma}(\bar{\theta}, \bar{\phi})|\bar{\sigma}| - \hat{\gamma}(\theta, \phi)|\sigma|, \tag{6.54}$$

*where $(\bar{\theta}, \bar{\phi})$ and $(\theta, \phi)$ are the spherical coordinates of $\bar{n}$ and $n$, respectively.*

Proof. By Lemma 6.3, we have

$$
\begin{aligned}
&|\sigma|\Big(\hat{\boldsymbol{G}}_k^\alpha(\theta,\phi)\nabla_\Gamma \boldsymbol{X}|_\sigma\Big) : \nabla_\Gamma \boldsymbol{X}|_\sigma \\
&\quad = |\sigma| \operatorname{Tr}\left[\left(\sum_{1\le j\le i\le 2} l_{ij}\boldsymbol{\tau}_j(U\boldsymbol{\tau}_i)^T\right)(\hat{\gamma}(\theta,\phi)I_3 - \boldsymbol{n}\boldsymbol{\xi}^T + \alpha\boldsymbol{\xi}\boldsymbol{n}^T + k(\theta,\phi)\boldsymbol{n}\boldsymbol{n}^T)\left(\sum_{1\le j\le i\le 2} l_{ij}(U\boldsymbol{\tau}_i)\boldsymbol{\tau}_j^T\right)\right] \\
&\quad = |\sigma| \Bigg[\hat{\gamma}(\theta,\phi)\sum_{1\le j\le i\le 2} l_{ij}^2 + (\alpha-1)\sum_{1\le j\le i,p\le 2} l_{ij}l_{pj}(U\boldsymbol{\tau}_p\cdot\boldsymbol{\xi})(U\boldsymbol{\tau}_i\cdot\boldsymbol{n}) \\
&\qquad\qquad + k(\theta,\phi)\sum_{1\le j\le i,p\le 2} l_{ij}l_{pj}(U\boldsymbol{\tau}_p\cdot\boldsymbol{n})(U\boldsymbol{\tau}_i\cdot\boldsymbol{n})\Bigg].
\end{aligned}
\tag{6.55}
$$

Since $\nabla_\Gamma \mathbf{id} = \boldsymbol{\tau}_1\boldsymbol{\tau}_1^T + \boldsymbol{\tau}_2\boldsymbol{\tau}_2^T$, we obtain

$$
\begin{aligned}
&|\sigma|\Big(\hat{\boldsymbol{G}}_k^\alpha(\theta,\phi)\nabla_\Gamma \boldsymbol{X}|_\sigma\Big) : \nabla_\Gamma \mathbf{id}|_\sigma \\
&\quad = |\sigma| \operatorname{Tr}\left[\left(\sum_{i=1}^{2} \boldsymbol{\tau}_i\boldsymbol{\tau}_i^T\right)(\hat{\gamma}(\theta,\phi)I_3 + \alpha\boldsymbol{\xi}\boldsymbol{n}^T)\left(\sum_{1\le j\le i\le 2} l_{ij}(U\boldsymbol{\tau}_i)\boldsymbol{\tau}_j^T\right)\right] \\
&\quad = |\sigma| \left[\sum_{1\le j\le i\le 2} \hat{\gamma}(\theta,\phi)l_{ij}(U\boldsymbol{\tau}_i\cdot\boldsymbol{\tau}_j) + \alpha\sum_{1\le j\le i\le 2} l_{ij}(U\boldsymbol{\tau}_i\cdot\boldsymbol{n})(\boldsymbol{\tau}_j\cdot\boldsymbol{\xi})\right].
\end{aligned}
\tag{6.56}
$$

Equation (6.52) gives $|\bar{\sigma}| = |\sigma| l_{11}l_{22}$. Thus, by Theorem 6.3, for sufficiently large $k(\theta,\phi)$ satisfying $k(\theta,\phi) \ge k_{\min}^\alpha(\theta,\phi)$, we have

$$
\begin{aligned}
&|\sigma|\Big(\hat{\boldsymbol{G}}_k^\alpha(\theta,\phi)\nabla_\Gamma \boldsymbol{X}|_\sigma\Big) : \Big(\nabla_\Gamma \boldsymbol{X}|_\sigma - \nabla_\Gamma \mathbf{id}|_\sigma\Big) - \big(\hat{\gamma}(\bar{\theta},\bar{\phi})|\bar{\sigma}| - \hat{\gamma}(\theta,\phi)|\sigma|\big) \\
&\quad = |\sigma|[1, l_{21}, l_{22}, l_{11}]M^\alpha(U,k;\boldsymbol{n})[1, l_{21}, l_{22}, l_{11}]^T \ge 0.
\end{aligned}
\tag{6.57}
$$

The last inequality follows from the positive semidefiniteness of $M^\alpha(U,k;\boldsymbol{n})$. □

Remark 6.6. To test the necessity of (6.44) within the $\alpha$-surface energy matrix family, we use an orientation-reversing map on the tangent plane. In contrast to the planar substitution in Remark 3.5, the map $\boldsymbol{X} = -p\mathbf{id}$ preserves the ordered triangle normal in three dimensions, since both tangent edge vectors change sign. Instead, let

$$
R := \boldsymbol{\tau}_1\boldsymbol{\tau}_1^T - \boldsymbol{\tau}_2\boldsymbol{\tau}_2^T - \boldsymbol{n}\boldsymbol{n}^T \in SO(3), \qquad \boldsymbol{X} = pR\mathbf{id}, \qquad p > 0. \tag{6.58}
$$

This is a rotation by $\pi$ about $\boldsymbol{\tau}_1$, followed by scaling. The tangent edge directions are mapped to $p\boldsymbol{\tau}_1$ and $-p\boldsymbol{\tau}_2$, so $\bar{\boldsymbol{n}} = -\boldsymbol{n}$, $\bar{\theta} = \pi - \theta$, $\bar{\phi} = \pi + \phi$, and $|\bar{\sigma}| = p^2|\sigma|$. Writing $\boldsymbol{P} = I_3 - \boldsymbol{n}\boldsymbol{n}^T$, we have

$$
\nabla_\Gamma \boldsymbol{X} = p\left(\boldsymbol{\tau}_1\boldsymbol{\tau}_1^T - \boldsymbol{\tau}_2\boldsymbol{\tau}_2^T\right), \qquad \Big(\hat{\boldsymbol{G}}_k^\alpha \nabla_\Gamma \boldsymbol{X}\Big) : \Big(\nabla_\Gamma \boldsymbol{X} - \boldsymbol{P}\Big) = 2p^2\hat{\gamma}(\theta,\phi). \tag{6.59}
$$

Indeed, the tangential block of $\hat{\boldsymbol{G}}_k^\alpha$ is $\hat{\gamma}(\theta,\phi)I_2$, and the two linear terms cancel. The local energy estimate (6.54) therefore yields

$$
2p^2\hat{\gamma}(\theta,\phi) \ge p^2\hat{\gamma}(\pi-\theta,\pi+\phi) - \hat{\gamma}(\theta,\phi). \tag{6.60}
$$

Letting $p \to +\infty$ gives (6.44). Thus, for $\alpha = -1$, the antipodal condition is necessary and sufficient for the local energy estimate within the stated matrix family, and is optimal in that framework. A broader sharpness claim for a different surface energy matrix would require checking its pairing with the same orientation-correct test; the trace condition

$$
\Big(\hat{\boldsymbol{G}}(\theta,\phi)\boldsymbol{P}(\theta,\phi)\Big) : \boldsymbol{P}(\theta,\phi) = 2\hat{\gamma}(\theta,\phi) \tag{6.61}
$$

is not used here as a substitute for that verification.

Remark 6.7. For $\alpha = -1$, analyses based on the $\gamma(\boldsymbol{n})$ formulation in [107, 17, 13] establish energy stability of the corresponding structure-preserving parametric finite element method under $3\gamma(\boldsymbol{n}) \geq \gamma(-\boldsymbol{n})$. Together with the results above and those in [14], this suggests the conjecture that the energy stability condition in $\mathbb{R}^d$ takes the form $(5-d)\gamma(\boldsymbol{n}) \geq \gamma(-\boldsymbol{n})$. In particular, for hypersurfaces in $\mathbb{R}^4$, this would formally give $\gamma(\boldsymbol{n}) = \gamma(-\boldsymbol{n})$. Extending the present analysis to higher dimensions is difficult, however, because the local energy estimates used here apply only in $\mathbb{R}^2$ and $\mathbb{R}^3$.

**6.4.3. Unconditional energy stability.** We now prove the unconditional energy stability of (6.40).

Proof. For each $1 \leq j \leq J$, apply Lemma 6.4 with $\sigma = [\boldsymbol{q}_{j_1}^m, \boldsymbol{q}_{j_2}^m, \boldsymbol{q}_{j_3}^m]$, $\bar{\sigma} = [\boldsymbol{q}_{j_1}^{m+1}, \boldsymbol{q}_{j_2}^{m+1}, \boldsymbol{q}_{j_3}^{m+1}]$, and $\boldsymbol{X} = \boldsymbol{X}^{m+1}$ to obtain

$$\begin{aligned} &|\sigma_j^m|\Big(\hat{\boldsymbol{G}}_k^\alpha(\theta_j^m, \phi_j^m)\nabla_\Gamma \boldsymbol{X}^{m+1}|_{\sigma_j^m}\Big) : \Big(\nabla_\Gamma \boldsymbol{X}^{m+1}|_{\sigma_j^m} - \nabla_\Gamma \boldsymbol{X}^m|_{\sigma_j^m}\Big) \\ &\quad \geq \hat{\gamma}(\theta_j^{m+1}, \phi_j^{m+1})|\sigma_j^{m+1}| - \hat{\gamma}(\theta_j^m, \phi_j^m)|\sigma_j^m|. \end{aligned} \tag{6.62}$$

Summing over $j = 1, \ldots, J$ and using (6.42b), we obtain

$$\begin{aligned} &\Big\langle \hat{\boldsymbol{G}}_k^\alpha(\theta^m, \phi^m)\nabla_\Gamma \boldsymbol{X}^{m+1}, \nabla_\Gamma(\boldsymbol{X}^{m+1} - \boldsymbol{X}^m)\Big\rangle_{\Gamma^m}^h \\ &= \sum_{j=1}^J |\sigma_j^m|\Big(\hat{\boldsymbol{G}}_k^\alpha(\theta_j^m, \phi_j^m)\nabla_\Gamma \boldsymbol{X}^{m+1}|_{\sigma_j^m}\Big) : \Big(\nabla_\Gamma \boldsymbol{X}^{m+1}|_{\sigma_j^m} - \nabla_\Gamma \boldsymbol{X}^m|_{\sigma_j^m}\Big) \\ &\geq \sum_{j=1}^J \hat{\gamma}(\theta_j^{m+1}, \phi_j^{m+1})|\sigma_j^{m+1}| - \sum_{j=1}^J \hat{\gamma}(\theta_j^m, \phi_j^m)|\sigma_j^m| \\ &= W^{m+1} - W^m. \end{aligned} \tag{6.63}$$

Taking $\varphi^h = \mu^{m+1}$ and $\boldsymbol{\omega}^h = \boldsymbol{X}^{m+1} - \boldsymbol{X}^m$ in (6.40) gives

$$\begin{aligned} &\Big\langle \hat{\boldsymbol{G}}_k^\alpha(\theta^m, \phi^m)\nabla_\Gamma \boldsymbol{X}^{m+1}, \nabla_\Gamma(\boldsymbol{X}^{m+1} - \boldsymbol{X}^m)\Big\rangle_{\Gamma^m}^h \\ &\quad = \Big(\mu^{m+1}\boldsymbol{n}^{m+\frac{1}{2}}, \boldsymbol{X}^{m+1} - \boldsymbol{X}^m\Big)_{\Gamma^m}^h = -\tau\Big(\nabla_\Gamma \mu^{m+1}, \nabla_\Gamma \mu^{m+1}\Big)_{\Gamma^m}^h. \end{aligned} \tag{6.64}$$

Combining these two identities establishes energy stability:

$$W^{m+1} - W^m \leq -\tau\Big(\nabla_\Gamma \mu^{m+1}, \nabla_\Gamma \mu^{m+1}\Big)_{\Gamma^m}^h \leq 0. \tag{6.65}$$

□

## 6.5. Existence of the minimal stabilizing function

### 6.5.1. Preliminary lemmas and an outline of the proof.

Lemma 6.5 (Sylvester's criterion). *A symmetric matrix $A \in \mathbb{R}^{m\times m}$ is positive definite if and only if all its leading principal minors are positive.*

Lemma 6.6 ([14]). *Let $A\colon SO(3)\times\mathbb{R} \to \mathbb{R}^{m\times m}$ and $D\colon SO(3) \to \mathbb{R}^{m\times m}$ be continuous symmetric $m\times m$ matrix fields satisfying the following conditions:*

*(1) $A$ depends linearly on $\lambda$, that is,*

$$A(U,\lambda) = A(U,0) + \lambda D(U), \qquad D(U) \text{ is positive semidefinite.} \tag{6.66}$$

*(2) There exists a constant $k_{m-1} \geq 0$ such that*

$$A_{m-1}(U,\lambda) \text{ is positive definite}, \qquad \forall U \in SO(3),\ \forall \lambda \geq k_{m-1}, \tag{6.67}$$

*where $A_{m-1}$ denotes the $(m-1)$st leading principal submatrix of $A$.*

*(3) For every $U \in SO(3)$, there exist a constant $k_{m,U} \geq k_{m-1}$ and an open neighborhood $\mathcal{U}_U$ of $U$ such that*

$$\det(A(U', k_{m,U})) \geq 0, \qquad \forall U' \in \mathcal{U}_U. \tag{6.68}$$

*Then there exists a finite constant $k_m \geq k_{m-1}$ such that, for every $\lambda \geq k_m$, we have*

$$A(U, \lambda) \text{ is positive semidefinite}, \qquad \forall U \in SO(3). \tag{6.69}$$

Lemma 6.7 (Jacobi's formula). *Let $A = (a_{i,j})_{m\times m}$ be a matrix whose entries are functions. Then*

$$\frac{\partial \det(A)}{\partial \beta} = \operatorname{Tr}\left(\operatorname{adj}(A)\,\frac{\partial A}{\partial \beta}\right), \tag{6.70a}$$

$$\frac{\partial^2 \det(A)}{\partial \beta \partial \varphi} = \operatorname{Tr}\left(\operatorname{adj}(A)\,\frac{\partial^2 A}{\partial \beta \partial \varphi}\right) + \sum_{i\neq j} \det \begin{bmatrix} a_{1,1} & a_{1,2} & \cdots & a_{1,m} \\ \vdots & \vdots & \ddots & \vdots \\ \frac{\partial a_{i,1}}{\partial \beta} & \frac{\partial a_{i,2}}{\partial \beta} & \cdots & \frac{\partial a_{i,m}}{\partial \beta} \\ \vdots & \vdots & \ddots & \vdots \\ \frac{\partial a_{j,1}}{\partial \varphi} & \frac{\partial a_{j,2}}{\partial \varphi} & \cdots & \frac{\partial a_{j,m}}{\partial \varphi} \\ \vdots & \vdots & \ddots & \vdots \\ a_{m,1} & a_{m,2} & \cdots & a_{m,m} \end{bmatrix}. \tag{6.70b}$$

Lemma 6.8 (A representation of $SO(3)$). *For every $U \in SO(3)$, there exists $\mathbf{\Phi} = (\varphi, \vartheta, \psi) \in (2\pi\mathbb{T})^3$ such that*

$$U[\boldsymbol{\tau}_1, \boldsymbol{\tau}_2, \boldsymbol{n}] = [\boldsymbol{\tau}_1, \boldsymbol{\tau}_2, \boldsymbol{n}]U(\mathbf{\Phi}), \tag{6.71}$$

*where $U$ can be represented by*

$$U(\mathbf{\Phi}) = R_z(\psi)R_y(\vartheta)R_x(\varphi), \tag{6.72}$$

*Here*

$$R_x(\varphi) = \begin{bmatrix} 1 & 0 & 0 \\ 0 & \cos\varphi & -\sin\varphi \\ 0 & \sin\varphi & \cos\varphi \end{bmatrix}, \tag{6.73a}$$

$$R_y(\vartheta) = \begin{bmatrix} \cos\vartheta & 0 & \sin\vartheta \\ 0 & 1 & 0 \\ -\sin\vartheta & 0 & \cos\vartheta \end{bmatrix}, \tag{6.73b}$$

$$R_z(\psi) = \begin{bmatrix} \cos\psi & -\sin\psi & 0 \\ \sin\psi & \cos\psi & 0 \\ 0 & 0 & 1 \end{bmatrix}. \tag{6.73c}$$

We establish the existence of the minimal stabilizing function by proving that $M^\alpha(U, \lambda; \boldsymbol{n})$ is positive semidefinite for sufficiently large $\lambda$.

Let $M_{m-1}$ denote the $(m-1)$st leading principal submatrix of $M^\alpha(U, \lambda; \boldsymbol{n})$. The proof proceeds as follows.

(i) First, we establish the positive definiteness of $M_3$ by verifying $\det(M_1), \det(M_2), \det(M_3) > 0$ and applying Sylvester's criterion.

(ii) Next, we analyze the nonnegativity of $\det(M^\alpha)$ in two cases:
- The *noncritical case*: $2\hat{\gamma}(\theta, \phi) > \hat{\gamma}(\pi - \theta, \pi + \phi)$;
- The *critical case*: there exists $\boldsymbol{n}^* = \boldsymbol{n}(\theta^*, \phi^*) \in \mathbb{S}^2$ such that $2\hat{\gamma}(\theta^*, \phi^*) = \hat{\gamma}(\pi - \theta^*, \pi + \phi^*)$.

The proof in the noncritical case follows essentially the argument in [14], so we omit the details. In the critical case, the determinant and its gradient vanish along the one-dimensional manifold of antipodal rotations. The representation of $SO(3)$ gives a positive definite Hessian in the two normal directions for sufficiently large stabilization. A uniform Taylor estimate in these directions establishes local nonnegativity.

(iii) Finally, Lemma 6.6 gives the positive semidefiniteness of $M^\alpha(U, \lambda; \boldsymbol{n})$, completing the proof of Theorem 6.3.

### 6.5.2. Positive definiteness of $M_3$.

LEMMA 6.9. *There exists a constant $k_2 > 0$ such that, for every $\lambda \geq k_2$, we have*

$$\det(M_2(U, \lambda; \boldsymbol{n})) > 0, \qquad \forall U \in SO(3). \tag{6.74}$$

PROOF. Set $g := \hat{\gamma}(\theta, \phi) > 0$ and denote

$$Y := U\boldsymbol{\tau}_2 \cdot \boldsymbol{n}, \qquad E := (\alpha - 1)(U\boldsymbol{\tau}_2 \cdot \boldsymbol{\xi}). \tag{6.75}$$

Using $(a+b)^2 \leq 2a^2 + 2b^2$ and $|U\boldsymbol{\tau}_2 \cdot \boldsymbol{\tau}_1| \leq 1$, we obtain

$$\begin{aligned}
\det(M_2) &= gM_{22} - M_{21}^2 \\
&= g\left(g + EY + \lambda Y^2\right) - \frac{1}{4}\left[g(U\boldsymbol{\tau}_2 \cdot \boldsymbol{\tau}_1) + \alpha(\boldsymbol{\tau}_1 \cdot \boldsymbol{\xi})Y\right]^2 \\
&\geq g^2\left[1 - \frac{1}{2}(U\boldsymbol{\tau}_2 \cdot \boldsymbol{\tau}_1)^2\right] + gEY + \left[\lambda g - \frac{\alpha^2}{2}(\boldsymbol{\tau}_1 \cdot \boldsymbol{\xi})^2\right] Y^2 \\
&\geq \frac{1}{2}g^2 + gEY + \left[\lambda g - \frac{\alpha^2}{2}(\boldsymbol{\tau}_1 \cdot \boldsymbol{\xi})^2\right] Y^2 \\
&= \frac{1}{4}g^2 + \left(\frac{g}{2} + EY\right)^2 + \left[\lambda g - \frac{\alpha^2}{2}(\boldsymbol{\tau}_1 \cdot \boldsymbol{\xi})^2 - E^2\right] Y^2.
\end{aligned} \tag{6.76}$$

Since both $U\boldsymbol{\tau}_2$ and $\boldsymbol{\tau}_1$ are unit vectors,

$$|E| \leq |\alpha - 1|\,|\boldsymbol{\xi}|, \qquad |\boldsymbol{\tau}_1 \cdot \boldsymbol{\xi}| \leq |\boldsymbol{\xi}|, \qquad \forall U \in SO(3). \tag{6.77}$$

Choose any constant $k_2 > 0$ satisfying

$$k_2 \geq \frac{\left[\frac{\alpha^2}{2} + (\alpha - 1)^2\right] |\boldsymbol{\xi}|^2}{g}. \tag{6.78}$$

Then, for every $U \in SO(3)$ and every $\lambda \geq k_2$,

$$\det(M_2(U, \lambda; \boldsymbol{n})) \geq \frac{1}{4}g^2 > 0. \tag{6.79}$$

□

THEOREM 6.4. *There exists a constant $k_3 > 0$ such that, for every $\lambda \geq k_3$, we have*

$$M_3(U, \lambda; \boldsymbol{n}) \text{ is positive definite}, \qquad \forall U \in SO(3). \tag{6.80}$$

PROOF. For brevity, set $g := \hat{\gamma}(\theta, \phi) > 0$ and denote

$$Y := U\boldsymbol{\tau}_2 \cdot \boldsymbol{n}, \qquad E := (\alpha - 1)(U\boldsymbol{\tau}_2 \cdot \boldsymbol{\xi}), \tag{6.81a}$$

$$A := g(U\boldsymbol{\tau}_2 \cdot \boldsymbol{\tau}_1), \qquad B := \alpha(\boldsymbol{\tau}_1 \cdot \boldsymbol{\xi}), \tag{6.81b}$$

$$C := g(U\boldsymbol{\tau}_2 \cdot \boldsymbol{\tau}_2), \qquad D := \alpha(\boldsymbol{\tau}_2 \cdot \boldsymbol{\xi}). \tag{6.81c}$$

Since $M_{22} = M_{33} = g + EY + \lambda Y^2$, we have

$$\begin{aligned}
\det(M_3) &= gM_{22}M_{33} - M_{21}^2 M_{33} - M_{31}^2 M_{22} \\
&= \left(g + EY + \lambda Y^2\right)\left\{g\left(g + EY + \lambda Y^2\right) - \frac{1}{4}\left[(A + BY)^2 + (C + DY)^2\right]\right\} \\
&:= P(Y)Q(Y),
\end{aligned} \tag{6.82}$$

where

$$P(Y) := g + EY + \lambda Y^2, \tag{6.83a}$$

$$Q(Y) := g^2 - \frac{1}{4}(A^2 + C^2) + \left[gE - \frac{1}{2}(AB + CD)\right] Y + \left[\lambda g - \frac{1}{4}(B^2 + D^2)\right] Y^2. \tag{6.83b}$$

We next derive bounds that are uniform in $U \in SO(3)$. Since

$$A^2 + C^2 = g^2\left[(U\boldsymbol{\tau}_2 \cdot \boldsymbol{\tau}_1)^2 + (U\boldsymbol{\tau}_2 \cdot \boldsymbol{\tau}_2)^2\right] \leq g^2, \tag{6.84}$$

let

$$S \coloneqq gE - \frac{1}{2}(AB + CD), \qquad R \coloneqq \frac{1}{4}(B^2 + D^2). \tag{6.85}$$

By the compactness of $SO(3)$ and the continuity of the above quantities, the constants

$$E_* \coloneqq \max_{U \in SO(3)} |E|, \qquad S_* \coloneqq \max_{U \in SO(3)} |S| \tag{6.86}$$

are finite. Completing the square gives

$$P(Y) = \frac{3}{4}g + \left(\frac{\sqrt{g}}{2} + \frac{E}{\sqrt{g}}Y\right)^2 + \left(\lambda - \frac{E^2}{g}\right)Y^2, \tag{6.87a}$$

$$Q(Y) \geq \frac{1}{2}g^2 + SY + \left(\lambda g - R\right)Y^2 \tag{6.87b}$$

$$= \frac{1}{4}g^2 + \left(\frac{g}{2} + \frac{S}{g}Y\right)^2 + \left(\lambda g - R - \frac{S^2}{g^2}\right)Y^2. \tag{6.87c}$$

Choose

$$k_3 \coloneqq \max\left\{k_2, \frac{E_*^2}{g}, \frac{R}{g} + \frac{S_*^2}{g^3}\right\}, \tag{6.88}$$

where $k_2$ is the constant in Lemma 6.9. Then, for every $U \in SO(3)$ and every $\lambda \geq k_3$,

$$P(Y) \geq \frac{3}{4}g > 0, \qquad Q(Y) \geq \frac{1}{4}g^2 > 0. \tag{6.89}$$

Consequently,

$$\det(M_3) \geq \frac{3}{16}g^3 > 0. \tag{6.90}$$

Together with $\det(M_1) = g > 0$ and Lemma 6.9, Sylvester's criterion shows that $M_3(U, \lambda; \boldsymbol{n})$ is positive-definite for every $U \in SO(3)$ and every $\lambda \geq k_3$. □

### 6.5.3. The noncritical case.

Lemma 6.10. *If $U\boldsymbol{n} \neq -\boldsymbol{n}$, then there exist a constant $k_{m,U} > 0$ and an open neighborhood $\mathcal{U}_U$ of $U$ such that*

$$\det(M^\alpha(U', k_{m,U}; \boldsymbol{n})) \geq 0, \qquad \forall U' \in \mathcal{U}_U. \tag{6.91}$$

Lemma 6.11. *Suppose that $U\boldsymbol{n} = -\boldsymbol{n}$. If $2\hat{\gamma}(\theta, \phi) > \hat{\gamma}(\pi - \theta, \pi + \phi)$, then there exist a constant $k_{m,U} > 0$ and an open neighborhood $\mathcal{U}_U$ of $U$ such that*

$$\det(M^\alpha(U', k_{m,U}; \boldsymbol{n})) \geq 0, \qquad \forall U' \in \mathcal{U}_U. \tag{6.92}$$

The proofs of these two lemmas follow essentially the arguments in [14], so we omit the details.

**6.5.4. Analysis of the critical case.** We now analyze the critical case $2\hat{\gamma}(\theta^*, \phi^*) = \hat{\gamma}(\pi - \theta^*, \pi + \phi^*)$ and establish a necessary and sufficient condition for the gradient of $\det(M^\alpha)$ to vanish in this case.

Lemma 6.12. *Let $\boldsymbol{n}^* \in \mathbb{S}^2$ satisfy $2\hat{\gamma}(\theta^*, \phi^*) = \hat{\gamma}(\pi - \theta^*, \pi + \phi^*)$. Then*

$$2\partial_\theta\hat{\gamma}(\theta^*, \phi^*) + \partial_\theta\hat{\gamma}(\pi - \theta^*, \pi + \phi^*) = 0, \tag{6.93a}$$

$$2\partial_\phi\hat{\gamma}(\theta^*, \phi^*) - \partial_\phi\hat{\gamma}(\pi - \theta^*, \pi + \phi^*) = 0. \tag{6.93b}$$

Proof. Consider the function

$$f(\theta, \phi) \coloneqq \frac{\hat{\gamma}(\pi - \theta, \pi + \phi)}{\hat{\gamma}(\theta, \phi)}, \qquad \forall (\theta, \phi) \in [0, \pi] \times 2\pi\mathbb{T}. \tag{6.94}$$

We have $f(\theta,\phi) \le 2$, with maximum value 2 attained at $(\theta^*,\phi^*)$. Therefore,

$$\begin{aligned}\partial_\theta f(\theta^*,\phi^*) &= \frac{-\partial_\theta\hat\gamma(\pi-\theta^*,\pi+\phi^*)\hat\gamma(\theta^*,\phi^*) - \hat\gamma(\pi-\theta^*,\pi+\phi^*)\partial_\theta\hat\gamma(\theta^*,\phi^*)}{\hat\gamma^2(\theta^*,\phi^*)} \\ &= -\frac{\partial_\theta\hat\gamma(\pi-\theta^*,\pi+\phi^*) + 2\partial_\theta\hat\gamma(\theta^*,\phi^*)}{\hat\gamma(\theta^*,\phi^*)} = 0,\end{aligned} \tag{6.95}$$

that is,

$$2\partial_\theta\hat\gamma(\theta^*,\phi^*) + \partial_\theta\hat\gamma(\pi-\theta^*,\pi+\phi^*) = 0. \tag{6.96}$$

Similarly, we obtain

$$2\partial_\phi\hat\gamma(\theta^*,\phi^*) - \partial_\phi\hat\gamma(\pi-\theta^*,\pi+\phi^*) = 0. \tag{6.97}$$

□

Lemma 6.13. *For a given $\boldsymbol{n}^* := \boldsymbol{n}(\theta^*,\phi^*) \in \mathbb{S}^2$, suppose that $(U|_{\boldsymbol{\Phi}=\boldsymbol{\Phi}_0})\boldsymbol{n}^* = -\boldsymbol{n}^*$. If $2\hat\gamma(\theta^*,\phi^*) = \hat\gamma(\pi-\theta^*,\pi+\phi^*)$, then*

$$\nabla_{\boldsymbol{\Phi}} \det(M^\alpha(U,\lambda;\boldsymbol{n}^*))\Big|_{\boldsymbol{\Phi}=\boldsymbol{\Phi}_0} = \boldsymbol{0}, \tag{6.98}$$

*if and only if*

$$\alpha = -1 \quad \textit{or} \quad \nabla\hat\gamma(\theta^*,\phi^*) = \boldsymbol{0}. \tag{6.99}$$

Proof. Write $U\boldsymbol{n} := \bar{\boldsymbol{n}} = (\sin\bar\theta\cos\bar\phi, \sin\bar\theta\sin\bar\phi, \cos\bar\theta)^T$, and let $\bar{\boldsymbol{\tau}}_1, \bar{\boldsymbol{\tau}}_2$ be the tangent vectors defined in (6.8). Then

$$\partial_\varphi U\boldsymbol{n} = \bar{\boldsymbol{\tau}}_1\frac{\partial\bar\theta}{\partial\varphi} + \sin\bar\theta\,\bar{\boldsymbol{\tau}}_2\frac{\partial\bar\phi}{\partial\varphi}, \tag{6.100a}$$

$$\partial_\vartheta U\boldsymbol{n} = \bar{\boldsymbol{\tau}}_1\frac{\partial\bar\theta}{\partial\vartheta} + \sin\bar\theta\,\bar{\boldsymbol{\tau}}_2\frac{\partial\bar\phi}{\partial\vartheta}, \tag{6.100b}$$

$$\partial_\psi U\boldsymbol{n} = \bar{\boldsymbol{\tau}}_1\frac{\partial\bar\theta}{\partial\psi} + \sin\bar\theta\,\bar{\boldsymbol{\tau}}_2\frac{\partial\bar\phi}{\partial\psi}. \tag{6.100c}$$

By Lemma 6.8, we may assume without loss of generality that $U = U(\pi,0,\psi)$. At $\boldsymbol{\Phi}_0(\psi) = (\pi,0,\psi)$, we have

$$\bar{\boldsymbol{n}} = -\boldsymbol{n}, \qquad \bar{\boldsymbol{\tau}}_1 = \boldsymbol{\tau}_1, \qquad \bar{\boldsymbol{\tau}}_2 = -\boldsymbol{\tau}_2. \tag{6.101}$$

Lemma 6.8 gives

$$\partial_\varphi U\boldsymbol{n} = -\sin\psi\,\boldsymbol{\tau}_1 + \cos\psi\,\boldsymbol{\tau}_2, \tag{6.102a}$$

$$\partial_\vartheta U\boldsymbol{n} = -\cos\psi\,\boldsymbol{\tau}_1 - \sin\psi\,\boldsymbol{\tau}_2, \tag{6.102b}$$

$$\partial_\psi U\boldsymbol{n} = \boldsymbol{0}. \tag{6.102c}$$

Substituting (6.101) into (6.102) and comparing with (6.100) yields

$$\begin{aligned}&\partial_\varphi\bar\theta = -\sin\psi, && \partial_\varphi\bar\phi = -\cos\psi/\sin\bar\theta, \\ &\partial_\vartheta\bar\theta = -\cos\psi, && \partial_\vartheta\bar\phi = \sin\psi/\sin\bar\theta, \\ &\partial_\psi\bar\theta = 0, && \partial_\psi\bar\phi = 0.\end{aligned} \tag{6.103}$$

By (6.103), at $(\bar\theta,\bar\phi) = (\pi-\theta,\pi+\phi)$, we obtain

$$\begin{aligned}\partial_\varphi\hat\gamma(\bar\theta,\bar\phi) &= \partial_\theta\hat\gamma(\bar\theta,\bar\phi)\partial_\varphi\bar\theta + \partial_\phi\hat\gamma(\bar\theta,\bar\phi)\partial_\varphi\bar\phi \\ &= -\sin\psi\,\partial_\theta\hat\gamma(\pi-\theta,\pi+\phi) - \frac{\cos\psi}{\sin\theta}\,\partial_\phi\hat\gamma(\pi-\theta,\pi+\phi).\end{aligned} \tag{6.104}$$

Similarly,

$$\partial_\vartheta \hat{\gamma}(\bar{\theta},\bar{\phi}) = -\cos\psi\,\partial_\theta\hat{\gamma}(\pi-\theta,\pi+\phi) + \frac{\sin\psi}{\sin\theta}\,\partial_\phi\hat{\gamma}(\pi-\theta,\pi+\phi), \tag{6.105a}$$

$$\partial_\psi \hat{\gamma}(\bar{\theta},\bar{\phi}) = 0. \tag{6.105b}$$

The definitions of $M^\alpha$ and its adjugate give

$$\operatorname{adj}\Big(M^\alpha(U(\boldsymbol{\Phi}_0),\lambda;\boldsymbol{n})\Big) = \frac{3}{4}\hat{\gamma}^3(\theta,\phi)\begin{bmatrix}\mathbf{0} & \mathbf{0}\\ \mathbf{0} & \mathbf{1}\end{bmatrix}, \qquad \mathbf{1} \coloneqq \begin{bmatrix}1 & 1\\ 1 & 1\end{bmatrix}, \tag{6.106}$$

and

$$\frac{\partial}{\partial\varphi}M^\alpha(U,\lambda;\boldsymbol{n})\Big|_{\boldsymbol{\Phi}=\boldsymbol{\Phi}_0} = \begin{bmatrix}\cdots & \cdots & \cdots\\ \vdots & -(\alpha-1)F & -\frac{1}{2}\partial_\varphi\hat{\gamma}(\bar{\theta},\bar{\phi})\\ \vdots & -\frac{1}{2}\partial_\varphi\hat{\gamma}(\bar{\theta},\bar{\phi}) & 0\end{bmatrix}, \tag{6.107a}$$

$$\frac{\partial}{\partial\vartheta}M^\alpha(U,\lambda;\boldsymbol{n})\Big|_{\boldsymbol{\Phi}=\boldsymbol{\Phi}_0} = \begin{bmatrix}\cdots & \cdots & \cdots\\ \vdots & 0 & -\frac{1}{2}\partial_\vartheta\hat{\gamma}(\bar{\theta},\bar{\phi})\\ \vdots & -\frac{1}{2}\partial_\vartheta\hat{\gamma}(\bar{\theta},\bar{\phi}) & -(\alpha-1)G\end{bmatrix}, \tag{6.107b}$$

$$\frac{\partial}{\partial\psi}M^\alpha(U,\lambda;\boldsymbol{n})\Big|_{\boldsymbol{\Phi}=\boldsymbol{\Phi}_0} = \begin{bmatrix}\cdots & \cdots & \cdots\\ \vdots & 0 & 0\\ \vdots & 0 & 0\end{bmatrix}, \tag{6.107c}$$

where

$$F \coloneqq U\boldsymbol{\tau}_2\cdot\boldsymbol{\xi} = \sin\psi\,\partial_\theta\hat{\gamma}(\theta,\phi) - \frac{\cos\psi}{\sin\theta}\,\partial_\phi\hat{\gamma}(\theta,\phi), \tag{6.108a}$$

$$G \coloneqq U\boldsymbol{\tau}_1\cdot\boldsymbol{\xi} = \cos\psi\,\partial_\theta\hat{\gamma}(\theta,\phi) + \frac{\sin\psi}{\sin\theta}\partial_\phi\hat{\gamma}(\theta,\phi). \tag{6.108b}$$

Combining Lemma 6.7 with (6.104), we obtain

$$\begin{aligned}\frac{1}{\frac{3}{4}\hat{\gamma}^3(\theta,\phi)}\frac{\partial}{\partial\varphi}\det\Big(M^\alpha(U,\lambda;\boldsymbol{n})\Big)\Big|_{\boldsymbol{\Phi}=\boldsymbol{\Phi}_0} &= -\partial_\varphi\hat{\gamma}(\bar{\theta},\bar{\phi}) - (\alpha-1)F\\ &= -\sin\psi\Big[(\alpha-1)\partial_\theta\hat{\gamma}(\theta,\phi) - \partial_\theta\hat{\gamma}(\pi-\theta,\pi+\phi)\Big]\\ &\quad + \frac{\cos\psi}{\sin\theta}\Big[(\alpha-1)\partial_\phi\hat{\gamma}(\theta,\phi) + \partial_\phi\hat{\gamma}(\pi-\theta,\pi+\phi)\Big].\end{aligned} \tag{6.109}$$

Similarly,

$$\begin{aligned}\frac{1}{\frac{3}{4}\hat{\gamma}^3(\theta,\phi)}\frac{\partial}{\partial\vartheta}\det\Big(M^\alpha(U,\lambda;\boldsymbol{n})\Big)\Big|_{\boldsymbol{\Phi}=\boldsymbol{\Phi}_0} &= -\partial_\vartheta\hat{\gamma}(\bar{\theta},\bar{\phi}) - (\alpha-1)G\\ &= -\cos\psi\Big[(\alpha-1)\partial_\theta\hat{\gamma}(\theta,\phi) - \partial_\theta\hat{\gamma}(\pi-\theta,\pi+\phi)\Big]\\ &\quad - \frac{\sin\psi}{\sin\theta}\Big[(\alpha-1)\partial_\phi\hat{\gamma}(\theta,\phi) + \partial_\phi\hat{\gamma}(\pi-\theta,\pi+\phi)\Big],\end{aligned} \tag{6.110}$$

and

$$\frac{\partial}{\partial\psi}\det\Big(M^\alpha(U,\lambda;\boldsymbol{n})\Big)\Big|_{\boldsymbol{\Phi}=\boldsymbol{\Phi}_0} = 0. \tag{6.111}$$

By Lemma 6.12, for $\boldsymbol{n}^* \in \mathbb{S}^2$ satisfying $2\hat{\gamma}(\theta^*, \phi^*) = \hat{\gamma}(\pi - \theta^*, \pi + \phi^*)$, we have

(6.112a)
$$\frac{\partial}{\partial \varphi}\det\Big(M^\alpha(U, \lambda; \boldsymbol{n}^*)\Big)\Big|_{\boldsymbol{\Phi}=\boldsymbol{\Phi}_0} = \frac{3(\alpha+1)\hat{\gamma}^3(\theta^*, \phi^*)}{4}\left[-\sin\psi\,\partial_\theta\hat{\gamma}(\theta^*, \phi^*) + \frac{\cos\psi}{\sin\theta^*}\,\partial_\phi\hat{\gamma}(\theta^*, \phi^*)\right],$$

(6.112b)
$$\frac{\partial}{\partial \vartheta}\det\Big(M^\alpha(U, \lambda; \boldsymbol{n}^*)\Big)\Big|_{\boldsymbol{\Phi}=\boldsymbol{\Phi}_0} = \frac{3(\alpha+1)\hat{\gamma}^3(\theta^*, \phi^*)}{4}\left[-\cos\psi\,\partial_\theta\hat{\gamma}(\theta^*, \phi^*) - \frac{\sin\psi}{\sin\theta^*}\,\partial_\phi\hat{\gamma}(\theta^*, \phi^*)\right],$$

(6.112c)
$$\frac{\partial}{\partial \psi}\det\Big(M^\alpha(U, \lambda; \boldsymbol{n}^*)\Big)\Big|_{\boldsymbol{\Phi}=\boldsymbol{\Phi}_0} = 0.$$

Thus, the gradient of the determinant vanishes if and only if

$$(\alpha+1)\begin{bmatrix} -\sin\psi & \cos\psi/\sin\theta^* \\ -\cos\psi & -\sin\psi/\sin\theta^* \end{bmatrix}\nabla\hat{\gamma}(\theta^*, \phi^*) = \mathbf{0}, \tag{6.113}$$

Equivalently,

$$\alpha = -1 \quad \text{or} \quad \nabla\hat{\gamma}(\theta^*, \phi^*) = \mathbf{0}. \tag{6.114}$$

□

Lemma 6.14. *Let $\boldsymbol{n}^* \in \mathbb{S}^2$ satisfy $2\hat{\gamma}(\theta^*, \phi^*) = \hat{\gamma}(\pi - \theta^*, \pi + \phi^*)$. If $U\boldsymbol{n}^* = -\boldsymbol{n}^*$ and $\boldsymbol{n}^*$ satisfies* (6.99)*, then there exist a constant $k_{m,U} > 0$ and an open neighborhood $\mathcal{U}_U$ of $U$ such that*

$$\det(M^\alpha(U', k_{m,U}; \boldsymbol{n}^*)) \geq 0, \qquad \forall U' \in \mathcal{U}_U. \tag{6.115}$$

Proof. Fix the critical normal $\boldsymbol{n}^*$ from the lemma, and write $\boldsymbol{n} = \boldsymbol{n}^*$ throughout this proof. The notation $U(\boldsymbol{\Phi})$ represents the rotation in the local frame from Lemma 6.8. All derivatives below are evaluated through that representation. From the definition of $M^\alpha$, we know that

$$M^\alpha(U, \lambda; \boldsymbol{n}) = M^\alpha(U, 0; \boldsymbol{n}) + \lambda D(U), \tag{6.116}$$

where

$$D(U) \coloneqq \begin{bmatrix} 0 & 0 & 0 & 0 \\ 0 & (U\boldsymbol{\tau}_2\cdot\boldsymbol{n})^2 & 0 & (U\boldsymbol{\tau}_1\cdot\boldsymbol{n})(U\boldsymbol{\tau}_2\cdot\boldsymbol{n}) \\ 0 & 0 & (U\boldsymbol{\tau}_2\cdot\boldsymbol{n})^2 & 0 \\ 0 & (U\boldsymbol{\tau}_1\cdot\boldsymbol{n})(U\boldsymbol{\tau}_2\cdot\boldsymbol{n}) & 0 & (U\boldsymbol{\tau}_1\cdot\boldsymbol{n})^2 \end{bmatrix}. \tag{6.117}$$

By lemma 6.8, we rewrite $D$ as

$$D(\varphi, \vartheta, \psi) \coloneqq D(U) = \begin{bmatrix} 0 & 0 & 0 & 0 \\ 0 & \sin^2\varphi\cos^2\vartheta & 0 & -\sin\varphi\cos\vartheta\sin\vartheta \\ 0 & 0 & \sin^2\varphi\cos^2\vartheta & 0 \\ 0 & -\sin\varphi\cos\vartheta\sin\vartheta & 0 & \sin^2\vartheta \end{bmatrix}. \tag{6.118}$$

Therefore, at $\boldsymbol{\Phi}_0 = (\pi, 0, \psi)$, we have

$$\frac{\partial^2}{\partial\varphi^2}D = \operatorname{diag}(0,2,2,0), \qquad \frac{\partial^2}{\partial\vartheta^2}D = \operatorname{diag}(0,0,0,2), \qquad \frac{\partial^2}{\partial\varphi\partial\vartheta}D = \begin{bmatrix} 0 & 0 & 0 & 0 \\ 0 & 0 & 0 & 1 \\ 0 & 0 & 0 & 0 \\ 0 & 1 & 0 & 0 \end{bmatrix}, \tag{6.119}$$

and

$$\frac{\partial^2}{\partial\rho\partial\psi}D = \mathbf{0}, \qquad \rho \in \{\varphi, \vartheta, \psi\}. \tag{6.120}$$

At $\boldsymbol{\Phi}_0 = (\pi, 0, \psi)$, we also have

$$D(\boldsymbol{\Phi}_0) = \mathbf{0}, \qquad \partial_\rho D(\boldsymbol{\Phi}_0) = \mathbf{0}, \qquad \rho \in \{\varphi, \vartheta, \psi\}. \tag{6.121}$$

Consequently, $M^\alpha(U,\lambda;\boldsymbol{n})$ and its first derivatives with respect to $\boldsymbol{\Phi}$ are independent of $\lambda$ at $\boldsymbol{\Phi}_0$. By Jacobi's formula, the $\lambda$-dependent part of the second derivative of the determinant is therefore

$$\lambda \operatorname{Tr}\left(\operatorname{adj}\big(M^\alpha(U(\boldsymbol{\Phi}_0),0;\boldsymbol{n})\big)\,\partial_{\rho\beta}D(\boldsymbol{\Phi}_0)\right). \tag{6.122}$$

Let $\boldsymbol{v}=(0,0,1,1)^T$. By (6.106),

$$\operatorname{adj}\big(M^\alpha(U(\boldsymbol{\Phi}_0),0;\boldsymbol{n})\big)=\frac{3}{4}\hat\gamma^3(\theta,\phi)\boldsymbol{v}\boldsymbol{v}^T. \tag{6.123}$$

Hence,

$$\operatorname{Tr}\left(\operatorname{adj}(M^\alpha)\,\partial_{\varphi\varphi}D\right)=\frac{3}{4}\hat\gamma^3\,\boldsymbol{v}^T\operatorname{diag}(0,2,2,0)\boldsymbol{v}=\frac{3}{2}\hat\gamma^3, \tag{6.124a}$$

$$\operatorname{Tr}\left(\operatorname{adj}(M^\alpha)\,\partial_{\vartheta\vartheta}D\right)=\frac{3}{4}\hat\gamma^3\,\boldsymbol{v}^T\operatorname{diag}(0,0,0,2)\boldsymbol{v}=\frac{3}{2}\hat\gamma^3, \tag{6.124b}$$

$$\operatorname{Tr}\left(\operatorname{adj}(M^\alpha)\,\partial_{\varphi\vartheta}D\right)=0,\qquad \operatorname{Tr}\left(\operatorname{adj}(M^\alpha)\,\partial_{\rho\psi}D\right)=0. \tag{6.124c}$$

Here and below, the matrices in (6.124) are evaluated at $(U,\lambda;\boldsymbol{n})=(U(\boldsymbol{\Phi}_0),0;\boldsymbol{n})$, and $\hat\gamma=\hat\gamma(\theta,\phi)$. Thus,

$$\mathbf{H}_{\det(M^\alpha(U,\lambda;\boldsymbol{n}))}\Big|_{\boldsymbol{\Phi}=\boldsymbol{\Phi}_0}=\mathbf{H}_{\det(M^\alpha(U,0;\boldsymbol{n}))}\Big|_{\boldsymbol{\Phi}=\boldsymbol{\Phi}_0}+\frac{3\lambda}{2}\hat\gamma^3(\theta,\phi)\operatorname{diag}(1,1,0). \tag{6.125}$$

We now consider $\boldsymbol{n}^*$ satisfying $2\hat\gamma(\theta^*,\phi^*)=\hat\gamma(\pi-\theta^*,\pi+\phi^*)$. Define

$$F_\lambda(\varphi,\vartheta,\psi)\coloneqq\det\big(M^\alpha(U(\varphi,\vartheta,\psi),\lambda;\boldsymbol{n}^*)\big). \tag{6.126}$$

The rotations mapping $\boldsymbol{n}^*$ to $-\boldsymbol{n}^*$ form the one-dimensional submanifold

$$\mathcal{M}_*=\big\{U(\pi,0,\psi):\psi\in 2\pi\mathbb{T}\big\}. \tag{6.127}$$

Along this submanifold,

$$F_\lambda(\pi,0,\psi)=0,\qquad \forall\psi\in 2\pi\mathbb{T}. \tag{6.128}$$

Moreover, condition (6.99) and Lemma 6.13 imply

$$\nabla_{\boldsymbol{\Phi}}F_\lambda(\pi,0,\psi)=\mathbf{0},\qquad \forall\psi\in 2\pi\mathbb{T}. \tag{6.129}$$

Thus the zero eigenvalue in the Hessian corresponds to the tangent direction of $\mathcal{M}_*$.

Fix $U_0=U(\pi,0,\psi_0)\in\mathcal{M}_*$ and choose a closed interval $I$ containing $\psi_0$ on which $(\varphi,\vartheta,\psi)$ gives smooth local coordinates. Set

$$\boldsymbol{y}=(\varphi-\pi,\vartheta)^T. \tag{6.130}$$

By (6.125), the Hessian of $F_\lambda$ in the two directions normal to $\mathcal{M}_*$ is

$$\boldsymbol{H}_{\perp,\lambda}(\psi)=\boldsymbol{B}(\psi)+\frac{3\lambda}{2}\hat\gamma^3(\theta^*,\phi^*)I_2,\qquad \psi\in I, \tag{6.131}$$

where

$$\boldsymbol{B}(\psi)\coloneqq\left(\partial_{\rho\beta}\det(M^\alpha(U(\boldsymbol{\Phi}),0;\boldsymbol{n}^*))\Big|_{\boldsymbol{\Phi}=(\pi,0,\psi)}\right)_{\rho,\beta\in\{\varphi,\vartheta\}} \tag{6.132}$$

is continuous. Since $I$ is compact and $\hat\gamma(\theta^*,\phi^*)>0$, we may choose $k_{m,U_0}>0$ and $c>0$ such that

$$\boldsymbol{y}^T\boldsymbol{H}_{\perp,k_{m,U_0}}(\psi)\boldsymbol{y}\ge 2c|\boldsymbol{y}|^2,\qquad \forall\boldsymbol{y}\in\mathbb{R}^2,\quad \forall\psi\in I. \tag{6.133}$$

For each fixed $\psi\in I$, Taylor's formula in the normal variable $\boldsymbol{y}$, together with (6.128) and (6.129), gives

$$F_{k_{m,U_0}}(\pi+y_1,y_2,\psi)=\frac{1}{2}\boldsymbol{y}^T\boldsymbol{H}_{\perp,k_{m,U_0}}(\psi)\boldsymbol{y}+r(\boldsymbol{y},\psi), \tag{6.134}$$

where $r(\boldsymbol{y},\psi)=o(|\boldsymbol{y}|^2)$ uniformly for $\psi\in I$. Hence, after reducing the coordinate neighbourhood if necessary,

$$|r(\boldsymbol{y},\psi)|\le\frac{c}{2}|\boldsymbol{y}|^2. \tag{6.135}$$

Combining this estimate with (6.133), we obtain

$$F_{k_{m,U_0}}(\pi + y_1, y_2, \psi) \geq \frac{c}{2}|\boldsymbol{y}|^2 \geq 0. \tag{6.136}$$

The image of this coordinate neighbourhood is an open neighbourhood $\mathcal{U}_{U_0}$ of $U_0$ in $SO(3)$. Therefore,

$$\det(M^\alpha(U', k_{m,U_0}; \boldsymbol{n}^*)) \geq 0, \qquad \forall U' \in \mathcal{U}_{U_0}, \tag{6.137}$$

which proves the result. □

We can now prove Theorem 6.3.

Proof. (*Existence of the minimal stabilizing function*) Sufficiency follows directly from Lemma 6.6, Theorem 6.4, Lemma 6.10, Lemma 6.11, and Lemma 6.14.

For necessity, define

$$\mathcal{K}(\boldsymbol{n}) \coloneqq \left\{\lambda \geq 0 : \ M^\alpha(U, \lambda; \boldsymbol{n}) \text{ is positive semidefinite for every } U \in SO(3)\right\}. \tag{6.138}$$

If $k^\alpha_{\min}(\theta, \phi)$ is finite, this set is nonempty. It is closed because $M^\alpha$ is continuous in $\lambda$ and the positive semidefinite cone is closed. Hence

$$\lambda_0 \coloneqq k^\alpha_{\min}(\theta, \phi) = \inf \mathcal{K}(\boldsymbol{n}) \in \mathcal{K}(\boldsymbol{n}), \tag{6.139}$$

so $M^\alpha(U, \lambda_0; \boldsymbol{n})$ is positive semidefinite for every $U \in SO(3)$.

Taking $\boldsymbol{n} = \boldsymbol{n}^*$ and expanding at $\boldsymbol{\Phi}_0(\psi) = (\pi, 0, \psi)$ gives

$$\det(M^\alpha(U, \lambda_0; \boldsymbol{n}^*)) = \nabla_{\boldsymbol{\Phi}} \det(M^\alpha(U, \lambda_0; \boldsymbol{n}^*))\Big|_{\boldsymbol{\Phi}=\boldsymbol{\Phi}_0} \cdot (\boldsymbol{\Phi} - \boldsymbol{\Phi}_0) + O(\|\boldsymbol{\Phi} - \boldsymbol{\Phi}_0\|^2). \tag{6.140}$$

If $\nabla_{\boldsymbol{\Phi}} \det(M^\alpha(U, \lambda_0; \boldsymbol{n}^*))\Big|_{\boldsymbol{\Phi}=\boldsymbol{\Phi}_0} \neq \boldsymbol{0}$, then (6.140) shows that the determinant changes sign in a neighborhood of $\boldsymbol{\Phi}_0$. This contradicts the positive semidefiniteness of $M^\alpha(U, \lambda_0; \boldsymbol{n})$. Hence,

$$\nabla_{\boldsymbol{\Phi}} \det(M^\alpha(U, \lambda_0; \boldsymbol{n}^*))\Big|_{\boldsymbol{\Phi}=\boldsymbol{\Phi}_0} = \boldsymbol{0}. \tag{6.141}$$

Lemma 6.13 now yields (6.99). □

### 6.6. Numerical experiments

We present numerical examples to assess the *structure-preserving parametric finite element scheme* (6.40) for time-dependent surface evolution in three dimensions.

In computation, we approximate the minimal stabilizing function by first solving the optimization problem (6.50) at the interpolation nodes $\boldsymbol{n}_{ij} = (\sin\theta_i \cos\phi_j, \sin\theta_i \sin\phi_j, \cos\theta_i)^T$, where $\theta_i = \frac{i\pi}{20}$, $\phi_j = -\pi + \frac{j\pi}{10}$, and $0 \leq i, j \leq 20$. We then use bilinear interpolation to approximate $k^\alpha_{\min}(\theta, \phi)$ at other points.

For spatial discretization, we use `Gmsh` [70] to triangulate the initial surface $\Gamma_0$ with mesh size $h$, obtaining $\Gamma_{h,\tau}(0) = \Gamma_0 = \cup_{j=1}^J \sigma_j^0$. The corresponding time step is $\tau = \frac{2}{25}h^2$.

**6.6.1. Convergence rates.** For the convergence tests, the initial surface $\Gamma_0$ is a $2 \times 2 \times 1$ cuboid. We measure the distance between two surfaces $\Gamma_1, \Gamma_2$ using the manifold distance $M(\Gamma_1, \Gamma_2)$, defined by

$$M(\Gamma_1, \Gamma_2) \coloneqq |(\Omega_1 \backslash \Omega_2) \cup (\Omega_2 \backslash \Omega_1)| = 2|\Omega_1 \cup \Omega_2| - |\Omega_1| - |\Omega_2|, \tag{6.142}$$

where $\Omega_i$ is the region enclosed by $\Gamma_i$, $i = 1, 2$ [12, 20]. The error $e^h(t)$ between the numerical solution $\Gamma_{h,\tau}(t)$ and the exact solution $\Gamma(t)$ at time $t$ is defined by

$$e^h(t) \coloneqq M(\Gamma_{h,\tau}(t), \Gamma(t)). \tag{6.143}$$

where the intermediate surface $\Gamma_{h,\tau}(t)$ is defined by

$$\Gamma_{h,\tau}(t) \coloneqq \frac{t - t_m}{\tau} \Gamma_{h,\tau}(t^{m+1}) + \frac{t_{m+1} - t}{\tau} \Gamma_{h,\tau}(t^m), \qquad t \in [t_m, t_{m+1}]. \tag{6.144}$$

We approximate the exact solution by the fine-mesh solution $\Gamma_{h_e,\tau_e}(t)$, with $h_e = 2^{-4}$ and $\tau_e = \frac{2}{25}h_e^2$. To solve the implicit scheme (6.40), we use the Newton iteration [19] described in Appendix A, with stopping tolerance tol $= 10^{-12}$.

We consider the following two anisotropic surface energies in the convergence tests:

- Case I: $\hat{\gamma}(\theta,\phi) = \sqrt{1+\frac{3}{2}\left(1+\operatorname{sgn}(\sin\theta\cos\phi)\right)\sin^2\theta\cos^2\phi}$;
- Case II: $\hat{\gamma}(\theta,\phi) = 1+\beta\left(\cos^3\theta+\sin^3\theta\cos^3\phi+\sin^3\theta\sin^3\phi\right)$.

Case I is globally $C^1$ and piecewise $C^2$ across $\sin\theta\cos\phi = 0$. Its use in the numerical tests assesses the method for a density of lower regularity than the smooth-density assumption used in the analysis.

| $(h,\tau)$ | $e^h(1)$ | order | $e^h(1)$ | order | $e^h(1)$ | order | $e^h(1)$ | order | $e^h(1)$ | order |
|---|---|---|---|---|---|---|---|---|---|---|
| $(h_0,\tau_0)$ | 1.03e-1 | - | 9.64e-2 | - | 9.95e-2 | - | 1.02e-1 | - | 9.77e-2 | - |
| $(\frac{h_0}{2},\frac{\tau_0}{4})$ | 2.51e-2 | 2.03 | 2.41e-2 | 2.00 | 2.49e-2 | 2.00 | 2.52e-2 | 2.02 | 2.45e-2 | 1.99 |
| $(\frac{h_0}{2^2},\frac{\tau_0}{4^2})$ | 6.28e-3 | 2.00 | 5.91e-3 | 2.03 | 6.19e-3 | 2.01 | 6.36e-3 | 1.99 | 6.06e-3 | 2.02 |
| $\alpha$ | 1 | | $-1$ | | 0 | | 0.5 | | $-0.5$ | |

**Table 6.1.** Numerical errors and convergence rates for Case I.

| $(h,\tau)$ | $e^h(1)$ | order | $e^h(1)$ | order | $e^h(1)$ | order | $e^h(1)$ | order | $e^h(1)$ | order |
|---|---|---|---|---|---|---|---|---|---|---|
| $(h_0,\tau_0)$ | 1.55e-1 | - | 1.11e-1 | - | 9.47e-2 | - | 1.08e-1 | - | 9.76e-2 | - |
| $(\frac{h_0}{2},\frac{\tau_0}{4})$ | 3.29e-2 | 2.23 | 2.86e-2 | 1.95 | 2.37e-2 | 1.99 | 2.49e-2 | 2.11 | 2.42e-2 | 2.01 |
| $(\frac{h_0}{2^2},\frac{\tau_0}{4^2})$ | 8.48e-3 | 1.96 | 6.71e-3 | 2.09 | 6.10e-3 | 1.96 | 6.91e-3 | 1.85 | 5.94e-3 | 2.03 |
| $\alpha$ | 10 | | $-10$ | | 0 | | 5 | | $-5$ | |

**Table 6.2.** Numerical errors and convergence rates for Case II with $\beta = \frac{1}{8}$.

Tables 6.1 and 6.2 report the numerical errors and convergence rates for different $\alpha$. The results show approximately second-order convergence with respect to $h$, consistent with second-order spatial and first-order temporal accuracy of (6.40). The errors differ little across the tested values of $\alpha$, indicating robustness with respect to this parameter.

**6.6.2. Volume conservation and energy stability.** To examine volume conservation and energy dissipation, we introduce the normalized volume loss and normalized energy:

$$\left.\frac{\Delta V^h(t)}{V^h(0)}\right|_{t=t_m} := \frac{V^m - V^0}{V^0}, \qquad \left.\frac{W^h(t)}{W^h(0)}\right|_{t=t_m} := \frac{W^m}{W^0}. \tag{6.145}$$

We test the values $\alpha = 0, 1, -1$ with three anisotropic surface energies: Case I, Case II with $\beta = \frac{1}{8}$, and Case II with $\beta = \frac{1}{4}$. The initial surface is a $3\times3\times2$ cuboid, with mesh size $h = 2^{-4}$ and time step $\tau = \frac{2}{25}h^2$.

Figures 6.3 and 6.4 show the normalized volume loss $\frac{\Delta V^h(t)}{V(0)}$ and the Newton iteration count over time, respectively. The volume loss remains of order $10^{-15}$, close to roundoff error, confirming volume conservation. The Newton iteration count decreases from 4 to 2 within a short time, indicating the computational efficiency of (6.40).

Figure 6.5 shows the normalized energy $\frac{W^h(t)}{W^h(0)}$ over time for different surface energies and values of $\alpha$. The total energy decreases monotonically in these experiments, confirming the energy dissipation property of (6.40). In Figure 6.5(b) and (d), the energy curves for different $\alpha$ are nearly identical, showing that the computed energy decay depends little on this parameter.

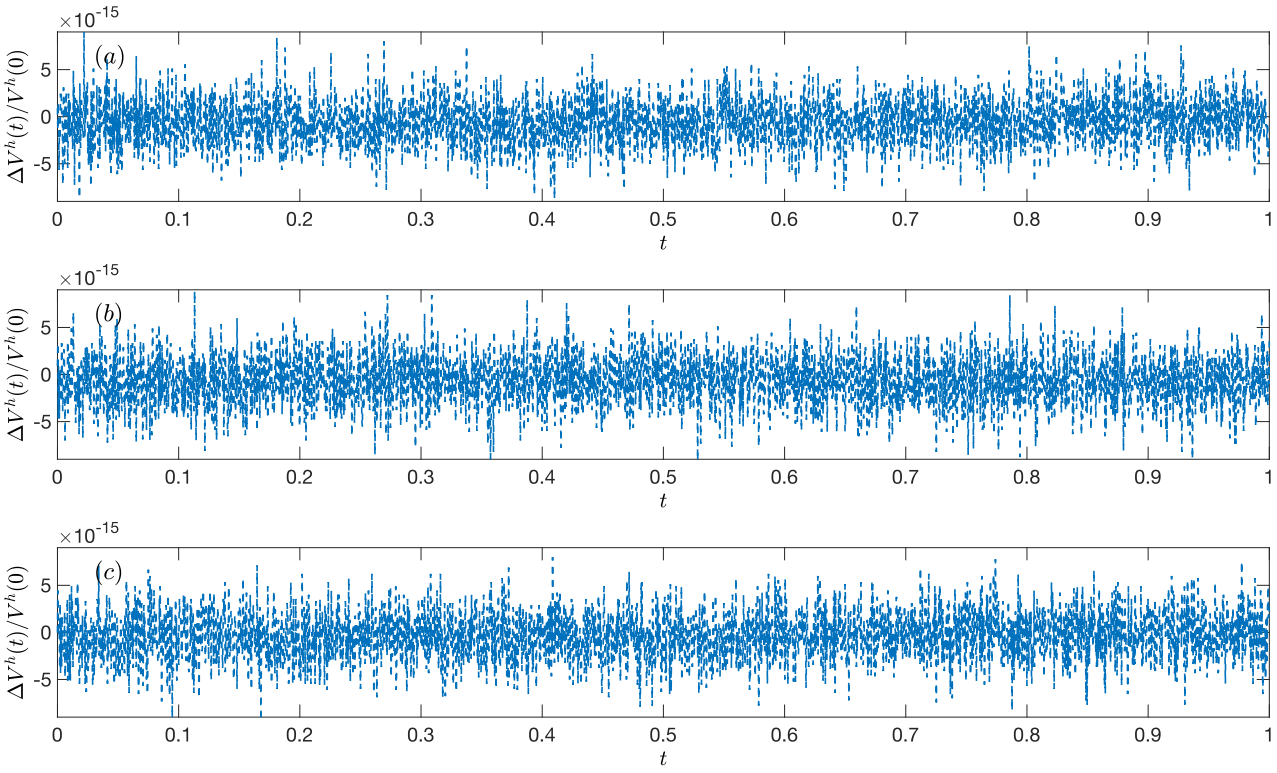



**Figure 6.3.** Normalized volume loss for (a) Case I, (b) Case II with $\beta = \frac{1}{8}$, and (c) Case II with $\beta = \frac{1}{4}$. The parameter values are $\alpha = 0, 1, -1$, respectively.

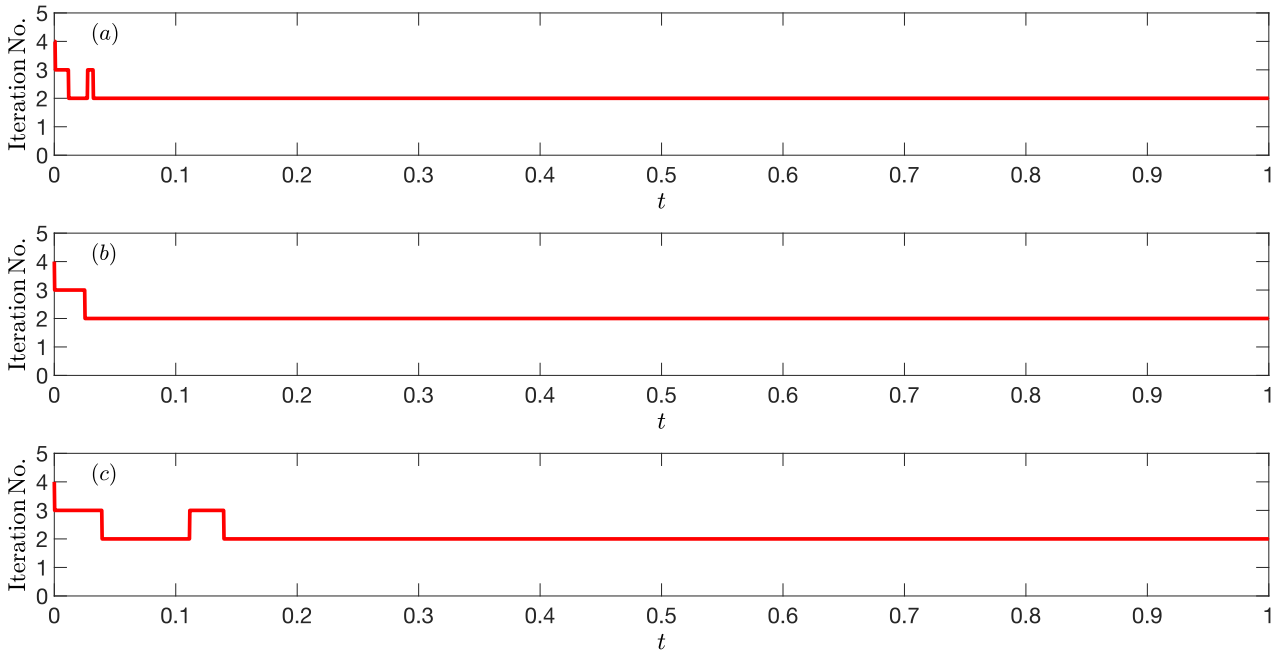



**Figure 6.4.** Newton iteration counts for (a) Case I, (b) Case II with $\beta = \frac{1}{8}$, and (c) Case II with $\beta = \frac{1}{4}$. The parameter values are $\alpha = 0, 1, -1$, respectively.

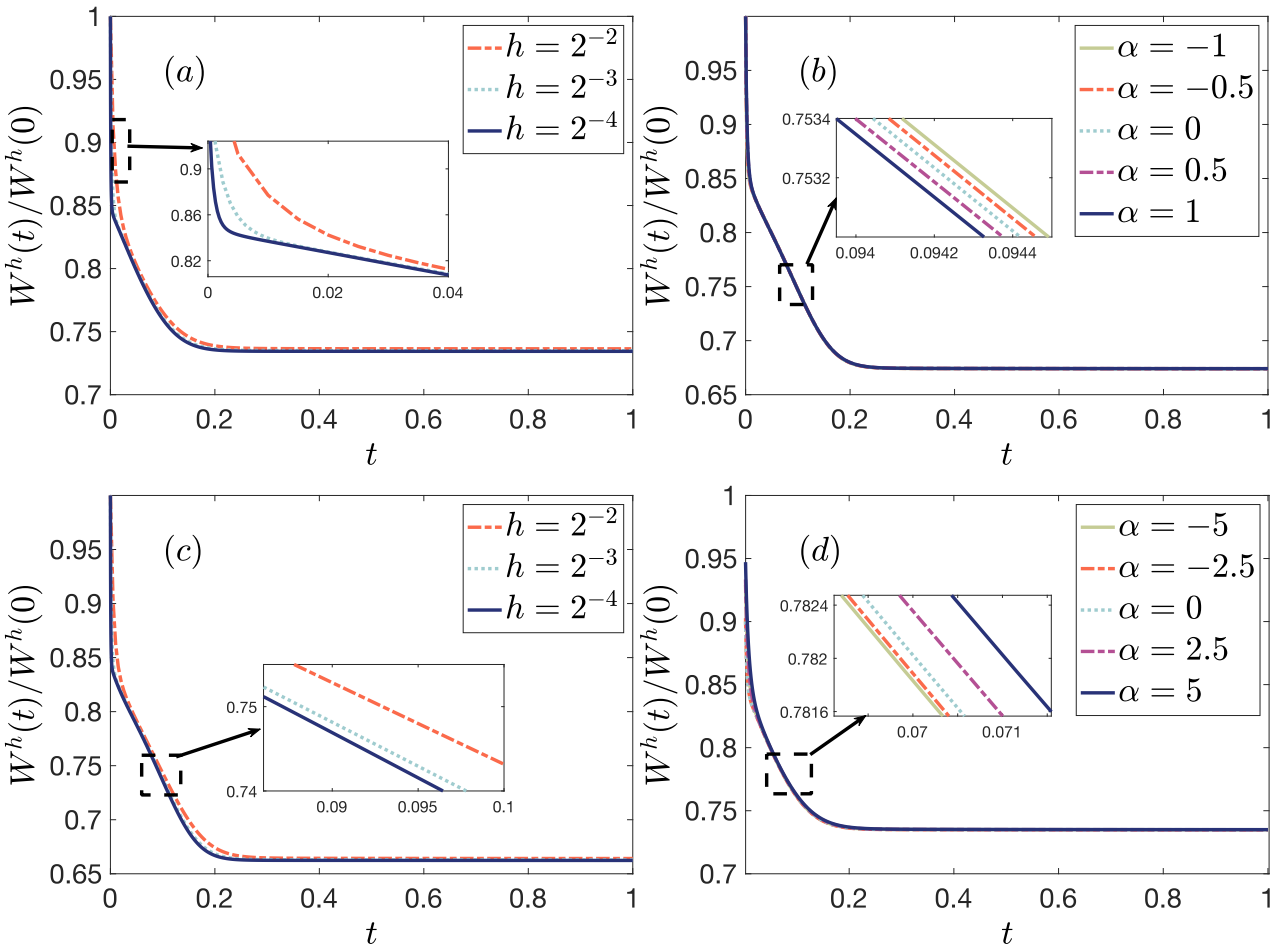



**Figure 6.5.** Normalized energy for (a) Case I with $\alpha = 0$, (b) Case II with $\beta = \frac{1}{8}$, (c) Case II with $\beta = \frac{1}{4}$ and $\alpha = -1$, and (d) Case I.

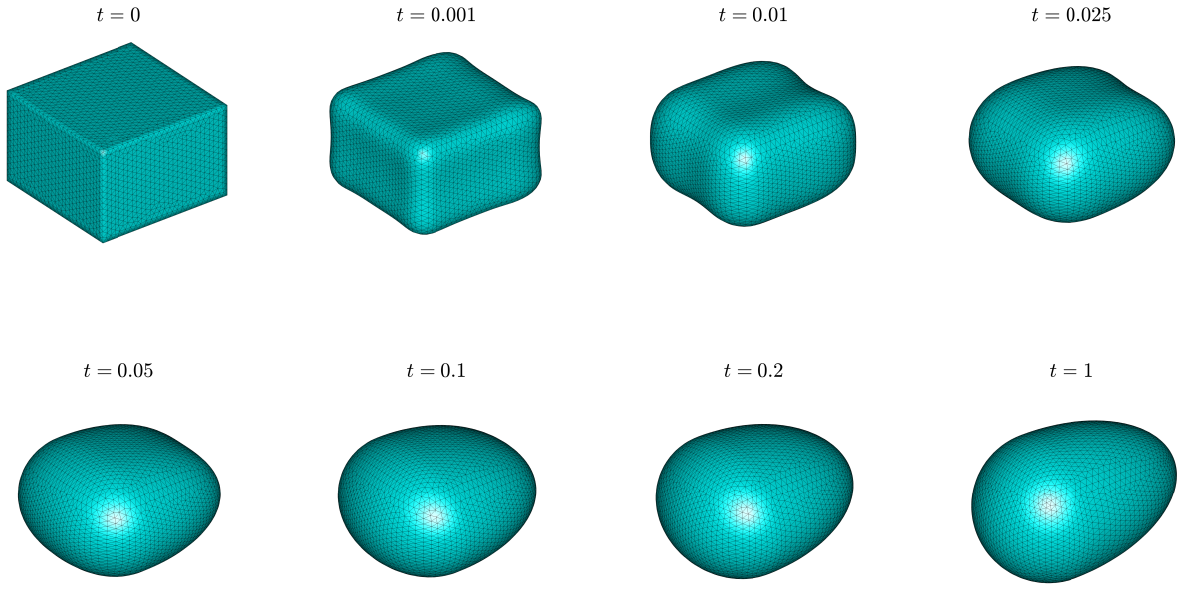



**Figure 6.6.** Evolution of a $3 \times 3 \times 2$ cuboid under anisotropic surface diffusion for Case I with $\alpha = 0$, at different times.

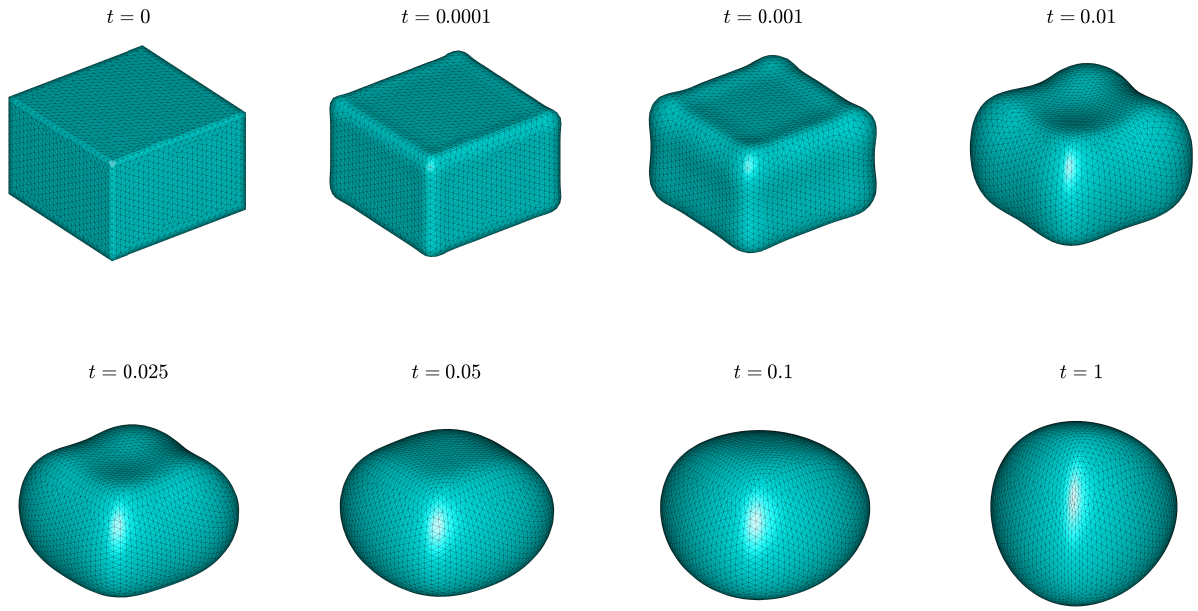



**Figure 6.7.** Evolution of a $3 \times 3 \times 2$ cuboid under anisotropic surface diffusion for Case II with $\beta = \frac{1}{4}$ and $\alpha = -1$, at different times.

**6.6.3. Morphological evolution of closed surfaces under anisotropic surface diffusion.** We apply (6.40) to simulate morphological evolution driven by *anisotropic surface diffusion*.

Next, we examine pinch-off of elongated cuboids under anisotropic surface diffusion. Figures 6.8 and 6.9 show simulations using (6.40) for $8 \times 1 \times 1$ and $16 \times 1 \times 1$ cuboids, respectively, with $h = 2^{-4}$, $\tau = 1 \times 10^{-4}$.

As in the isotropic evolutions reported in [19, 25], bulges first develop at the two ends of the cuboid while the sharp corners smooth out. The bulges then migrate toward the center, eventually producing pinch-off singularities. Compared with Figure 6.8, Figure 6.9 exhibits more singularities and different shapes at the two ends. These observations suggest the following:

(1) More elongated initial surfaces tend to break into more components under surface diffusion;
(2) Anisotropic surface diffusion with asymmetric surface energy can differ substantially from evolution with symmetric surface energy.

Surfaces with genus at least one, such as a torus, often undergo topological changes under surface diffusion. To examine this behavior, we perform two experiments with tori of major radius $R$ and minor radius $r$, using the fixed threefold anisotropy

$$\hat{\gamma}(\theta, \phi) = 1 + \beta \left( \cos^3 \theta + \sin^3 \theta \cos^3 \phi + \sin^3 \theta \sin^3 \phi \right) \tag{6.146}$$

and $\alpha = 0.5$. The results are shown in Figures 6.10 and 6.11.

In Figure 6.10, we take $R = 1$ and $r = 0.25$. The central hole gradually contracts and eventually disappears, changing the topology from genus one to genus zero. Although the present method cannot continue the evolution beyond a topological change, we expect the surface eventually to approach a simply connected shape determined by the surface energy, similar to that in Figure 6.7.

In Figure 6.11, we take $R = 1$ and $r = 0.2$, giving a larger ratio of major to minor radius. Three separate necks form and become more pronounced over time, eventually producing pinch-off singularities. The torus consequently breaks into disconnected components, illustrating another type of topological change under *anisotropic surface diffusion*. Because the surface energy is asymmetric, the singularities occur at different times.

The next example considers an orthogonal cross-beam, as shown in Figures 6.12 and 6.13. The initial surface is formed by two intersecting cuboids of dimensions $12 \times 1 \times 1$ and $8 \times 1 \times 1$. Necks develop on all four arms, with the two longer arms pinching off first at $t = 0.151$. Figure 6.13 also

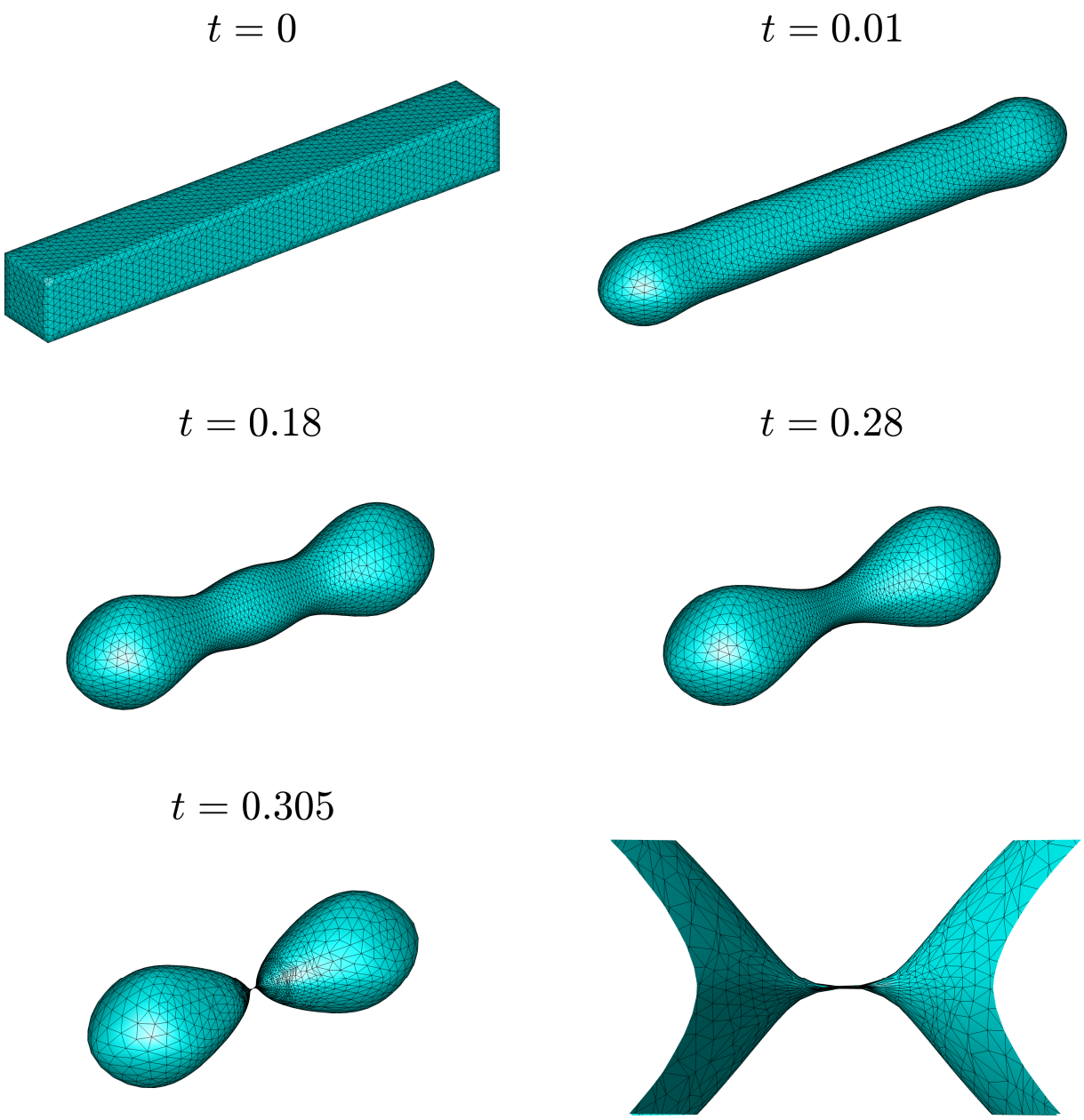



**Figure 6.8.** Snapshots of an $8 \times 1 \times 1$ cuboid evolving under anisotropic surface diffusion up to pinch-off, for fourfold anisotropy $\hat{\gamma}(\theta, \phi) = 1 + \frac{1}{4}\left(\cos^4\theta + \sin^4\theta\cos^4\phi + \sin^4\theta\sin^4\phi\right)$ with $\alpha = -0.5$.

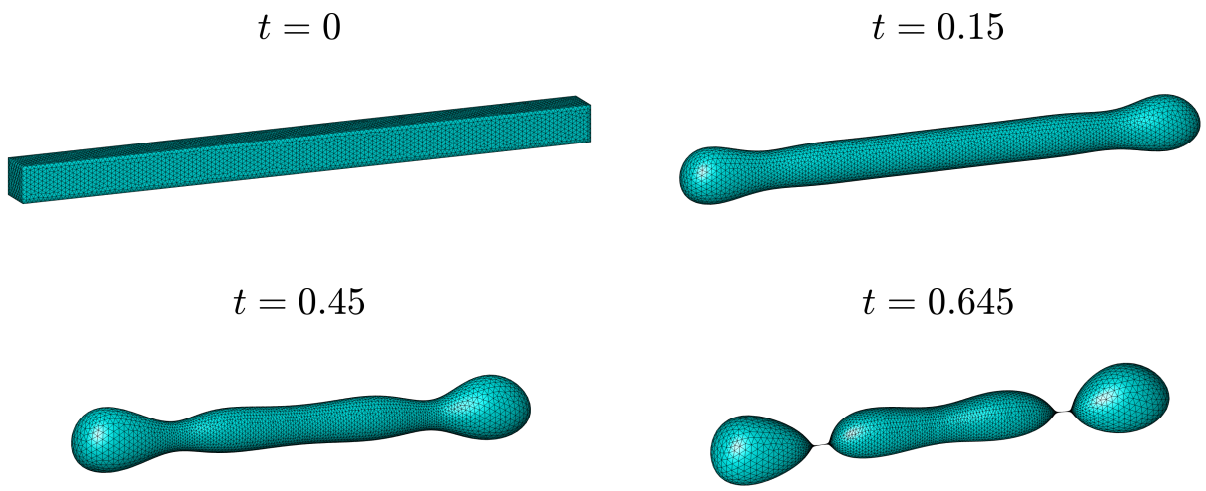



**Figure 6.9.** Snapshots of a $16 \times 1 \times 1$ cuboid evolving under anisotropic surface diffusion up to pinch-off, for Case II with $\beta = \frac{1}{8}$ and $\alpha = -0.5$.

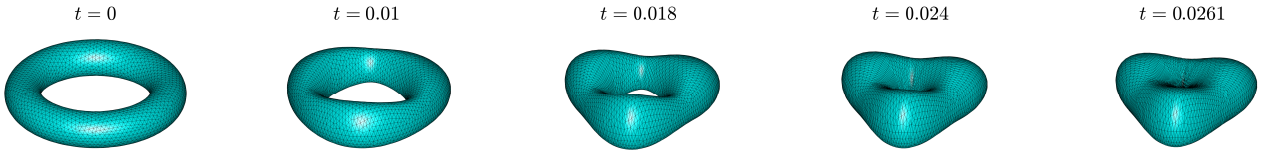



**Figure 6.10.** Snapshots of a $(1, 0.25)$-torus evolving under anisotropic surface diffusion for Case II with $\beta = 1/4$ and $\alpha = 0.5$.

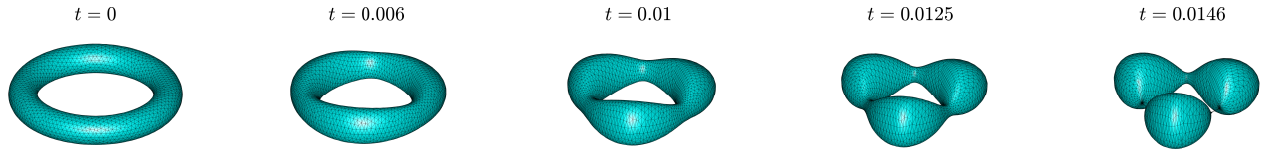



**Figure 6.11.** Snapshots of a $(1, 0.2)$-torus evolving under anisotropic surface diffusion up to pinch-off, for Case II with $\beta = 1/4$ and $\alpha = 0.5$.

shows the iteration count, normalized volume loss, and normalized energy. The results confirm that the scheme (6.40) preserves volume and decreases energy throughout the simulation.

In the final example, we use (6.40) to simulate a spherical lattice under anisotropic surface diffusion for Case II with $\beta = \frac{1}{4}$; see Figure 6.14. The six holes gradually expand, eventually causing a topological change that separates the surface into disconnected components. As in Figure 6.11, the asymmetric surface energy leads to different singularity times. This example illustrates the ability of (6.40) to handle complex initial geometries and resolve the dynamics of anisotropic surface diffusion.

## 6.7. Summary

This chapter extends the structure-preserving parametric finite element method based on the $\alpha$-surface energy matrix to anisotropic surface diffusion in three dimensions. The fully discrete scheme preserves volume exactly and, with $k(\theta, \phi) \geq k^{\alpha}_{\min}(\theta, \phi)$, is unconditionally energy stable for every $\alpha$ under $2\hat{\gamma}(\theta, \phi) - \hat{\gamma}(\pi - \theta, \pi + \phi) > 0$. For the symmetric matrix choice $\alpha = -1$, this condition can be relaxed to $2\hat{\gamma}(\theta, \phi) - \hat{\gamma}(\pi - \theta, \pi + \phi) \geq 0$. For $\alpha = -1$, this condition is necessary and sufficient for the local energy estimate within the stated matrix family, and is therefore optimal in that framework. Numerical experiments demonstrate the efficiency, accuracy, and structure-preserving

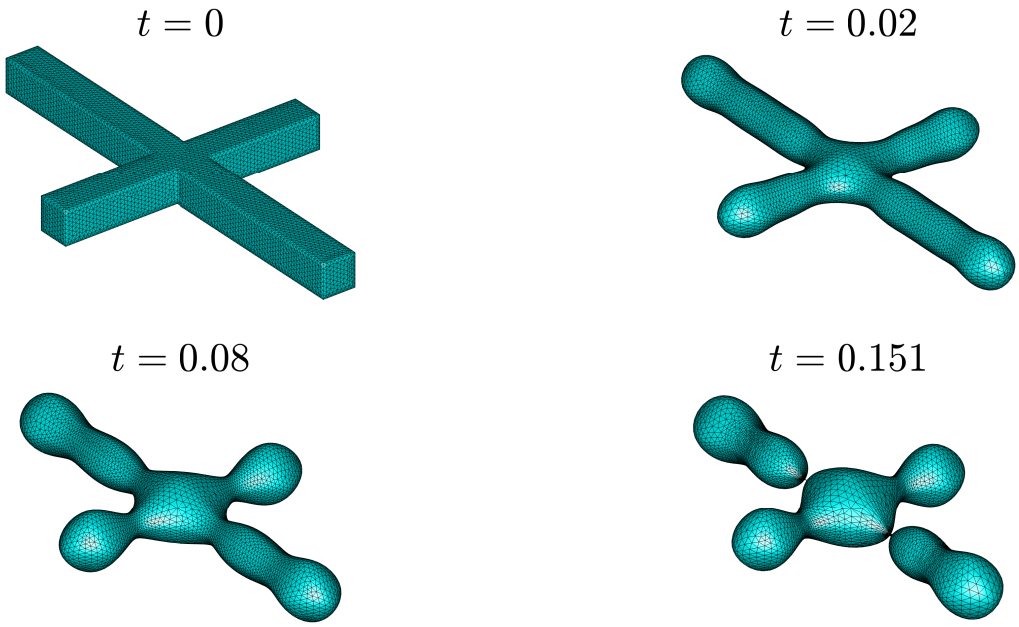



**Figure 6.12.** Evolution of an orthogonal cross-beam under anisotropic surface diffusion up to pinch-off, for fourfold anisotropy $\hat{\gamma}(\theta, \phi) = 1 + \frac{1}{4}\left(\cos^4\theta + \sin^4\theta\cos^4\phi + \sin^4\theta\sin^4\phi\right)$.

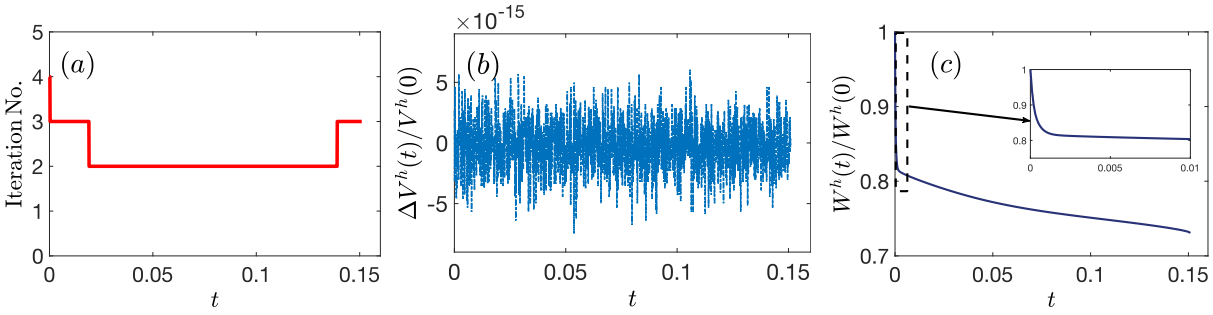



**Figure 6.13.** Evolution of an orthogonal cross-beam under anisotropic surface diffusion: (a) iteration count, (b) normalized volume loss, and (c) normalized energy.

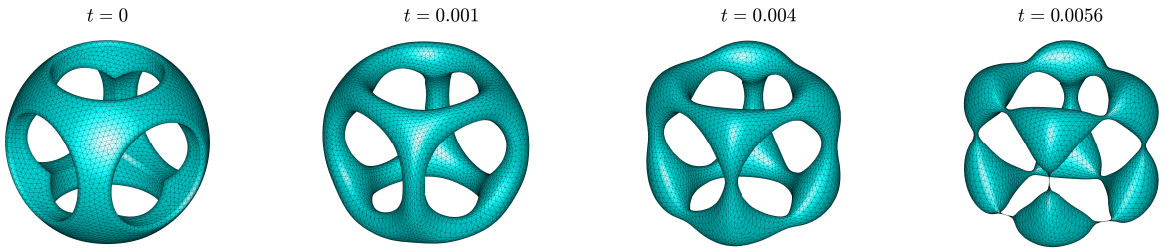



**Figure 6.14.** Evolution of a spherical lattice under anisotropic surface diffusion for Case II with $\beta = \frac{1}{4}$.

properties of the method for complex surface evolution, including stable computation and good mesh quality under strong anisotropy and complex geometry.

CHAPTER 7

# Application: solid-state dewetting in three dimensions

Solid-state dewetting in three dimensions can be viewed as the evolution of an *open surface* governed jointly by surface diffusion and a moving contact line. As a solid thin film moves on a flat substrate, a moving contact line forms at the junction of the three phases, introducing additional dynamics. Compared with the two-dimensional setting, the interface becomes an open surface and the contact points become a spatial curve. Anisotropic surface energy, geometric constraints on the contact line, and topological changes are strongly coupled, producing richer dynamics across multiple scales.

Structure-preserving numerical methods for three-dimensional solid-state dewetting are therefore needed for accurate long-time simulations and for predictions that can be compared with experiments. By resolving the effects of surface energy anisotropy, island shape selection, and sensitivity to material parameters, such methods provide a computational basis for controlled patterning in applications including sensors, optical and magnetic devices, and catalytic templates [136, 122, 101].

## 7.1. The sharp interface model

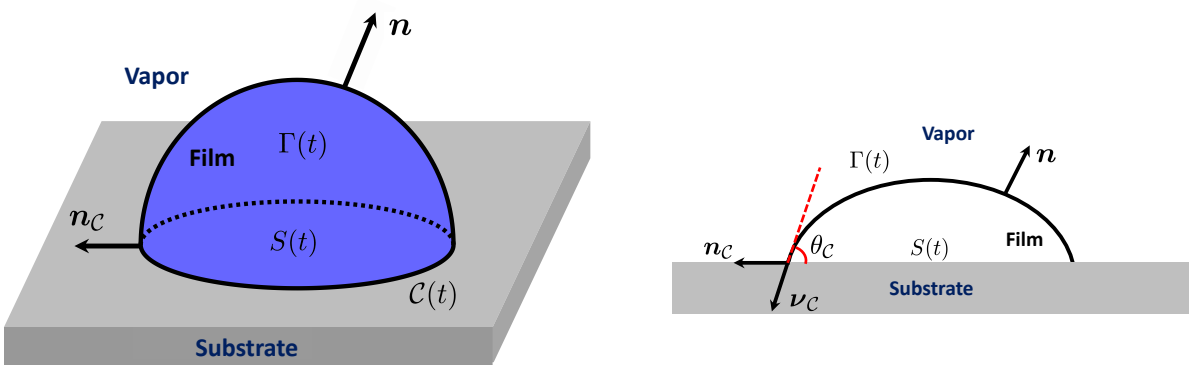



**Figure 7.1.** Solid-state dewetting of a solid thin film on a rigid flat substrate. Left: $\Gamma$ is the film/vapor interface, $S$ is the film/substrate interface, and $C$ is the contact line; $\boldsymbol{n}_C$ is the outward unit normal to $C$ in $S$. Right: geometry of the contact angle $\theta_C = \arccos(\boldsymbol{n}_C \cdot \boldsymbol{\nu}_C)$, where $\boldsymbol{\nu}_C$ is the conormal to $C$.

As in two dimensions, the sharp interface model for *solid-state dewetting* in three dimensions describes the evolution of an open surface

$$\Gamma(t) := \boldsymbol{X}(\cdot, t), \qquad \forall t > 0, \tag{7.1}$$

under *anisotropic surface diffusion* and *contact line migration*.

As illustrated in Figure 7.1, the *sharp interface model* for solid-state dewetting in three dimensions is given as follows [94]. The open surface $\Gamma(t)$ satisfies

$$\boldsymbol{n} \cdot \partial_t \boldsymbol{X} = \Delta_\Gamma \mu, \qquad \forall t > 0, \tag{7.2a}$$

$$\mu = \nabla_\Gamma \cdot \boldsymbol{\xi}, \tag{7.2b}$$

The interior law prescribes only the normal velocity; tangential motion corresponds to the choice of parametrization. At the contact line, the boundary law below selects in-plane normal motion on the substrate. The model is supplemented with the following boundary conditions at the contact line $C := \boldsymbol{X}_C = (x_C, y_C, z_C)^T$:

(i) The *contact line condition*:

$$z_C(\cdot, t) = 0, \qquad \forall t > 0; \tag{7.3}$$

(ii) The *relaxed contact angle condition*:

$$\partial_t \boldsymbol{X}_C = -\eta\Big(\boldsymbol{\nu}_C^\gamma \cdot \boldsymbol{n}_C - \cos\theta_Y\Big)\boldsymbol{n}_C, \qquad \forall t > 0; \tag{7.4}$$

(iii) The *zero-mass-flux condition*:

$$\Big(\boldsymbol{\nu}_C \cdot \nabla_\Gamma \mu\Big)\Big|_C = 0, \qquad \forall t > 0. \tag{7.5}$$

Here $\boldsymbol{n}_C = (n_{C,1}, n_{C,2}, 0)^T$ is the outward unit normal to $C$ in the substrate plane, $\boldsymbol{\nu}_C^\gamma := (\boldsymbol{\xi}\cdot\boldsymbol{n})\boldsymbol{\nu}_C - (\boldsymbol{\xi}\cdot\boldsymbol{\nu}_C)\boldsymbol{n}$, $\boldsymbol{\nu}_C$ is the conormal, $\eta > 0$ is the contact line mobility, and $\theta_Y$ is Young's angle.

The total free energy of the system is defined by

$$W(t) := \int_{\Gamma(t)} \hat{\gamma}(\theta,\phi)\,\mathrm{d}A - \cos\theta_Y\,|S(t)|, \tag{7.6}$$

where $|S(t)|$ is the area of the region $S(t)$ enclosed by $C$ in the substrate plane. Let $\Omega(t)$ be the region enclosed by $\Gamma(t)$ and $S(t)$, and let $V(t)$ be its volume. The system conserves total volume (mass) and exhibits energy dissipation with respect to the total surface free energy:

$$V(t) \equiv V(0), \qquad W(t) \le W(t') \le W(0), \qquad \forall t \ge t' \ge 0. \tag{7.7}$$

Following the derivation in Section 6.1, we can rewrite the sharp interface model (7.2)–(7.5) as

$$\boldsymbol{n}\cdot\partial_t\boldsymbol{X} - \Delta_\Gamma\mu = 0, \qquad \forall t > 0, \tag{7.8a}$$

$$\mu\boldsymbol{n} + \nabla_\Gamma\cdot\Big(\hat{\boldsymbol{G}}_k^\alpha(\theta,\phi)\nabla_\Gamma\boldsymbol{X}\Big) = \boldsymbol{0}, \tag{7.8b}$$

subject to (7.3)–(7.5) on $C$, where the surface energy matrix $\hat{\boldsymbol{G}}_k^\alpha$ is defined in (6.12).

## 7.2. Structure-preserving parametric finite element discretization

**7.2.1. The weak formulation.** Introduce the Sobolev space

$$H_0^1(\Gamma(t)) := \left\{u \in H^1(\Gamma(t)) :\ u|_{C(t)} = 0\right\}. \tag{7.9}$$

Multiplying (7.8a) by a test function $\varphi \in H^1(\Gamma(t))$ and integrating over $\Gamma(t)$, we apply integration by parts and the zero-mass-flux condition (7.5) to obtain

$$\Big(\boldsymbol{n}\cdot\partial_t\boldsymbol{X}, \varphi\Big)_{\Gamma(t)} + \Big(\nabla_\Gamma\mu, \nabla_\Gamma\varphi\Big)_{\Gamma(t)} = 0. \tag{7.10}$$

Observe that

$$\begin{aligned}\Big(\hat{\boldsymbol{G}}_k^\alpha(\theta,\phi)\nabla_\Gamma\boldsymbol{X}\Big)\boldsymbol{\nu}_C &= \left(\hat{\gamma}(\theta,\phi)I_3 - \boldsymbol{n}\boldsymbol{\xi}^T\right)(I - \boldsymbol{n}\boldsymbol{n}^T)\boldsymbol{\nu}_C \\ &= \left(\hat{\gamma}(\theta,\phi)I_3 - \boldsymbol{n}\boldsymbol{\xi}^T\right)\boldsymbol{\nu}_C \\ &= \hat{\gamma}(\theta,\phi)\boldsymbol{\nu}_C - (\boldsymbol{\xi}\cdot\boldsymbol{\nu}_C)\boldsymbol{n},\end{aligned} \tag{7.11}$$

The definition of $\boldsymbol{\nu}_C^\gamma$ and the identity $\boldsymbol{\xi}\cdot\boldsymbol{n} = \hat{\gamma}(\theta,\phi)$ therefore give

$$\Big(\hat{\boldsymbol{G}}_k^\alpha(\theta,\phi)\nabla_\Gamma\boldsymbol{X}\Big)\boldsymbol{\nu}_C = \boldsymbol{\nu}_C^\gamma. \tag{7.12}$$

The following identities are readily verified:

$$\boldsymbol{\nu}_C^\gamma\cdot\boldsymbol{n}_C = \cos\theta_Y - \frac{1}{\eta}\left(\partial_t\boldsymbol{X}_C\cdot\boldsymbol{n}_C\right), \tag{7.13a}$$

$$\boldsymbol{\nu}_C^\gamma = (\boldsymbol{\nu}_C^\gamma\cdot\boldsymbol{e}_z)\boldsymbol{e}_z + (\boldsymbol{\nu}_C^\gamma\cdot\boldsymbol{n}_C)\boldsymbol{n}_C, \tag{7.13b}$$

Here (7.13a) rewrites the relaxed contact angle condition (7.4), while (7.13b) decomposes $\boldsymbol{\nu}_C^\gamma$ along $\boldsymbol{e}_z = (0,0,1)^T, \boldsymbol{n}_C$.

Multiplying (7.8b) by $\boldsymbol{\omega} \in [H^1(\Gamma(t))]^2 \times H_0^1(\Gamma(t))$ and integrating by parts yields

$$\begin{aligned} 0 &= \Big(\mu \boldsymbol{n}, \boldsymbol{\omega}\Big)_{\Gamma(t)} - \Big\langle \hat{\boldsymbol{G}}_k^\alpha(\theta,\phi)\nabla_\Gamma \boldsymbol{X}, \nabla_\Gamma \boldsymbol{\omega}\Big\rangle_{\Gamma(t)} + \Big(\Big(\hat{\boldsymbol{G}}_k^\alpha(\theta,\phi)\nabla_\Gamma \boldsymbol{X}\Big)\boldsymbol{\nu}_C, \boldsymbol{\omega}\Big)_{C(t)} \\ &= \Big(\mu \boldsymbol{n}, \boldsymbol{\omega}\Big)_{\Gamma(t)} - \Big\langle \hat{\boldsymbol{G}}_k^\alpha(\theta,\phi)\nabla_\Gamma \boldsymbol{X}, \nabla_\Gamma \boldsymbol{\omega}\Big\rangle_{\Gamma(t)} + \Big(\boldsymbol{\nu}_C^\gamma, \boldsymbol{\omega}\Big)_{C(t)} \\ &= \Big(\mu \boldsymbol{n}, \boldsymbol{\omega}\Big)_{\Gamma(t)} - \Big\langle \hat{\boldsymbol{G}}_k^\alpha(\theta,\phi)\nabla_\Gamma \boldsymbol{X}, \nabla_\Gamma \boldsymbol{\omega}\Big\rangle_{\Gamma(t)} + \Big(\boldsymbol{\nu}_C^\gamma \cdot \boldsymbol{n}_C, \boldsymbol{\omega} \cdot \boldsymbol{n}_C\Big)_{C(t)}. \end{aligned} \tag{7.14}$$

Substituting (7.13a) and (7.13b) into (7.14) gives

$$\begin{aligned} 0 = \Big(\mu \boldsymbol{n}, \boldsymbol{\omega}\Big)_{\Gamma(t)} - \Big\langle \hat{\boldsymbol{G}}_k^\alpha(\theta,\phi)\nabla_\Gamma \boldsymbol{X}, \nabla_\Gamma \boldsymbol{\omega}\Big\rangle_{\Gamma(t)} + \cos\theta_Y \Big(\boldsymbol{n}_C, \boldsymbol{\omega}\Big)_{C(t)} \\ - \frac{1}{\eta}\Big(\partial_t \boldsymbol{X}_C \cdot \boldsymbol{n}_C,\ \boldsymbol{\omega} \cdot \boldsymbol{n}_C\Big)_{C(t)} \end{aligned} \tag{7.15}$$

The weak formulation of the *sharp interface model for solid-state dewetting* in three dimensions is therefore as follows. Given $\Gamma(0)$, find $\Gamma(t)$ for every $t > 0$ such that

$$\Big(\boldsymbol{n} \cdot \partial_t \boldsymbol{X}, \varphi\Big)_{\Gamma(t)} + \Big(\nabla_\Gamma \mu, \nabla_\Gamma \varphi\Big)_{\Gamma(t)} = 0, \qquad \forall \varphi \in H^1(\Gamma(t)), \tag{7.16a}$$

$$\begin{aligned} &\Big(\mu \boldsymbol{n}, \boldsymbol{\omega}\Big)_{\Gamma(t)} - \Big\langle \hat{\boldsymbol{G}}_k^\alpha(\theta,\phi)\nabla_\Gamma \boldsymbol{X}, \nabla_\Gamma \boldsymbol{\omega}\Big\rangle_{\Gamma(t)} + \cos\theta_Y \Big(\boldsymbol{n}_C, \boldsymbol{\omega}\Big)_{C(t)} \\ &\quad - \frac{1}{\eta}\Big(\partial_t \boldsymbol{X}_C \cdot \boldsymbol{n}_C,\ \boldsymbol{\omega} \cdot \boldsymbol{n}_C\Big)_{C(t)} = 0, \qquad \forall \boldsymbol{\omega} \in [H^1(\Gamma(t))]^2 \times H_0^1(\Gamma(t)). \end{aligned} \tag{7.16b}$$

for every $\varphi \in H^1(\Gamma(t))$ and $\boldsymbol{\omega} \in [H^1(\Gamma(t))]^2 \times H_0^1(\Gamma(t))$.

Theorem 7.1 (Volume conservation and energy dissipation). *Let* $(\boldsymbol{X}, \mu)$ *solve* (7.16). *Then the total film volume is conserved and the total free energy is dissipated, namely,*

$$V(t) \equiv V(0), \qquad W(t) \le W(t') \le W(0), \qquad \forall t \ge t' \ge 0. \tag{7.17}$$

**7.2.2. The fully discrete scheme.** Suppose that the boundary of the polyhedral surface $\Gamma^m$ consists of $N_C$ connected oriented line segments, denoted by

$$C^m := \bigcup_{j=1}^{N_C} l_j^m. \qquad m \ge 0. \tag{7.18}$$

Define the finite element spaces

$$\mathbb{K}^m := \Big\{ u \in C(\Gamma^m) \,\Big|\, u|_{\sigma_j^m} \in \mathcal{P}^1(\sigma_j^m),\ \forall 1 \le j \le J \Big\}, \tag{7.19a}$$

$$\mathbb{K}_0^m := \Big\{ \varphi^h \in \mathbb{K}^m \,\Big|\, \varphi^h|_{l_j^m} = 0,\ \forall 1 \le j \le N_C \Big\}, \tag{7.19b}$$

where $\mathcal{P}^1(\sigma_j^m)$ is the space of polynomials of degree $\le 1$ on $\sigma_j^m$. On $C^m$, we use the mass-lumped inner product

$$\Big(u, v\Big)_{C^m}^h := \frac{1}{2}\sum_{j=1}^{N_C} |l_j^m| \Big( (u \cdot v)(\boldsymbol{p}_{j_1}^m)^- + (u \cdot v)(\boldsymbol{p}_{j_2}^m)^- \Big), \tag{7.20}$$

where $\boldsymbol{p}_{j_1}^m$ and $\boldsymbol{p}_{j_2}^m$ are the endpoints of $l_j^m$, ordered according to the orientation of $C^m$. The discrete derivative $\partial_s$ on the boundary is defined by

$$\partial_s u|_{l_j^m} := \frac{u(\boldsymbol{p}_{j_2}^m) - u(\boldsymbol{p}_{j_1}^m)}{|l_j^m|}. \tag{7.21}$$

The extension to vector-valued functions is straightforward. Let $\boldsymbol{n}_C^m$ be the outward unit normal to $C^m$ in the substrate plane. On each segment $l_j^m = [\boldsymbol{p}_{j_1}^m, \boldsymbol{p}_{j_2}^m]$, it is given by

$$\boldsymbol{n}_{C,j}^m := \boldsymbol{n}_C^m|_{l_j^m} = \frac{(\boldsymbol{p}_{j_2}^m - \boldsymbol{p}_{j_1}^m) \times \boldsymbol{e}_z}{\|(\boldsymbol{p}_{j_2}^m - \boldsymbol{p}_{j_1}^m) \times \boldsymbol{e}_z\|}. \tag{7.22}$$

We can now state the *structure-preserving parametric finite element method* for solid-state dewetting. Given an initial triangulated surface $\Gamma^0$, for $m = 0, 1, 2, \cdots$, find the updated surface $\Gamma^{m+1}$ such that

$$\left(\boldsymbol{n}^{m+\frac{1}{2}} \cdot \frac{\boldsymbol{X}^{m+1} - \boldsymbol{X}^m}{\tau}, \varphi^h\right)_{\Gamma^m}^h + \left(\nabla_\Gamma \mu^{m+1}, \nabla_\Gamma \varphi^h\right)_{\Gamma^m}^h = 0, \qquad \forall \varphi^h \in \mathbb{K}^m, \tag{7.23a}$$

$$\begin{aligned} &\left(\mu^{m+1}\boldsymbol{n}^{m+\frac{1}{2}}, \boldsymbol{\omega}^h\right)_{\Gamma^m}^h - \left\langle \hat{\boldsymbol{G}}_k^\alpha(\theta^m, \phi^m)\nabla_\Gamma \boldsymbol{X}^{m+1}, \nabla_\Gamma \boldsymbol{\omega}^h\right\rangle_{\Gamma^m}^h + \cos\theta_Y \left(\boldsymbol{n}_C^{m,*}, \boldsymbol{\omega}^h\right)_{C^m}^h \\ &\quad - \frac{1}{\eta\tau}\left((\boldsymbol{X}_C^{m+1} - \boldsymbol{X}_C^m)\cdot \boldsymbol{n}_C^m,\ \boldsymbol{\omega}^h \cdot \boldsymbol{n}_C^m\right)_{C^m}^h = 0, \qquad \forall \boldsymbol{\omega}^h \in [\mathbb{K}^m]^2 \times \mathbb{K}_0^m, \end{aligned} \tag{7.23b}$$

where $\boldsymbol{n}_C^{m,*} := \frac{1}{2}(\partial_s \boldsymbol{X}_C^{m+1} + \partial_s \boldsymbol{X}_C^m) \times \boldsymbol{e}_z$.

**7.2.3. Structure preservation.** Let $V^m$ be the volume enclosed by $\Gamma^m$ and the substrate, as defined in (6.42a). Let $W^m$ be the total free energy at time $t^m$, defined by

$$W^m := \left(\hat{\gamma}(\theta^m, \phi^m), 1\right)_{\Gamma^m}^h - \cos\theta_Y |S^m|. \tag{7.24}$$

As in the closed-surface case, the *structure-preserving parametric finite element scheme* for solid-state dewetting preserves volume and dissipates energy at the discrete level.

Lemma 7.1 ([20]). *For the substrate region $S^m$, we have*

$$|S^{m+1}| - |S^m| = \left(\boldsymbol{n}_C^{m,*}, \boldsymbol{X}_C^{m+1} - \boldsymbol{X}_C^m\right)_{C^m}^h, \qquad \forall m \geq 0. \tag{7.25}$$

Theorem 7.2 (Structure-preserving properties). *Let $(\boldsymbol{X}^{m+1}, \mu^{m+1})$ solve (7.23). Then the total volume is conserved, namely,*

$$V^{m+1} = V^m = \cdots = V^0, \qquad \forall m \geq 0. \tag{7.26}$$

*Assume $k(\theta, \phi) \geq k_{\min}^\alpha(\theta, \phi)$. If $\alpha = -1$ and the anisotropy $\hat{\gamma}(\theta, \phi)$ satisfies*

$$2\hat{\gamma}(\theta, \phi) - \hat{\gamma}(\pi - \theta, \pi + \phi) \geq 0, \qquad \forall (\theta, \phi) \in [0, \pi] \times 2\pi\mathbb{T}, \tag{7.27}$$

*then the scheme is unconditionally energy stable, namely,*

$$W^{m+1} \leq W^m \leq \cdots \leq W^0, \qquad \forall m \geq 0. \tag{7.28}$$

*For $\alpha \neq -1$, a sufficient energy stability condition is $2\hat{\gamma}(\theta, \phi) - \hat{\gamma}(\pi - \theta, \pi + \phi) > 0$.*

Proof. The proof of volume conservation follows [19], so we omit the details and focus on energy stability.

Taking $\varphi^h = \mu^{m+1}$ in (7.23a) and $\boldsymbol{\omega}^h = \boldsymbol{X}^{m+1} - \boldsymbol{X}^m$ in (7.23b), and adding the resulting equations, we obtain

$$\begin{aligned} &\left\langle \hat{\boldsymbol{G}}_k^\alpha(\theta^m, \phi^m)\nabla_\Gamma \boldsymbol{X}^{m+1}, \nabla_\Gamma(\boldsymbol{X}^{m+1} - \boldsymbol{X}^m)\right\rangle_{\Gamma^m}^h - \cos\theta_Y \left(\boldsymbol{n}_C^{m,*}, \boldsymbol{X}^{m+1} - \boldsymbol{X}^m\right)_{C^m}^h \\ &\quad = -\tau\left(\nabla_\Gamma \mu^{m+1}, \nabla_\Gamma \mu^{m+1}\right)_{\Gamma^m}^h - \frac{1}{\eta\tau}\left((\boldsymbol{X}_C^{m+1} - \boldsymbol{X}_C^m)\cdot \boldsymbol{n}_C^m,\ (\boldsymbol{X}_C^{m+1} - \boldsymbol{X}_C^m)\cdot \boldsymbol{n}_C^m\right)_{C^m}^h. \end{aligned} \tag{7.29}$$

The local energy estimate (6.54) also holds for open surfaces. Following the derivation of (6.63), we obtain

$$\begin{aligned}&\left\langle \hat{\boldsymbol{G}}_k^{\alpha}(\theta^m,\phi^m)\nabla_\Gamma \boldsymbol{X}^{m+1}, \nabla_\Gamma(\boldsymbol{X}^{m+1}-\boldsymbol{X}^m)\right\rangle_{\Gamma^m}^h\\ &\qquad\geq \sum_{j=1}^J \hat{\gamma}(\theta_j^{m+1},\phi_j^{m+1})|\sigma_j^{m+1}| - \sum_{j=1}^J \hat{\gamma}(\theta_j^m,\phi_j^m)|\sigma_j^m|.\end{aligned} \tag{7.30}$$

Combining this estimate with Lemma 7.1 gives

$$\begin{aligned}W^{m+1}-W^m &= \sum_{j=1}^J \hat{\gamma}(\theta_j^{m+1},\phi_j^{m+1})|\sigma_j^{m+1}| - \sum_{j=1}^J \hat{\gamma}(\theta_j^m,\phi_j^m)|\sigma_j^m|\\ &\quad - \cos\theta_Y(|S^{m+1}|-|S^m|)\\ &\leq \left\langle \hat{\boldsymbol{G}}_k^{\alpha}(\theta^m,\phi^m)\nabla_\Gamma \boldsymbol{X}^{m+1}, \nabla_\Gamma(\boldsymbol{X}^{m+1}-\boldsymbol{X}^m)\right\rangle_{\Gamma^m}^h\\ &\quad - \cos\theta_Y\left(\boldsymbol{n}_C^{m,*}, \boldsymbol{X}^{m+1}-\boldsymbol{X}^m\right)_{C^m}^h\\ &= -\tau\left(\nabla_\Gamma\mu^{m+1},\nabla_\Gamma\mu^{m+1}\right)_{\Gamma^m}^h\\ &\quad - \frac{1}{\eta\tau}\left((\boldsymbol{X}_C^{m+1}-\boldsymbol{X}_C^m)\cdot\boldsymbol{n}_C^m,\ (\boldsymbol{X}_C^{m+1}-\boldsymbol{X}_C^m)\cdot\boldsymbol{n}_C^m\right)_{C^m}^h\\ &\leq 0.\end{aligned} \tag{7.31}$$

This proves energy dissipation. □

### 7.3. Morphological evolution of open surfaces in solid-state dewetting

We apply (7.23) to simulate the morphological evolution of open surfaces in *anisotropic solid-state dewetting*.

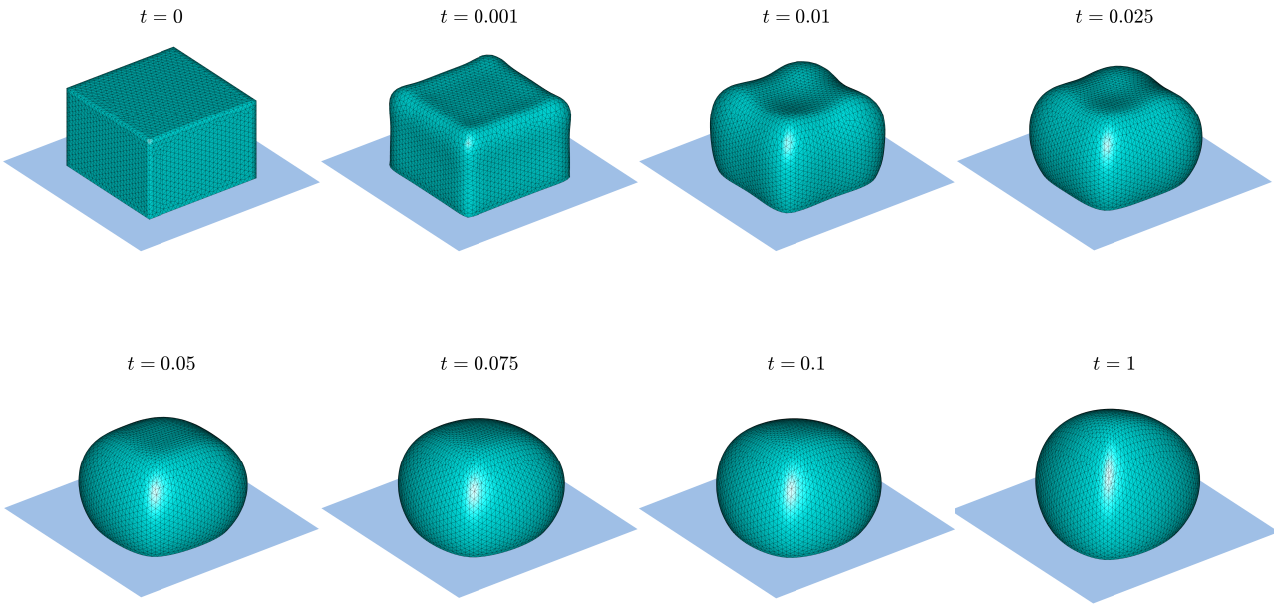



**Figure 7.2.** Evolution of a $3\times3\times2$ cuboid in solid-state dewetting for Case II with $\beta = 1/4$, $\alpha = 0$ and $\theta_Y = 2\pi/3$.

We mainly use the following two anisotropic surface energies in the numerical experiments:

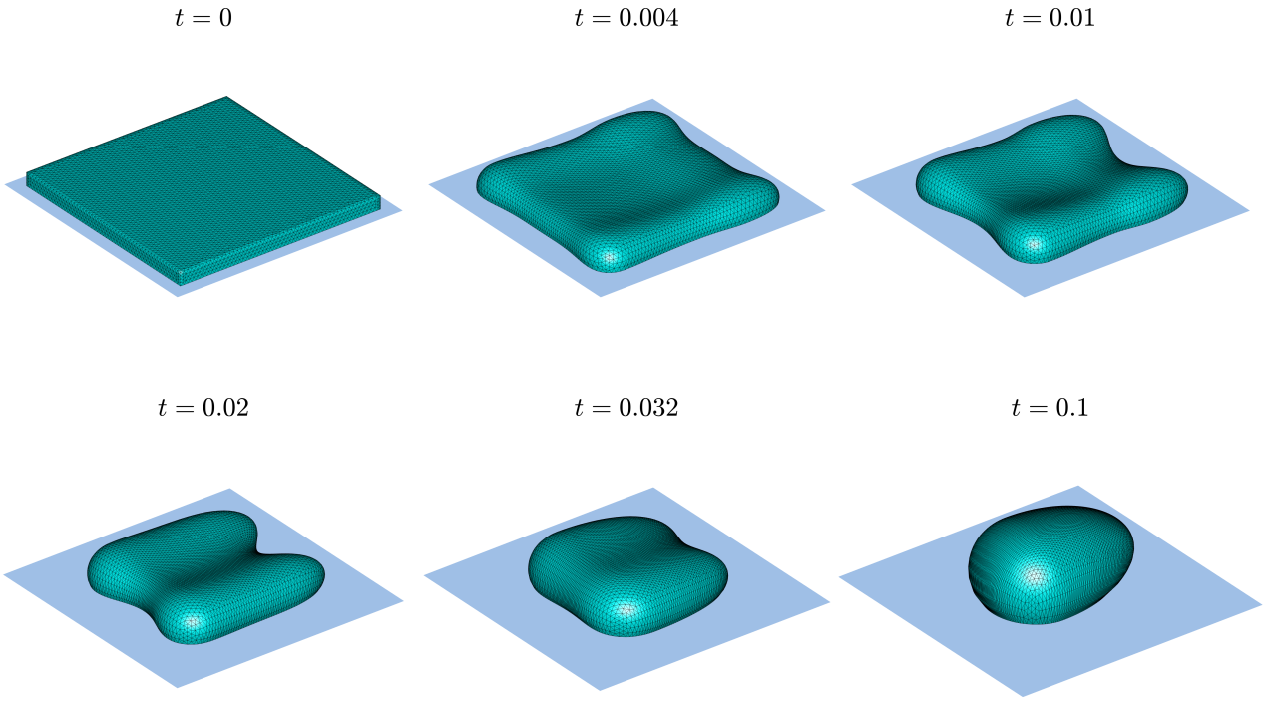



**Figure 7.3.** Evolution of a $3.2 \times 3.2 \times 0.2$ cuboid in solid-state dewetting for Case I with $\alpha = -1$ and $\theta_Y = 3\pi/4$.

- Case I: $\hat{\gamma}(\theta, \phi) = \sqrt{1 + \frac{3}{2}\left(1 + \operatorname{sgn}(\sin\theta\cos\phi)\right)\sin^2\theta\cos^2\phi}$;
- Case II: $\hat{\gamma}(\theta, \phi) = 1 + \beta\left(\cos^3\theta + \sin^3\theta\cos^3\phi + \sin^3\theta\sin^3\phi\right)$.

Figure 7.2 shows the evolution of a $3 \times 3 \times 2$ cuboid in *anisotropic solid-state dewetting* for Case II with $\beta = \frac{1}{4}$ and $\alpha = 0$. Good surface mesh quality is maintained throughout the evolution. Figure 7.3 shows the dewetting of a $3.2 \times 3.2 \times 0.2$ cuboid for Case I with $\alpha = -1$. Initially, the four corners of the square island retract significantly more slowly than the four edges. The island then relaxes toward equilibrium and eventually reaches a steady configuration. This shape agrees with a portion of the closed-surface equilibrium for the same anisotropy shown in Figure 6.6 of Chapter 6.

Next, we examine pinch-off of elongated cuboidal films during dewetting. Figures 7.4–7.7 show simulations using (7.23) for a $16 \times 1 \times 1$ cuboid and square rings, with mesh size $h = 2^{-3}$ and time step $\tau = 1 \times 10^{-4}$.

Figure 7.4 shows that facet-like protrusions develop at the two ends of the elongated film during the initial stage. Material then accumulates near the ends, and the film eventually pinches off into several isolated islands.

We now consider a film initially shaped as a square ring. Figure 7.5 shows the evolution of a wide ring obtained by removing a $2 \times 2 \times 1$ cuboid from the center of a $7 \times 7 \times 1$ cuboid. The initially sharp geometry smooths rapidly. The inner hole then contracts as material redistributes anisotropically. At later times, opposite sides of the surface come into contact, indicating an imminent topological change through which the annular film becomes simply connected.

Next, consider a narrow square ring obtained by removing a $5 \times 5 \times 1$ cuboid from the center of a $7 \times 7 \times 1$ cuboid. Figures 7.6 and 7.7 show the evolution and the boundaries in the $xOy$-plane for threefold and fourfold anisotropy, respectively. In both cases, four necks develop as expected from the Rayleigh-like instability.

Initially, the surface develops a wavy shape. The four corner regions then thicken while the middle portions along the edges narrow. As the thin regions approach zero width, the film ruptures into four isolated particles. The boundary behavior also differs between the two anisotropies: for the asymmetric threefold anisotropy, the boundary is approximately invariant under reflection

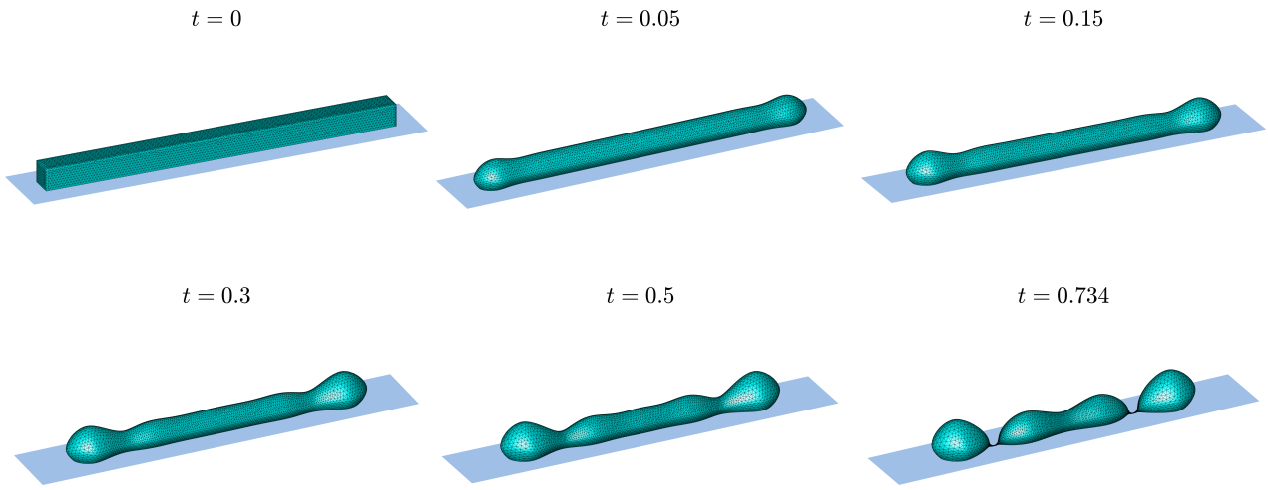



**Figure 7.4.** Evolution of a $16 \times 1 \times 1$ cuboid in solid-state dewetting up to pinch-off, for fourfold anisotropy $\hat{\gamma}(\theta, \phi) = 1 + \frac{1}{4}\left(\cos^4\theta + \sin^4\theta\cos^4\phi + \sin^4\theta\sin^4\phi\right)$ with $\theta_Y = 5\pi/6$.

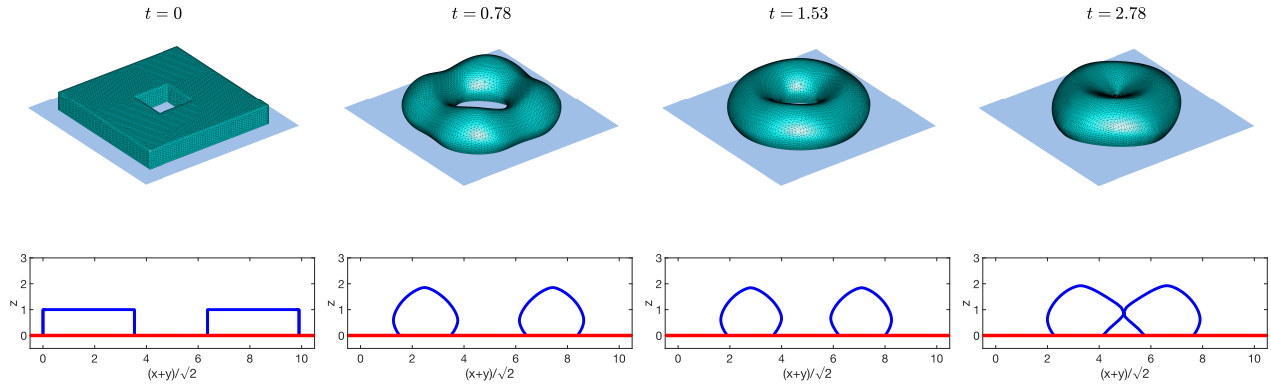



**Figure 7.5.** Evolution in solid-state dewetting of an initially wide square ring obtained by removing a $2 \times 2 \times 1$ cuboid from the center of a $7 \times 7 \times 1$ cuboid, together with its cross-sections in the plane $x = y$, for fourfold anisotropy $\hat{\gamma}(\theta, \phi) = 1 + \frac{1}{4}\left(\cos^4\theta + \sin^4\theta\cos^4\phi + \sin^4\theta\sin^4\phi\right)$ with $\theta_Y = 3\pi/4$.

across $x = y$; for the symmetric fourfold anisotropy, it exhibits a higher degree of symmetry, with pronounced $C_4$ rotational symmetry.

Narrower square rings exhibit stronger instability and tend to break into more isolated islands. For example, the very narrow ring in Figure 7.8 ultimately separates into eight islands.

Finally, we study the equilibrium shapes reached by solid films during dewetting. We use the anisotropy

$$\hat{\gamma}(\theta, \phi) = 1 + \beta\left(\cos^3\theta + \sin^3\theta\cos^3\phi + \sin^3\theta\sin^3\phi\right). \tag{7.32}$$

Figures 7.9 and 7.10 show the effects of Young's angle $\theta_Y$ and anisotropy strength $\beta$, respectively.

Figure 7.9 shows substantial differences between the equilibrium configurations for different $\theta_Y$. As $\theta_Y$ increases, the equilibrium surface is less truncated by the substrate and its contact radius decreases. At fixed enclosed volume, the shape changes from a shallow cap toward a nearly closed equilibrium surface.

Figure 7.10 shows the influence of the anisotropy strength $\beta$ on the equilibrium geometry. Increasing $\beta$ produces sharper boundaries and flatter surface regions, indicating faceting. The anisotropic features become more pronounced, with clear directional dependence of the shape. The computed

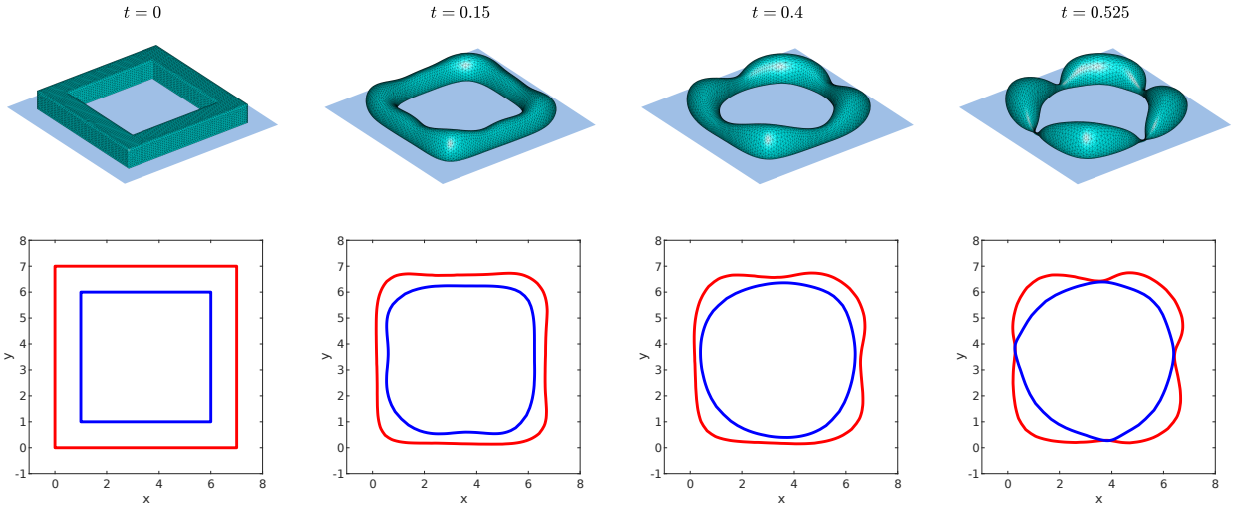



**Figure 7.6.** Snapshots of an initially narrow square ring evolving in solid-state dewetting up to pinch-off, for Case II with $\beta = \frac{1}{4}$ and $\theta_Y = 3\pi/4$.

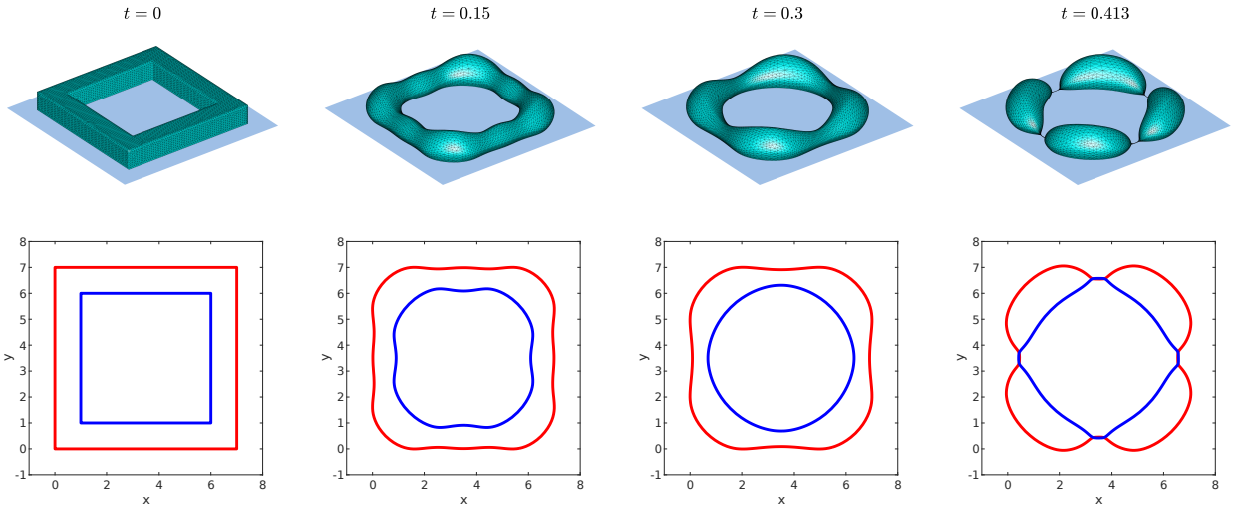



**Figure 7.7.** Snapshots of an initially narrow square ring evolving in solid-state dewetting up to pinch-off, for fourfold anisotropy $\hat{\gamma}(\theta, \phi) = 1 + \frac{1}{4}\left(\cos^4\theta + \sin^4\theta\cos^4\phi + \sin^4\theta\sin^4\phi\right)$ with $\theta_Y = 3\pi/4$.

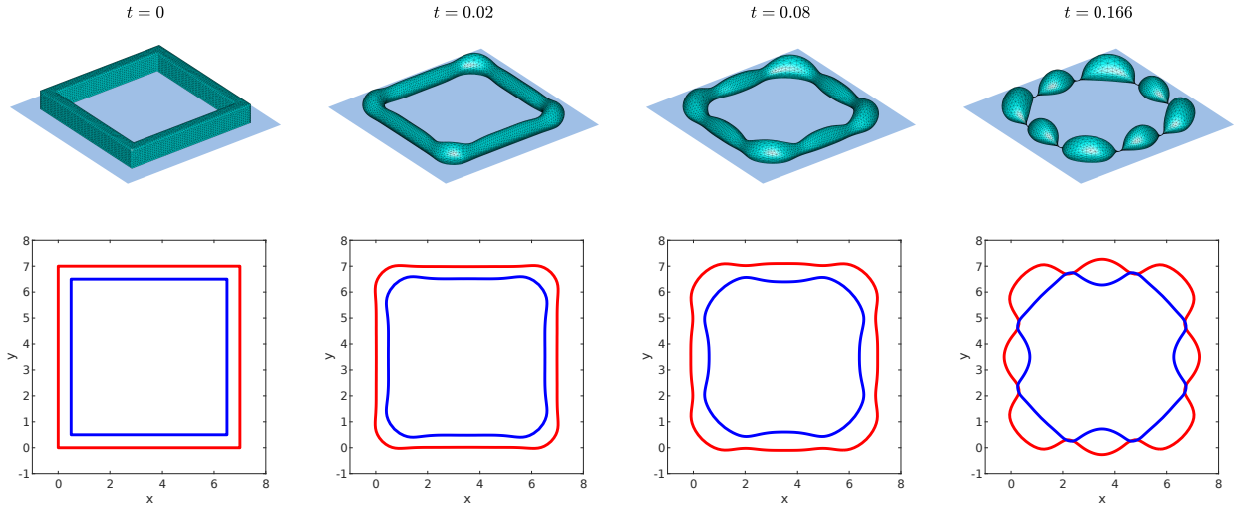



**Figure 7.8.** Evolution in solid-state dewetting of an initially very narrow square ring obtained by removing a $6 \times 6 \times 1$ cuboid from the center of a $7 \times 7 \times 1$ cuboid, for fourfold anisotropy $\hat{\gamma}(\theta, \phi) = 1 + \frac{1}{4}\left(\cos^4\theta + \sin^4\theta\cos^4\phi + \sin^4\theta\sin^4\phi\right)$ with $\theta_Y = 3\pi/4$.

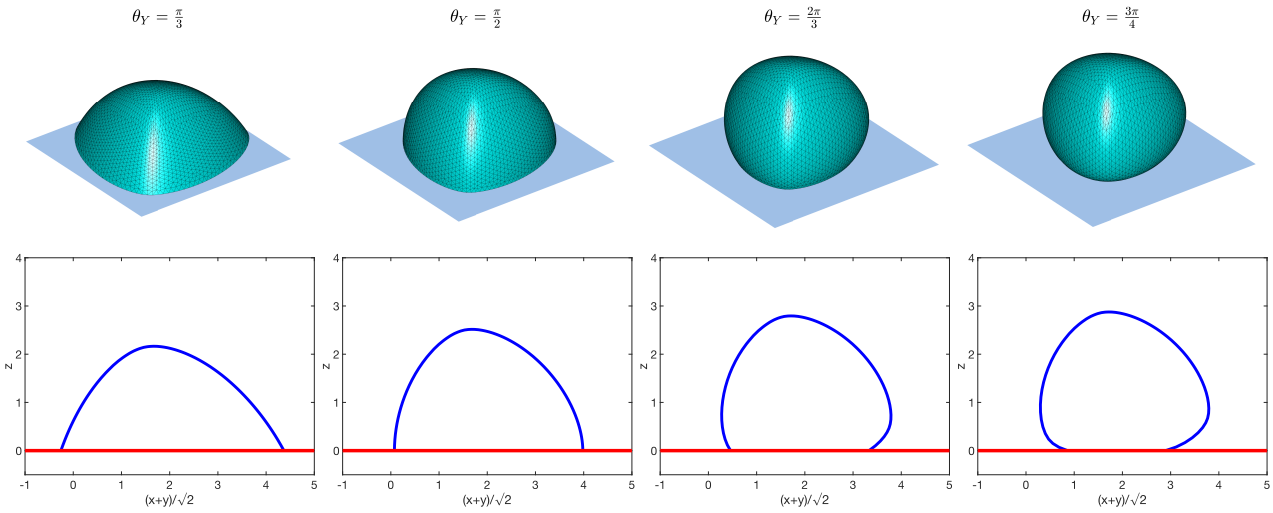



**Figure 7.9.** Equilibrium island shapes and their cross-sections in the plane $x = y$ for Case II with $\beta = \frac{1}{4}$, at different values of $\theta_Y$.

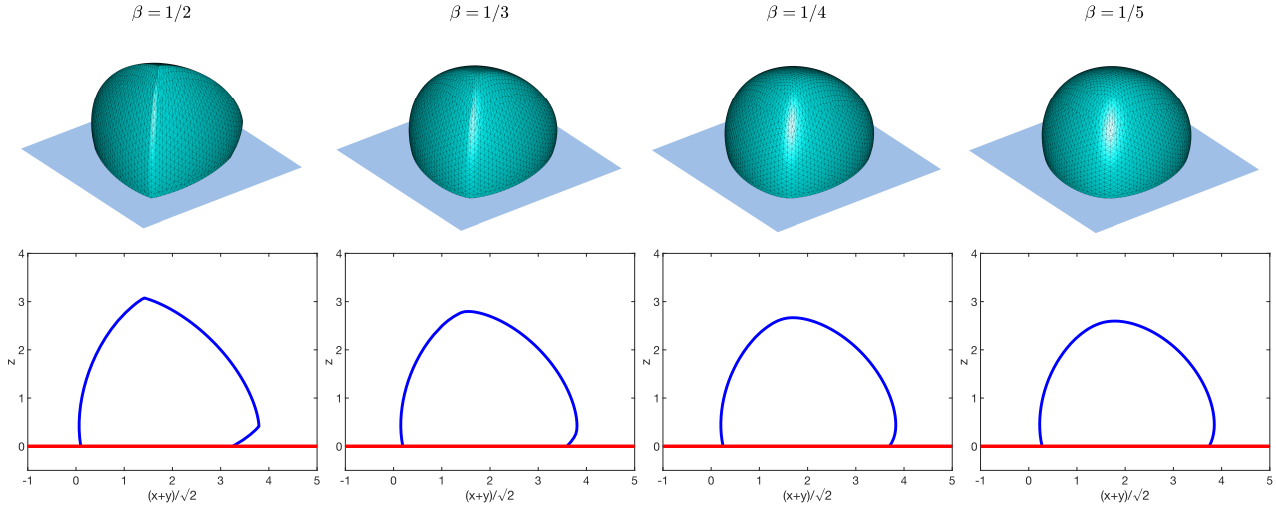



**Figure 7.10.** Equilibrium island shapes and their cross-sections in the plane $x = y$ for Case II with $\theta_Y = 7\pi/12$, at different anisotropy strengths $\beta$.

surfaces retain good mesh quality even under strong anisotropy, demonstrating the robustness and stability of (7.23).

CHAPTER 8

# Geometric gradient flows with curvature-dependent surface energy

The surface energy densities considered in the preceding chapters depend primarily on the interface normal. For interfaces with bending rigidity, orientation dependence alone does not describe the contribution of curvature to the energy. Curvature energies also provide higher-order regularization for strongly anisotropic interface models. In this chapter we consider closed surfaces in three dimensions and write the energy density as $f(\boldsymbol{n}, H)$, where $\boldsymbol{n}$ is the outward unit normal and $H$ is the mean curvature. This formulation includes the anisotropic surface energies considered earlier, the Willmore bending energy, and energies coupling the normal direction to the mean curvature.

The first variation and weak formulations of general curvature-dependent surface energies have been studied systematically; see [48]. For energies depending only on mean curvature, [16] constructs an energy-stable parametric finite element discretization using the curvature evolution equation. Solid-state dewetting models combining anisotropic surface energy with Willmore regularization are considered in [105]. Building on these variational and geometric identities, we apply the symmetric surface energy matrix of Chapter 6 to orientation-dependent energies at fixed curvature. A mass-lumped projection of the curvature derivative provides an admissible finite element test function for general coupled densities. The numerical results added to this chapter follow the author's manuscript [148].

We first derive the chemical potential and conservative weak formulation associated with $f(\boldsymbol{n}, H)$. We then give a fully discrete scheme for the position, chemical potential, mean curvature, and an auxiliary scalar. Convexity in curvature and a local energy estimate at fixed curvature yield discrete energy dissipation. A time-averaged area normal further gives a volume-preserving surface-diffusion scheme. These structural results concern the specified discrete energy and volume; they neither establish solvability of the nonlinear algebraic system nor constitute geometric error estimates. The final section reports convergence, structural diagnostics, computational cost, and shape relaxation experiments.

## 8.1. Surface energy and geometric identities

**8.1.1. The energy functional and conventions.** Let $\Gamma(t) \subset \mathbb{R}^3$ be a smooth, closed, orientable surface, parametrized by $\boldsymbol{X}(\cdot, t)\colon \Gamma_0 \to \Gamma(t)$. Write $\boldsymbol{v} = \partial_t \boldsymbol{X}$ for the velocity and $V_n = \boldsymbol{v} \cdot \boldsymbol{n}$ for its normal component. We use the conventions

$$\boldsymbol{P} = I_3 - \boldsymbol{n}\boldsymbol{n}^T = \nabla_\Gamma \boldsymbol{X}, \qquad \boldsymbol{A} = \nabla_\Gamma \boldsymbol{n}, \qquad H = \nabla_\Gamma \cdot \boldsymbol{n} = \operatorname{Tr} \boldsymbol{A}. \tag{8.1}$$

Here $\boldsymbol{A}$ is the Weingarten matrix, with $\boldsymbol{A}^T = \boldsymbol{A}$ and $\boldsymbol{A}\boldsymbol{n} = \boldsymbol{0}$. Our mean curvature $H$ is the sum of the principal curvatures, so a sphere of radius $R$ has $H = 2/R$. Surface gradients of vector fields follow the row-gradient convention of Chapter 6. The matrix inner product is $\boldsymbol{U} : \boldsymbol{V} = \operatorname{Tr}(\boldsymbol{U}^T \boldsymbol{V})$.

Consider the energy

$$W(\Gamma) = \int_\Gamma f(\boldsymbol{n}, H)\, \mathrm{d}A, \qquad f\colon \mathbb{S}^2 \times \mathbb{R} \to \mathbb{R}. \tag{8.2}$$

For the continuous derivation, assume sufficient smoothness of the surface and density for the derivatives and integrations by parts below. Denote the derivative with respect to the second variable by $f_H$, and set

$$\boldsymbol{a}(\boldsymbol{n}, H) = \nabla_{\mathbb{S}^2} f(\boldsymbol{n}, H) = \boldsymbol{P} \nabla_p \widetilde{f}(\boldsymbol{n}, H), \qquad r = f_H(\boldsymbol{n}, H), \tag{8.3}$$

Here $\widetilde{f}$ is any smooth extension of $f$ to a neighborhood in its first variable; directional derivatives are taken with $H$ fixed. The spherical gradient $\boldsymbol{a}$ is independent of the extension and satisfies $\boldsymbol{a} \cdot \boldsymbol{n} = 0$. Unless stated otherwise, we suppress the arguments of $f$, $\boldsymbol{a}$, and $r$.

Curvature dependence in this chapter means dependence on the mean curvature $H$. Independent dependence on Gaussian curvature or the full second fundamental form requires additional variational variables and geometric evolution identities, and is not included directly in (8.2).

**8.1.2. Evolution of the normal, curvature, and area element.** Throughout this chapter, $\partial_t$ denotes the material derivative along $\boldsymbol{X}$; the velocity may therefore have a tangential component. The unit normal satisfies

$$\partial_t \boldsymbol{n} = -(\nabla_\Gamma \boldsymbol{v})^T \boldsymbol{n}. \tag{8.4}$$

This identity follows by differentiating the orthogonality of $\boldsymbol{n}$ to the two parameter tangent vectors and the condition $|\boldsymbol{n}| = 1$. The transport formula for the area element is

$$\frac{\mathrm{d}}{\mathrm{d}t} \int_{\Gamma(t)} u \, \mathrm{d}A = \int_{\Gamma(t)} \left( \partial_t u + u \boldsymbol{P} : \nabla_\Gamma \boldsymbol{v} \right) \mathrm{d}A. \tag{8.5}$$

Lemma 8.1 (Weak evolution identity for mean curvature). *For the smooth surface evolution above and any scalar test function $\psi$,*

$$(\partial_t H, \psi)_{\Gamma(t)} = \left\langle \boldsymbol{n}(\nabla_\Gamma \psi)^T - \psi \boldsymbol{A}, \nabla_\Gamma \boldsymbol{v} \right\rangle_{\Gamma(t)}. \tag{8.6}$$

Proof. Take the material derivative of $H = \nabla_\Gamma \cdot \boldsymbol{n}$. Using (8.4) and the transport identity for surface differential operators gives

$$\partial_t H = -\nabla_\Gamma \cdot \left( (\nabla_\Gamma \boldsymbol{v})^T \boldsymbol{n} \right) - \boldsymbol{A} : \nabla_\Gamma \boldsymbol{v}. \tag{8.7}$$

The vector field $(\nabla_\Gamma \boldsymbol{v})^T \boldsymbol{n}$ is tangential. Multiplying by $\psi$ and integrating by parts on the closed surface yields (8.6). This weak identity also appears in [16]. □

In particular, if $\boldsymbol{v} = V_n \boldsymbol{n}$, then (8.7) reduces to

$$\partial_t H = -\Delta_\Gamma V_n - |\boldsymbol{A}|^2 V_n. \tag{8.8}$$

Identity (8.6) involves only first spatial derivatives of the position velocity and test function, making it suitable for a piecewise linear parametric finite element discretization.

## 8.2. First variation and conservative weak formulations

**8.2.1. Scalar and tensor forms of the chemical potential.** The chain rule, (8.4), and the transport formula give

$$\begin{aligned} \frac{\mathrm{d}W}{\mathrm{d}t} &= (r, \partial_t H)_{\Gamma(t)} + \left\langle f\boldsymbol{P} - \boldsymbol{n}\boldsymbol{a}^T, \nabla_\Gamma \boldsymbol{v} \right\rangle_{\Gamma(t)} \\ &= \left\langle \boldsymbol{S}, \nabla_\Gamma \boldsymbol{v} \right\rangle_{\Gamma(t)}, \end{aligned} \tag{8.9}$$

where

$$\boldsymbol{S} = f\boldsymbol{P} - \boldsymbol{n}\boldsymbol{a}^T - r\boldsymbol{A} + \boldsymbol{n}(\nabla_\Gamma r)^T. \tag{8.10}$$

Since $\boldsymbol{S}\boldsymbol{n} = \boldsymbol{0}$, this tensor is tangential in its differentiation index.

Proposition 8.1 (First variation of the energy). *Define the chemical potential $\mu$ by $\delta W[\boldsymbol{\omega}] = (\mu \boldsymbol{n}, \boldsymbol{\omega})_\Gamma$. Then*

$$\mu = \nabla_\Gamma \cdot \boldsymbol{a} - \Delta_\Gamma f_H + f H - f_H |\boldsymbol{A}|^2, \tag{8.11}$$

*with the equivalent vector weak formulation*

$$(\mu \boldsymbol{n}, \boldsymbol{\omega})_\Gamma = \langle \boldsymbol{S}, \nabla_\Gamma \boldsymbol{\omega} \rangle_\Gamma. \tag{8.12}$$

Proof. First consider a normal perturbation $\boldsymbol{\omega} = \eta\boldsymbol{n}$. Since $\nabla_\Gamma(\eta\boldsymbol{n}) = \boldsymbol{n}(\nabla_\Gamma\eta)^T + \eta\boldsymbol{A}$, identity (8.9) gives

$$\delta W[\eta\boldsymbol{n}] = \int_\Gamma \left[-\boldsymbol{a}\cdot\nabla_\Gamma\eta + \nabla_\Gamma r\cdot\nabla_\Gamma\eta + (fH - r|\boldsymbol{A}|^2)\eta\right]\,\mathrm{d}A. \tag{8.13}$$

Integration by parts on the closed surface yields (8.11). A tangential perturbation only reparametrizes the surface and has zero first variation. Thus, for an arbitrary vector perturbation, the first variation obtained from (8.9) equals $(\mu\boldsymbol{n}, \boldsymbol{\omega})_\Gamma$, proving (8.12). □

In terms of derivatives of the neighborhood extension, (8.11) is equivalent to

$$\mu = \nabla_\Gamma\cdot\nabla_{\boldsymbol{p}}\widetilde{f} - \Delta_\Gamma f_H + \big(f - \nabla_{\boldsymbol{p}}\widetilde{f}\cdot\boldsymbol{n}\big)H - f_H|\boldsymbol{A}|^2. \tag{8.14}$$

The normal components introduced by the extension cancel, so the chemical potential does not depend on the extension. In particular, $f = \gamma(\boldsymbol{n})$ recovers anisotropic weighted curvature, while $f = H^2/2$ gives

$$\mu = -\Delta_\Gamma H + \frac{1}{2}H^3 - H|\boldsymbol{A}|^2. \tag{8.15}$$

**8.2.2. Unified weak formulation and continuous structure.** To make the pairing of the curvature terms explicit, define

$$\mathcal{B}_\Gamma(\boldsymbol{w}, \psi) = \left\langle \boldsymbol{n}(\nabla_\Gamma\psi)^T - \psi\boldsymbol{A}, \nabla_\Gamma\boldsymbol{w}\right\rangle_\Gamma. \tag{8.16}$$

For the $L^2$ gradient flow $V_n = -\mu$, seek $(\boldsymbol{X}, \mu, H, r)$ satisfying

$$(\partial_t\boldsymbol{X}\cdot\boldsymbol{n}, \varphi)_\Gamma = -(\mu, \varphi)_\Gamma, \tag{8.17a}$$

$$(\mu\boldsymbol{n}, \boldsymbol{\omega})_\Gamma = \langle f\boldsymbol{P} - \boldsymbol{n}\boldsymbol{a}^T, \nabla_\Gamma\boldsymbol{\omega}\rangle_\Gamma + \mathcal{B}_\Gamma(\boldsymbol{\omega}, r), \tag{8.17b}$$

$$(\partial_t H, \psi)_\Gamma = \mathcal{B}_\Gamma(\partial_t\boldsymbol{X}, \psi), \tag{8.17c}$$

$$(r, \zeta)_\Gamma = (f_H(\boldsymbol{n}, H), \zeta)_\Gamma. \tag{8.17d}$$

The scalar test functions belong to $H^1$ spaces in which all terms are well defined, and vector test functions belong to their threefold product. The solution must also have the regularity required by the nonlinear terms. The initial conditions satisfy

$$\boldsymbol{X}(\cdot, 0) = \boldsymbol{X}_0, \qquad H(\cdot, 0) = -\boldsymbol{n}_0\cdot\Delta_{\Gamma_0}\boldsymbol{X}_0. \tag{8.18}$$

At the continuous level, (8.17d) is simply $r = f_H$. We retain the auxiliary unknown to provide a weak relation for the finite element projection of the nonlinear term.

Proposition 8.2 (Continuous energy dissipation). *A smooth geometric solution of* (8.17) *satisfies*

$$\frac{\mathrm{d}W}{\mathrm{d}t} = -\|\mu\|^2_{L^2(\Gamma)} \le 0. \tag{8.19}$$

Proof. Take, respectively, in (8.17b) and (8.17c), $\boldsymbol{\omega} = \partial_t\boldsymbol{X}$ and $\psi = r$. By (8.9), $\mathrm{d}W/\mathrm{d}t = (\mu\boldsymbol{n}, \partial_t\boldsymbol{X})_\Gamma$. Finally, take $\varphi = \mu$ in (8.17a). □

For the surface-diffusion law $V_n = \Delta_\Gamma\mu$, replace (8.17a) by

$$(\partial_t\boldsymbol{X}\cdot\boldsymbol{n}, \varphi)_\Gamma = -(\nabla_\Gamma\mu, \nabla_\Gamma\varphi)_\Gamma. \tag{8.20}$$

Taking $\varphi = \mu$ and $\varphi = 1$, respectively, gives

$$\frac{\mathrm{d}W}{\mathrm{d}t} = -\|\nabla_\Gamma\mu\|^2_{L^2(\Gamma)}, \qquad \frac{\mathrm{d}\mathcal{V}}{\mathrm{d}t} = \int_\Gamma V_n\,\mathrm{d}A = 0, \tag{8.21}$$

Here $\mathcal{V}$ is the enclosed volume. A nondegenerate curvature dependence generally makes the $L^2$ flow a fourth-order equation and surface diffusion a sixth-order equation.

### 8.3. A symmetric surface energy matrix at fixed curvature

**8.3.1. Construction and action of the matrix.** For fixed $s \in \mathbb{R}$, regard $\boldsymbol{n} \mapsto f(\boldsymbol{n}, s)$ as an orientation-dependent surface energy density. Define its positively one-homogeneous extension and Cahn–Hoffman vector by

$$F(\boldsymbol{p}, s) = |\boldsymbol{p}| f\left(\frac{\boldsymbol{p}}{|\boldsymbol{p}|}, s\right), \qquad \boldsymbol{\xi}(\boldsymbol{n}, s) = \nabla_{\boldsymbol{p}} F(\boldsymbol{n}, s) = f(\boldsymbol{n}, s)\boldsymbol{n} + \boldsymbol{a}(\boldsymbol{n}, s). \tag{8.22}$$

Here $\boldsymbol{p} \neq \boldsymbol{0}$ and $s$ is a parameter. Following the construction in Chapter 6 with $\alpha = -1$, set

$$\boldsymbol{Z}_k(\boldsymbol{n}, s) = f(\boldsymbol{n}, s) I_3 - \boldsymbol{n}\boldsymbol{\xi}(\boldsymbol{n}, s)^T - \boldsymbol{\xi}(\boldsymbol{n}, s)\boldsymbol{n}^T + k(\boldsymbol{n}, s)\boldsymbol{n}\boldsymbol{n}^T. \tag{8.23}$$

This matrix is symmetric and satisfies

$$\boldsymbol{Z}_k(\boldsymbol{n}, H)\nabla_\Gamma \boldsymbol{X} = f\boldsymbol{P} - \boldsymbol{n}\boldsymbol{a}^T. \tag{8.24}$$

The first term in (8.17b) can therefore be written as $\langle \boldsymbol{Z}_k(\boldsymbol{n}, H)\nabla_\Gamma \boldsymbol{X}, \nabla_\Gamma \boldsymbol{\omega}\rangle_\Gamma$. The stabilizing term leaves the continuous geometric equation unchanged and controls changes of normal direction and element area at the discrete level.

**8.3.2. Local energy estimate and parameter dependence.**

Lemma 8.2 (Local energy estimate at fixed curvature). *Let $\sigma$ and $\bar{\sigma}$ be nondegenerate oriented triangles, and let $\boldsymbol{X}$ map the vertices of $\sigma$ affinely to the corresponding vertices of $\bar{\sigma}$. Denote their unit normals by $\boldsymbol{n}$ and $\bar{\boldsymbol{n}}$, respectively. For fixed $s$, assume $f(\cdot, s) > 0$, $f(\cdot, s) \in C^2(\mathbb{S}^2)$, and*

$$2f(\boldsymbol{n}, s) - f(-\boldsymbol{n}, s) \geq 0, \qquad \forall \boldsymbol{n} \in \mathbb{S}^2. \tag{8.25}$$

*Then there is a finite stabilizing threshold $k_0(\boldsymbol{n}, s)$ such that, whenever $k(\boldsymbol{n}, s) \geq k_0(\boldsymbol{n}, s)$,*

$$|\sigma|\big(\boldsymbol{Z}_k(\boldsymbol{n}, s)\nabla_\sigma \boldsymbol{X}\big) : \big(\nabla_\sigma \boldsymbol{X} - \nabla_\sigma \mathbf{id}\big) \geq |\bar{\sigma}| f(\bar{\boldsymbol{n}}, s) - |\sigma| f(\boldsymbol{n}, s). \tag{8.26}$$

Proof. Fix $s$ and choose the directional energy in Chapter 6 as $\hat{\gamma}_s(\theta, \phi) = f(\boldsymbol{n}(\theta, \phi), s)$, with $\alpha = -1$. Matrix (8.23) is then the corresponding symmetric surface energy matrix. The existence result for the minimal stabilizing function and the local energy estimate (6.54) in that chapter yield (8.26). □

The threshold may depend on the curvature parameter $s$. Its finiteness for every fixed $s$ does not imply a uniform bound on all of $\mathbb{R}$. Below, the local energy estimate is therefore required at the new curvature values at the quadrature nodes; the stabilizing parameter is not restricted in advance to a function of the normal alone.

If the density vanishes for some parameter values, the local energy estimate must be checked separately. The strictly positive-density result cannot be applied directly. For example, $f(\boldsymbol{n}, s) = s^2/2$ is independent of orientation. Taking $k = 2f$ gives $\boldsymbol{Z}_k = fI_3$, and the isotropic triangle-area estimate shows that (8.26) also holds at $s = 0$.

### 8.4. A fully discrete scheme with an auxiliary projection

**8.4.1. Discrete geometry and quadrature of nonlinear terms.** Let $\Gamma^m = \bigcup_{j=1}^J \overline{\sigma_j^m}$ be a triangulation at time level $m$, with $K$ vertices $\boldsymbol{q}_i^m$. Connectivity is fixed across time levels. The old position is the identity map $\boldsymbol{X}^m = \mathbf{id}$, while $\boldsymbol{X}^{m+1} \in [\mathbb{K}^m]^3$ maps old vertices to new vertices. Write

$$\mathbb{K}^m = \{u \in C(\Gamma^m) : u|_{\sigma_j^m} \in \mathcal{P}^1(\sigma_j^m)\}, \quad \nabla_m = \nabla_{\Gamma^m}. \tag{8.27}$$

The normal $\boldsymbol{n}^m$ is the facetwise unit normal of the actual triangles, and $\boldsymbol{P}^m = I_3 - \boldsymbol{n}^m(\boldsymbol{n}^m)^T$. Scalars such as $H^{m+1}$ are first defined on the old mesh and then transported to the new mesh with the vertices. We use $H_i^{m+1}$ for these common nodal coefficients.

Let $u_{j\ell}$ be the interior trace of $u$ at vertex $\ell$ of element $\sigma_j^m$. Define the mass-lumped inner products

$$(u, v)_m^h = \frac{1}{3}\sum_{j=1}^J |\sigma_j^m| \sum_{\ell=1}^3 u_{j\ell} v_{j\ell}, \qquad \langle \boldsymbol{U}, \boldsymbol{V}\rangle_m^h = \frac{1}{3}\sum_{j=1}^J |\sigma_j^m| \sum_{\ell=1}^3 \boldsymbol{U}_{j\ell} : \boldsymbol{V}_{j\ell}. \tag{8.28}$$

The vector inner product is defined analogously. Nonlinear densities and matrix coefficients are evaluated at these element-vertex traces; for example, $f(\boldsymbol{n}^m, H^{m+1})_{j\ell} = f(\boldsymbol{n}_j^m, H_{j\ell}^{m+1})$. Adjacent elements may assign different normals to the same global vertex. Such a nonlinear coefficient is therefore generally not a continuous finite element function.

To define a discrete Weingarten matrix, first recover a continuous nodal normal $\boldsymbol{N}^m \in [\mathbb{K}^m]^3$ by

$$\boldsymbol{N}_i^m = \frac{\sum_{j:\, i\in\sigma_j^m} |\sigma_j^m| \boldsymbol{n}_j^m}{\left| \sum_{j:\, i\in\sigma_j^m} |\sigma_j^m| \boldsymbol{n}_j^m \right|}, \tag{8.29}$$

Assume that the denominator is nonzero. A computable recovered matrix is

$$\boldsymbol{A}^m = \boldsymbol{P}^m \frac{\nabla_m \boldsymbol{N}^m + (\nabla_m \boldsymbol{N}^m)^T}{2} \boldsymbol{P}^m. \tag{8.30}$$

Here $\boldsymbol{A}^m$ approximates the Weingarten matrix facetwise; it is not the elementwise derivative of the piecewise constant facet normal. Other discrete curvature matrices are possible. The energy proof below only requires the same $\boldsymbol{A}^m$ in the two paired equations. The approximation accuracy of the recovered matrix requires separate mesh-dependent analysis and verification.

Define the discrete bilinear form

$$\mathcal{B}_m(\boldsymbol{w}, \psi) = \left\langle \boldsymbol{n}^m (\nabla_m \psi)^T - \psi \boldsymbol{A}^m, \nabla_m \boldsymbol{w} \right\rangle_m^h. \tag{8.31}$$

The corresponding discrete energy is

$$W^m = (f(\boldsymbol{n}^m, H^m), 1)_m^h = \frac{1}{3} \sum_{j=1}^{J} |\sigma_j^m| \sum_{\ell=1}^{3} f(\boldsymbol{n}_j^m, H_{j\ell}^m). \tag{8.32}$$

**8.4.2. The auxiliary scalar and the full discrete system.** Given $\boldsymbol{X}^m$, $H^m$, and a time step $\tau_m > 0$, seek

$$(\boldsymbol{X}^{m+1}, \mu^{m+1}, H^{m+1}, r^{m+1}) \in [\mathbb{K}^m]^3 \times (\mathbb{K}^m)^3, \tag{8.33}$$

such that, for all $\varphi, \psi, \zeta \in \mathbb{K}^m$ and $\boldsymbol{\omega} \in [\mathbb{K}^m]^3$,

$$\left( \frac{\boldsymbol{X}^{m+1} - \boldsymbol{X}^m}{\tau_m} \cdot \boldsymbol{n}^m, \varphi \right)_m^h = -(\mu^{m+1}, \varphi)_m^h, \tag{8.34a}$$

$$(\mu^{m+1} \boldsymbol{n}^m, \boldsymbol{\omega})_m^h = \mathcal{D}_m(\boldsymbol{X}^{m+1}, \boldsymbol{\omega}) + \mathcal{B}_m(\boldsymbol{\omega}, r^{m+1}), \tag{8.34b}$$

$$(H^{m+1} - H^m, \psi)_m^h = \mathcal{B}_m(\boldsymbol{X}^{m+1} - \boldsymbol{X}^m, \psi), \tag{8.34c}$$

$$(r^{m+1}, \zeta)_m^h = (f_H(\boldsymbol{n}^m, H^{m+1}), \zeta)_m^h, \tag{8.34d}$$

For a fixed candidate $H^{m+1}$ within this time step, write

$$\mathcal{D}_m(\boldsymbol{X}, \boldsymbol{\omega}) = \left\langle \boldsymbol{Z}_k(\boldsymbol{n}^m, H^{m+1}) \nabla_m \boldsymbol{X}, \nabla_m \boldsymbol{\omega} \right\rangle_m^h. \tag{8.35}$$

The coefficients of $\mathcal{D}_m$ depend on the unknown curvature, so the full system is generally nonlinear. The curvature increment equation is not divided by $\tau_m$, since its right-hand side already contains the position increment.

Equation (8.34d) gives a mass-lumped projection of $f_H$; it does not require elementwise pointwise equality with $r^{m+1}$. More explicitly, put $M_i^m = \frac{1}{3} \sum_{j:\, i\in\sigma_j^m} |\sigma_j^m| > 0$. Then

$$r_i^{m+1} = \frac{1}{3M_i^m} \sum_{j:\, i\in\sigma_j^m} |\sigma_j^m| f_H(\boldsymbol{n}_j^m, H_i^{m+1}). \tag{8.36}$$

Thus $r^{m+1}$ is an admissible continuous piecewise linear test function. Its nodal values can be eliminated directly using the curvature coefficients, without solving a separate global projection system.

The projection retains the exact pairing needed in the proof. Taking $\zeta = H^{m+1} - H^m$ gives

$$(r^{m+1}, H^{m+1} - H^m)_m^h = (f_H(\boldsymbol{n}^m, H^{m+1}), H^{m+1} - H^m)_m^h. \tag{8.37}$$

There is no need to use the generally discontinuous function $f_H(\boldsymbol{n}^m, H^{m+1})$ directly as a test function, or to differentiate it along the surface. The force and curvature equations both use $r^{m+1}$ and $\nabla_m r^{m+1}$.

### 8.5. Fully discrete energy dissipation

THEOREM 8.1 (Fully discrete energy stability). *Assume that $s \mapsto f(\boldsymbol{n}, s)$ is differentiable and convex for every $\boldsymbol{n} \in \mathbb{S}^2$, and that* (8.26) *holds at the new curvature value at each element quadrature node. Suppose that* (8.34) *has a solution and that all triangles on the old and new surfaces are nondegenerate. Then, for every $\tau_m > 0$,*

$$W^{m+1} + \tau_m \|\mu^{m+1}\|_{m,h}^2 \le W^m, \qquad \|u\|_{m,h}^2 = (u,u)_m^h. \tag{8.38}$$

*In particular, the local energy estimate holds if the smoothness, positivity, and directional assumptions of Lemma 8.2 hold at all relevant curvature values and $k(\boldsymbol{n}, s)$ is chosen sufficiently large at the corresponding nodes.*

PROOF. In (8.34a), (8.34b), and (8.34c), take, respectively, $\varphi = \mu^{m+1}$, $\boldsymbol{\omega} = \boldsymbol{X}^{m+1} - \boldsymbol{X}^m$, and $\psi = r^{m+1}$. All three test functions belong to the required finite element spaces, so

$$\begin{aligned} -\tau_m \|\mu^{m+1}\|_{m,h}^2 &= \mathcal{D}_m(\boldsymbol{X}^{m+1}, \boldsymbol{X}^{m+1} - \boldsymbol{X}^m) + \mathcal{B}_m(\boldsymbol{X}^{m+1} - \boldsymbol{X}^m, r^{m+1}) \\ &= \mathcal{D}_m(\boldsymbol{X}^{m+1}, \boldsymbol{X}^{m+1} - \boldsymbol{X}^m) + (H^{m+1} - H^m, r^{m+1})_m^h. \end{aligned} \tag{8.39}$$

Introduce an intermediate energy on the old geometry:

$$\widehat{W}^{m+1|m} = \frac{1}{3} \sum_{j=1}^{J} |\sigma_j^m| \sum_{\ell=1}^{3} f(\boldsymbol{n}_j^m, H_{j_\ell}^{m+1}). \tag{8.40}$$

For each element $j$ and vertex $j_\ell$, apply the local energy estimate with $s = H_{j_\ell}^{m+1}$. Summing over the element vertices gives

$$\mathcal{D}_m(\boldsymbol{X}^{m+1}, \boldsymbol{X}^{m+1} - \boldsymbol{X}^m) \ge W^{m+1} - \widehat{W}^{m+1|m}. \tag{8.41}$$

On the other hand, convexity in curvature implies

$$f_H(\boldsymbol{n}, b)(b - a) \ge f(\boldsymbol{n}, b) - f(\boldsymbol{n}, a). \tag{8.42}$$

Apply this inequality at every old element vertex and use the projection pairing (8.37) to obtain

$$(H^{m+1} - H^m, r^{m+1})_m^h \ge \widehat{W}^{m+1|m} - W^m. \tag{8.43}$$

Substitute (8.41) and (8.43) into (8.39). The intermediate energies cancel, yielding (8.38). □

The proof estimates geometry and curvature separately: the local surface energy matrix controls the former, while convexity and the auxiliary projection control the latter. Joint convexity in the normal and curvature is not required, nor is the nonnegativity of $f - H f_H$. The same pairing argument applies to any stabilizing matrix satisfying the corresponding local estimate.

REMARK 8.1. Unconditional energy stability means that the estimate has no time-step restriction. It does not guarantee solvability of the nonlinear equations for arbitrary time steps, prevent mesh degeneration, or bound the difference between $H^m$ and the geometric curvature. These questions are distinct from (8.38).

### 8.6. Volume-preserving gradient flows

**8.6.1. The discrete volume increment.** Using the time-averaged normal $\boldsymbol{n}^{m+\frac{1}{2}}$ from Chapter 7, we obtain the following relation between the position increment and the discrete volume change.

LEMMA 8.3 (Discrete volume increment). *For a closed triangular mesh with consistent outward orientation and fixed connectivity, the signed volume*

$$\mathcal{V}^m = \frac{1}{6} \sum_{j=1}^{J} \boldsymbol{q}_{j_1}^m \cdot (\boldsymbol{q}_{j_2}^m \times \boldsymbol{q}_{j_3}^m) \tag{8.44}$$

*satisfies*

$$\mathcal{V}^{m+1} - \mathcal{V}^m = (\boldsymbol{X}^{m+1} - \boldsymbol{X}^m, \boldsymbol{n}^{m+\frac{1}{2}})_m^h. \tag{8.45}$$

Proof. Apply the volume transport formula to the closed surface obtained by linear interpolation between the two time levels, and pull the integral back to the old surface. The definition of $\boldsymbol{n}^{m+\frac{1}{2}}$, together with the exactness of mass lumping for elementwise linear functions, gives (8.45). □

**8.6.2. Surface diffusion and the volume-constrained curvature flow.** The surface-diffusion scheme retains (8.34c) and (8.34d), and replaces the first two equations by

$$\left(\frac{\boldsymbol{X}^{m+1} - \boldsymbol{X}^m}{\tau_m} \cdot \boldsymbol{n}^{m+\frac{1}{2}}, \varphi\right)_m^h = -(\nabla_m \mu^{m+1}, \nabla_m \varphi)_m, \tag{8.46a}$$

$$(\mu^{m+1}\boldsymbol{n}^{m+\frac{1}{2}}, \boldsymbol{\omega})_m^h = \mathcal{D}_m(\boldsymbol{X}^{m+1}, \boldsymbol{\omega}) + \mathcal{B}_m(\boldsymbol{\omega}, r^{m+1}). \tag{8.46b}$$

The gradient inner product is integrated exactly on the old surface; for piecewise linear functions it agrees with the corresponding mass-lumped quadrature. Both equations must use the same time-averaged normal. The geometric coefficients in $\mathcal{B}_m$ remain at the old time level, and both curvature pairings use the same bilinear form.

Theorem 8.2 (Discrete volume conservation and energy dissipation). *Under the assumptions of Theorem 8.1, a solution of the system comprising* (8.46), (8.34c), *and* (8.34d) *satisfies*

$$\mathcal{V}^{m+1} = \mathcal{V}^m, \qquad W^{m+1} + \tau_m \|\nabla_m \mu^{m+1}\|^2_{L^2(\Gamma^m)} \le W^m. \tag{8.47}$$

Proof. Take $\varphi = 1$ in (8.46a). Its right-hand side vanishes, and Lemma 8.3 gives volume conservation. Next take $\varphi = \mu^{m+1}$ and $\boldsymbol{\omega} = \boldsymbol{X}^{m+1} - \boldsymbol{X}^m$, and use $\psi = r^{m+1}$ in the curvature equation. This gives

$$\mathcal{D}_m(\boldsymbol{X}^{m+1}, \boldsymbol{X}^{m+1} - \boldsymbol{X}^m) + (H^{m+1} - H^m, r^{m+1})_m^h = -\tau_m \|\nabla_m \mu^{m+1}\|^2_{L^2(\Gamma^m)}. \tag{8.48}$$

The geometric and curvature-convexity estimates now follow exactly as in the proof of Theorem 8.1, yielding the energy inequality. □

For the volume-constrained $L^2$ gradient flow, replace the right-hand side of (8.46a) by $-(\mu^{m+1} - \lambda^{m+1}, \varphi)_m^h$, where

$$\lambda^{m+1} = \frac{(\mu^{m+1}, 1)_m^h}{(1,1)_m^h}. \tag{8.49}$$

The remaining equations are unchanged. Taking $\varphi = 1$ and $\varphi = \mu^{m+1}$ gives volume conservation and, respectively,

$$W^{m+1} + \tau_m \|\mu^{m+1} - \lambda^{m+1}\|^2_{m,h} \le W^m. \tag{8.50}$$

## 8.7. Numerical results

The experiments in this section are taken from [148] and concern the three-dimensional schemes above. The densities satisfy the positivity, directional, and curvature-convexity assumptions used in the energy estimates. Initial nodal curvature is evaluated from the analytical curvature of the prescribed smooth surface; curvature is subsequently evolved as an independent unknown.

**8.7.1. Initialization and stabilization.** The curvature is initialized analytically at the mesh vertices and then updated by the discrete curvature equation, rather than recomputed after every step. The force and curvature equations use the same recovered Weingarten matrix (8.30). Nonlinear systems are solved by Newton iteration; the tolerance used in the coupled ellipsoidal tests below is $10^{-11}$.

For an ellipsoidal density $\gamma_Q(\boldsymbol{n}) = \sqrt{\boldsymbol{n}^T Q \boldsymbol{n}}$ with $Q$ symmetric positive definite, an admissible symmetric-matrix stabilization is

$$\begin{aligned} \boldsymbol{a}_Q(\boldsymbol{n}) &= (I_3 - \boldsymbol{n}\boldsymbol{n}^T) Q \boldsymbol{n} / \gamma_Q(\boldsymbol{n}), \\ k_Q(\boldsymbol{n}) &= \gamma_Q(\boldsymbol{n}) + \frac{\lambda_{\max}(Q) + |\boldsymbol{a}_Q(\boldsymbol{n})|^2}{\gamma_Q(\boldsymbol{n})}. \end{aligned} \tag{8.51}$$

For the coupled density (8.53), the implementation uses

$$k(\boldsymbol{n}, H) = k_{G_0}(\boldsymbol{n}) + 0.025 H^2 k_{G_1}(\boldsymbol{n}) + 0.001 H^4. \tag{8.52}$$

This is the explicit construction given in the source appendix of [148]; it applies to the convergence, energy–volume, and timing tests with that density.

The polynomial-anisotropy morphology tests use $k = 2f + 4$. For the orientation-dependent Helfrich-type test, the implementation uses $k = 2f + 4 + 0.4(H - 2)^2$. These are the settings in the accompanying numerical implementation. Their observed energy decrease and stepwise local-gap checks do not by themselves prove that these specific constants dominate the global minimal stabilizing function for every possible configuration. The unconditional theorem above retains its stated local-energy-estimate assumption.

**8.7.2. Error and convergence rate.** For surfaces, we apply the following coupled energy density

$$f(\boldsymbol{n}, H) = \sqrt{\boldsymbol{n}^T \boldsymbol{G}_0 \boldsymbol{n}} + \frac{0.05}{2} \sqrt{\boldsymbol{n}^T \boldsymbol{G}_1 \boldsymbol{n}}\, H^2 + \frac{0.002}{4} H^4, \qquad \boldsymbol{n} \in \mathbb{S}^2, \tag{8.53}$$

where

$$\boldsymbol{G}_0 = \operatorname{diag}(1, 1.3, 1.6), \qquad \boldsymbol{G}_1 = \begin{pmatrix} 1.5 & 0.15 & 0 \\ 0.15 & 1 & 0.1 \\ 0 & 0.1 & 0.8 \end{pmatrix}.$$

The initial surface is the ellipsoid

$$\frac{x_1^2}{1.4^2} + x_2^2 + \frac{x_3^2}{0.8^2} = 1. \tag{8.54}$$

We subdivide an icosahedron and project its vertices onto the ellipsoid, giving meshes with $N = 42, 162, 642, 2562$ vertices. Let $h_\ell = h_0/2^\ell$, with $h_0 = 1/2$ and $\ell = 0, 1, 2, 3$, denote the subdivision parameter. We take $\tau_\ell = C h_\ell^2$ for $C = 0.08$ and $0.04$, and compare the solutions at $t = 0.1, 0.2, 0.3$.

We measure geometric error by the manifold distance. For surfaces this is the volume of the symmetric difference of the enclosed regions:

$$e^{h_\ell}(t) \coloneqq M\big(\Gamma_{h_\ell,\tau_\ell}(t), \Gamma_{h_{\ell+1},\tau_{\ell+1}}(t)\big) = \big|\Omega_{h_\ell,\tau_\ell}(t) \triangle \Omega_{h_{\ell+1},\tau_{\ell+1}}(t)\big|, \qquad \ell = 0, 1, 2. \tag{8.55}$$

Here $\Omega_{h_\ell,\tau_\ell}(t)$ denotes the enclosed region. The finest mesh is used to form the last successive-mesh distance. In the tables, $h$ is the subdivision parameter, while the order is calculated from the largest initial edge length $h_{\max,\ell}$:

$$p_{h_{\max}} = \frac{\log\big(e^{h_{\ell-1}}(t)/e^{h_\ell}(t)\big)}{\log\big(h_{\max,\ell-1}/h_{\max,\ell}\big)}, \qquad \ell = 1, 2. \tag{8.56}$$

All reported rates are computed from unrounded distances. The nonlinear tolerance is $10^{-11}$, and the curvature is evolved as an independent unknown throughout.

Tables 8.1 and 8.2 exhibit second-order convergence in the manifold distance on the finer meshes. The $L^2$ rates vary more with the observation time and $C$, whereas the fine-mesh surface-diffusion rates remain between 1.997 and 2.003.

Each surface-diffusion computation preserves the volume of its own initial polyhedral mesh. Consequently, the successive-mesh distance satisfies $M(\Gamma_{h_\ell}, \Gamma_{h_{\ell+1}}) \geq |V_{h_\ell}(0) - V_{h_{\ell+1}}(0)|$, up to the nonlinear-solver tolerance. The reported rates therefore measure geometric convergence under coupled space–time refinement, including the initial volume discretization error; they do not separately establish temporal order, curvature accuracy, or the error of the dynamic evolution.

**Table 8.1.** Error and convergence rates for the $L^2$ flow of surfaces.

| $C$ | $(h,\tau)$ | $e^h(t=0.1)$ | order | $e^h(t=0.2)$ | order | $e^h(t=0.3)$ | order |
|---|---|---|---|---|---|---|---|
| 0.08 | $(h_0,\tau_0)$ | 2.58e-1 | – | 2.69e-2 | – | 1.20e-2 | – |
| | $(\frac{h_0}{2},\frac{\tau_0}{4})$ | 7.38e-2 | 1.946 | 6.70e-3 | 2.161 | 3.65e-3 | 1.848 |
| | $(\frac{h_0}{2^2},\frac{\tau_0}{4^2})$ | 1.90e-2 | 1.994 | 1.59e-3 | 2.119 | 9.70e-4 | 1.951 |
| 0.04 | $(h_0,\tau_0)$ | 3.16e-1 | – | 8.40e-2 | – | 1.15e-2 | – |
| | $(\frac{h_0}{2},\frac{\tau_0}{4})$ | 8.98e-2 | 1.955 | 2.90e-2 | 1.655 | 3.16e-3 | 2.003 |
| | $(\frac{h_0}{2^2},\frac{\tau_0}{4^2})$ | 2.31e-2 | 1.997 | 7.80e-3 | 1.931 | 8.21e-4 | 1.982 |

**Table 8.2.** Error and convergence rates for surface diffusion.

| $C$ | $(h,\tau)$ | $e^h(t=0.1)$ | order | $e^h(t=0.2)$ | order | $e^h(t=0.3)$ | order |
|---|---|---|---|---|---|---|---|
| 0.08 | $(h_0,\tau_0)$ | 4.57e-1 | – | 4.35e-1 | – | 4.35e-1 | – |
| | $(\frac{h_0}{2},\frac{\tau_0}{4})$ | 1.23e-1 | 2.037 | 1.18e-1 | 2.024 | 1.18e-1 | 2.023 |
| | $(\frac{h_0}{2^2},\frac{\tau_0}{4^2})$ | 3.17e-2 | 1.999 | 3.04e-2 | 2.002 | 3.04e-2 | 2.003 |
| 0.04 | $(h_0,\tau_0)$ | 4.37e-1 | – | 4.35e-1 | – | 4.35e-1 | – |
| | $(\frac{h_0}{2},\frac{\tau_0}{4})$ | 1.19e-1 | 2.024 | 1.18e-1 | 2.023 | 1.18e-1 | 2.023 |
| | $(\frac{h_0}{2^2},\frac{\tau_0}{4^2})$ | 3.06e-2 | 1.997 | 3.03e-2 | 2.003 | 3.03e-2 | 2.003 |

**8.7.3. Volume and energy change.** To verify the structure-preserving properties of the schemes, we introduce the normalized volume change and the normalized energy as follows:

$$\frac{\Delta V^h(t)}{V^h(0)}\Big|_{t=t_m} := \frac{V^m - V^0}{V^0}, \qquad \frac{W^h(t)}{W^h(0)}\Big|_{t=t_m} := \frac{W^m}{W^0}. \tag{8.57}$$

We use the ellipsoid (8.54) and the coupled energy (8.53), with $\tau = 0.08h^2$ for $h = 2^{-1}, 2^{-2}, 2^{-3}$. The volume histories and normalized energy are shown in figures 8.1 and 8.2.

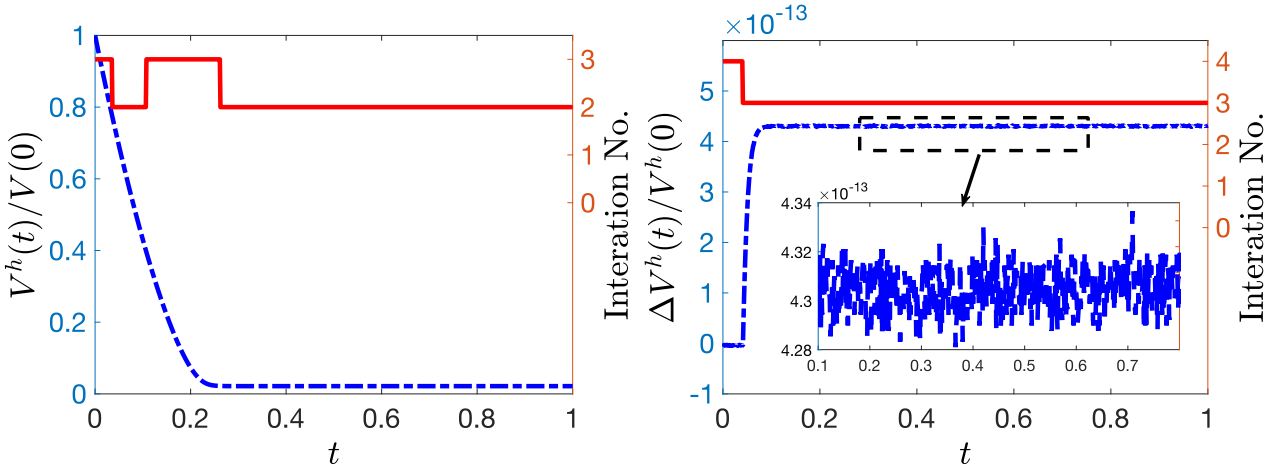



**Figure 8.1.** Volume histories and Newton iteration counts with $h = 2^{-3}$: (left) $V^h(t)/V^h(0)$ for the $L^2$ flow; (right) $\Delta V^h(t)/V^h(0)$ for surface diffusion.

It can be observed that the normalized energy decreases monotonically for both the $L^2$ flow and surface diffusion. For surface diffusion, the volume is well preserved, with the volume loss controlled

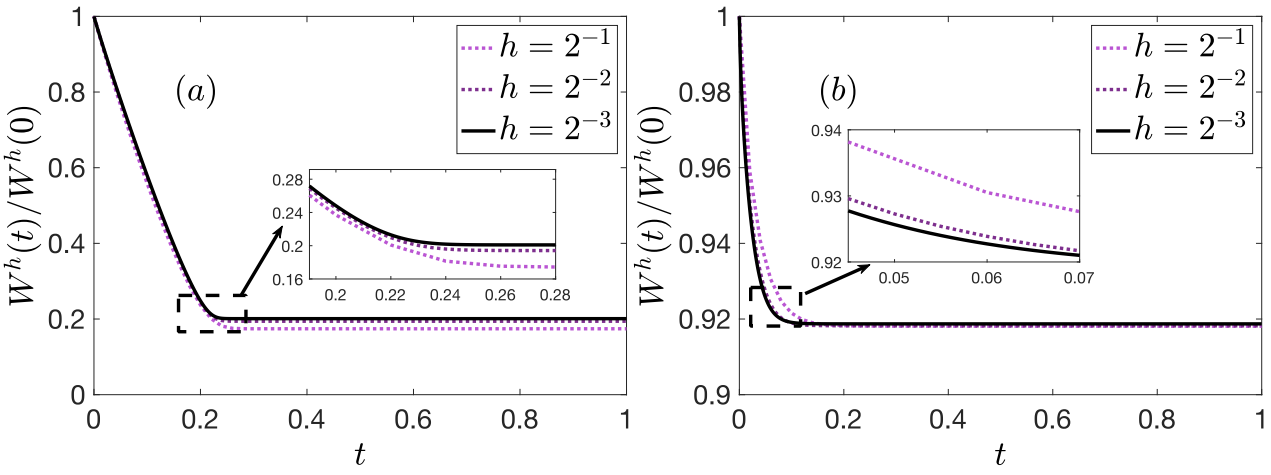



**Figure 8.2.** Normalized energy for: (a) $L^2$ flow; (b) surface diffusion.

at the order of $10^{-13}$, close to machine precision. The number of Newton iterations is also plotted in figure 8.1. It decreases to a steady value of about 2 for the $L^2$ flow and 3 for surface diffusion, indicating that the nonlinear solver is efficient and robust.

Unlike mean curvature flow, which shrinks a smooth closed convex surface to a point, the $L^2$ flow considered here exhibits a positive volume plateau. This behavior can be explained by the competing contributions to the energy (8.53). Under a uniform rescaling $\Gamma \mapsto \lambda\Gamma$, the surface, quadratic-curvature, and quartic-curvature energy contributions scale as

$$W(\lambda\Gamma) = \lambda^2 W_{\text{surf}}(\Gamma) + W_{H^2}(\Gamma) + \lambda^{-2} W_{H^4}(\Gamma). \tag{8.58}$$

Thus, while the surface energy favors contraction, the quartic-curvature term increasingly penalizes further shrinkage as the surface becomes smaller. Their competition provides a finite preferred scale, consistent with the observed leveling off of both the energy and the enclosed volume as the surface approaches an equilibrium configuration.

To assess the computational cost, we use the same ellipsoid and coupled density with $\tau = 0.00125$ and $T = 0.02$. Table 8.3 reproduces the median wall-clock time per step over three serial runs on an Apple M1 Pro with 16 GB RAM, using Python 3.14 and SciPy 1.18.1 with one BLAS thread. Timings include assembly, Newton iteration, and step diagnostics; initialization and file output are excluded. The nonlinear tolerance is $10^{-11}$. Here $\bar{I}$ and $I_{\max}$ denote the mean and maximum Newton iteration counts over the time steps.

**Table 8.3.** Wall-clock time per step and Newton iterations.

| | $L^2$ flow | | | Surface diffusion | | |
|---|---|---|---|---|---|---|
| $N$ | Time (s) | $\bar{I}$ | $I_{\max}$ | Time (s) | $\bar{I}$ | $I_{\max}$ |
| 162 | 0.0203 | 2.81 | 3 | 0.0447 | 4.00 | 4 |
| 642 | 0.102 | 3.00 | 3 | 0.214 | 4.00 | 4 |
| 2562 | 0.859 | 3.00 | 3 | 1.57 | 4.00 | 4 |

**8.7.4. Morphology of the evolving surfaces.** We next examine the shapes produced by the $L^2$ flow and surface diffusion. The colors indicate the discrete curvature $H^m$. The first three examples use separable surface and bending energies. The last example introduces orientation-dependent bending rigidity, coupling the normal and curvature. The ellipsoid and six-lobed surface are discretized with 642 vertices and evolved with $\tau = 0.00125$. To monitor the mesh, we use the triangle quality

$$q_\sigma = \frac{4\sqrt{3}|\sigma|}{\ell_1^2 + \ell_2^2 + \ell_3^2}, \qquad q_{\min} = \min_{\sigma \subset \Gamma^m} q_\sigma, \tag{8.59}$$

where $\ell_1, \ell_2, \ell_3$ are the edge lengths of $\sigma$. The value is 1 for an equilateral triangle and tends to 0 as the triangle degenerates. We use $q_{\min} < 0.05$ as a stopping criterion.

We first consider the ellipsoid (8.54) with the regularized anisotropic energy density

$$f(\boldsymbol{n}, H) = \gamma(\boldsymbol{n}) + \frac{\epsilon^2}{2} H^2, \qquad \gamma(\boldsymbol{n}) = 1 + \frac{1}{4}(n_1^3 + n_2^3 + n_3^3), \qquad \epsilon^2 = 0.05. \tag{8.60}$$

Figures 8.3 and 8.4 display its evolution under the $L^2$ flow and surface diffusion, respectively. The ellipsoid shrinks under the $L^2$ flow, whereas under surface diffusion it evolves towards a nearly stationary anisotropic shape.

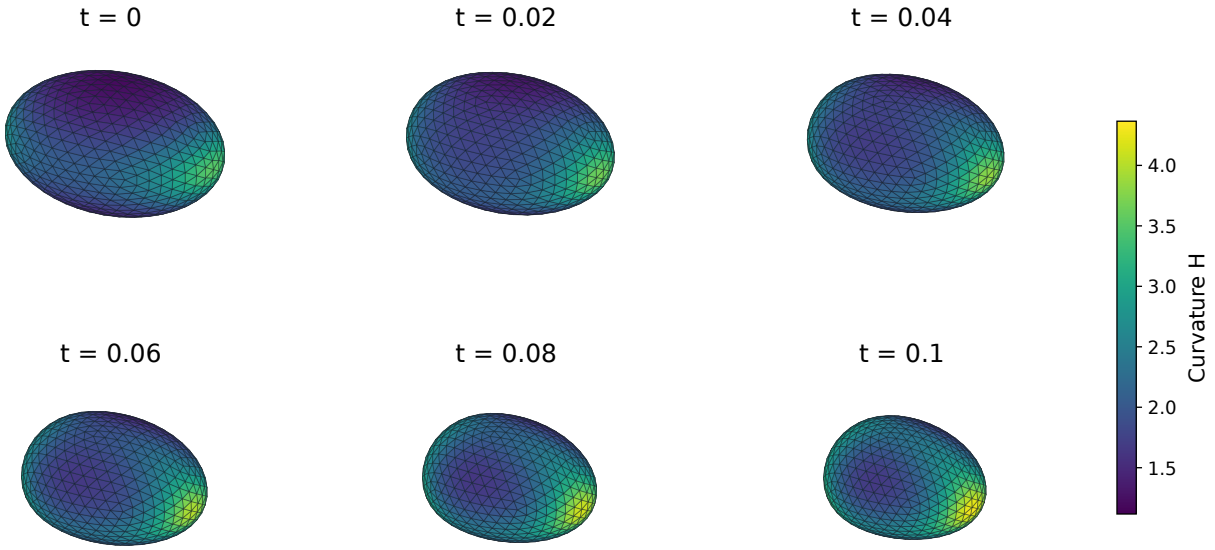



**Figure 8.3.** Evolution of the ellipsoid under the $L^2$ flow.

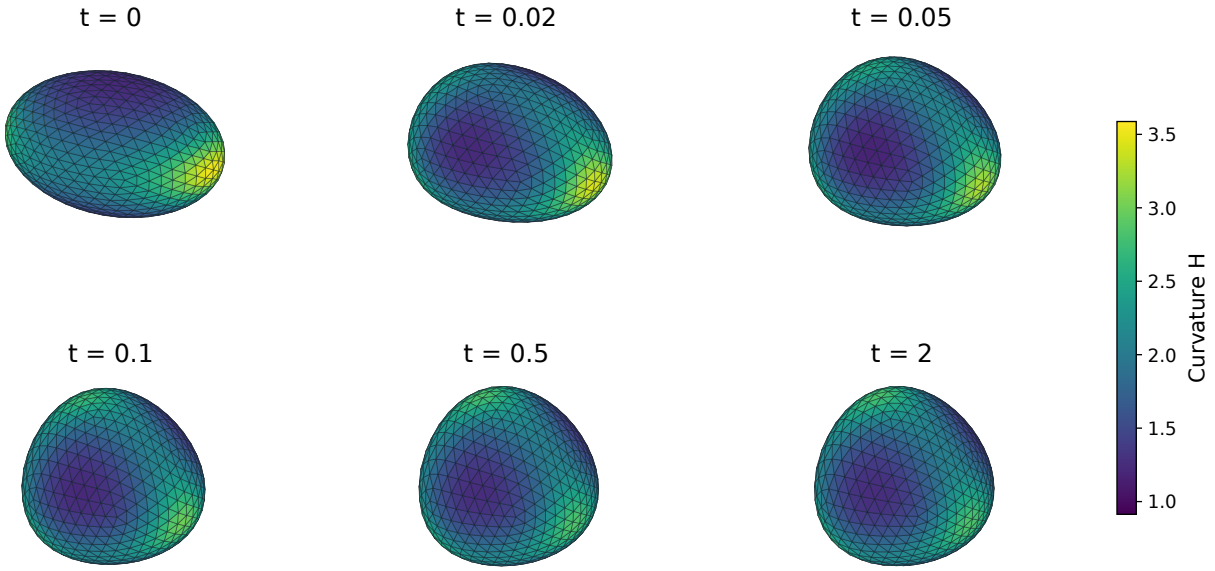



**Figure 8.4.** Evolution of the ellipsoid under surface diffusion.

Next we consider a six-lobed surface with a regularized anisotropic energy of cubic symmetry,

$$f(\boldsymbol{n}, H) = \gamma(\boldsymbol{n}) + \frac{\epsilon^2}{2} H^2, \qquad \gamma(\boldsymbol{n}) = 1 + \frac{1}{4}(n_1^4 + n_2^4 + n_3^4), \qquad \epsilon^2 = 0.05. \tag{8.61}$$

Figures 8.5 and 8.6 show the evolution of the six-lobed surface under the $L^2$ flow and surface diffusion, respectively. Both flows smooth out the initial lobes and indentations. Similar to the ellipsoid case, the surface continues to shrink under the $L^2$ flow. Under surface diffusion, it preserves its enclosed volume while relaxing towards an anisotropic equilibrium.

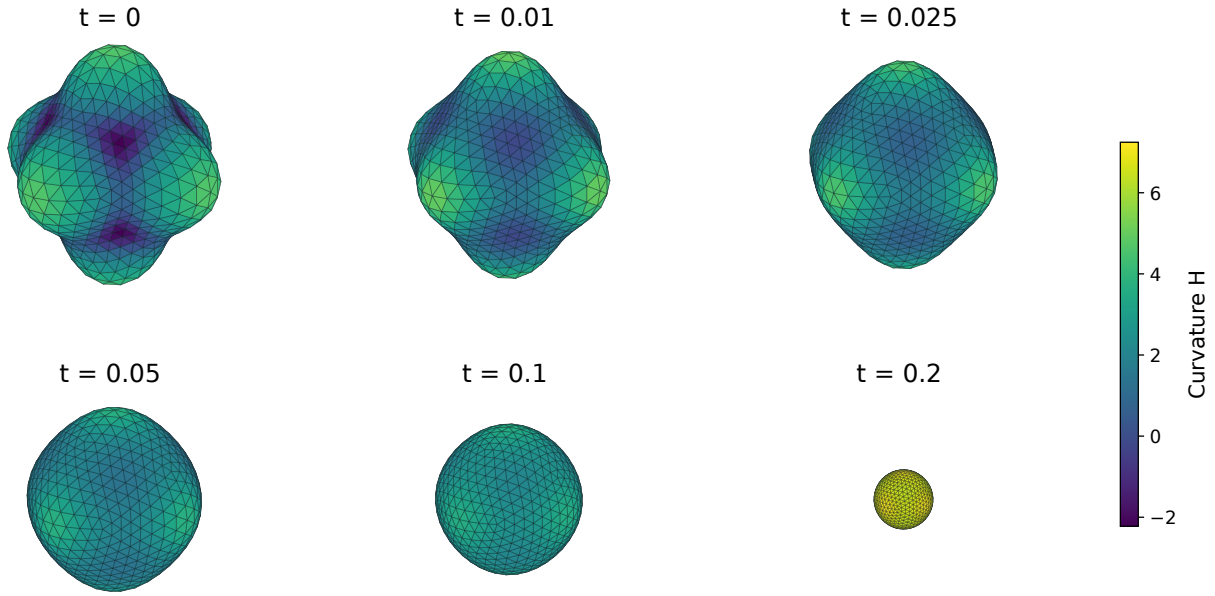



**Figure 8.5.** Evolution of the six-lobed surface under the $L^2$ flow.

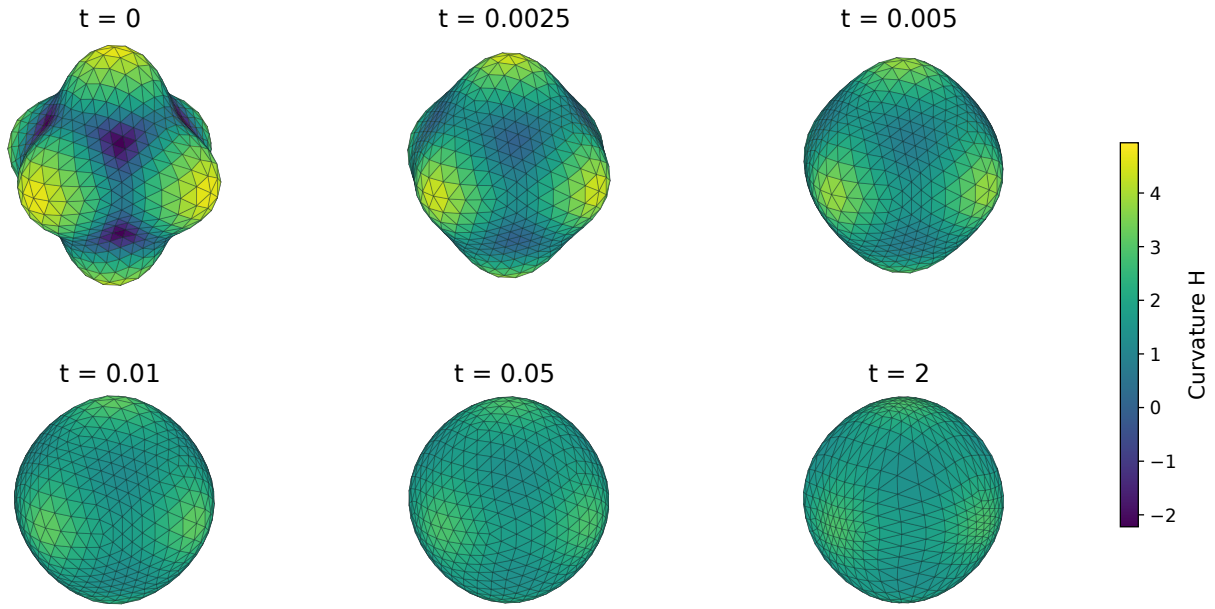



**Figure 8.6.** Evolution of the six-lobed surface under surface diffusion.

To examine the evolution of a surface with nontrivial topology, we take an initial torus with major radius $R = 1$ and minor radius $r = 0.6$. The energy density is chosen as

$$f(\boldsymbol{n}, H) = \gamma(\boldsymbol{n}) + \frac{\epsilon^2}{2} H^2, \qquad \gamma(\boldsymbol{n}) = 1 + \frac{1}{8}(n_1^3 + n_2^3 + n_3^3), \qquad \epsilon^2 = 0.05. \tag{8.62}$$

As shown in Figure 8.7, the torus contracts and its central hole progressively narrows. Both the enclosed volume and the energy decrease monotonically during the evolution.

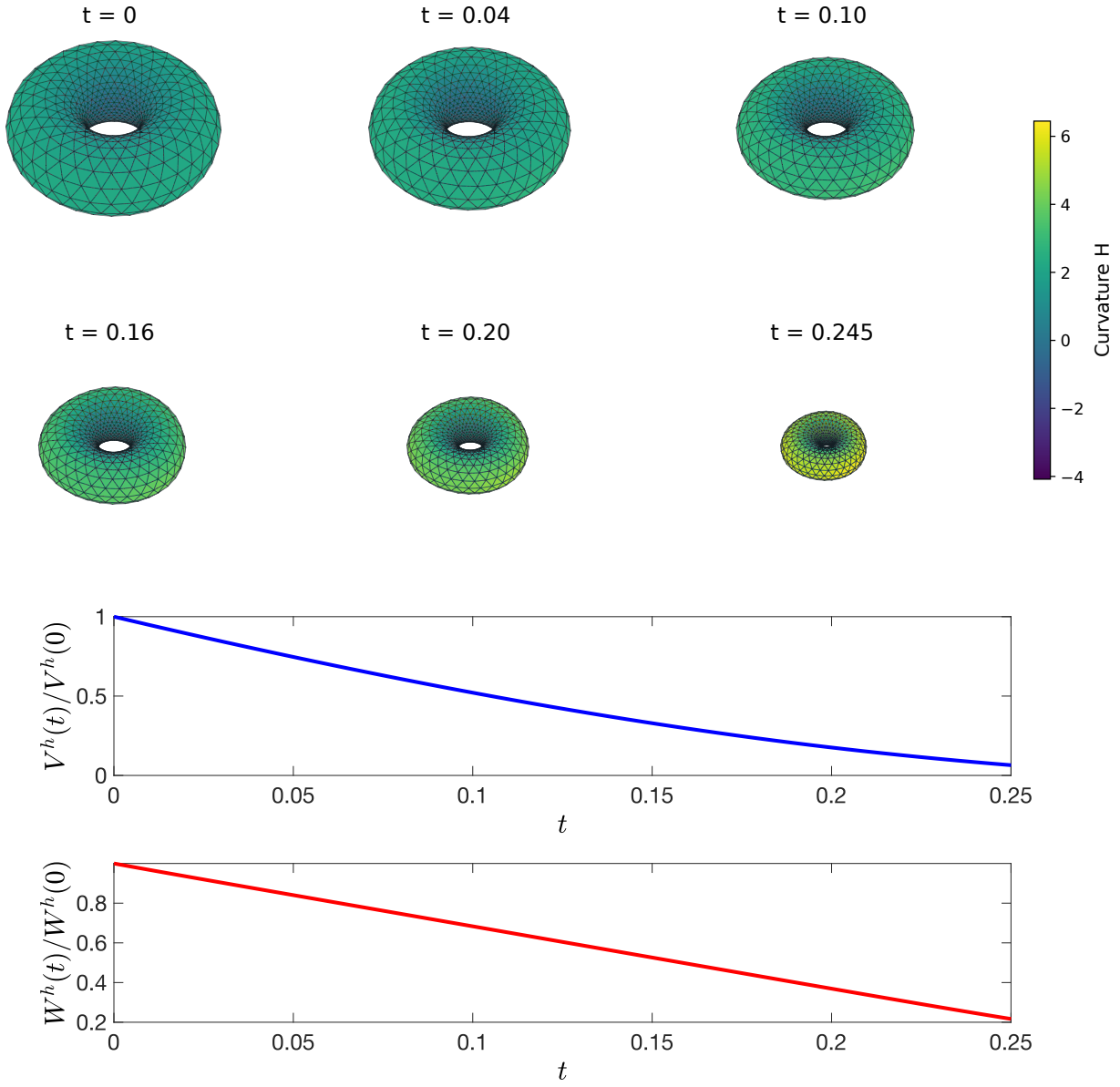



**Figure 8.7.** Evolution of the torus under the $L^2$ flow with 896 vertices and $\tau = 0.005$.

Finally, we consider surface diffusion of a biconcave disk with an orientation-dependent Helfrich-type energy. The classical Helfrich model for lipid bilayers penalizes deviations from a spontaneous curvature [81], which may reflect leaflet asymmetry [126]. The biconcave initial shape is motivated by the connection between bending energy and red-cell shapes [38]. We choose

$$\begin{aligned} f(\boldsymbol{n}, H) &= \gamma(\boldsymbol{n}) + \frac{\epsilon^2}{2} a(\boldsymbol{n})(H - H_*)^2, \\ \gamma(\boldsymbol{n}) &= 1 + \frac{1}{4}\sum_{i=1}^{3} n_i^4, \qquad a(\boldsymbol{n}) = 1 + 2n_3^2, \end{aligned} \tag{8.63}$$

with $\epsilon^2 = 0.05$ and $H_* = 2$.

The density is nonseparable and strictly convex in $H$. For a given curvature deviation, the bending penalty is three times larger when $\boldsymbol{n}$ is parallel to $\boldsymbol{e}_3$ than when it is perpendicular to $\boldsymbol{e}_3$. The orientation dependence and coefficients are chosen for this experiment and are not fitted to a particular membrane material. No membrane-area constraint is imposed.

We use 2562 vertices and $\tau = 0.005$. Figure 8.8 shows that the central depressions gradually disappear as the disk becomes more rounded. The energy decreases rapidly at first and then more slowly, reaching $W^h(0.4)/W^h(0) \approx 0.6748$, while the relative volume change remains below $1.5 \times 10^{-13}$ in magnitude. The computation is stopped at $t = 0.4$ when the mesh-quality threshold is reached.

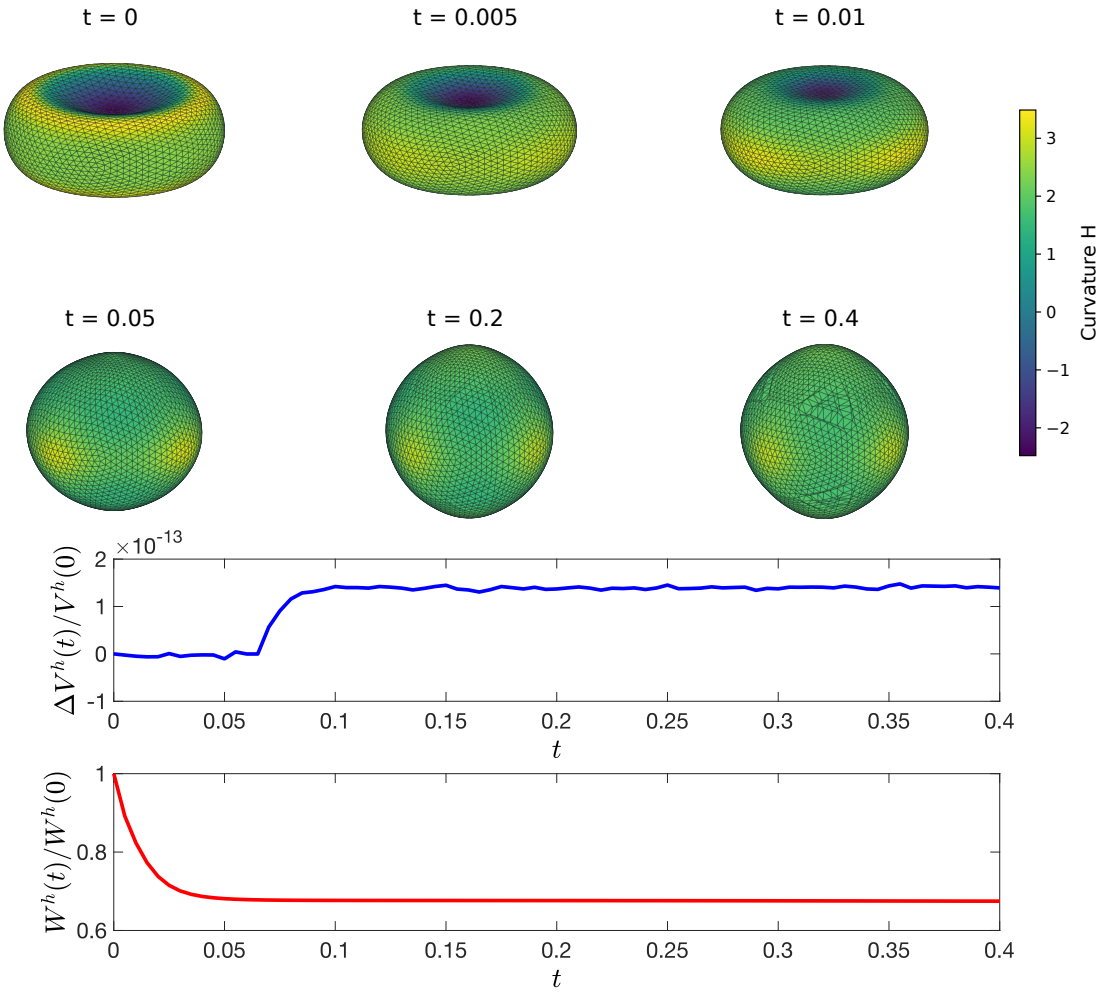



**Figure 8.8.** Evolution of the biconcave disk under surface diffusion with energy (8.63).

## 8.8. Concluding remarks

This chapter develops a unified weak formulation of the first variation, curvature evolution, and geometric gradient flows for $W = \int_\Gamma f(\boldsymbol{n}, H)\,\mathrm{d}A$ on closed surfaces in three dimensions. At fixed curvature, the symmetric surface energy matrix extends the local energy estimate to changes of orientation and element area. A mass-lumped projection of the curvature derivative brings the coupled nonlinear terms into the continuous piecewise linear test space. Under curvature convexity and the corresponding local energy estimate, solutions of the fully discrete scheme dissipate energy without a time-step restriction. The time-averaged area normal also preserves discrete volume for surface diffusion and the volume-constrained curvature flow. The numerical results from [148] exhibit approximately second-order geometric convergence, monotone energy dissipation, and volume conservation to nonlinear-solver accuracy. They also illustrate the competition between

orientation-dependent surface tension and bending during shape relaxation. Rigorous convergence analysis, nonlinear solvability, and curvature consistency remain open.

CHAPTER 9

# Conclusions and future work

## 9.1. Main results

This thesis develops structure-preserving parametric finite element methods for anisotropic geometric flows on planar curves and surfaces in three dimensions. The methods retain the relevant enclosed-measure law and discrete energy dissipation. For planar orientation-dependent energies, the symmetric formulation is unconditionally energy-stable under

$$3\hat{\gamma}(\theta) - \hat{\gamma}(\theta - \pi) \geq 0, \qquad \hat{\gamma} \in C^2(2\pi\mathbb{T}).$$

Within the local energy estimate framework, this directional condition is both necessary and sufficient for the analyzed symmetric construction. Interpreting the normal velocity as a map depending on geometric variables and the background curve provides a common formulation of several anisotropic flows. The methods are applied to crystalline-film evolution and solid-state dewetting. Their extension to surfaces preserves discrete volume and is unconditionally energy-stable under the corresponding symmetric condition

$$2\hat{\gamma}(\theta, \phi) - \hat{\gamma}(\pi - \theta, \pi + \phi) \geq 0, \qquad \hat{\gamma} \in C^2(\mathbb{S}^2).$$

The necessity and sufficiency statements concern the specified local energy estimates. Numerical examples demonstrate accuracy, structural preservation, and useful mesh behavior for complex geometries and anisotropies.

Chapter 2 introduces a stabilized parametric finite element method for anisotropic surface diffusion of closed planar curves. A stabilized surface energy matrix $\hat{\boldsymbol{G}}_k(\theta)$ gives a conservative formulation and its weak form. Piecewise linear parametric finite elements and a semi-implicit Euler step yield the fully discrete scheme. The analysis defines a minimal stabilizing function, establishes its existence, obtains a local energy estimate, and proves unconditional energy stability. The angular representation permits detailed treatment of the critical case under the additional assumptions stated in that chapter. It also admits globally $C^1$, piecewise $C^2$ anisotropies, broadening the class of densities covered by the analysis.

Chapter 3 constructs a symmetric surface energy matrix $\hat{\boldsymbol{Z}}_k(\theta)$ and a structure-preserving method with the optimal directional condition $3\hat{\gamma}(\theta) - \hat{\gamma}(\theta - \pi) \geq 0$ within the local energy estimate framework. The fully discrete surface-diffusion scheme preserves area exactly. A sharp estimate gives a global bound for the minimal stabilizing function without an additional restriction at equality. The local estimate then proves unconditional energy stability for sufficiently large stabilization. Numerical tests exhibit second-order spatial and first-order temporal accuracy. In the normal-vector representation, the scheme is a symmetrized parametric finite element method of the type developed in [9, 103]; the analysis relaxes the evenness assumption to $3\gamma(\boldsymbol{n}) - \gamma(-\boldsymbol{n}) \geq 0$.

Chapter 4 applies these methods to crystalline-film evolution and solid-state dewetting in two dimensions. The examples examine how the initial aspect ratio and the symmetry of the energy affect necking and pinch-off. For open curves, the weak formulation incorporates contact-line relaxation and leads to a structure-preserving scheme. Computations for strongly anisotropic energies recover multiple equilibrium configurations from different initial shapes, in agreement with the theoretical predictions.

Chapter 5 unifies a family of planar conservative formulations using an $\alpha$-surface energy matrix. The methods share the strict energy stability condition $3\hat{\gamma}(\theta) - \hat{\gamma}(\theta - \pi) > 0$. For the symmetric choice $\alpha = -1$, the condition becomes non-strict and is optimal for the local estimate. The analysis identifies this parameter choice as unique within the family. Apart from differences in mesh distribution, the computations show similar accuracy, cost, and structural properties across the tested values of $\alpha$. The

formulation extends to area-preserving anisotropic curvature flow, anisotropic surface diffusion, and more general normal-velocity laws.

Chapter 6 extends the $\alpha$-surface energy matrix framework to anisotropic surface evolution in three dimensions. The strict condition is $2\gamma(\boldsymbol{n}) - \gamma(-\boldsymbol{n}) > 0$. As in two dimensions, the symmetric choice attains the non-strict condition and the corresponding optimal local estimate. The numerical examples assess convergence, volume conservation, energy dissipation, and the evolution of complex closed surfaces.

Chapter 7 extends the framework to open surfaces in three-dimensional solid-state dewetting. A relaxed contact-angle condition couples the surface to the moving contact line. The fully discrete parametric scheme preserves enclosed volume and dissipates energy. The examples explore shape evolution from complex initial geometries, the influence of anisotropy on contact-line motion, and necking in solid films.

Chapter 8 treats closed-surface energies $W = \int_\Gamma f(\boldsymbol{n}, H)\,\mathrm{d}A$. A mass-lumped projection of the curvature derivative pairs a symmetric surface energy matrix at fixed curvature with the curvature evolution equation. Under curvature convexity and the local directional energy estimate, solutions of the fully discrete scheme satisfy an unconditional energy inequality. A time-averaged area normal preserves discrete volume for surface diffusion and the volume-constrained $L^2$ flow. The numerical results imported from [148] exhibit approximately second-order convergence in the manifold distance, monotone energy dissipation, and volume errors at the level of the nonlinear tolerance. Shape-relaxation examples demonstrate the competition between anisotropic surface tension and bending, including an orientation-dependent Helfrich-type density. These observations do not replace a solvability or error analysis.

## 9.2. Directions for further study

- The principal orientation-dependent schemes have first-order temporal and second-order spatial accuracy. Higher-order methods, especially in time, would be valuable for both analysis and applications. For the curvature-dependent schemes, the convergence observed in coupled space–time refinement should be complemented by separate temporal and spatial error estimates.
- The numerical examples show stable convergence rates. A rigorous convergence analysis remains challenging because tangential node motion is determined implicitly by the discretization.
- Parametric methods rely on a global parametrization that remains a diffeomorphism of the initial manifold. They therefore require additional treatment when singularities or topological changes occur. Phase-field or level-set methods may capture the subsequent evolution; numerical surgery adapted to anisotropic flows is another possible approach.
- For the curvature-dependent schemes, further questions include nonlinear solvability, approximation by the recovered curvature matrix, and consistency between evolved and geometric curvature. The completed experiments provide an initial basis for systematic mesh-quality and long-time studies. Incorporating boundary variations and contact-line dissipation would extend this framework to solid-state dewetting with curvature regularization.
- Anisotropic curvature-driven evolution appears throughout materials science and physics. Inverse problems based on experimental observations, including data-driven and AI-assisted approaches, may help identify energy densities and guide experiments.

APPENDIX A

# Solvers for the nonlinear schemes

All numerical schemes in this thesis are nonlinear and require suitable iterative solvers. We describe solvers for curve and surface evolution using the scheme (5.30) from Chapter 5 and the scheme (6.40) from Chapter 6, respectively.

## A.1. Iterative solvers for curve evolution

**A.1.1. Picard iteration.** For the nonlinear system (5.30), we use the following Picard iteration. At iteration $i$, find $(\boldsymbol{X}^{m+1,i+1}, \mu^{m+1,i+1}) \in [\mathbb{K}_p^h]^2 \times \mathbb{K}_p^h$ such that

$$\left(\boldsymbol{n}^{m+\frac{1}{2},i} \cdot \frac{\boldsymbol{X}^{m+1,i+1} - \boldsymbol{X}^m}{\tau}, \varphi^h\right)_{\Gamma^m}^h + \left(\mu^{m+1,i+1}, \varphi^h\right)_{\Gamma^m}^h = 0, \qquad \forall \varphi^h \in \mathbb{K}_p^h, \tag{A.1a}$$

$$\left(\mu^{m+1,i+1}\boldsymbol{n}^{m+\frac{1}{2},i}, \boldsymbol{\omega}^h\right)_{\Gamma^m}^h - \left(\hat{\boldsymbol{G}}_k^\alpha(\theta^m)\partial_s \boldsymbol{X}^{m+1,i+1}, \partial_s \boldsymbol{\omega}^h\right)_{\Gamma^m}^h = 0, \qquad \forall \boldsymbol{\omega}^h \in [\mathbb{K}_p^h]^2, \tag{A.1b}$$

where

$$\boldsymbol{n}^{m+\frac{1}{2},i} := -\frac{1}{2}\left(\partial_s \boldsymbol{X}^m + \partial_s \boldsymbol{X}^{m+1,i}\right)^\perp = -\frac{1}{2|\partial_\rho \boldsymbol{X}^m|}\left(\partial_\rho \boldsymbol{X}^m + \partial_\rho \boldsymbol{X}^{m+1,i}\right)^\perp. \tag{A.2}$$

For $m \geq 0$, we typically choose the initial guess $\boldsymbol{X}^{m+1,0} = \boldsymbol{X}^m$, $\mu^{m+1,0} = \mu^m$ and iterate until the stopping criteria

$$\|\boldsymbol{X}^{m+1,i+1} - \boldsymbol{X}^{m+1,i}\|_\infty = \max_{1\leq j\leq N} |\boldsymbol{X}^{m+1,i+1}(\rho_j) - \boldsymbol{X}^{m+1,i}(\rho_j)| \leq \text{tol}, \tag{A.3a}$$

$$\|\mu^{m+1,i+1} - \mu^{m+1,i}\|_\infty = \max_{1\leq j\leq N} |\mu^{m+1,i+1}(\rho_j) - \mu^{m+1,i}(\rho_j)| \leq \text{tol}, \tag{A.3b}$$

hold, where tol is a prescribed tolerance.

Remark A.1. The linear system is uniquely solvable under mild assumptions on $\boldsymbol{n}^{m+\frac{1}{2},i}$. A detailed discussion is given in [21].

**A.1.2. Newton iteration.** Newton iteration is often more efficient and converges faster than Picard iteration, particularly for weak nonlinearities. To solve (5.30) for $(\boldsymbol{X}^{m+1}, \mu^{m+1})$, we use the following Newton iteration. At iteration $i$, compute the Newton correction $(\boldsymbol{X}^\delta, \mu^\delta) \in [\mathbb{K}_p^h]^2 \times \mathbb{K}_p^h$ such that

$$\begin{aligned}&\left(\boldsymbol{n}^{m+\frac{1}{2},i} \cdot \frac{\boldsymbol{X}^\delta}{\tau}, \varphi^h\right)_{\Gamma^m}^h + \left(\frac{\boldsymbol{X}^{m+1,i} - \boldsymbol{X}^m}{\tau} \cdot \frac{(-\partial_\rho \boldsymbol{X}^\delta)^\perp}{2|\partial_\rho \boldsymbol{X}^m|}, \varphi^h\right)_{\Gamma^m}^h + \left(\mu^\delta, \varphi^h\right)_{\Gamma^m}^h \\ &\quad = -\left(\boldsymbol{n}^{m+\frac{1}{2},i} \cdot \frac{\boldsymbol{X}^{m+1,i} - \boldsymbol{X}^m}{\tau}, \varphi^h\right)_{\Gamma^m}^h - \left(\mu^{m+1,i}, \varphi^h\right)_{\Gamma^m}^h, \qquad \forall \varphi^h \in \mathbb{K}_p^h,\end{aligned} \tag{A.4a}$$

$$\begin{aligned}&\left(\mu^\delta \boldsymbol{n}^{m+\frac{1}{2},i}, \boldsymbol{\omega}^h\right)_{\Gamma^m}^h + \left(\mu^{m+1,i}, \frac{(-\partial_\rho \boldsymbol{X}^\delta)^\perp}{2|\partial_\rho \boldsymbol{X}^m|} \cdot \boldsymbol{\omega}^h\right)_{\Gamma^m}^h - \left(\hat{\boldsymbol{G}}_k^\alpha(\theta^m)\partial_s \boldsymbol{X}^\delta, \partial_s \boldsymbol{\omega}^h\right)_{\Gamma^m}^h \\ &\quad = -\left(\mu^{m+1,i}\boldsymbol{n}^{m+\frac{1}{2},i}, \boldsymbol{\omega}^h\right)_{\Gamma^m}^h + \left(\hat{\boldsymbol{G}}_k^\alpha(\theta^m)\partial_s \boldsymbol{X}^{m+1,i}, \partial_s \boldsymbol{\omega}^h\right)_{\Gamma^m}^h, \qquad \forall \boldsymbol{\omega}^h \in [\mathbb{K}_p^h]^2,\end{aligned} \tag{A.4b}$$

and update

$$\boldsymbol{X}^{m+1,i+1} := \boldsymbol{X}^{m+1,i} + \boldsymbol{X}^\delta, \qquad \mu^{m+1,i+1} := \mu^{m+1,i} + \mu^\delta. \tag{A.5}$$

In the computations in this thesis, we use the initial guess $\boldsymbol{X}^{m+1,0} = \boldsymbol{X}^m$, $\mu^{m+1,0} = \mu^m$ and the stopping criterion

$$\|\boldsymbol{X}^{m+1,i+1} - \boldsymbol{X}^{m+1,i}\|_\infty + \|\mu^{m+1,i+1} - \mu^{m+1,i}\|_\infty \le \mathrm{tol}, \tag{A.6}$$

where tol is a prescribed tolerance.

Remark A.2. The iteration (A.4) follows by linearizing (5.30) at $(\boldsymbol{X}^{m+1,i}, \mu^{m+1,i})$ through a first-order Taylor expansion and setting $\boldsymbol{X}^{m+1,i+1} = \boldsymbol{X}^{m+1,i} + \boldsymbol{X}^\delta$, $\mu^{m+1,i+1} = \mu^{m+1,i} + \mu^\delta$. Further details are given in [91].

## A.2. Iterative solvers for surface evolution

**A.2.1. Picard iteration.** For the nonlinear system (6.40), we use the following Picard iteration. At iteration $i$, find $(\boldsymbol{X}^{m+1,i+1}, \mu^{m+1,i+1}) \in [\mathbb{K}^m]^3 \times \mathbb{K}^m$ such that

$$\left(\boldsymbol{n}^{m+\frac{1}{2},i} \cdot \frac{\boldsymbol{X}^{m+1,i+1} - \boldsymbol{X}^m}{\tau}, \varphi^h\right)^h_{\Gamma^m} + \left(\nabla_\Gamma \mu^{m+1,i+1}, \nabla_\Gamma \varphi^h\right)^h_{\Gamma^m} = 0, \qquad \forall \varphi^h \in \mathbb{K}^m, \tag{A.7a}$$

$$\left(\mu^{m+1,i+1}\boldsymbol{n}^{m+\frac{1}{2},i}, \boldsymbol{\omega}^h\right)^h_{\Gamma^m} - \left\langle \hat{\boldsymbol{G}}^\alpha_k(\theta^m, \phi^m)\nabla_\Gamma \boldsymbol{X}^{m+1,i+1}, \nabla_\Gamma \boldsymbol{\omega}^h\right\rangle^h_{\Gamma^m} = 0, \qquad \forall \boldsymbol{\omega}^h \in [\mathbb{K}^m]^3. \tag{A.7b}$$

Here the vector $\boldsymbol{n}^{m+\frac{1}{2},i}$ is defined by

$$\boldsymbol{n}^{m+\frac{1}{2},i}\Big|_{\sigma_j^m} := \frac{\mathcal{J}\{\sigma_j^m\} + 4\mathcal{J}\{\sigma_j^{m+\frac{1}{2},i}\} + \mathcal{J}\{\sigma_j^{m+1,i}\}}{6|\mathcal{J}\{\sigma_j^m\}|}, \qquad \sigma_j^{m+\frac{1}{2},i} := \frac{1}{2}(\sigma_j^m + \sigma_j^{m+1,i}). \tag{A.8}$$

The initial guess and stopping criteria are the same as in the curve case.

Remark A.3. As in the curve case, the linear system is uniquely solvable under mild assumptions on $\boldsymbol{n}^{m+\frac{1}{2},i}$; see [21].

**A.2.2. Newton iteration.** For the nonlinear system (6.40), we use the following Newton iteration. At iteration $i$, compute the Newton correction $(\boldsymbol{X}^\delta, \mu^\delta) \in [\mathbb{K}^m]^3 \times \mathbb{K}^m$ such that

$$\begin{aligned}
&\left(\boldsymbol{n}^{m+\frac{1}{2},i} \cdot \frac{\boldsymbol{X}^\delta}{\tau}, \varphi^h\right)^h_{\Gamma^m} + \left(\frac{\boldsymbol{X}^{m+1,i} - \boldsymbol{X}^m}{\tau} \cdot \mathcal{G}^{m+\frac{1}{2},i}_{\boldsymbol{X}^\delta}, \varphi^h\right)^h_{\Gamma^m} + \left(\nabla_\Gamma \mu^\delta, \nabla_\Gamma \varphi^h\right)^h_{\Gamma^m} \\
&\quad = -\left(\boldsymbol{n}^{m+\frac{1}{2},i} \cdot \frac{\boldsymbol{X}^{m+1,i} - \boldsymbol{X}^m}{\tau}, \varphi^h\right)^h_{\Gamma^m} - \left(\nabla_\Gamma \mu^{m+1,i}, \nabla_\Gamma \varphi^h\right)^h_{\Gamma^m}, \qquad \forall \varphi^h \in \mathbb{K}^m,
\end{aligned} \tag{A.9a}$$

$$\begin{aligned}
&\left(\mu^\delta \boldsymbol{n}^{m+\frac{1}{2},i}, \boldsymbol{\omega}^h\right)^h_{\Gamma^m} + \left(\mu^{m+1,i}, \mathcal{G}^{m+\frac{1}{2},i}_{\boldsymbol{X}^\delta} \cdot \boldsymbol{\omega}^h\right)^h_{\Gamma^m} - \left(\hat{\boldsymbol{G}}^\alpha_k(\theta^m, \phi^m)\nabla_\Gamma \boldsymbol{X}^\delta, \nabla_\Gamma \boldsymbol{\omega}^h\right)^h_{\Gamma^m} \\
&\quad = -\left(\mu^{m+1,i}\boldsymbol{n}^{m+\frac{1}{2},i}, \boldsymbol{\omega}^h\right)^h_{\Gamma^m} + \left\langle \hat{\boldsymbol{G}}^\alpha_k(\theta^m, \phi^m)\nabla_\Gamma \boldsymbol{X}^{m+1,i}, \nabla_\Gamma \boldsymbol{\omega}^h\right\rangle^h_{\Gamma^m}, \qquad \forall \boldsymbol{\omega}^h \in [\mathbb{K}^m]^3,
\end{aligned} \tag{A.9b}$$

where

$$\mathcal{G}^{m+\frac{1}{2},i}_{\boldsymbol{X}^\delta}\Big|_{\sigma_j^m} := \frac{\mathbf{g}^{23} \times \boldsymbol{X}^\delta(\boldsymbol{q}^m_{j_1}) + \mathbf{g}^{31} \times \boldsymbol{X}^\delta(\boldsymbol{q}^m_{j_2}) + \mathbf{g}^{12} \times \boldsymbol{X}^\delta(\boldsymbol{q}^m_{j_3})}{6|\mathcal{J}\{\sigma_j^m\}|}, \tag{A.10}$$

and

$$\mathbf{g}^{lk} := 2\boldsymbol{X}^{m+1,i}(\boldsymbol{q}^m_{j_k}) + \boldsymbol{X}^m(\boldsymbol{q}^m_{j_k}) - 2\boldsymbol{X}^{m+1,i}(\boldsymbol{q}^m_{j_l}) - \boldsymbol{X}^m(\boldsymbol{q}^m_{j_l}), \qquad 1 \le l, k \le 3. \tag{A.11}$$

The remaining settings are the same as in Section A.1.2.

APPENDIX B

# Three-dimensional anisotropic surface energies

We list several commonly used three-dimensional anisotropies $\gamma(\boldsymbol{n})$. Under the mapping

$$\boldsymbol{n}(\theta,\phi) = (n_1, n_2, n_3)^T \coloneqq (\sin\theta\cos\phi, \sin\theta\sin\phi, \cos\theta)^T, \tag{B.1}$$

they can be expressed in the $\hat{\gamma}(\theta,\phi)$ formulation.

- Riemannian metric anisotropy

$$\gamma(\boldsymbol{n}) = \sum_{l=1}^{k} \sqrt{\boldsymbol{n}^T \boldsymbol{G}_l \boldsymbol{n}}, \qquad \forall \boldsymbol{n} \in \mathbb{S}^2, \tag{B.2}$$

  where $\boldsymbol{G}_l \in \mathbb{R}^{3\times 3}$ is symmetric positive definite.

- $l^r$-norm anisotropy

$$\gamma(\boldsymbol{n}) = (|n_1|^r + |n_2|^r + |n_3|^r)^{\frac{1}{r}}, \qquad r \geq 2, \qquad \boldsymbol{n} \in \mathbb{S}^2. \tag{B.3}$$

- Cubic anisotropy

$$\gamma(\boldsymbol{n}) = 1 + \beta(n_1^4 + n_2^4 + n_3^4), \qquad \forall \boldsymbol{n} \in \mathbb{S}^2. \tag{B.4}$$

- Three-fold symmetric anisotropy

$$\gamma(\boldsymbol{n}) = 1 + \beta(n_1^3 + n_2^3 + n_3^3), \qquad \forall \boldsymbol{n} \in \mathbb{S}^2. \tag{B.5}$$

- [001], [011], [111]-oriented anisotropy

$$\gamma(\boldsymbol{n}) = 1 + \beta(n_1^4 + n_2^4), \qquad \text{[001] orientation}, \tag{B.6a}$$

$$\gamma(\boldsymbol{n}) = 1 + \beta(n_1^4 + \frac{n_2^4 + n_3^4}{2} + 3n_2^2 n_3^2), \qquad \text{[011] orientation}, \tag{B.6b}$$

$$\gamma(\boldsymbol{n}) = 1 + \beta\left(\frac{n_1^4 + n_2^4}{2} + \frac{n_3^4}{3} + n_1^2 n_2^2 + 2n_3^2(n_1^2 + n_2^2) + \frac{2\sqrt{2}}{3} n_1^3 n_3 - 2\sqrt{2} n_1 n_2^2 n_3\right), \qquad \text{[111] orientation}, \tag{B.6c}$$

- Piecewise BGN anisotropy

$$\gamma(\boldsymbol{n}) = \sqrt{(\frac{5}{2} + \frac{3}{2}\mathrm{sgn}(n_1))n_1^2 + n_2^2 + n_3^2}, \qquad \forall \boldsymbol{n} \in \mathbb{S}^2. \tag{B.7}$$

- Ellipsoidal anisotropy

$$\gamma(\boldsymbol{n}) = \sqrt{a_1 n_1^2 + a_2 n_2^2 + a_3 n_3^2}, \qquad a_1, a_2, a_3 > 0, \qquad \forall \boldsymbol{n} \in \mathbb{S}^2. \tag{B.8}$$

# Bibliography


[1] B. Andrews. "Volume-preserving anisotropic mean curvature flow". In: *Indiana University Mathematics Journal* (2001), pp. 783–827.

[2] B. Andrews, B. Chow, C. Guenther, and M. Langford. *Extrinsic geometric flows*. Vol. 206. American Mathematical Society, 2022.

[3] S. Angenent. "Parabolic equations for curves on surfaces Part I. Curves with p-integrable curvature". In: *Annals of Mathematics* (1990), pp. 451–483.

[4] L. Armelao, D. Barreca, G. Bottaro, A. Gasparotto, S. Gross, C. Maragno, and E. Tondello. "Recent trends on nanocomposites based on Cu, Ag and Au clusters: A closer look". In: *Coordination Chemistry Reviews* 250.11-12 (2006), pp. 1294–1314.

[5] S. Balachandar and J. K. Eaton. "Turbulent dispersed multiphase flow". In: *Annual Review of Fluid Mechanics* 42.1 (2010), pp. 111–133.

[6] E. Bänsch, P. Morin, and R. H. Nochetto. "A finite element method for surface diffusion: the parametric case". In: *Journal of Computational Physics* 203.1 (2005), pp. 321–343.

[7] W. Bao, H. Garcke, R. Nürnberg, and Q. Zhao. "Volume-preserving parametric finite element methods for axisymmetric geometric evolution equations". In: *Journal of Computational Physics* 460 (2022), p. 111180.

[8] W. Bao, H. Garcke, R. Nürnberg, and Q. Zhao. "A structure-preserving finite element approximation of surface diffusion for curve networks and surface clusters". In: *Numerical Methods for Partial Differential Equations* 39.1 (2023), pp. 759–794.

[9] W. Bao, W. Jiang, and Y. Li. "A symmetrized parametric finite element method for anisotropic surface diffusion of closed curves". In: *SIAM Journal on Numerical Analysis* 61.2 (2023), pp. 617–641.

[10] W. Bao, W. Jiang, D. J. Srolovitz, and Y. Wang. "Stable equilibria of anisotropic particles on substrates: a generalized Winterbottom construction". In: *SIAM Journal on Applied Mathematics* 77.6 (2017), pp. 2093–2118.

[11] W. Bao, W. Jiang, Y. Wang, and Q. Zhao. "A parametric finite element method for solid-state dewetting problems with anisotropic surface energies". In: *Journal of Computational Physics* 330 (2017), pp. 380–400.

[12] W. Bao and Y. Li. "A symmetrized parametric finite element method for anisotropic surface diffusion in three dimensions". In: *SIAM Journal on Scientific Computing* 45.4 (2023), A1438–A1461.

[13] W. Bao and Y. Li. "A structure-preserving parametric finite element method for geometric flows with anisotropic surface energy". In: *Numerische Mathematik* 156.2 (2024), pp. 609–639.

[14] W. Bao and Y. Li. "A unified structure-preserving parametric finite element method for anisotropic surface diffusion". In: *Mathematics of Computation* 94.355 (2025), pp. 2113–2149.

[15] W. Bao and Y. Li. "An energy-stable parametric finite element method for the planar Willmore flow". In: *SIAM Journal on Numerical Analysis* 63.1 (2025), pp. 103–121.

[16] W. Bao, Y. Li, and D. Wang. "An energy-stable parametric finite element method for the Willmore flow in three dimensions". In: *arXiv preprint arXiv:2506.21025* (2025).

[17] W. Bao, Y. Li, W. Ying, and Y. Zhang. "A structure-preserving parametric approximation for anisotropic geometric flows via an $\alpha$-surface energy matrix". In: *Journal of Computational Physics* 561 (2026), p. 114976. DOI: 10.1016/j.jcp.2026.114976.

[18] W. Bao, Y. Li, and Q. Zhao. "A structure-preserving parametric finite element method for solid-state dewetting on curved substrates". In: *Communications in Nonlinear Science and Numerical Simulation* 146 (2025), p. 108767.

[19] W. Bao and Q. Zhao. "A structure-preserving parametric finite element method for surface diffusion". In: *SIAM Journal on Numerical Analysis* 59.5 (2021), pp. 2775–2799.

[20] W. Bao and Q. Zhao. "An energy-stable parametric finite element method for simulating solid-state dewetting problems in three dimensions". In: *Journal of Computational Mathematics* 41.4 (2023), pp. 771–796.

[21] J. W. Barrett, H. Garcke, and R. Nürnberg. "A parametric finite element method for fourth order geometric evolution equations". In: *Journal of Computational Physics* 222.1 (2007), pp. 441–467.

[22] J. W. Barrett, H. Garcke, and R. Nürnberg. "On the variational approximation of combined second and fourth order geometric evolution equations". In: *SIAM Journal on Scientific Computing* 29.3 (2007), pp. 1006–1041.

[23] J. W. Barrett, H. Garcke, and R. Nürnberg. "A variational formulation of anisotropic geometric evolution equations in higher dimensions". In: *Numerische Mathematik* 109.1 (2008), pp. 1–44.

[24] J. W. Barrett, H. Garcke, and R. Nürnberg. "Numerical approximation of anisotropic geometric evolution equations in the plane". In: *IMA Journal of Numerical Analysis* 28.2 (2008), pp. 292–330.

[25] J. W. Barrett, H. Garcke, and R. Nürnberg. "On the parametric finite element approximation of evolving hypersurfaces in R3". In: *Journal of Computational Physics* 227.9 (2008), pp. 4281–4307.

[26] J. W. Barrett, H. Garcke, and R. Nürnberg. "Parametric approximation of Willmore flow and related geometric evolution equations". In: *SIAM Journal on Scientific Computing* 31.1 (2008), pp. 225–253.

[27] J. W. Barrett, H. Garcke, and R. Nürnberg. "On stable parametric finite element methods for the Stefan problem and the Mullins–Sekerka problem with applications to dendritic growth". In: *Journal of Computational Physics* 229.18 (2010), pp. 6270–6299.

[28] J. W. Barrett, H. Garcke, and R. Nürnberg. "Parametric approximation of surface clusters driven by isotropic and anisotropic surface energies". In: *Interfaces and Free Boundaries* 12.2 (2010), pp. 187–234.

[29] J. W. Barrett, H. Garcke, and R. Nürnberg. "Parametric finite element approximations of curvature-driven interface evolutions". In: *Handbook of Numerical Analysis* 21 (2020), pp. 275–423.

[30] O. Bekhtereva, Y. Gavrilyuk, V. Lifshits, and B. Churusov. "Indium Surface Phase Formation on Si (111) Surface and their Role in Diffusion and Desorption. Poverkhnost'". In: *Physika, Khimiia i Mekhanika* 8 (1988), p. 54.

[31] M. Brassel and E. Bretin. "A modified phase field approximation for mean curvature flow with conservation of the volume". In: *Mathematical Methods in the Applied Sciences* 34.10 (2011), pp. 1157–1180.

[32] C. E. Brennen. *Fundamentals of multiphase flow*. Cambridge University Press, 2005.

[33] J. E. Brothers and F. Morgan. "The isoperimetric theorem for general integrands." In: *Michigan Mathematical Journal* 41.3 (1994), pp. 419–431.

[34] F. Buatier de Mongeot, W. Zhu, A. Molle, R. Buzio, C. Boragno, U. Valbusa, < f. E. Wang, and Z. Zhang. "Nanocrystal formation and faceting instability in Al (110) homoepitaxy: True upward adatom diffusion at step edges and island corners". In: *Physical Review Letters* 91.1 (2003), p. 016102.

[35] M. Burger, F. Haußer, C. Stöcker, and A. Voigt. "A level set approach to anisotropic flows with curvature regularization". In: *Journal of Computational Physics* 225.1 (2007), pp. 183–205.

[36] W. Burton, N. Cabrera, and F. Frank. "The growth of crystals and the equilibrium structure of their surfaces". In: *Philosophical Transactions of the Royal Society of London. Series A, Mathematical and Physical Sciences* 243.866 (1951), pp. 299–358.

[37] J. Cahn and D. Hoffman. "A vector thermodynamics for anisotropic surfaces—II. Curved and faceted surfaces". In: *Acta Metallurgica* 22.10 (1974), pp. 1205–1214.

[38] P. B. Canham. "The minimum energy of bending as a possible explanation of the biconcave shape of the human red blood cell". In: *Journal of Theoretical Biology* 26.1 (1970), pp. 61–81. DOI: 10.1016/S0022-5193(70)80032-7.

[39] A. Chambolle, M. Morini, M. Novaga, and M. Ponsiglione. "Existence and uniqueness for anisotropic and crystalline mean curvature flows". In: *Journal of the American Mathematical Society* 32.3 (2019), pp. 779–824.

[40] L.-S. Chang, E. Rabkin, B. Straumal, B. Baretzky, and W. Gust. "Thermodynamic aspects of the grain boundary segregation in Cu (Bi) alloys". In: *Acta Materialia* 47.15-16 (1999), pp. 4041–4046.

[41] L. Q. Chen and J. Shen. "Applications of semi-implicit Fourier-spectral method to phase field equations". In: *Computer Physics Communications* 108.2-3 (1998), pp. 147–158.

[42] Y.-G. Chen, Y. Giga, and S. Goto. "Uniqueness and existence of viscosity solutions of generalized mean curvature flow equations". In: *Fundamental Contributions to the Continuum Theory of Evolving Phase Interfaces in Solids: A Collection of Reprints of 14 Seminal Papers*. Springer, 1999, pp. 375–412.

[43] T. H. Colding and W. P. Minicozzi. "Generic mean curvature flow I; generic singularities". In: *Annals of mathematics* (2012), pp. 755–833.

[44] K. Deckelnick, G. Dziuk, and C. M. Elliott. "Computation of geometric partial differential equations and mean curvature flow". In: *Acta Numerica* 14 (2005), pp. 139–232.

[45] K. Deckelnick, G. Dziuk, and C. M. Elliott. "Fully discrete finite element approximation for anisotropic surface diffusion of graphs". In: *SIAM Journal on Numerical Analysis* 43.3 (2005), pp. 1112–1138.

[46] K. Deckelnick, H. Garcke, and B. Kovács. "Error estimates for a surface finite element method for anisotropic mean curvature flow". In: *arXiv preprint arXiv:2508.01078* (2025).

[47] A. Dinghas. "Über einen geometrischen Satz von Wulff für die Gleichgewichtsform von Kristallen". In: *Zeitschrift für Kristallographie-Crystalline Materials* 105.1-6 (1943), pp. 304–314.

[48] G. Doğan and R. H. Nochetto. "First variation of the general curvature-dependent surface energy". In: *ESAIM: Mathematical Modelling and Numerical Analysis* 46.1 (2012), pp. 59–79. DOI: 10.1051/m2an/2011019.

[49] E. Dornel, J.-C. Barbe, F. De Crécy, G. Lacolle, and J. Eymery. "Surface diffusion dewetting of thin solid films: Numerical method and application to Si/ SiO 2". In: *Physical Review B—Condensed Matter and Materials Physics* 73.11 (2006), p. 115427.

[50] P. Du, M. Khenner, and H. Wong. "A tangent-plane marker-particle method for the computation of three-dimensional solid surfaces evolving by surface diffusion on a substrate". In: *Journal of Computational Physics* 229.3 (2010), pp. 813–827.

[51] Q. Du and X. Feng. "The phase field method for geometric moving interfaces and their numerical approximations". In: *Handbook of Numerical Analysis* 21 (2020), pp. 425–508.

[52] Z. Duan, M. Li, and C. Zhou. "Solid-state dewetting of axisymmetric thin film on axisymmetric curved-surface substrates: modeling and simulation". In: *Physica D: Nonlinear Phenomena* (2025), p. 134871.

[53] G. Dziuk. "An algorithm for evolutionary surfaces". In: *Numerische Mathematik* 58.1 (1990), pp. 603–611.

[54] G. Dziuk. "Convergence of a semi-discrete scheme for the curve shortening flow". In: *Mathematical Models and Methods in Applied Sciences* 4.04 (1994), pp. 589–606.

[55] G. Dziuk. “Discrete anisotropic curve shortening flow”. In: *SIAM Journal on Numerical Analysis* 36.6 (1999), pp. 1808–1830.

[56] G. Dziuk and C. Elliott. “$L^2$-estimates for the evolving surface finite element method”. In: *Mathematics of Computation* 82.281 (2013), pp. 1–24.

[57] J. J. Eggleston, G. B. McFadden, and P. W. Voorhees. “A phase-field model for highly anisotropic interfacial energy”. In: *Physica D: Nonlinear Phenomena* 150.1-2 (2001), pp. 91–103.

[58] C. M. Elliott and H. Garcke. *Existence results for diffusive surface motion laws*. Sonderforschungsbereich 256, 1994.

[59] C. M. Elliott and H. Garcke. “Diffusional phase transitions in multicomponent systems with a concentration dependent mobility matrix”. In: *Physica D: Nonlinear Phenomena* 109.3-4 (1997), pp. 242–256.

[60] J. Escher, Y. Giga, and K. Ito. “On a limiting motion and self-intersections of curves moved by the intermediate surface diffusion flow”. In: *Nonlinear Analysis: Theory, Methods & Applications* 47.6 (2001), pp. 3717–3728.

[61] J. Escher, U. F. Mayer, and G. Simonett. “The surface diffusion flow for immersed hypersurfaces”. In: *SIAM Journal on Mathematical Analysis* 29.6 (1998), pp. 1419–1433.

[62] J. Escher and P. B. Mucha. “The surface diffusion flow on rough phase spaces”. In: *Discrete and Continuous Dynamical Systems* 26.2 (2010), pp. 431–453.

[63] T. Eto, H. Garcke, and R. Nürnberg. “A parametric finite element method for a degenerate multiphase Stefan problem with triple junctions”. In: *Computational Methods in Applied Mathematics* 26.1 (2026), pp. 43–67.

[64] I. Fonseca, A. Pratelli, and B. Zwicknagl. “Shapes of epitaxially grown quantum dots”. In: *Archive for Rational Mechanics and Analysis* 214.2 (2014), pp. 359–401.

[65] F. Frank. “Metal surfaces”. In: *ASM, Cleveland, OH* (1963).

[66] M. Gage and R. S. Hamilton. “The heat equation shrinking convex plane curves”. In: *Journal of Differential Geometry* 23.1 (1986), pp. 69–96.

[67] H. Garcke, R. Nürnberg, and Q. Zhao. “Structure-preserving discretizations of two-phase Navier–Stokes flow using fitted and unfitted approaches”. In: *Journal of Computational Physics* 489 (2023), p. 112276.

[68] H. Garcke, R. Nürnberg, and Q. Zhao. “An energy-stable parametric finite element method for Willmore flow with normal-tangential velocity splitting”. In: *arXiv preprint arXiv:2507.00193* (2025).

[69] H. Garcke, R. Nürnberg, and Q. Zhao. “A variational front-tracking method for multiphase flow with triple junctions”. In: *Mathematics of Computation* 95.358 (2026), pp. 647–682.

[70] C. Geuzaine and J.-F. Remacle. “Gmsh: A 3-D finite element mesh generator with built-in pre-and post-processing facilities”. In: *International Journal for Numerical Methods in Engineering* 79.11 (2009), pp. 1309–1331.

[71] J. W. Gibbs. “The collected works of J. Willard Gibbs”. In: (1961).

[72] Y. Giga and N. Požár. “Motion by crystalline-like mean curvature: a survey”. In: *Bulletin of Mathematical Sciences* 12.02 (2022), p. 2230004.

[73] A. Golovin, S. Davis, and A. Nepomnyashchy. “Model for faceting in a kinetically controlled crystal growth”. In: *Physical Review E* 59.1 (1999), p. 803.

[74] A. Golovin, M. Levine, T. Savina, and S. Davis. “Faceting instability in the presence of wetting interactions: A mechanism for the formation of quantum dots”. In: *Physical Review B—Condensed Matter and Materials Physics* 70.23 (2004), p. 235342.

[75] M. A. Grayson. “The heat equation shrinks embedded plane curves to round points”. In: *Journal of Differential geometry* 26.2 (1987), pp. 285–314.

[76] F. Guillén-González and G. Tierra. “On linear schemes for a Cahn–Hilliard diffuse interface model”. In: *Journal of Computational Physics* 234 (2013), pp. 140–171.

[77] K. F. Gurski and G. B. McFadden. "The effect of anisotropic surface energy on the Rayleigh instability". In: *Proceedings of the Royal Society of London. Series A: Mathematical, Physical and Engineering Sciences* 459.2038 (2003), pp. 2575–2598.

[78] M. E. Gurtin. *Thermomechanics of evolving phase boundaries in the plane*. 1993.

[79] M. E. Gurtin and M. E. Jabbour. "Interface Evolution in Three Dimensions with Curvature-Dependent Energy and Surface Diffusion: Interface-Controlled Evolution, Phase Transitions, Epitaxial Growth of Elastic Films". In: *Archive for Rational Mechanics and Analysis* 163.3 (2002), pp. 171–208.

[80] Y. Han, B. Unal, F. Qin, D. Jing, C. J. Jenks, D.-J. Liu, P. Thiel, and J. Evans. "Kinetics of facile bilayer island formation at low temperature: Ag/NiAl (110)". In: *Physical review letters* 100.11 (2008), p. 116105.

[81] W. Helfrich. "Elastic Properties of Lipid Bilayers: Theory and Possible Experiments". In: *Zeitschrift für Naturforschung C* 28.11–12 (1973), pp. 693–703. DOI: 10.1515/znc-1973-11-1209.

[82] C. Herring. "Some theorems on the free energies of crystal surfaces". In: *Physical Review* 82.1 (1951), p. 87.

[83] H. Hilton. *Mathematical Crystallography and the Theory of Groups of Movements, Clarendon*. 1903.

[84] D. W. Hoffman and J. W. Cahn. "A vector thermodynamics for anisotropic surfaces: I. Fundamentals and application to plane surface junctions". In: *Surface Science* 31 (1972), pp. 368–388.

[85] J. Hu and B. Li. "Evolving finite element methods with an artificial tangential velocity for mean curvature flow and Willmore flow". In: *Numerische Mathematik* 152.1 (2022), pp. 127–181.

[86] G. Huisken. "Flow by mean curvature of convex surfaces into spheres". In: *Journal of Differential Geometry* 20.1 (1984), pp. 237–266.

[87] G. Huisken. "Asymptotic behavior for singularities of the mean curvature flow". In: *Journal of Differential Geometry* 31.1 (1990), pp. 285–299.

[88] G. Huisken and C. Sinestrari. "Convexity estimates for mean curvature flow and singularities of mean convex surfaces". In: *Acta Mathematica* 183.1 (1999), pp. 45–70.

[89] G. Huisken and C. Sinestrari. "Mean curvature flow singularities for mean convex surfaces". In: *Calculus of Variations and Partial Differential Equations* 8.1 (1999), pp. 1–14.

[90] W. Jiang, W. Bao, C. V. Thompson, and D. J. Srolovitz. "Phase field approach for simulating solid-state dewetting problems". In: *Acta Materialia* 60.15 (2012), pp. 5578–5592.

[91] W. Jiang and B. Li. "A perimeter-decreasing and area-conserving algorithm for surface diffusion flow of curves". In: *Journal of Computational Physics* 443 (2021), p. 110531.

[92] W. Jiang, Y. Wang, Q. Zhao, D. J. Srolovitz, and W. Bao. "Solid-state dewetting and island morphologies in strongly anisotropic materials". In: *Scripta Materialia* 115 (2016), pp. 123–127.

[93] W. Jiang and Q. Zhao. "Sharp-interface approach for simulating solid-state dewetting in two dimensions: a Cahn–Hoffman $\xi$-vector formulation". In: *Physica D: Nonlinear Phenomena* 390 (2019), pp. 69–83.

[94] W. Jiang, Q. Zhao, and W. Bao. "Sharp-interface model for simulating solid-state dewetting in three dimensions". In: *SIAM Journal on Applied Mathematics* 80.4 (2020), pp. 1654–1677.

[95] E. Jiran and C. Thompson. "Capillary instabilities in thin films". In: *Journal of Electronic Materials* 19.11 (1990), pp. 1153–1160.

[96] E. Jiran and C. Thompson. "Capillary instabilities in thin, continuous films". In: *Thin Solid Films* 208.1 (1992), pp. 23–28.

[97] B. Kovács, B. Li, and C. Lubich. "A convergent evolving finite element algorithm for mean curvature flow of closed surfaces". In: *Numerische Mathematik* 143.4 (2019), pp. 797–853.

[98] B. Kovács, B. Li, and C. Lubich. "A convergent evolving finite element algorithm for Willmore flow of closed surfaces". In: *Numerische Mathematik* 149.3 (2021), pp. 595–643.

[99] M. v. Laue. "Der Wulffsche Satz für die Gleichgewichtsform von Kristallen". In: *Zeitschrift für Kristallographie-Crystalline Materials* 105.1-6 (1943), pp. 124–133.

[100] F. Leroy, F. Cheynis, T. Passanante, and P. Müller. "Influence of facets on solid state dewetting mechanisms: Comparison between Ge and Si on SiO 2". In: *Physical Review B—Condensed Matter and Materials Physics* 88.3 (2013), p. 035306.

[101] F. Leroy, F. Cheynis, Y. Almadori, S. Curiotto, M. Trautmann, J. Barbé, P. Müller, et al. "How to control solid state dewetting: A short review". In: *Surface Science Reports* 71.2 (2016), pp. 391–409.

[102] B. Li. "Parametric finite element approximations of curvature flows". In: *Mathematica Numerica Sinica* 44.2 (2022). In Chinese, pp. 145–162. DOI: 10.12286/jssx.j2021-0871.

[103] M. Li, Y. Li, and L. Pei. "A symmetrized parametric finite element method for simulating solid-state dewetting problems". In: *Applied Mathematical Modelling* 121 (2023), pp. 731–750.

[104] M. Li and Q. Zhao. "Parametric finite element approximations for anisotropic surface diffusion with axisymmetric geometry". In: *Journal of Computational Physics* 497 (2024), p. 112632.

[105] M. Li and C. Zhou. "Energy-stable parametric finite element approximations for regularized solid-state dewetting problems in strongly anisotropic materials". In: *Journal of Nonlinear Science* 35.3 (2025), p. 52.

[106] M. Li and C. Zhou. "Structure-preserving parametric finite element methods for simulating axisymmetric solid-state dewetting problems with anisotropic surface energies". In: *Journal of Computational Physics* 531 (2025), p. 113944.

[107] M. Li and C. Zhou. "Structure-preserving parametric finite element methods for simulating axisymmetric solid-state dewetting problems with anisotropic surface energies". In: *Journal of Computational Physics* 531 (2025), p. 113944.

[108] Y. Li and W. Bao. "An energy-stable parametric finite element method for anisotropic surface diffusion". In: *Journal of Computational Physics* 446 (2021), p. 110658.

[109] H. Liebmann. "IX. Der Curie-Wulff'sche Satz über Combinationsformen von Krystallen". In: *Zeitschrift für Kristallographie-Crystalline Materials* 53.1-6 (1914), pp. 171–177.

[110] C. Mantegazza. *Lecture notes on mean curvature flow*. Vol. 290. Springer Science & Business Media, 2011.

[111] A. Maxwell, C. V. Thompson, and W. C. Carter. "A level-set method for simulating solid-state dewetting in systems with strong crystalline anisotropy". In: *Acta Materialia* 282 (2025), p. 120368.

[112] J. Mizsei. "How can sensitive and selective semiconductor gas sensors be made?" In: *Sensors and Actuators B: Chemical* 23.2-3 (1995), pp. 173–176.

[113] W. W. Mullins. "Two-dimensional motion of idealized grain boundaries". In: *Journal of Applied Physics* 27.8 (1956), pp. 900–904.

[114] W. W. Mullins. "Theory of thermal grooving". In: *Journal of Applied Physics* 28.3 (1957), pp. 333–339.

[115] W. W. Mullins. "Proof that the Two-Dimensional Shape of Minimum Surface Free Energy is Convex". In: *Journal of Mathematical Physics* 3.4 (1962), pp. 754–759.

[116] R. Nuryadi, Y. Ishikawa, and M. Tabe. "Formation and ordering of self-assembled Si islands by ultrahigh vacuum annealing of ultrathin bonded silicon-on-insulator structure". In: *Applied surface science* 159 (2000), pp. 121–126.

[117] S. Osher and R. P. Fedkiw. "Level set methods: an overview and some recent results". In: *Journal of Computational physics* 169.2 (2001), pp. 463–502.

[118] B. Palmer. "Stability of the Wulff shape". In: *Proceedings of the American Mathematical Society* 126.12 (1998), pp. 3661–3667.

[119] D. Peng, S. Osher, B. Merriman, and H.-K. Zhao. "The geometry of Wulff crystal shapes and its relations with Riemann problems". In: *Nonlinear Partial Differential Equations* 238 (1999), pp. 251–303.

[120] M. Plateau. "XXXVII. On the recent theories of the constitution of jets of liquid issuing from circular orifices". In: *The London, Edinburgh, and Dublin Philosophical Magazine and Journal of Science* 12.79 (1856), pp. 286–297.

[121] E. Radice, M. Salvalaglio, and R. Bergamaschini. "Phase-field modelling of anisotropic solid-state dewetting on patterned substrates". In: *Acta Materialia* 292 (2025), p. 120992.

[122] S. Randolph, J. Fowlkes, A. Melechko, K. Klein, H. Meyer III, M. Simpson, and P. Rack. "Controlling thin film structure for the dewetting of catalyst nanoparticle arrays for subsequent carbon nanofiber growth". In: *Nanotechnology* 18.46 (2007), p. 465304.

[123] O. Reynolds. *Papers on mechanical and physical subjects*. CUP Archive, 1983.

[124] T. V. Savina, A. A. Golovin, S. H. Davis, A. A. Nepomnyashchy, and P. W. Voorhees. "Faceting of a growing crystal surface by surface diffusion". In: *Physical Review E* 67.2 (2003), p. 021606.

[125] V. Schmidt, J. V. Wittemann, S. Senz, and U. Gösele. "Silicon nanowires: a review on aspects of their growth and their electrical properties". In: *Advanced Materials* 21.25-26 (2009), pp. 2681–2702.

[126] B. Seguin and E. Fried. "Microphysical derivation of the Canham–Helfrich free-energy density". In: *Journal of Mathematical Biology* 68.3 (2014), pp. 647–665. DOI: 10.1007/s00285-013-0647-9.

[127] D. Sevcovic and K. Mikula. "Evolution of plane curves driven by a nonlinear function of curvature and anisotropy". In: *SIAM Journal on Applied Mathematics* 61.5 (2001), pp. 1473–1501.

[128] E. Shustorovich. *Metal-surface reaction energetics. Theory and application to heterogeneous catalysis, chemisorption, and surface diffusion*. New York, NY (United States); VCH Publishers Inc., 1990.

[129] M. Siegel, M. Miksis, and P. Voorhees. "Evolution of material voids for highly anisotropic surface energy". In: *Journal of the Mechanics and Physics of Solids* 52.6 (2004), pp. 1319–1353.

[130] H. M. Soner. "Motion of a set by the curvature of its boundary". In: *Journal of Differential Equations* 101.2 (1993), pp. 313–372.

[131] D. J. Srolovitz. "On the stability of surfaces of stressed solids". In: *Acta Metallurgica* 37.2 (1989), pp. 621–625.

[132] D. J. Srolovitz and S. A. Safran. "Capillary instabilities in thin films. I. Energetics". In: *Journal of Applied Physics* 60.1 (1986), pp. 247–254.

[133] T. Tang and Z. Qiao. "Efficient numerical methods for phase-field equations". In: *Scientia Sinica Mathematica* 50.6 (2020). In Chinese, pp. 775–794. DOI: 10.1360/SSM-2020-0042.

[134] J. Taylor. "Existence and structure of solutions to a class of nonelliptic variational problems". In: *Symposia Mathematica*. Vol. 14. 1974, pp. 499–508.

[135] J. E. Taylor and J. W. Cahn. "Linking anisotropic sharp and diffuse surface motion laws via gradient flows". In: *Journal of Statistical Physics* 77.1 (1994), pp. 183–197.

[136] C. V. Thompson. "Solid-state dewetting of thin films". In: *Annual Review of Materials Research* 42.1 (2012), pp. 399–434.

[137] P. Voorhees, S. Coriell, G. McFadden, and R. Sekerka. "The effect of anisotropic crystal-melt surface tension on grain boundary groove morphology". In: *Journal of Crystal Growth* 67.3 (1984), pp. 425–440.

[138] Y. Wang. "Modeling and Simulations for Solid-state Dewetting Problems in Two Dimension". PhD thesis. National University of Singapore, 2016.

[139] Y. Wang, W. Jiang, W. Bao, and D. J. Srolovitz. "Sharp interface model for solid-state dewetting problems with weakly anisotropic surface energies". In: *Physical Review B* 91.4 (2015), p. 045303.

[140] B. White. "The size of the singular set in mean curvature flow of mean-convex sets". In: *Journal of the American Mathematical Society* 13.3 (2000), pp. 665–695.

[141] G. Wulff. “Zur Frage der Geschwindigkeit des Wachstums und der Auflösung der Kristall achen”. In: *Z. Kristallogr* 34 (1901), pp. 449–530.

[142] Y. Xu and C.-W. Shu. “Local discontinuous Galerkin method for surface diffusion and Willmore flow of graphs”. In: *Journal of Scientific Computing* 40.1 (2009), pp. 375–390.

[143] L. Xue and Y. Han. “Pattern formation by dewetting of polymer thin film”. In: *Progress in Polymer Science* 36.2 (2011), pp. 269–293.

[144] S. Yazaki. “On an area-preserving crystalline motion”. In: *Calculus of Variations and Partial Differential Equations* 14.1 (2002), pp. 85–105.

[145] J. Ye and C. V. Thompson. “Mechanisms of complex morphological evolution during solid-state dewetting of single-crystal nickel thin films”. In: *Applied Physics Letters* 97.7 (2010).

[146] J. Ye and C. V. Thompson. “Templated Solid-State Dewetting to Controllably Produce Complex Patterns”. In: *Advanced Materials* 23.13 (2011), pp. 1567–1571.

[147] W. Zhang and I. Gladwell. “Evolution of two-dimensional crystal morphologies by surface diffusion with anisotropic surface free energies”. In: *Computational Materials Science* 27.4 (2003), pp. 461–470.

[148] Y. Zhang. *A unified structure-preserving framework for geometric flows with coupled orientation and curvature dependence*. Sept. 29, 2026. arXiv: 2609.36419 [math.NA]. URL: https://arxiv.org/abs/2609.36419v1.

[149] Y. Zhang, Y. Li, and W. Ying. “A stabilized parametric finite element method for surface diffusion with an arbitrary surface energy”. In: *Journal of Computational Physics* 523 (2025), p. 113605. DOI: 10.1016/j.jcp.2024.113605.

[150] Q. Zhao, W. Jiang, and W. Bao. “A parametric finite element method for solid-state dewetting problems in three dimensions”. In: *SIAM Journal on Scientific Computing* 42.1 (2020), B327–B352.

[151] Q. Zhao, W. Jiang, and W. Bao. “An energy-stable parametric finite element method for simulating solid-state dewetting”. In: *IMA Journal of Numerical Analysis* 41.3 (2021), pp. 2026–2055.

[152] O. Zik and E. Moses. “Fingering instability in combustion: An extended view”. In: *Physical Review E* 60.1 (1999), p. 518.

# Notation Index


$(\cdot,\cdot)_\Gamma$, 18
$(\cdot,\cdot)^h_{\Gamma^h}$, 21
$\langle\cdot,\cdot\rangle^h_{\Gamma^h}$, 91

$A(t)$, 19
$A^h(t)$, 22
$A^m$, 23
$A_o(t)$, 51
$A^m_o$, 52

$C$, 113

$e^h(t)$, 30

$\hat{\boldsymbol{G}}(\theta)$, 10
$\gamma(\boldsymbol{n})$, 3
$\hat{\gamma}(\theta)$, 3
$\hat{\gamma}(\theta,\phi)$, 5
$\boldsymbol{G}_k(\boldsymbol{n})$, 11
$\hat{\boldsymbol{G}}_k(\theta)$, 16
$\hat{\boldsymbol{G}}^\alpha_k(\theta,\phi)$, 89
$\nabla_\Gamma f$, $\nabla_\Gamma\cdot\boldsymbol{f}$, 87

$H^1(\mathbb{I})$, $H^1_p(\mathbb{I})$, 18
$H^1_0(\Gamma)$, 114
$H^1(\Gamma)$, $[H^1(\Gamma)]^3$, 90

$\mathcal{J}\{\sigma\}$, 91

$k(\theta,\phi)$, 89
$\mathbb{K}^h_0$, 52
$k_0(\theta)$, 24
$\kappa$, 4
$\mathbb{K}(\Gamma^m)$, $\mathbb{K}^m$, 91
$\mathbb{K}^h$, $\mathbb{K}^h_p$, 21
$k^\alpha_{\min}(\theta)$, $k^\alpha_0(\theta)$, 66
$k^\alpha_{\min}(\theta,\phi)$, 93

$L^2(\mathbb{I})$, 18
$L^2(\Gamma)$, 90

$M^\alpha(U,\lambda;\boldsymbol{n})$, 93
$M(\Gamma_1,\Gamma_2)$, 30
$\mu$, 4

$\partial_s f$, 21
$\boldsymbol{\mathcal{P}}^k$, 21

$R^h_{\gamma'}$, 30

$\mathbb{S}^{d-1}$, 3

$\theta_Y$, 114

$\boldsymbol{U}:\boldsymbol{V}$, 90

$V(t)$, 91
$V^m$, 92
$V_n$, 6

$W(\Gamma)$, 3
$W(t)$, 19
$W^h(t)$, 22
$W^m$, 23
$W_o(t)$, 51
$W^m_o$, 52

$\boldsymbol{\xi}(\boldsymbol{n})$, 4
$\boldsymbol{\xi}(\theta)$, $\boldsymbol{\xi}(\theta,\phi)$, 5

$\boldsymbol{Z}_k(\boldsymbol{n})$, 10
$\hat{\boldsymbol{Z}}_k(\theta)$, 36

# Subject Index


almost slit domain, 84
Anisotropic curvature flow, 6
Anisotropic surface diffusion, 6
anisotropy, 1
asymptotically quasi-uniform, 32
auxiliary functions, 24, 38

Cahn-Hoffman, 4
chemical potential, 4
conormal, 114
conservative form, 17
contact line mobility, 50
curvature-driven problems, 1

discrete surface gradient, 92
discrete surface Jacobian matrix, 92
Divergence theorem, 90

energy-stable parametric finite element method, 61
equilibrium, 7
evolving surface finite element method, 8

facet-like, 118
faceting, 119
finite subcover theorem, 29
first variation, 4
Frank diagram, 3
Frobenius inner product, 90

generalized Winterbottom construction, 55
genus, 108

level set method, 8
Local energy estimate, 24, 38

manifold distance, 30
marker-particle method, 8
mass-lumped inner product, 21, 91
mean value theorem, 27
minimal stabilizing function, 24, 38, 93

normal velocity, 6
normal velocity laws, 71
normalized area loss, 30
normalized energy, 30, 105
normalized volume loss, 105
numerical error, 30

parametric finite element method, 8
pinch-off, 47, 108, 118
positive homogeneity, 24

Rayleigh-like instability, 118
robustness, 30
round-off error, 32

semi-implicit Euler method, 22
sharp interface model, 113
sharp-interface model, 49
signed area, 84
Sobolev space, 114
Sobolev spaces, 18, 64, 90
solid-state dewetting, 49, 113
stabilizing function, 16, 36, 62, 89
subadditivity, 24
sublinear, 24
surface divergence, 87
surface Jacobian matrix, 87
surface stiffness, 3
symmetrized structure-preserving parametric finite element method, 10

tolerance, 30
transport lemma, 19

volume-preserving anisotropic curvature flow, 6

weak formulation, 18
weighted curvature, 16
weighted mesh ratio, 30
Wulff shape, 7